The Charge Asymmetry in W Bosons Production in $p\overline{p}$ Collisions at the $\sqrt{s} = 1.96$ TeV using the DØ Detector at the Fermilab Tevatron

David Khatidze

Submitted in partial fulfillment of the
requirements for the degree
of Doctor of Philosophy
in the Graduate School of Arts and Sciences

COLUMBIA UNIVERSITY
2009

Abstract

The Charge Asymmetry in W Bosons Production in $p\overline{p}$ Collisions at the $\sqrt{s} = 1.96$ TeV using the DØ Detector at the Fermilab Tevatron

David Khatidze

We present a measurement of the W boson charge asymmetry in $p\bar{p}$ collisions using $W \to e\nu$ decays using 750 pb^{-1} of data collected with the DØ detector at the Fermilab Tevatron. The electron coverage is extended to $|\eta| < 3.2$ and is thus sensitive to Ws generated with low and high x partons. We also measured the charge asymmetry for events with electron $E_T > 25$ GeV, $25 < E_T < 35$ GeV and $E_T > 35$ GeV. By dividing events into different electron E_T regions, we can probe different W boson rapidity regions, and can provide more constraints on the parton distribution functions (PDFs). Theoretical predictions made using CTEQ6.6 and MRST2004NLO PDFs are compared with the measurement. Our measurement is the most precise W charge asymmetry measurement to date, and this single measurement is superior in precision to the combined world average of all previous W charge asymmetry measurements done at the Tevatron. The measured asymmetry errors are less than the CTEQ6.6 PDF uncertainty for most rapidity bins. The inclusion of our results will further constrain future PDF fits and improve the predictions.

Table of Contents

0.1 Thesis Overview

The Standard Model (SM) of particle physics is a theory which describes fundamental particles and their interactions. In the SM of particle physics the proton is made up of fundamental constituents called quarks. Protons and neutrons are made of quarks and make up most of the everyday matter around us. To understand the nature of the proton, it is important to understand the detailed make up of the proton. The properties of the quarks in the proton are described by the Parton Distribution Functions (PDF). In this thesis we will present a measurement of the ratio of PDFs of the two types of quarks that make up the proton. The structure of this thesis is as follows. In Chapter 1 we present the a brief description of the SM and the physical quantities that we will be measuring, as well as the current experimental situation. In Chapters 2 and 3 we describe the detector, D0, that was used to make this measurement, where I highlight in Chapter 3 the Silicon Track Trigger (STT) which is the detector system that I worked on. In Chapter 4 we describe the methods that we use to reconstruct the particles and their properties from the digital signals that we receive from the detector and Chapter 5 talks about how we select data that is useful for this analysis from the wealth of data collected at D0. Chapters 6, 7, 8 and 9 are the body of the thesis where we present the measurement itself. In Chapter 10 we show results and in Chapter 11 we draw conclusions. After the conclusions you can see the copy of the paper on this analysis published in PRL[1].

Chapter 1

Theory and Previous Experimental Status

1.1 The Standard Model

According to the SM, particles are divided in two groups, bosons and fermions. Fermions are particles with odd half integer spin and they are the building blocks of the matter around us. Bosons have integer spin and mediate the fundamental forces between fermions.

There are four fundamental forces in nature, electromagnetic, strong, weak and gravitational, only the first three of which are included in the SM (Table 1.1). Photons mediate the electromagnetic force between particles that have electric charge. The photon is massless and its interaction falls as $1/r^2$. The weak interaction is mediated by W and Z bosons, they are both very massive and act only at very small distances. The strong interaction charge is called 'color' (which is simply a name for the strong charge and has nothing to do with visual color) and the interaction between colored particles is mediated by gluons. There are three colors (each of which has corresponding anti-color), 'red', 'green' and 'blue'. Gluons themselves are colored and therefore they can interact with each other.

Fermions are divided into two families, leptons and quarks, which in turn are each divided into three generations. Tau leptons, muons and electrons interact through the electromagnetic and weak forces. Each charged lepton has a corresponding neutrino which only interacts through the weak force. The quark generations are (u and d), (c and s) and (t and b) and they can interact via all of the forces. The fundamental fermions are summarized in Table 1.2.

Particles composed of quarks are called hadrons. There are two types of hadrons,

Force	Gauge Boson	Symbol	Charge	Mass(GeV/c^2)	Spin
Electromagnetic	Photon	γ	0	0	1
Weak	Z	Z	0	91.2	1
Weak	$W^{\pm}$	$W^{\pm}$	± 1	80.4	1
Strong	Gluon	g	0	0	1

Table 1.1: Fundamental forces and gauge bosons with their properties.

Name	Symbol	charge	Mass(MeV/c^2)	Spin	Interactions
electron	e	-1	0.511	1/2	Electromagnetic, Weak
electron neutrino	ν_e	0	<0.000003	1/2	Weak
up quark	u	2/3	≈ 3	1/2	All
down quark	d	-1/3	≈ 5	1/2	All
muon	μ	-1	105.6	1/2	Electromagnetic, Weak
muon neutrino	ν_μ	0	<0.19	1/2	Weak
charm quark	c	2/3	≈ 1200	1/2	All
strange quark	s	-1/3	≈ 100	1/2	All
tau	τ	-1	1777	1/2	Electromagnetic, Weak
tau neutrino	ν_τ	0	<18.2	1/2	Weak
top quark	t	2/3	≈ 178000	1/2	All
bottom quark	b	-1/3	≈ 4500	1/2	All

Table 1.2: Fundamental fermions and their properties.

baryons and mesons. Baryons are composed of three quarks (or three antiquarks) while mesons are composed of a quark-antiquark pair.

The neutron is a baryon with a valence quark combination of *udd* with a 0 electric charge. A slightly different quark combination, *uud*, makes up a proton with charge 1. To date no particle with net color has been observed, hadrons have to be color-neutral. Because of the non-Abelian nature of the strong force, which means that gluons mediating the strong force interact with each other as well as with the quarks, the strong force increases with the distance. At large inter-quark distances it becomes energetically favorable to create a quark-antiquark pair. This pair interacts with the original quarks to generate more quarks, until the kinetic energy of the original quarks has been used to create clusters of quarks with no net color. As there are no hadrons with net color, each quark in a baryon must have a different color (which in combination give a neutral

color) and mesons must have color-anticolor quarks.

1.2 Parton Distribution Functions

The concept of a cross section is used to express the likelihood of an interaction between particles. The cross section σ is an effective area that characterizes how the particles will interact. The term is derived from the purely classical picture of point-like projectiles directed to an area that includes a solid target. Assuming that an interaction will occur if the projectile hits the solid target, and will not occur if it misses, the total interaction probability for the single projectile will be the ratio of the area of the section of the solid (the cross section, represented by σ) to the total targeted area. This basic concept is then extended to the cases where the interaction probability in the targeted area assumes intermediate values - because the target itself is not homogeneous, or because the interaction is mediated by a non-uniform field.

The cross section is one of the most frequently measured quantities in high energy physics. Modeling hadronic cross sections is complicated by the structure of the hadron. A $p\bar{p}$ interaction is actually the interaction between a quark or a gluon from the proton and another from the antiproton. The formula for the inelastic $p\bar{p}$ interaction cross section is given by the equation

$$\sigma_{P+\overline{P}\to X} = \sum_{ij} \int d\mathbf{p}_i d\mathbf{p}_j f_i(x_i) f_j(x_j) \sigma_{ij\to X}(\mathbf{p}_i \mathbf{p}_j) \tag{1.1}$$

Here, the sum is over all partons (quarks and gluons) and $\sigma_{ij\to X}(\mathbf{p}_i\mathbf{p}_j)$ is the partonic cross section. The $f_i(x_i)$ is the probability of finding parton i in the proton with $x_i = |\mathbf{p}_i|/|\mathbf{p}|$, where $\mathbf{p}$ is the momentum of the proton. These functions are called parton distribution functions (PDF), they are incalculable but they can be probed experimentally.

The experiments designed to study PDFs do not directly measure the parton distribution functions for u and d quarks, u(x) and d(x) (for simplicity we use u(x) and d(x) instead of $f_u(x_u)$ and $f_d(x_d)$). Deep Inelastic Scattering (DIS) experiments measure structure functions which are functions of the PDFs [2]. The W boson charge asymmetry measures the $d(\mathrm{x})/u(\mathrm{x})$ ratio. It is the work of collaborations of high energy theorists to extract from these experimental measurements the underlying PDF.

Two of the most prominent of these collaborations are CTEQ (Coordinated Theoretical-Experimental Project on QCD) [7] and MRST (Martin-Roberts-Stirling-Thorne) [8]. The two collaborations produce PDFs that are remarkably similar despite many differ-

ences in the collaborations' techniques.

1.3 W boson production

At $p\bar{p}$ colliders W bosons are most often produced by the annihilation of an u quark from the proton and a $\overline{d}$ quark from the antiproton, or a d quark from the proton and an $\overline{u}$ from the antiproton (Fig. 1.1). The u quark generally carries more of the protons momentum than d quark, therefore the W^+ tends to go in the proton's direction and the W^- in the antiproton's direction. Fig. 1.2, which is created using the simulated data, shows the y distribution of W^+ and W^- bosons, where y is the rapidity, defined below.

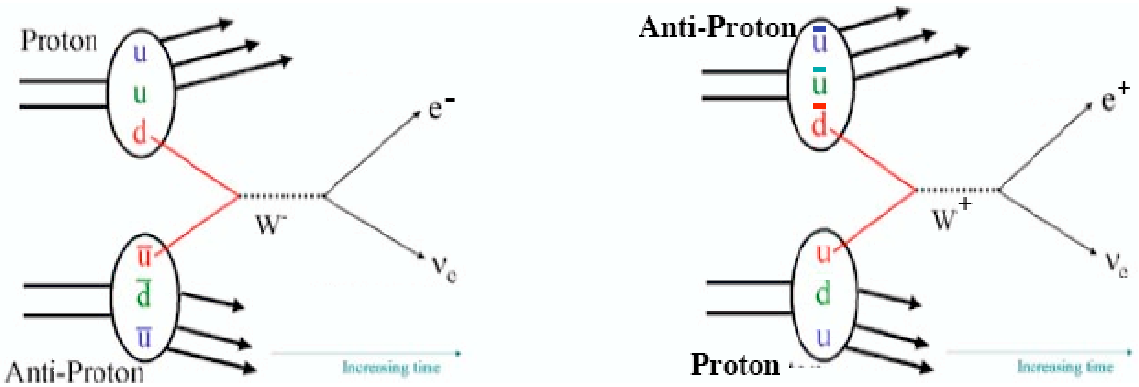

Figure 1.1: Production of a W^- by the annihilation of a d quark from the proton and an $\overline{u}$ from the antiproton, and of a W^+ by the annihilation of an u quark from the proton and a $\overline{d}$ quark from the antiproton.

The W asymmetry for a given rapidity, $A(y)$ is defined as the number of the W^+s at that rapidity minus the number of the W^-s at the same rapidity divided by the sum of the two.

$$A(y) = \frac{\frac{d\sigma_{W^+}}{dy} - \frac{d\sigma_{W^-}}{dy}}{\frac{d\sigma_{W^+}}{dy} + \frac{d\sigma_{W^-}}{dy}} \tag{1.2}$$

where the $\frac{d\sigma_{W^\pm}}{dy}$ is the $W^\pm$ density in the y direction.

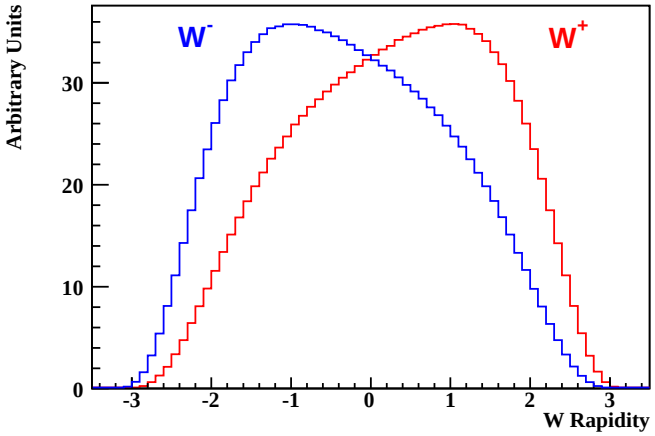

Figure 1.2: Simulated W^+ and W^- rapidity distributions.

1.4 Rapidity and momentum fraction

Both the protons and antiprotons at the Tevatron are highly relativistic, as are many particles produced by their interaction. Therefore it is convenient to measure the boost of the W boson as a Lorentz invariant quantity.

Since beams only have momentum in one dimension, coordinates can be defined so that all of the momentum lies along one axis, in our case z-axis. The rapidity, y, is a quantity that is Lorentz invariant under transformations along the z-axis. It is defined as

$$y = \frac{1}{2} ln \frac{E + p_z}{E - p_z} \tag{1.3}$$

where E is energy and p_z is the z-momentum of the particle.

From the conservation of energy in $q\bar{q} \rightarrow X$ processes, $E_X = E_q + E_{\overline{q}}$. Since the particles are highly relativistic, $E_q = p_q$ and

$$E_X = p_q + p_{\overline{q}} \tag{1.4}$$

From the conservation of momentum, $\mathbf{P}_X = \mathbf{P}_q + \mathbf{P}_{\overline{q}}$. Since all momenta are along the z axis, this equation reduces to the scalar equation

$$p_X = p_q - p_{\overline{q}} \tag{1.5}$$

substituting 1.4 and 1.5 into 1.3 we get

$$y = \frac{1}{2} ln \frac{p_q}{p_{\overline{q}}} \tag{1.6}$$

where we can write 1.6 in terms of $x_i = \frac{p_i}{p}$

$$y = \frac{1}{2} ln \frac{x_q}{x_{\overline{q}}} \tag{1.7}$$

or

$$e^{2y} = \frac{x_q}{x_{\overline{q}}} \tag{1.8}$$

which shows that the rapidity of the W boson is a measure of the relative momenta of the partons. More explicitly, the relation

$$E_X^2 = p_X^2 + m_X^2 \rightarrow x_q x_{\overline{q}} = \frac{m_X^2}{s} \tag{1.9}$$

where $\sqrt{s} = 2E_{beam}$ can be used to solve for x_q and $x_{\overline{q}}$.

$$x_q = \frac{m_X e^y}{\sqrt{s}} \tag{1.10}$$

$$x_{\overline{q}} = \frac{m_X e^{-y}}{\sqrt{s}} \tag{1.11}$$

These equations show that the wider the range of rapidities probed, the wider the range of x.

1.5 Hadronic cross section

Eq 1.1 can be used to calculate the cross section for a generic $p\bar{p}$ process. The W^+ is produced only by annihilation of u and $\overline{d}$ quarks. Therefore the sum in eq 1.1 reduces to

$$\sigma_{P+\overline{P}\to W^+} = \int d\mathbf{p}_u d\mathbf{p}_{\overline{d}} f_u(x_1) f_d(x_2) \sigma_{u\overline{d}\to W^+}(\mathbf{p}_u \mathbf{p}_{\overline{d}}) \tag{1.12}$$

For the sake of simplicity, $f_u(x)$ will be known as $u(x)$ and $f_d(x)$ as $d(x)$. It is assumed that the PDFs for quarks are the same as those for antiquarks, $u(x) = \overline{u}(x)$ and $d(x) = \overline{d}(x)$.

In the limit that the W boson mass resonance width is very narrow

$$\sigma_{u\overline{d}\to W^+}(\mathbf{p}_u \mathbf{p}_{\overline{d}}) = k\delta((p_u + p_{\overline{d}})^2 - M_W^2) \tag{1.13}$$

Converting from momentum to momentum fraction, this becomes

$$\sigma_{u\overline{d}\to W^+}(p_u p_{\overline{d}}) = k^{'}\delta((x_1 x_2 - \frac{M_W^2}{s}) \tag{1.14}$$

And equation 1.12 becomes

$$\sigma_{P+\overline{P}\to W^+} = K \int dx_1 dx_2 u(x_1) d(x_2) \delta((x_1 x_2 - \frac{M_W^2}{s}) \tag{1.15}$$

Integrating over x_2, using 1.10 and differentiating by y yields:

$$\frac{d\sigma_{P+\overline{P}\to W^+}}{dy} = K^{'} u(x_1) d(x_2) \tag{1.16}$$

The coefficients $k, k^{'}, K$ and $K^{'}$ correspond to the values of the W production cross sections. These coefficients get canceled in the ratio, so we do not need to know their values exactly.

This equation, along with its conjugate, the differential cross section for production of W^- bosons, is substituted into eq 1.2 to derive a formula for the asymmetry

$$A(y) = \frac{u(x_1)d(x_2) - u(x_2)d(x_1)}{u(x_1)d(x_2) + u(x_2)d(x_1)} \tag{1.17}$$

This equation can be rearranged to clarify that the asymmetry is a probe of the ratio $u(x)/d(x)$

$$A(y) = \frac{u(x_1)/d(x_1) - u(x_2)/d(x_2)}{u(x_1)/d(x_1) + u(x_2)/d(x_2)} \tag{1.18}$$

1.6 W boson decay

It is impossible to directly detect the W boson as it decays almost instantly, therefore Ws are identified by their decay products. About 70% of the time Ws decay hadronically, but it is nearly impossible to separate $W \to q\bar{q}$ from the direct production of quark

antiquark pairs. The remaining 30% of the time W decays into a lepton and a neutrino. A lepton and a neutrino provide a relatively distinct signal of a lepton and missing energy in the detector (corresponding to the neutrino which is not observed in the detector). W bosons decay equally into all three leptons and corresponding neutrinos, but this analysis studies only electron channel.

Naively, it might be expected that when a W decays, the electron and neutrino momentum could point in any direction as long as momentum is conserved. However, the leptonic decay of the W boson is governed by a V-A coupling [10], which constrains the angular distribution of the electrons by placing restrictions on the helicity of the particles involved.

Helicity is the relationship between a particle's momentum and its angular spin, defined as

$$H = \frac{sp}{|sp|} \tag{1.19}$$

where s is the spin of the particle and p is the momentum.

The $V-A$ nature of the electroweak theory requires that W bosons couple exclusively to left-handed quarks and leptons or right-handed antiquarks and antileptons. This means that to produce a W^+ boson, the u must be left-handed, and the $\overline{d}$ right-handed, as in Figure 1.3-a. Similarly, in Figure 1.3-b, when the W^+ boson decays electronically, the e^+ (an antiparticle) must be right-handed and the ν_e left-handed.The direction of motion of the e^+ is antiparallel that of the proton, whereas the direction of the W^+ boson tends to be parallel to it. This means that the electron decay of the W boson is asymmetric and this asymmetry tends to cancel the production asymmetry.

The measured lepton asymmetry is a convolution of the W production asymmetry and the $V-A$ decay asymmetry of leptons, and is defined as

$$A(y_e) = \frac{d\sigma(e^+)/dy - d\sigma(e^-)/dy}{d\sigma(e^+)/dy + d\sigma(e^-)/dy} \tag{1.20}$$

Fortunately, the lepton decay distribution is well-understood, so that a measurement of the electron asymmetry provides information about the ratio of $d(\mathrm{x})/u(\mathrm{x})$ equivalent to that which could be obtained by measuring the W boson asymmetry. Fig. 1.4 shows the W boson and decayed charged lepton asymmetry distributions.

The experimental measurement of the $W \to e\nu$ cross-section times branching ratio as a function of rapidity of the electron or positron is:

$$\sigma(y) \times Br(W^\pm \to e^\pm \nu) = \frac{N_{e^\pm}(y)}{\mathcal{L} \times \mathcal{A} \times \varepsilon} \tag{1.21}$$

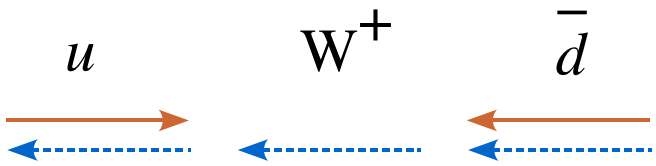

(a) W^+ boson production in $p\overline{p}$ collisions.

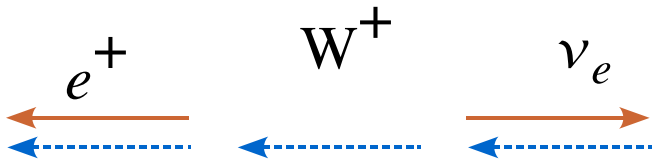

(b) Leptonic decay of W^+ bosons.

Figure 1.3: The momentum (solid line) and spin (dashed line) of particles in W^+ boson production and leptonic decay. If the momentum vector of the e^+ is reversed, its helicity becomes negative, which is not allowed. Reversing the direction of the momentum vector and the spin vector would maintain the positive helicity required, but reversal of the spin vector is not allowed because the angular momentum must be conserved.

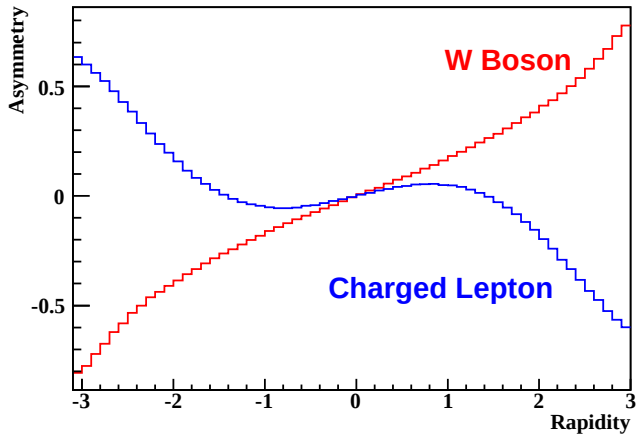

Figure 1.4: W boson and charged lepton asymmetry, no selection or E_T cuts applied. The measured lepton asymmetry is a convolution of the W production asymmetry and the $V-A$ decay asymmetry of leptons.

If the luminosity ($\mathcal{L}$), acceptance ($\mathcal{A}$) and electron selection efficiency ε are charge independent, they cancel in the ratio and the asymmetry measurement is reduced to a counting experiment:

$$A(y) = \frac{N_{e^+}(y) - N_{e^-}(y)}{N_{e^+}(y) + N_{e^-}(y)} \tag{1.22}$$

This thesis presents the measurement of the asymmetry in $\sim 750\text{pb}^{-1}$ of data and discusses the comparison of this distribution to theoretical predictions. For calculating the theoretical predictions we use RESBOS [5] and PHOTOS[6] together as the event generator. RESBOS is a Monte Carlo for Resummed Boson production and decay. It is used to compute the differential cross section for the processes $p\overline{p} \to B \to l_1 l_2$, where B is a boson ($W^{\pm}, Z, ...$) and l_1, l_2 are leptons. PHOTOS is a Monte Carlo program for QED single photon radiative corrections in decays, and is run on the output of RESBOS to simulate the final state photon radiations. RESBOS uses next-to-leading-order (NLO) perturbative calculation, which means that for the calculations it uses leading order (tree level) Feynman diagram and Feynman diagrams with the first order radiative corrections only Fig. 1.5.

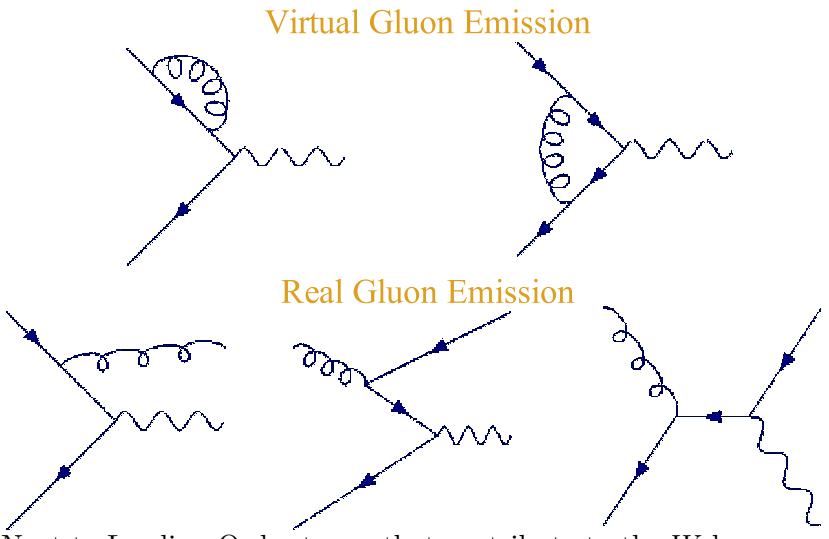

Figure 1.5: Next-to-Leading Order terms that contribute to the W boson cross section.

1.7 Previous experimental results

The lepton charge asymmetry from W decay was measured by the CDF collaboration in the electron and muon channels during Run I of the Tevatron Collider [9; 10] ($\sim$ 100 pb^{-1}) and in the electron channel using Run II data [11] ($\sim$ 170 pb^{-1}). DØ also

measured the lepton asymmetry in muon channel [12] (~ 300 pb^{-1}) using Run II data. The measurement described here is based on a larger data sample (~ 750 pb^{-1}) than these analyses and uses new technique by introducing electron types (more on that in Sec. 5.2).

Chapter 2

The Experimental Apparatus

2.1 Tevatron

The Fermi Tevatron Collider, which is located in the Fermi National Accelerator Laboratory (Fermilab), is the most powerful collider currently in operation in the world with center of mass energy of 1.96 TeV.

The Tevatron (Fig. 2.1) is a proton-antiproton collider, with beams of protons and antiprotons traveling in opposite directions around a circular ring of radius 1km. Producing, injecting and accelerating these beams is a complex process. The first stage of the acceleration is provided by the Cockcroft-Walton preaccelerator. Inside this device gaseous hydrogen is ionized to produce H^- ions, these ions are then accelerated to an energy 750 KeV. They continue on to a linear accelerator, Linac, which is 500 feet long and uses oscillating electric fields to accelerate H^- ions to 400 MeV. Before entering the third stage, the Booster, these ions pass through a carbon foil which removes the two electrons, leaving only the proton.

The Booster is a circular accelerator that uses magnets to bend the protons in a circular path. During each revolution around the Booster, protons experience an electric field that further accelerates them, eventually increasing their energy to 8 GeV. After this, protons are sent to the next stage of acceleration to the Main Injector, another synchrotron.

The Main Injector serves two purposes. First it is used to raise the energy to 150 GeV for injection into the Tevatron. Second, the Main Injector is used to accelerate the protons to 120 GeV, where they are directed on a nickel target to produce antiprotons. The target is followed by a lithium lens to focus the secondary particles and a dipole magnet to select 8 GeV antiprotons. These are then sent to the Debuncher, an 8 GeV synchrotron, to reduce the momentum spread. They are then stored in the Accumulator

ring and when a sufficient number have been accumulated, they are sent to the Main Injector.

The limiting factor for the luminosity was the number of antiprotons, that is why a new component, the Recycler, was added to the accelerator complex. When the Accumulator reaches its maximum capacity, the antiprotons are transferred to the Recycler, an 8 GeV storage ring with permanent magnets.

The Tevatron receives protons from the Main Injector and antiprotons from the Accumulator or the Recycler and accelerates them up to 0.98 TeV. Protons are accelerated in one direction and antiprotons in the opposite direction around the ring. Both protons and antiprotons are grouped in 36 bunches, where proton bunches contain $\approx 10^{11}$ particles and antiproton bunches have $\approx 10^{10}$ particles. The bunches cross each other every 396 ns at six points along the ring and at two of these, B0 and D0, are located two general purpose detectors, CDF (Collider Detector Facility) and D0.

The duration during which proton and antiproton beams circulate in the Tevatron is called a "store". Each store typically lasts several hours, sometimes even for more than 24 hours. Each collision of the proton and antiproton bunches recorded is called an event, events are grouped in "runs". Each store consists of several runs. Most parameters of the detector's operation are stored in databases in run-averaged format.

As the experiment continues operating, more and more data is accumulated. Currently (April 2009) 5.72 fb^{-1} of data is recorded for offline analysis out of 6.49 fb^{-1} delivered by the DØ detector (Fig. 2.2).

2.2 The D0 Detector

The D0 detector is a general purpose detector constructed to study $p\bar{p}$ collisions. The detector was initially commissioned in 1992 for Run I of the Tevatron, and it was significantly upgraded for the start of Run II in 2001.

In the detector, protons enter from the north side and antiprotons from the south, colliding in the center. Closest to the collision point is the tracking system, which consists of the Silicon Microstrip Tracker (SMT) and the Central Fiber Tracker (CFT), which are within a 2T field produced by a superconducting solenoid magnet. The tracker is surrounded by the calorimeter and in turn the muon system.

2.2.1 The Coordinate System

D0 uses a right-handed coordinate system, with the center of the detector defined to be (0,0,0). The direction of the proton beam defines the positive z axis, the y axis points

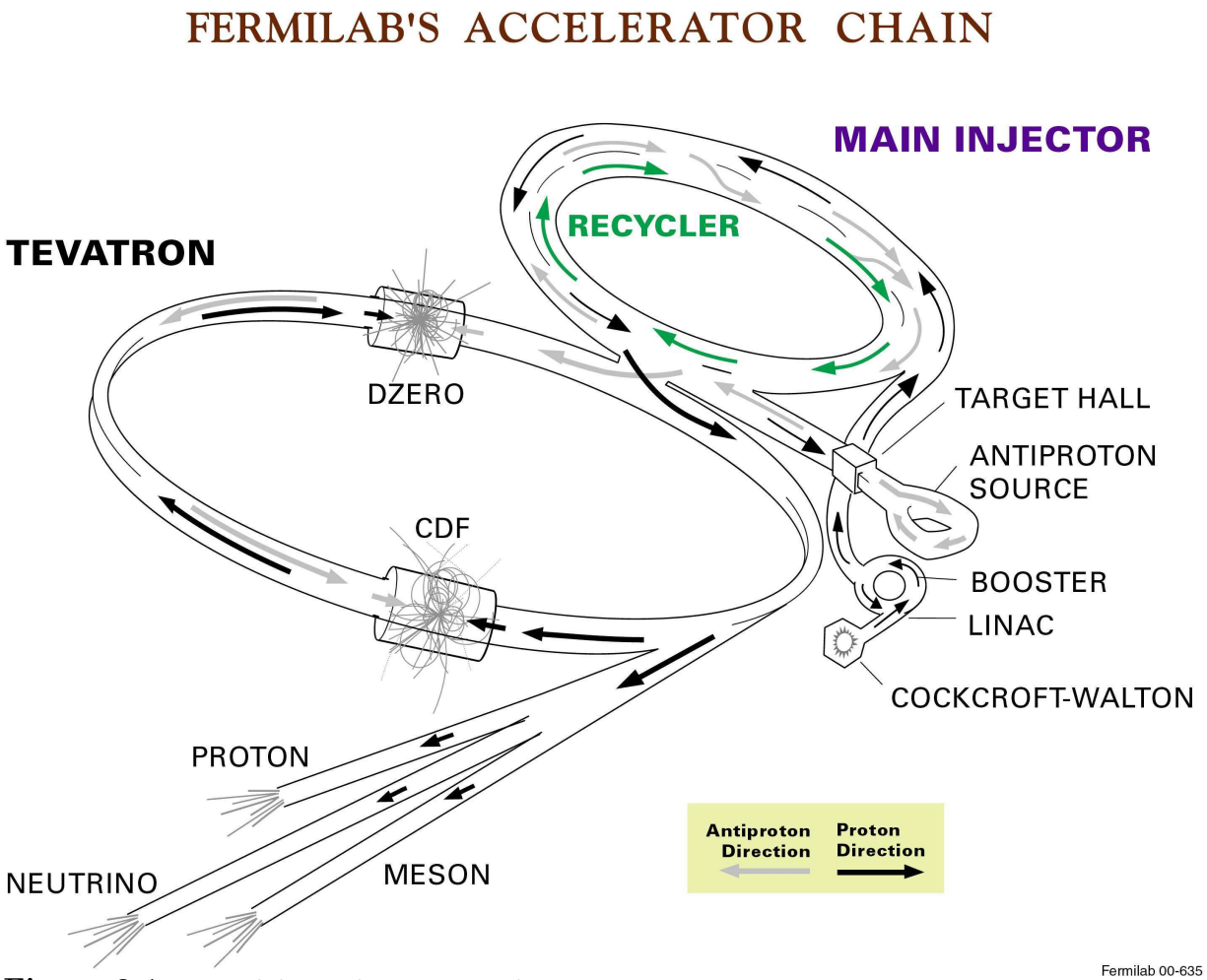

Figure 2.1: Fermilab accelerator complex.

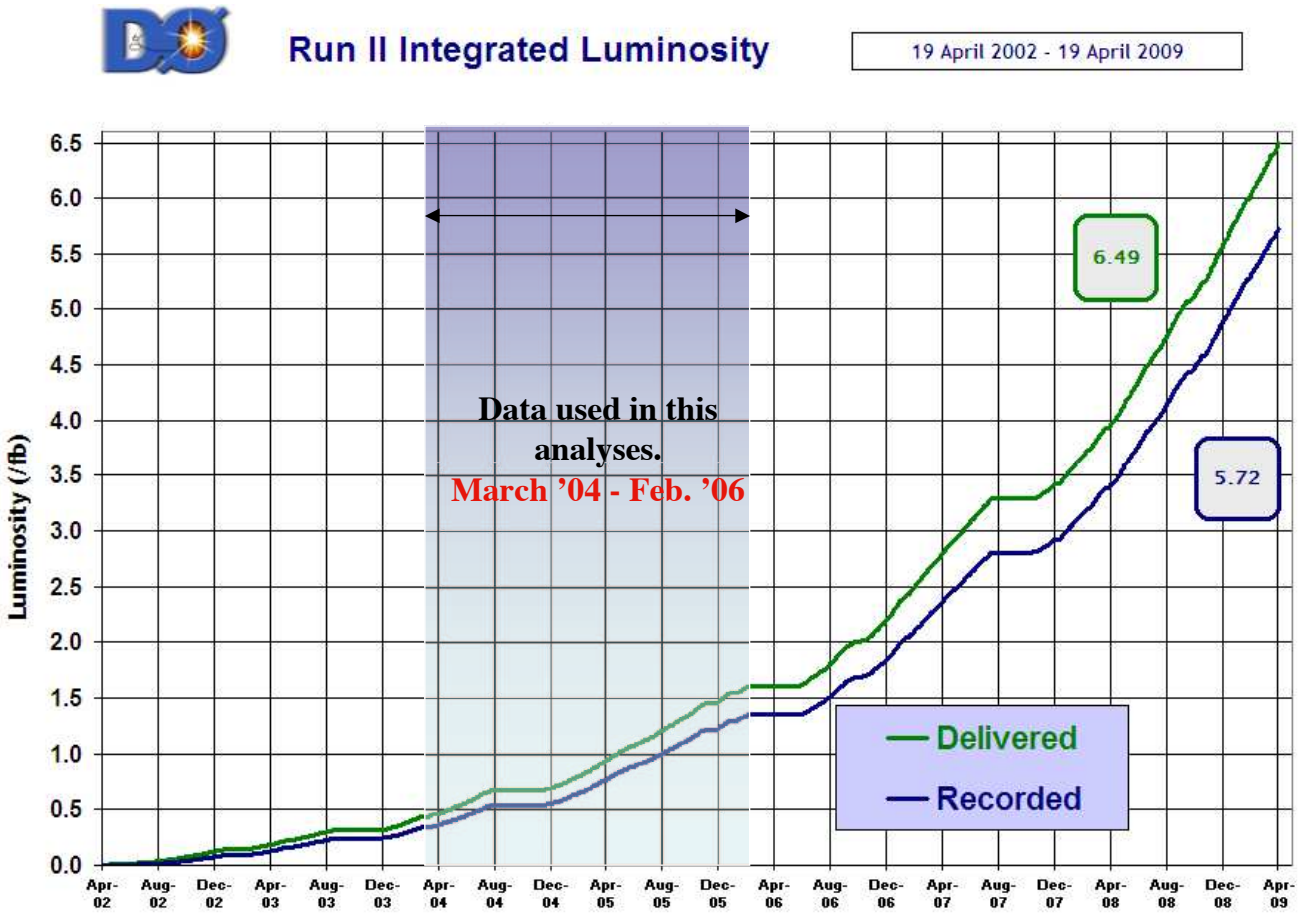

Figure 2.2: Delivered and recorded luminosities for the second stage of the DØ operation (Run II). The shaded area corresponds to the data used in this analysis.

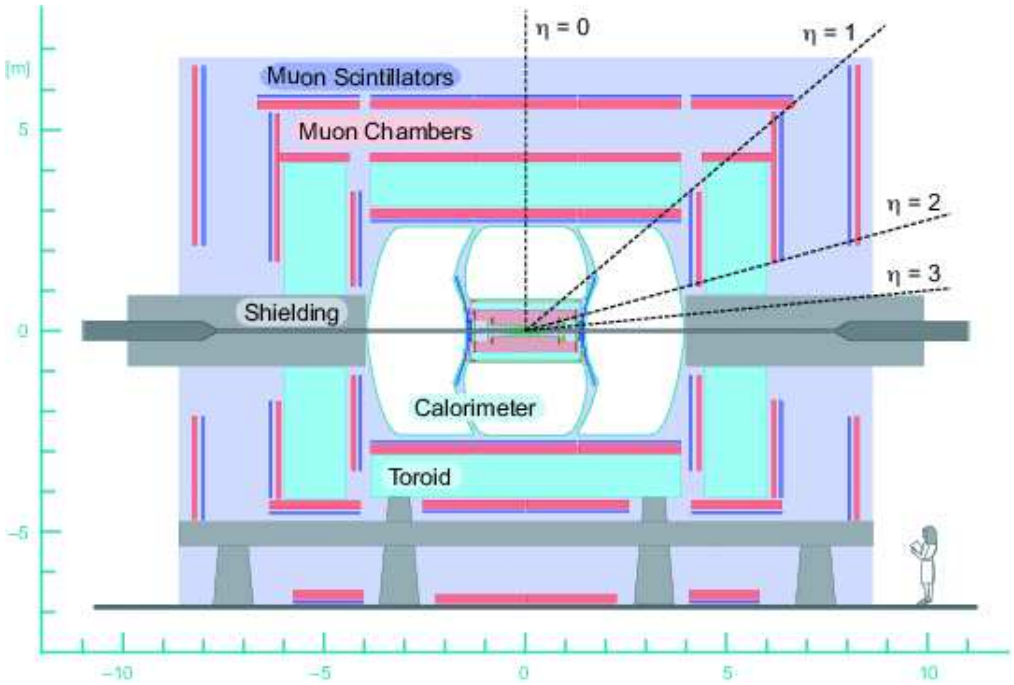

Figure 2.3: D0 detector.

upwards and the x axis to the center of the Tevatron. The azimuthal and polar angles are defined as:

$$\phi = tan^{-1}(y/x) \tag{2.1}$$

$$\theta = tan^{-1}(r/x) \tag{2.2}$$

where $r^2 = x^2 + y^2$. Since the partons participating in the collision carry a varying amount of their parent hadron's momentum, physics interactions often have large boosts along the beam direction. Moreover, many particles produced in the collisions escape down the uninstrumented beam pipe, therefore the observed momentum along the beam axis is not conserved. The total momentum in the transverse plane (p_x, p_y) does equal zero though, hence transverse values are often used. The most commonly used ones are

- $E_T = Esin\theta$ Transverse energy
- $p_T = psin\theta$ Transverse momentum
- MET, Missing transverse energy

The polar angle θ is usually replaced by the pseudorapidity, η, which is defined as

$$\eta = -ln(tan(\theta/2)) \tag{2.3}$$

which is an approximation of the true rapidity

$$y = \frac{1}{2} ln \frac{E + p_z}{E - p_z} \tag{2.4}$$

in the relativistic limit. Intervals in rapidity are invariant under a Lorentz boost in the z direction, which makes them a more convenient coordinate.

2.2.2 Tracking System

The tracking system (shown in Fig. 2.4) consists of the silicon microstrip tracker (SMT), the central fiber tracker (CFT), the superconducting solenoid and the preshower detector. The SMT is the innermost part of the tracker that provides good spatial resolution very close to the beamline. The CFT provides a fast trigger for tracks as well as a measurement of momentum (in conjunction with the SMT) of the track by measuring the curvature in the magnetic field. The preshower detectors are used to compensate for the energy loss in the solenoid and to provide additional separation for electrons and photons from the QCD jets.

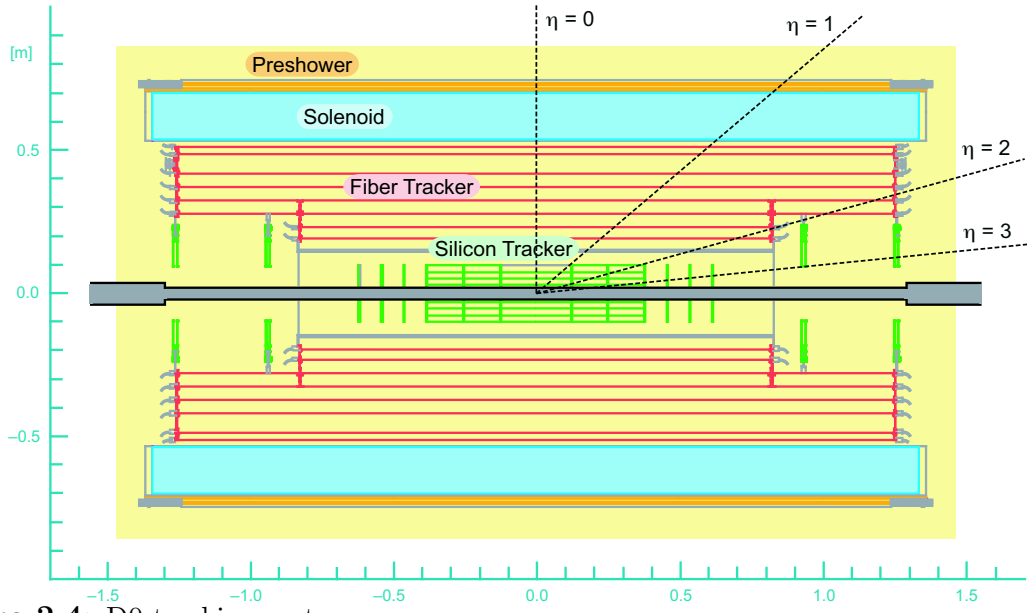

Figure 2.4: D0 tracking system.

2.2.3 Silicon Microstrip Tracker

The SMT uses the silicon *pn* junction technology to create a detector that can make position measurements of the order of $\approx 10\mu$m. It is made of two different structures, barrels and disks. Both structures have thin silicon strips of fine cathode lines on their surface. These silicon microstrips are solid state detector devices which give a signal when charged particles pass through them. The particles deposit small amounts of their energy in the material through ionization, producing electron-hole pairs. These pairs are collected at the nearest cathode which produces a signal that can be used to determine where the particle passed through the silicon. As there are many cathode lines with very small spacing, this gives a very accurate measurement of the position at which the particle crossed the material.

The position and design of the silicon detector is such that tracks can be reconstructed within $|\eta| < 3$. The relatively large length of the interaction region ($\sigma \approx 25$ cm) complicated the design of the SMT, resulting in the hybrid barrel-disk structure (Fig. 2.5). The barrels are located at the center of the interaction region so that the vertex is likely to be within the acceptance region. The disks are placed further out along the beamline to obtain maximum coverage.

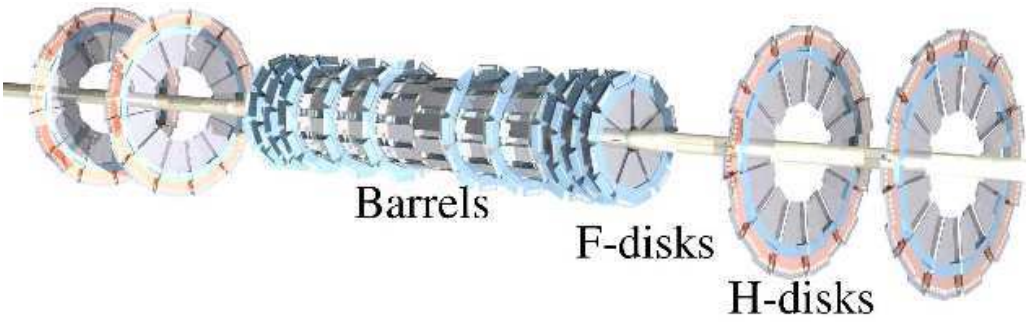

Figure 2.5: Silicon microstrip tracker.

The four barrels closest to the center have four layers of double sided silicon microstrips in the axial direction and at ninety degrees to the axial direction, which allows the reconstruction of the three dimensional hits. The outermost barrels have only single sided silicon strips in the axial direction and two degrees to the axial.

The innermost disks, called "F-disks", are made up of double sided silicon strips one at minus fifteen degrees and the other at plus fifteen degrees. The outermost parts of the SMT are the "H-disks", these are larger diameter disks made up from single sided silicon strips that allow the detection of tracks at small angles to the beam direction.

For details about various sensor types in the SMT see Table 2.1.

Module	Type	Layer	Pitch (μm) p/n	Length (cm)	Inner Radius (cm)	Outer Radius
F-disks	DS	-	50/62.5	7.93	2.57	9.96
H-disks	SS	-	40	7.63^i	9.5	26
			80 readout	6.33^o		
Central	DSDM	1, 3	50/153.5	12.0	2.715	7.582
Barrels (4)	DS	2, 4	50/62.5	6.0	4.55	10.51
Outer	SS	1, 3	50	6.0	2.715	7.582
Barrels (2)	DS	2, 4	50/62.5	6.0	4.55	10.51

Table 2.1: SMT sensor specifications. SS stands for single sided, DS - double sided, DSDM - double sided double metal. i indicates the length of the inner H-disk sensor, o is the length of the outer H-disk sensor.

The SMT is read out by 128-channel readout chips called SVXIIe chips. These chips are designed to work with double sided detectors and can accept both positive and negative currents as input signals. The chips are mounted on a high density interconnect or HDI. The data passes from the HDI to the sequencer boards which are connected to the readout buffer. The whole SMT consists of a total of about 800,000 readout channels.

2.2.4 Central Fiber Tracker

The CFT surrounds the SMT and covers the pseudorapidity region of $|\eta| < 2$. It consists of ribbons of scintillating fiber which produce light when atomic electrons are excited by traversing charged particles. Clear fiber then acts as a waveguide for the produced photons carrying the light to the end of the cables. The diameter of the fibers is 835 μm.

The fibers are formed into doublet layers and are mounted on eight concentric cylinders arranged in layers with the smallest radius being $r = 20$ cm and largest $r = 52$ cm. The length of the outer layer is 2.52 m, while the inner layer is only 1.66 because of the large size of the SMT's H-disks. Each cylinder has an axial fiber doublet layer providing an $r - \phi$ measurement and a doublet layer with alternating stereo angles allowing the three dimensional reconstruction of tracks.

At one end of the fiber an aluminum mirror reflects the light back in the opposite direction, at the other end are optical fiber waveguides that conduct the light to Visible Light Photon Counters (VLPCs). The VLPCs are arsenic doped silicon diodes, operating at temperatures of 8-10 K, which convert collected photons into an electrical signal. They

have high gain (22,000 to 65,000 electrons per incoming photon), less than 0.1% average noise, and a position resolution of $\approx 100\mu$m.

2.2.5 Solenoid

The solenoid surrounding the tracking system is 2.73 m long and 1.42 m in diameter. It is a superconducting magnet and creates a highly uniform magnetic field of 2 Tesla. The trajectory of a charged particle is bent by the magnet thus allowing the measurement of its momentum. The magnet operates at 4749 A and stores 5.3 MJ energy.

2.2.6 Preshower detectors

The preshower detectors help in electron identification and triggering and also provide the electromagnetic energy correction for losses in the solenoid and other parts of detector material such as cables and supports. There are two kinds of preshower detectors, the central (CPS) and forward (FPS). The CPS is located in the 51 mm gap between the solenoid and the central calorimeter and covers the $|\eta| < 1.3$ region. It consists of three concentric layers of scintillating strips, an inner axial and two outer stereo layers. The strips have a triangular cross section with a base of 7 mm and a 1mm hole in the center. A wavelength shifting fiber passes through this hole and is read out by VLPC's in the same manner as the fiber tracker.

The two FPS are mounted on the faces of the end calorimeters and cover the $1.5 < |\eta| < 2.5$ region. They have a design similar to the CPS and use scintillating strips. A layer of lead is sandwiched between two scintillator planes to increase the amount of absorbing material. In the $1.5 < |\eta| < 1.65$ region particles go through a significant thickness of the solenoid so no additional layer of the lead is required.

2.2.7 Calorimeter

Calorimeters are used to measure the energy and position of particles. As particles pass through the calorimeter they interact with the medium and lose energy, which can be measured. High energy electrons passing through the medium will lose energy by emitting photons via *bremsstrahlung* radiation. These photons will produce electron-positron pairs, which in turn will emit more photons, thus a cascade or "shower" of electromagnetic particles will be formed and this will continue until the energy of the electrons and positrons is small enough ($\approx$ 10 MeV), at which point they start to lose energy via ionization rather than bremsstrahlung. The total energy of these particles

is equal to the energy of the original electron and that energy can be measured by the ionization of atoms. A typical radiation length is a length over which a high energy electron loses all but 1/e of its energy. The EM layer (defined later in this chapter) of the calorimeter is ≈22 radiation length, so that electrons deposit almost all of their energies there.

Hadronic particles, on the other hand, interact with the atomic nuclei of matter via the strong force, instead of the electromagnetic force. They produce secondary particles which themselves interact, forming new particles with less energy, thus creating a hadronic shower. The average distances traveled by hadrons before an interaction is longer than in an electromagnetic case, hence hadronic showers penetrate further in the calorimeter than electromagnetic showers. When the energy of particles in the hadronic shower decreases sufficiently, they are detected by ionization loss. The neutral hadrons are detected by the production of secondary charged particles.

The D0 calorimeter is segmented into cells, each of which consists of absorbing materials, that induce shower formation and active materials where atoms are ionized by the passage of charged particles. The absorbers in the D0 calorimeter are depleted uranium, copper and stainless steel and liquid argon serves as the active material. The ionized charge is collected on the copper plates that are on each cell and the initial energy of the particle is measured by adding up the charge from all plates within the shower.

The D0 calorimeter is a compensating calorimeter, which means that it equalizes the response of the calorimeter signals from hadrons and electrons. This is achieved by tuning the thickness and materials chosen for the absorber. The depleted uranium absorber provides backgrounds at low energies due to its own radioactive breakdown, but low energy neutrons from nuclear breakup cause fission in the uranium producing charged particles which compensate for the lower visible energy in hadronic showers. The ionization energy from these fission effects can be measured in the same way as the ionization energy from leptons.

The calorimeter consists of three modules: the central calorimeter (CC) and two endcap calorimeters (EC) on each end, see Fig. 2.6. The CC consists of an innermost electromagnetic (EM) section, followed by fine hadronic (FH) and coarse hadronic (CH) sections. Each is subdivided into a number of layers and is segmented in z and ϕ. There are four EM layers where almost all of the EM shower is deposited, three FH layers which capture most of the hadronic showers' energy and one CH layer which captures the tail of hadronic shower in the calorimeter. Some design parameters are listed in Table. 2.2

Most of the cells in the CC and EC have a segmentation of 0.1×0.1 in $\eta \times \phi$ space. To

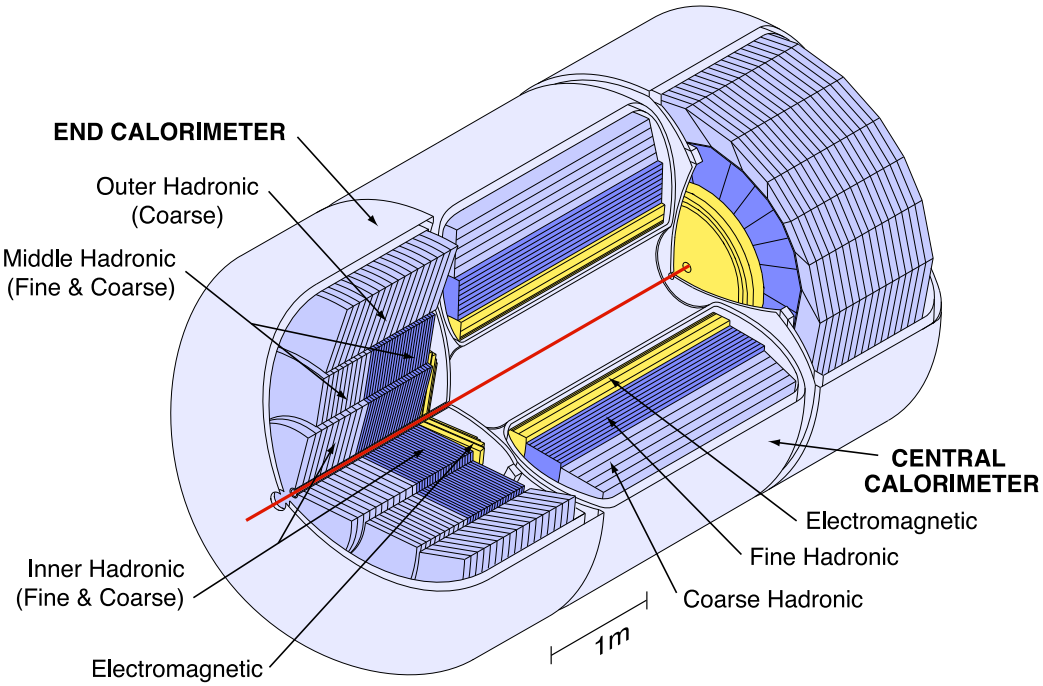

Figure 2.6: Schematic drawing of calorimeter.

Module Type	EM	FH	CH
Rapidity Coverage	±1.2	±1.0	±0.6
Number of Modules	32	16	16
Absorber	Ur	U-Nb	Cu
Absorber Thickness (mm)	3	6	46.5
Argon Gap (mm)	2.3	2.3	2.3
Total Radiation Lengths	20.5	96.0	32.9
Total Nuclear Absorption Lengths	0.76	3.2	3.2

Table 2.2: Some parameters of the Central Calorimeter.

measure the position of particles more precisely, the third section in the EM calorimeter has finer segmentation (0.05×0.05) and is situated at the expected maximum for the EM shower. For cells with $|\eta| > 3.2$, the cell size increases to 0.2×0.2 as shown in Fig. 2.7.

Between the CC and EC there are several regions where particles travel mostly through the support material. The Inter Cryostat Detector (ICD) is used to detect such particles. The ICD consists of a single layer of 384 scintillating tiles matched in size to the calorimeter cells.

The relative momentum resolution for the calorimeter system is measured in data

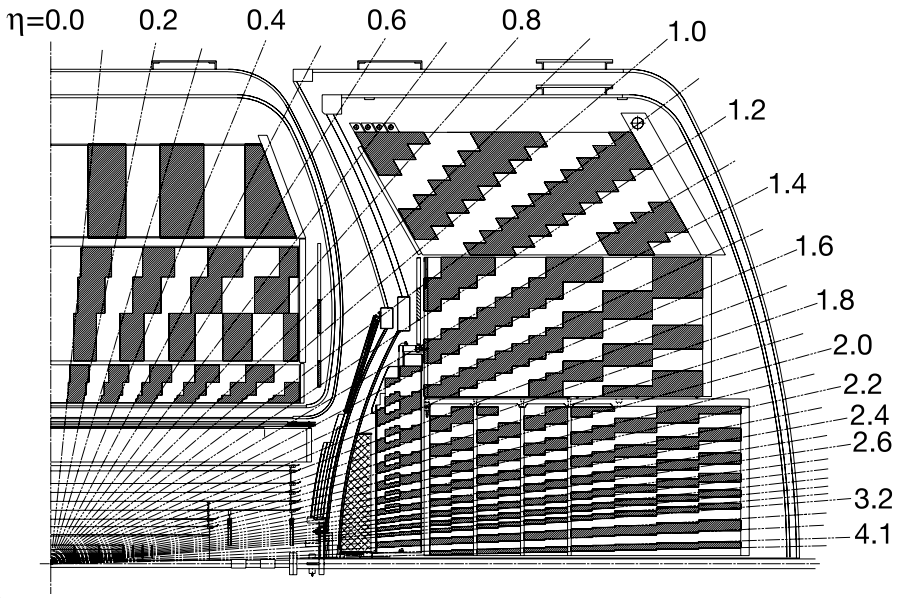

Figure 2.7: A part of the calorimeter showing the segmentation pattern.

and found to be $\sigma(p_T)/p_T \approx 0.13$ for 50 GeV jets in the CC and $\sigma(p_T)/p_T \approx 0.12$ for 50 GeV jets in the ECs. The energy resolution for the electrons in the CC is $\sigma(E)/E \approx 0.16/\sqrt{E} \oplus 0.04$. where E is measured in GeV and $\oplus$ means addition in quadrature.

2.2.8 Muon System

The muon system is positioned farthest from the interaction region. The system consists of scintillators for time measurement and proportional drift tubes for position measurement. There is a magnetic iron toroid that adds more interaction lengths and provides additional means to measure the momentum of the muon.

Muons first interact with the scintillator paddle to record the time at which the hit occurred relative to the beam crossing time. Then the muon continues to leave hits in the proportional drift tubes, which allows one to measure the original direction of the muon. After that the muon enters the iron of the 1.8T toroid magnet. The muon is multiple scattered through the iron and bent by the magnetic field, after which it emerges and its trajectory is measured by the proportional drift tubes once again. By measuring the momentum before and after the muon goes through the magnet, a track may be fitted and the amount of bend from the magnet measured. If the muon cannot penetrate the toroid, then the measurement from the tracker is the only momentum measurement available.

The muon system consists of three sections, the central section ($|\eta| < 1$) and the forward section ($1 < |\eta| < 2$). Each of these is divided into three layers, A, B, and C.

The A layer is the closest to the calorimeter, the toroid magnet is between layers A and B, and then there is the outermost C layer.

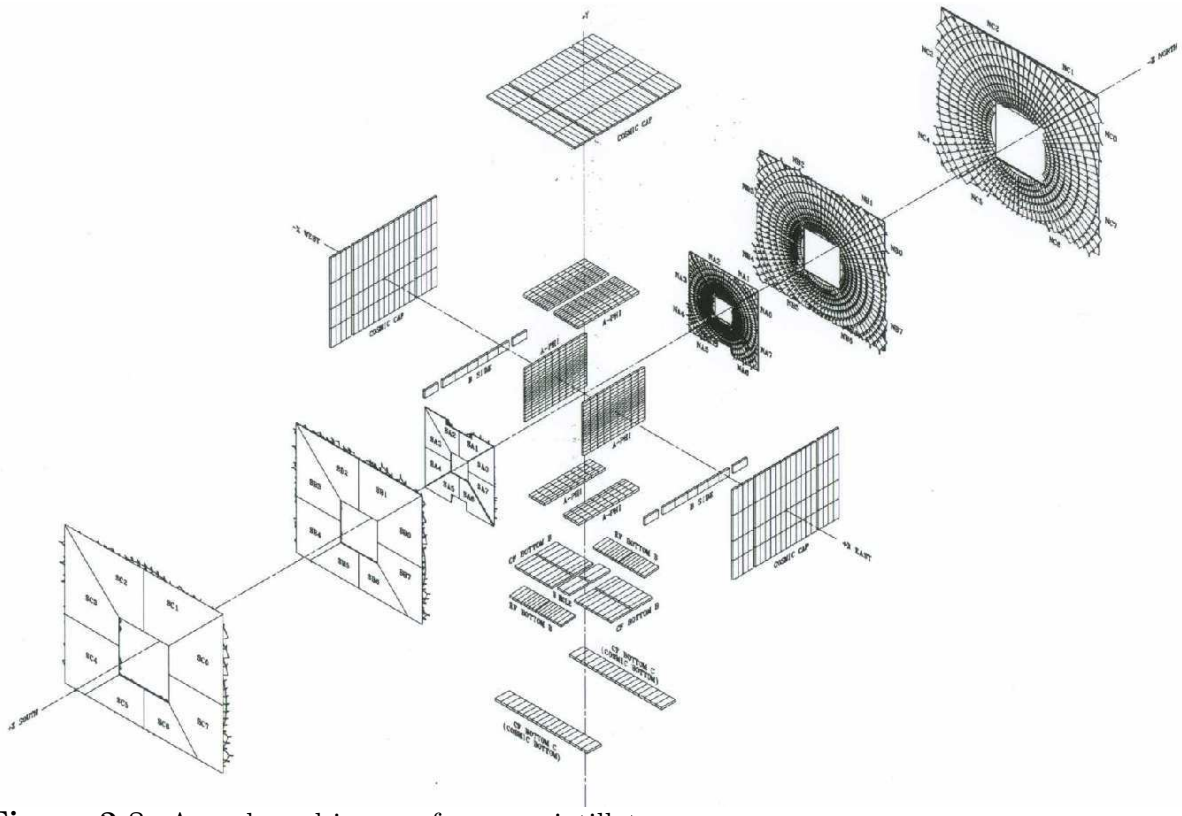

Figure 2.8: An enlarged image of muon scintillators.

In the forward sections there are mini drift tubes instead of drift chambers. The only difference between these tubes and the larger chambers is the lower occupancy due to the much smaller cross sectional area of the small tubes and an improvement in response time.

Chapter 3

Trigger and data acquisition

Beam crossings occur every 396ns and with current technology it is impossible to read out all of them. Thus the readout is triggered only if the event possesses qualities that are indicative of interesting physics. The D0 detector has three levels of triggering (Fig. 3.1), the first level is implemented in hardware for individual detector subsystems. The requirement on the Level 1 trigger (L1) is that it should reduce the rate from 1.8 MHz to ≈1 kHz. If a potential trigger is estimated to have an excessive rate which occupies too much of the available bandwidth, then the trigger may be prescaled, so that only a fraction of the events are passed to the next level trigger. For example, a prescale of three indicates that only one out of three randomly chosen triggered events is isolated. Then the data is passed to a Level 2 trigger (L2), which further refines the measurements of event quantities, as well as correlating information across detectors. If the event goes through Level 2, it is sent to the final third layer of triggering (L3). There it will undergo a fast reconstruction and the final decision will be made about whether or not to record the event (Fig. 3.2).

Level 3 uses information from all detector parts and analyzes the data on a farm of individual linux nodes, therefore it is important to make sure that information for each event from different detectors are re-assembled properly and sent to the appropriate farm node. If an event passes Level 2, the data for that event is transferred out from each of the readout crates by a Single Board Computer (SBC), sitting in each crate, via a large ethernet switch. The data are sent to one or more Level 3 farm nodes specified by a routing instruction from the routing master (RM) process running on an SBC in a special crate. The farm node receives a list of crates from the routing master and checks to make sure all crates arrive before beginning the reconstruction.

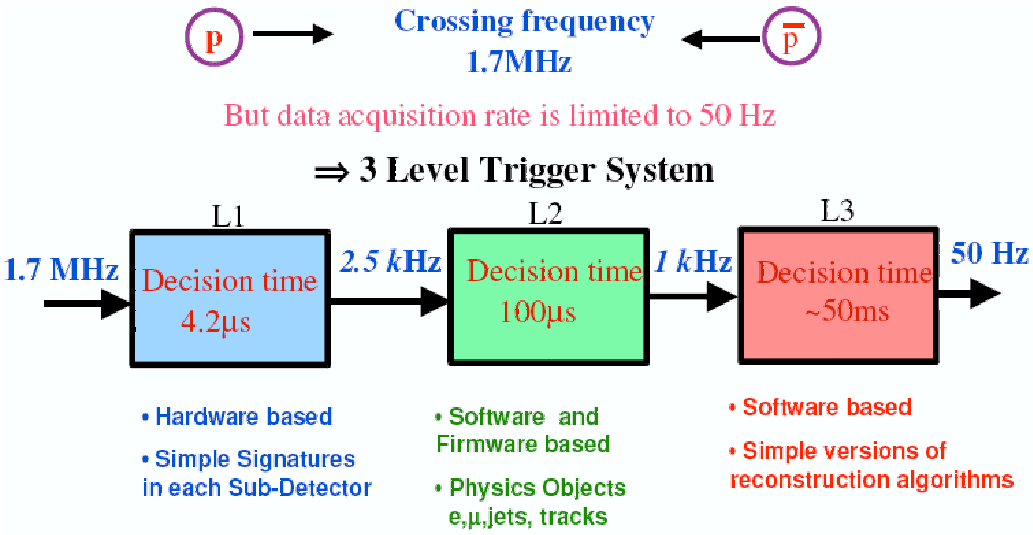

Figure 3.1: The three levels of the DØ trigger system with the times it takes each of them to make a decision.

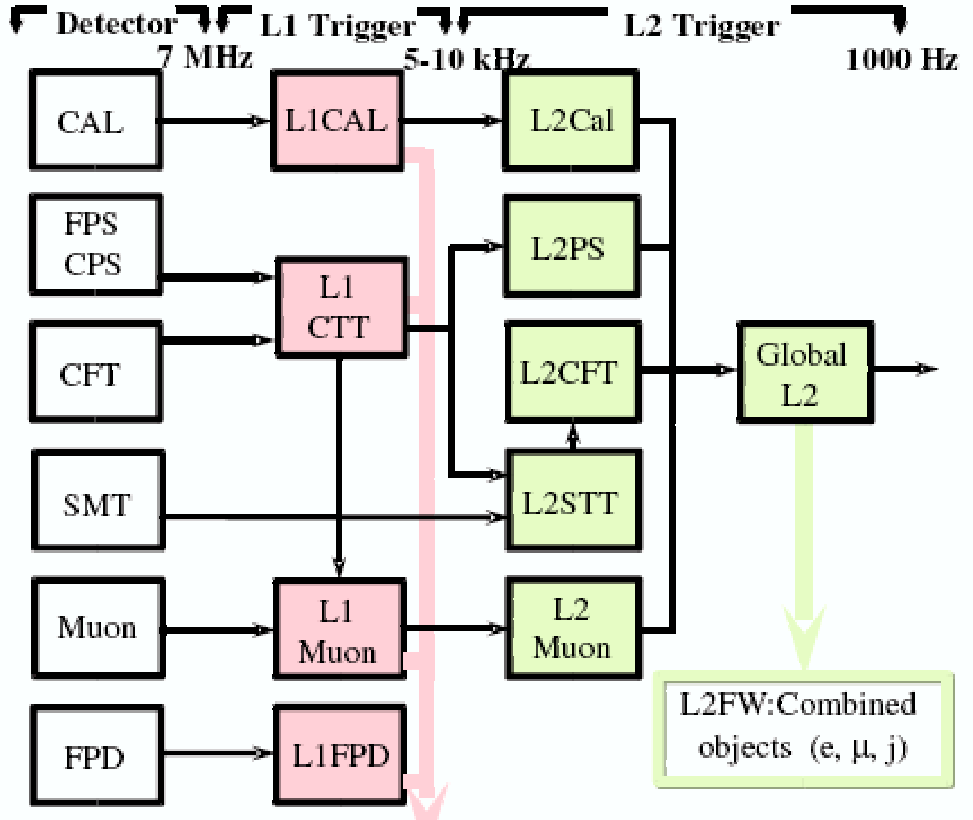

Figure 3.2: D0 trigger system. The second column consists of Level 1 triggers and the third column consists of Level 2 triggers. The first column represents the detector subsystemss that feed data to the different Level 1 and Level 2 triggers.

3.1 Level 1

At Level 1 there are only a few quantities available within the D0 detector. These can roughly be summarized in the following list.

- Calorimeter quantities: the energy deposited in the trigger towers. Level 1 triggers can require one or more towers above pre-programmed thresholds. The Level 1 trigger towers consist of energy sums of the projective towers with segmentation 0.2×0.2 in $\eta \times \phi$. Additional trigger terms are constructed from global quantities such as the total energy, the total calorimeter energy projected in the transverse plane, and the missing transverse energy, or energy imbalance in the transverse plain.

- Muon system quantities: at Level 1 the muon system trigger terms use scintillation counters, wire chamber hits and the CTT (a Level 1 trigger that uses data from the CFT and the preshower detectors). The hit information in the wire chambers is used to form track stubs which are then used to confirm the scintillator hits in each layer. Triggers are formed by matching confirmed scintillator hits between layers. Also tracks from the Level 1 track trigger are matched to hits in the muon scintillator system. Some cosmic muons can penetrate the D0 detector, so muon triggers incorporate a cosmic muon veto, which is implemented using the timing information relative to the beam crossing.

- Track triggers: the Level 1 track trigger reconstructs the trajectories of charged particles using data from the central fiber tracker and the central and forward preshower detectors. Hits are used to search for tracks via pre-programmed look up tables (LUT). This is done by considering different possible hit patterns and programming those that are consistent with particle tracks in the LUTs. The candidates remapped onto the geometry of the SMT are used as seeds for the Silicon Track Trigger (STT) which is one of the Level 2 triggers.

3.2 Level 2

The Level 2 trigger combines and refines the output of the Level 1 trigger. It includes pre-processors for each detector sub system and a global processor for combining information from the entire detector. The preprocessor subsystems include the tracking, preshower, calorimeter, and muon systems. These systems work in parallel and transform the Level

1 trigger information into physics objects (tracks, energy cluster, etc.). For example, the calorimeter preprocessor collects information from all the Level 1 trigger towers and uses that information in clustering algorithms in order to build simple jet and electron candidates. The Level 2 CTT sorts the list of Level 1 CTT tracks according to their transverse momentum. The Level 2 muon trigger combines both wire and scintillator hits to form muon objects with track quality and transverse momentum information. The Level 2 Silicon Track Trigger (STT), is different in that it receives information from the detector itself (the SMT) and the Level 1 trigger (L1CTT). A detailed description of the STT, which I worked on, follows in the next section.

3.2.1 STT

The Level 2 silicon track trigger performs high precision online reconstruction of tracks found in the CFT by utilizing the much finer spatial resolution of the SMT. The STT improves the momentum measurement of the charged particle tracks at the trigger level and allows a precise measurement of the impact parameter of tracks, which helps tag the decays of the long-lived particles.

Even though all detector elements are used in offline track reconstruction, there is not enough time to use SMT data in Level 1 triggering due to long read out times for the SMT ($\approx 15\mu$s while Level 1 decisions should be made in $\approx 4\mu$s). To use SMT data for the precise momentum measurement at the trigger level, the STT was introduced. The STT uses about 50μs to process SMT and CFT data, which is within Level 2 decision time ($\approx 100\mu$a) and it measures the impact parameter with precision of $\approx 20\mu$m.

The Fig. 3.3 shows the basic principle of the STT. From each event, tracks from the L1CTT are sent to the STT. A $\pm$ 2 mm "road" is formed around each track and the SMT hits that are within these roads are associated with the track. Hits in the innermost and outermost layers of the CFT and hits in at least four out of five layers of the SMT are used. The results of the track fit are then sent to the L2CTT.

The STT hardware design mainly uses custom-designed digital electronics modules. Logic daughterboards plug into a motherboard and a common motherboard design is used throughout the system. Data is received from the L1CTT and the SMT via optical fibers which plug into custom receiver cards located in the rear card cage of the VME crate that houses the trigger electronics. The data is processed in the FPGAs located on the daughter boards. There are three types of daughterboards: the Fiber Road Card (FRC), the Silicon Trigger Card (STC) and the Track Fit Card (TFC). On each motherboard there is one more board called the Buffer Controller (BC), which buffers data for readout through the data acquisition system once an event has been accepted

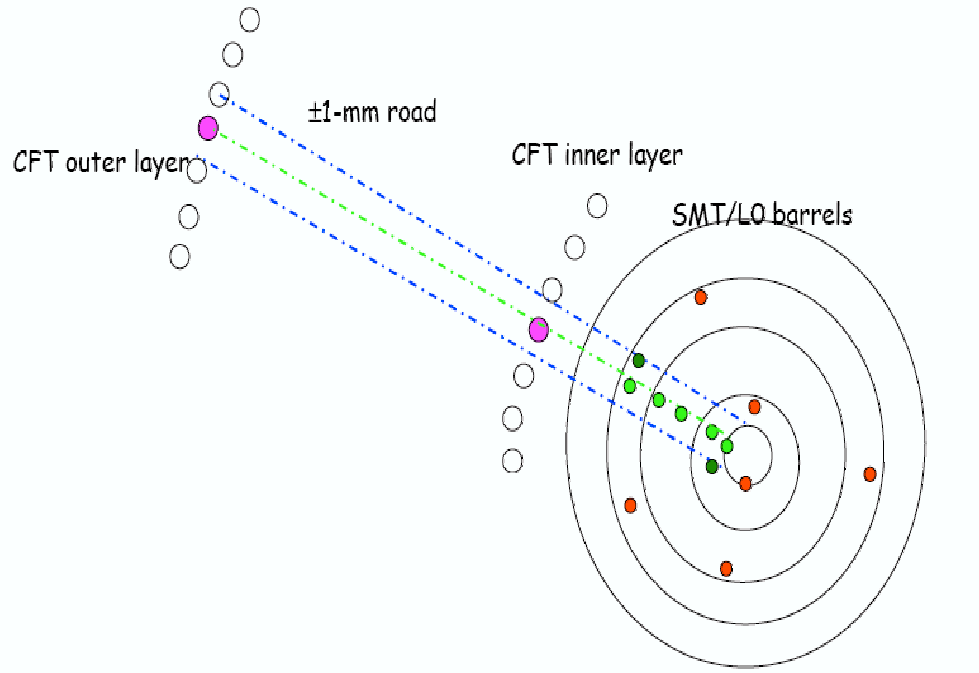

Figure 3.3: Basic principle of the STT is to find silicon hits in the roads defined by the CFT.

by the trigger system.

The STT consists of six identical crates each receiving data from two 30 degree SMT sectors. Each crate consists of one FRC, ten STCs and two TFCs.

- Fiber Road Card (FRC)

  The FRC is composed of four main elements that are implemented on three FPGAs. The four elements are the trigger receiver, the road receiver, the trigger/road data formatter and the buffer manager. The trigger receiver receives the D0-wide synchronization signals from the trigger framework. The road receiver receives track information from the L1CTT and sends it to the trigger/road data formatter, which in turn combines this data with the relevant SCL (Serial Command Link) data from the trigger framework and transmits the data to the STCs and TFCs. The buffer manager is responsible for buffering the events and for the readout to the Level 3 system. Every event that passes a Level 1 trigger gets to the STT and is sent to the Buffer Controller (BC). The buffer manager first assigns the buffer where the event must be stored and waits for the trigger framework to send the Level 2 trigger decision. If the event passes Level 2, the buffer manager sends a signal to the BCs to prepare the event for readout to Level 3 via a Single Board Computer (SBC). Thus the FRC serves as the STT's main communication link with the rest of the detector.

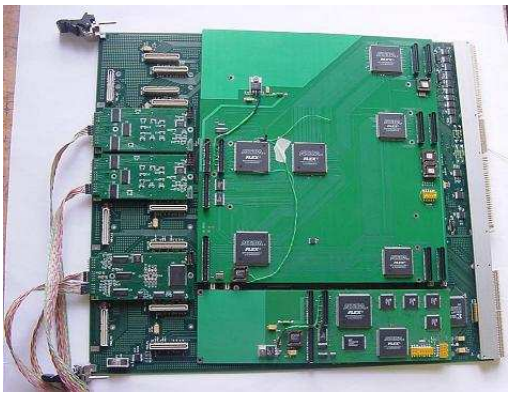

Figure 3.4: An FRC board.

- Silicon Trigger Card (STC)

  The STCs receive data from the axial and stereo strips of the silicon ladders. They first use downloaded LUTs to mask out noisy and dead silicon strips and then perform a strip by strip gain and offset correction. Then they perform a fast clustering algorithm. A cluster is a group of contiguous strips with pulse heights above a given threshold (8 Analog-to-Digital Counts). The cluster centroids are determined and matched with the tracks from the FRC. If a cluster centroid is within $\pm$ 2 mm of a CTT track, then it is kept, otherwise it is discarded. The list of centroids associated with CTT tracks is then transmitted to the Track Fitting Cards (TFC). STC data is also sent to Level 3 via the BC for monitoring purposes.

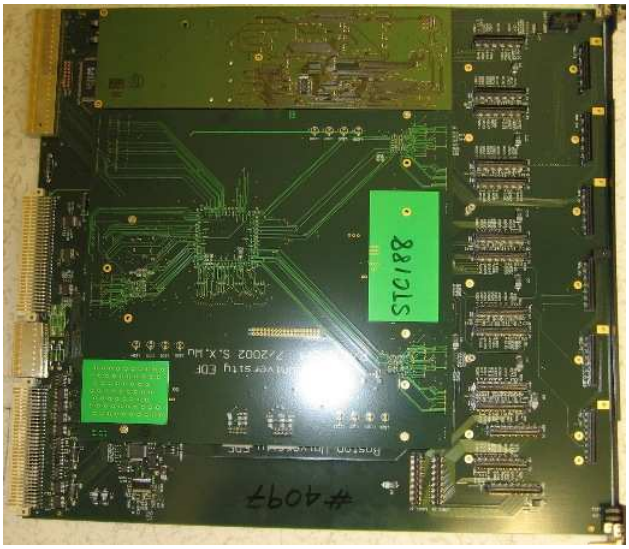

Figure 3.5: An STC board.

- Track Fit Card (TFC)

The TFC (Fig. 3.6) receives track information from the FRC and centroids of silicon clusters from the STCs. Each STT crate has two TFCs to cover each of the two 30^o sectors of the SMT. The processing in the TFC begins with the translation of the silicon hardware coordinates to the ϕ and r coordinates that are more appropriate for fitting. This is done using pre-computed LUTs. The TFC uses only the hits from the inner and outer layers of the CTT. Then it looks at the silicon hits associated with the CTT track and in each layer selects the hit which is closest in ϕ to the center of the road. A fit is performed only if there are hits in at least four of the five SMT layers. If there are hits in all five layers, and the χ^2 of the fit is larger than a pre-determined value (5.5), then the hit which contributes most to the χ^2 is discarded and the track is refit.

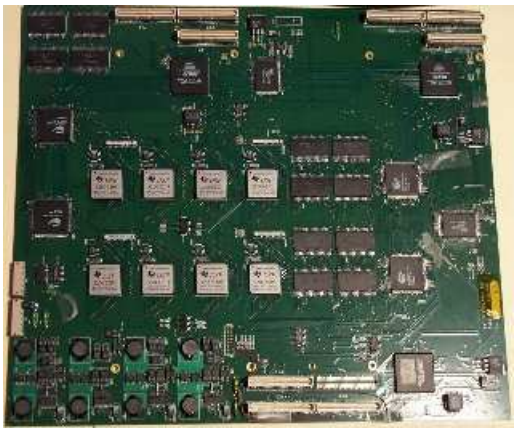

Figure 3.6: A TFC board.

The track is fit to the linearized function:

$$\phi(r) = b/r + \kappa r + \phi_0 \tag{3.1}$$

where b is the impact parameter with respect to the detector origin, κ is the curvature of the track and ϕ_0 is the direction of the track at the point of closest approach. The TFC also corrects for the beam position offset from the detector origin. Online tracking measures the beam spot and it is downloaded to the TFCs at the beginning of every run. The distance the beam spot fluctuates during a run is $\approx 10\mu$m, which is less than the beam spot size ($\approx 35\mu$m) and there is no need for further adjustments during the run. The correction is applied to the final hit selection and the track fitting. The TFC outputs the track parameters and the fit χ^2 to the L2CTT, where tracks are sorted according to the p_T and impact

parameter, and then passed onto the L2Global for the global trigger decision. The data is also sent to Level 3.

3.3 Level 3

The third and final stage of the trigger is a dedicated computer farm that performs a fast reconstruction using a simpler version of the offline reconstruction code. The number of farm nodes is ever changing as new ones are added and old ones or problematic ones are removed, during the time when data for this analysis was taken, the farm had about 200 nodes. The final trigger decision is made on high level "physics" objects, such as electrons, muons, jets, as well as on the relationships between such objects.

Upon a L2 accept the data are sent to one or more farm nodes. These farm nodes run two different programs, the event builder and the event filter. The event builder process builds a complete event from the fragments received from different subdetectors and makes it available to the event filter process, which makes the final decision. The accepted events are written to tape for offline analysis. The size of the event may vary, but on the average it is 0.3 MB.

Chapter 4

Event Reconstruction

The sample used in this analysis was collected from March 2004 to February 2006. Runs declared bad due to hardware failures where removed from this sample, leaving total of 750 ± 46 pb^{-1} of integrated luminosity. The information recorded by the detector is in the form of digital signals, which need to be interpreted as physics objects. This is performed by the standard reconstruction software package, D0RECO [18]. D0RECO starts by processing the raw data into high level objects, such as energy clusters in the calorimeter and tracks in the tracking system. These objects are in turn combined to form the physical particles: electrons, photons, etc.

4.1 Track and vertex reconstruction

Hits from the SMT and CFT are used to reconstruct the trajectories of the charged particles and the event vertex. The reconstruction of tracks starts with three SMT hits from the inner radius out, in order to make a track hypothesis. The second hit must be within $\Delta\phi$ of 0.08 on the next innermost layer. The third hit on the next innermost layer must lie on a circle of radius greater than 30 cm (corresponding to E_T of 180 MeV) and have an axial impact parameter of less than 2.5 cm. The overall fit must have a $\chi^2 < 16$. Each track is extrapolated to the next layer of the SMT or CFT repeatedly, and hits are added to the track hypothesis if the increase in χ^2 is less than 16. If there are multiple hits in a given layer, they become the new hypotheses. The track hypotheses are ordered by the number of hits, and those with the same number of hits and the fewest number of misses, and those with equal number of hits and misses are ordered by the χ^2 of the fit.

To further reduce the number of fake tracks, primary vertices are determined using the accepted tracks and every track that comes close to the vertex is given two additional

hits in the rankings. Using this new weight the tracks are resorted and a new pool of tracks is determined.

This method would preclude tracks with no SMT hits, therefore the same procedure is repeated starting with three CFT hits, but to control the huge combinatorics with stereo hit associations, the tracks must pass near the primary vertex determined by the SMT tracks.

There are two types of vertices: primary and secondary. A primary vertex is the original interaction point with the largest number of associated tracks, while a secondary vertex is a displaced vertex due to long-lived meson decay. The x and y coordinates of the primary vertex are close to zero since the cross sectional extent of the beam is $\approx$ 40 μm. However, the z coordinate has a range with an rms width of 28 cm and center close to zero. The primary vertex candidates are found by first selecting global tracks with at least one hit in the SMT and then fitting a vertex position from these tracks. A primary vertex must contain at least three tracks. Secondary vertex candidates are found by forming a good seed from two tracks that do not point to the primary vertex and fitting a secondary vertex. Then adding another track and refitting, repeating the procedure until there are no more good tracks. There can be more than one secondary vertex.

4.2 Electron identification

A cluster finding algorithm is used to find electromagnetic showers in the calorimeter. The algorithm begins with a list of EM towers with significant energy, where an EM tower is defined as the sum of energies measured by the calorimeter in all four EM layers plus the first FH layer within 0.1×0.1 in $\eta \times \phi$. The algorithm starts with the tower with the highest E_T (the seed), then looks at all neighboring towers and includes the highest energy neighbor in the cluster. The process continues until there are no more towers with a neighbor above the threshold of 500 MeV. If the E_T of the cluster is not above 1.5 GeV, the cluster is rejected. Electromagnetic shower candidates are required to have an EM fraction ($EMfrac$) above 0.9 and an isolation (iso) less than 0.2, where the EMfrac is the ratio of the EM energy over the total energy of the cluster

$$EMfrac = \frac{E_{EM}}{E_{Total}} \tag{4.1}$$

and the isolation is defined as

$$iso = \frac{E_{cone} - E_{core}}{E_{core}} \tag{4.2}$$

where E_{cone} is the energy in a cone of radius $R = \sqrt{\Delta\eta^2 + \Delta\phi^2} = 0.4$ around the direction of the cluster, summed over the entire depth of the calorimeter except the CH layers and E_{core} is the energy in a cone of radius $R = 0.2$, summed over the EM layers only. To calculate the direction of the cluster, two points are used, one of which is the vertex from which the particle originated. The other point is the center of the deposited energy in the third layer of the EM calorimeter. We use the third layer as it has finer $\eta \times \phi$ granularity than other layers, 0.05×0.05 versus 0.1×0.1.

Since charged hadrons deposit less than 10% of their energy in the EM calorimeter and electrons from W and Z boson decays tend to be isolated from other particles, EMfrac and iso provide powerful discrimination between the EM objects and hadron jets (Fig. 4.1).

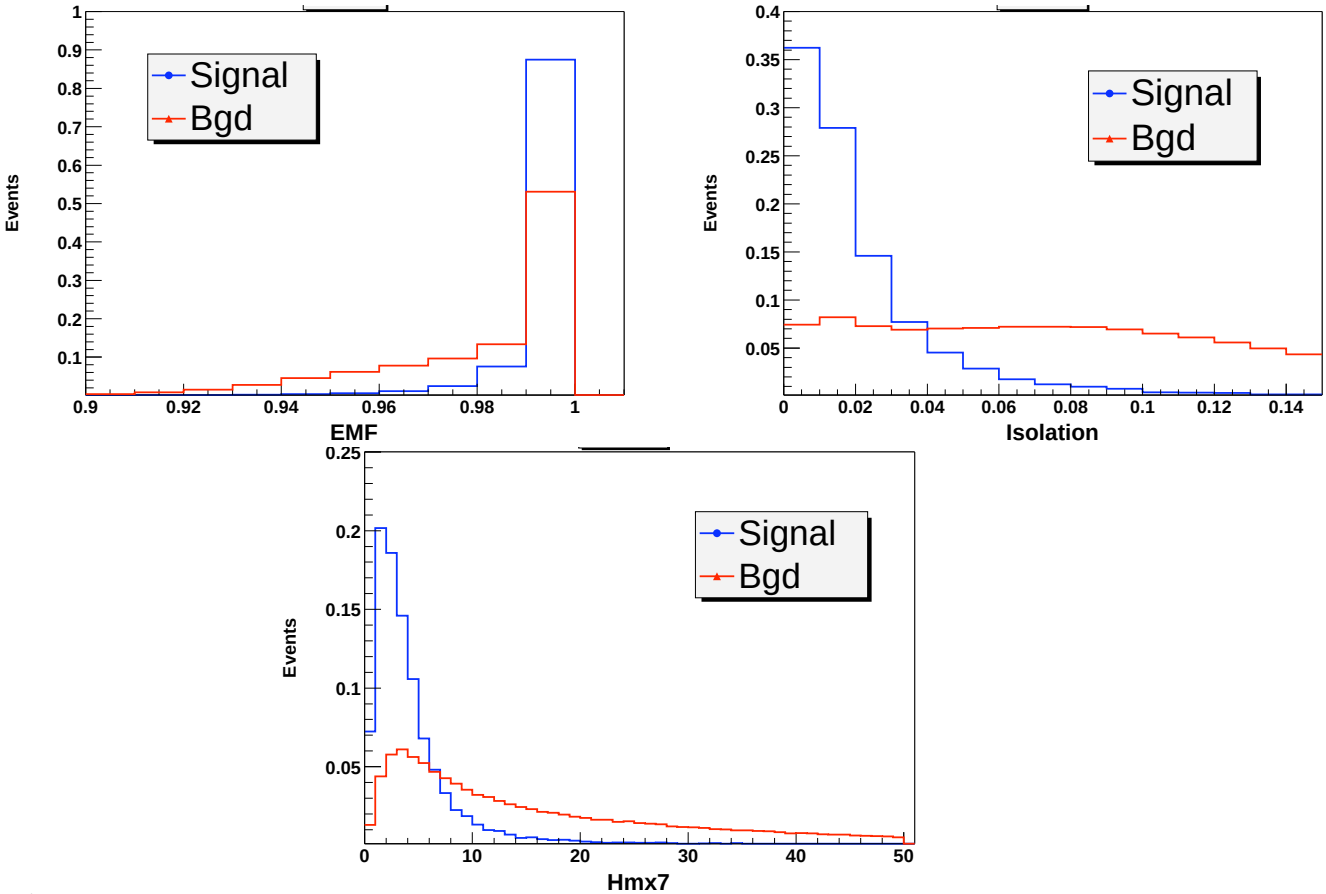

Figure 4.1: EMfrac (top left), iso (top right) and H-matrix(7) (bottom) distributions for real and fake electrons.

A cluster that passes the default thresholds enters the final stage of the reconstruction. At this stage various quantities that describe cluster properties are computed and

stored. A few examples are cluster energy, E_T, η, ϕ. In addition, a multi-variate tool called the $H-Matrix$ is used to determine how well the shape of the EM cluster agrees with that expected for an electromagnetic shower. The variables used in the H-matrix are: the fractional energies in the four EM layers, the shower width in the η direction, the logarithm of the cluster energy and the position of the primary vertex. There are two different $H-Matrix$ functions for CC and EC, called $H-Matrix(7)$ for CC and $H-Matrix(8)$ for EC.

The electron energy is computed from the signals in all the EM towers within a window of 0.5×0.5 in $\eta \times \phi$ for the CC or within a 10 cm radius in EM3 for the EC, centered on the tower with the largest energy.

The electrons are required to be in the well understood region of the calorimeter, which is called the fiducial region. There are 32 identical modules in the CC region with edges at $\phi = 2\pi N/32$, where N=0,1,...,31. The excluded regions are $\mathrm{mod}(\phi, 2\pi/32) < 0.1$ and $\mathrm{mod}(\phi, 2\pi/32) > 0.9$.

An important source of background for electrons is photons from π^0 and η meson decays. This background is reduced by requiring that the ϕ position of a track from a charged particle in the tracking system be consistent with the ϕ position of the cluster in the calorimeter. For track matching the following χ^2 variable is used:

$$\chi^2 = (\Delta\phi/\sigma_\phi)^2 + (\Delta z/\sigma_z)^2 \tag{4.3}$$

where $\Delta\phi, \Delta z$ are the angle difference and the spatial difference between the electron position and track position extrapolated to the inner face of the calorimeter and σ_ϕ, σ_z are the associated experimental resolutions of the tracker and the calorimeter combined.

Below are general conditions an electron candidate must satisfy to be selected for this analysis (there will be some more specific criteria in the next chapter):

- EMFrac > 0.9
- iso < 0.15
- H-Matrix(7) < 50 for CC ($|\eta_{det}| < 1.1$)
- H-Matrix(8) < 75 for EC ($1.5 < |\eta_{det}| < 3.2$)
- $E_T > 25$ GeV
- Track match probability $P(\chi^2) > 0.001$
- Track $E_T > 10$ GeV

- Should be in the fiducial region

η_{det} is the 'detector η'. There are two η-s used in this analysis, the detector η and the physics η. The detector η is derived from the angle between the center of the detector and the cluster position in the EM calorimeter; the physics η is derived from the physical polar angle between the interaction vertex (which may not be at the center of the detector because of the size of the interaction region) and the cluster position. The physics η is thus related to the true angle made by the particle with respect to the detector, whereas the detector η is related to the position of the particle in the detector.

The above conditions define what we call a 'loose' electron sample. The method we use in this analysis (Chapt. 6) also requires a 'tight' electron sample, which is different from the loose sample by the $H-Matrix$ requirements. For the tight sample the $H-Matrix$ requirements are

- H-Matrix(7) < 10 for CC ($|\eta_{det}| < 1.1$)
- H-Matrix(8) < 10 for EC ($1.5 < |\eta_{det}| < 3.2$)

4.3 Neutrino identification

The neutrinos are not detected by the D0 detector, their presence is inferred from the overall momentum imbalance in the event. Since the total momentum is conserved in the transversed plane, a large missing E_T, denoted as $\not\!\!E_T$, indicates the presence of high E_T neutrino(s). The raw missing transverse momentum is calculated by taking the vector sum over transverse momenta of all calorimeter clusters calculated from all cells except those from the coarse hadronic layer. After getting the raw missing transverse energy, the electron energy corrections are applied on EM clusters with E_T >5 GeV, $EMfrac$ >0.9 and iso<0.15 to get the correct missing transverse energy.

4.4 Jet identification

Outgoing quarks and gluons from the hard scatter form jets, which are detected in the calorimeter after they hadronize. The purpose of the jet algorithm, called the cone algorithm, is to reconstruct these jets from the energy deposits in the calorimeter towers in such a way that the kinematic properties can be related to those of the initial quark or gluon. The algorithm begins with a list of seed towers in the calorimeter with E_T >500 MeV and creates 'proto-jets' around them. If a proto-jet shares no towers with any other

cluster, then it becomes jet. If the candidate does share towers with other proto-jets, then each is considered separately. If the energy shared with the lower E_T proto-jet is greater than half the energy of the other jet, then algorithm assumes that the two proto-jets are made of energy originating from a single real jet and the two proto-jets are merged. If the energy is less than half, then the jets are split apart with the shared cells being assigned to the nearest jet. In this case the algorithm assumes there were two initial jets. The energies of the jets are recalculated and the list of jets is remade. This continues until no further towers are shared.

The quantities used to reconstruct jets in data are: N90, which is the number of towers that contain 90% of the jet's energy; CHF, the fraction of energy deposited in the coarse hadronic layer of the calorimeter; HCR, the ratio of the highest transverse momenutm cell in the jet to the second highest; as well as EMfrac which we already described for the electron. The conditions that a jet candidate has to satisfy for this analysis are:

- N90 > 1
- $0.05 <$ EMfrac < 0.7
- CHF < 0.4
- HCR < 10
- $E_T > 20$ GeV
- $|\eta_{det}| < 1.1$ (CC) or $1.5 < |\eta_{det}| < 3.2$ (EC)

Chapter 5

Data Selection

The data at D0 come from the $p\overline{p}$ collisions that occur inside the D0 detector. Millions of collisions occur every second and only the most interesting ones are recorded by the detector for offline analysis. For this analysis interesting collisions are the ones in which a W boson is created. Such collisions are quite rare, for comparison, the cross section for any inelastic scattering (the one where any reaction takes place) is ≈ 75 mb, while the cross section for the W boson production is 2 nb. In other words, in every 100 million events only 3 contain a W boson, so it is a challenge to pick the correct events without being overwhelmed by background processes. The tools that allow us to do that are called triggers. Triggers look at the parameters of the event and if they pass the predefined sets of requirements, the event is recorded. In our case, Ws quickly decay into an electron and a neutrino and the neutrino escapes undetected, so we use the triggers that look for an electron.

5.1 Triggers

At any given time during the detector operation there is a set of triggers that is used to collect the data. Over time new triggers are introduced for different kinds of reasons (higher luminosities, change in data taking priorities, etc.) and the new set of triggers replaces the old one. These sets are called trigger versions. The oldest data used in this analysis was collected using trigger version 12 (v12 data), we also use data collected with v13 and v14 trigger versions. Below is the list of all the triggers from all three trigger versions that were used to collect data for this analysis. For an event to be selected it had to pass at least one of the following single electron triggers:

- v12: E1_SH30, E1_SHT20, E2_SH30, E2_SHT20, E3_SH30, E3_SHT20.
- v13: E1_SH30, E1_SHT22, E2_SH30, E2_SHT22, E3_SH30, E3_SHT22.

- v14: E1_ISHT22, E1_SHT25, E1_ISH30, E1_SH35, E3_ISHT22, E3_SHT25, E3_ISH30, E3_SH35, E4_ISHT22, E4_SHT25, E4_ISH30, E4_SH35.

All of these triggers look for a single electron using the calorimeter information. E1 means that the electron deposits all of its energy in a single tower, while E2, E3 and E4 account for the cases when a single electron deposits its energy in more than one calorimeter tower. SH means the loose shower shape requirement, while SHT stands for the tight shower shape requirement. The letter I in front of SH means that the electron is also required to pass an isolation cut. The numbers at the end correspond to the E_T cuts. So, for example, E1_ISHT22 will fire for an electron with $E_T > 22$ GeV deposited in a single tower that also passes the tight shower shape and isolation requirements. Below is the detailed description of all triggers. Recall that since, we have 3 level triggering, our trigger requirements for each level are listed separately. Note that the trigger criteria abbreviations used at L1, L2 and L3 in Tables 5.1 - 5.3 are explained in more detail in Tables 5.4 - 5.6.

Trigger	L1	L2	L3
E1_SH30	cem(1, 11)	-	ELE_NLV_SH(1, 30)
E1_SHT20	cem(1, 11)	-	ELE_NLV_SHT(1, 20)
E2_SH30	cem(2, 6)	-	ELE_NLV_SH(1, 30)
E2_SHT20	cem(2, 6)	-	ELE_NLV_SHT(1, 20)
E3_SH30	cem(2, 3)cem(1, 9)	-	ELE_NLV_SH(1, 30)
E3_SHT20	cem(2, 3)cem(1, 9)	-	ELE_NLV_SHT(1, 20)

Table 5.1: Single EM v12 triggers used in this analysis.

Trigger	L1	L2	L3
E1_SH30	cem(1, 11)	calem(15, x)	ELE_NLV_SH(1, 30)
E1_SHT22	cem(1, 11)	calem(15, x)	ELE_NLV_SHT(1, 22)
E2_SH30	cem(2, 6)	calem(15, x)	ELE_NLV_SH(1, 30)
E2_SHT22	cem(2, 6)	calem(15, x)	ELE_NLV_SHT(1, 22)
E3_SH30	cem(2, 3)cem(1, 9)	calem(15, x)	ELE_NLV_SH(1, 30)
E3_SHT22	cem(2, 3)cem(1, 9)	calem(15, x)	ELE_NLV_SHT(1, 22)

Table 5.2: Single EM v13 triggers used in this analysis.

Trigger	L1	L2	L3
E1_SH35	cem(1, 12)	calem(15, x)	ELE_NLV_SH(1, 35)
E1_ISH30	cem(1, 12)	calem(15, x)	ELE_NLV_SH(1, 30) IsoEle_SH(1, 30)
E1_ISHT22	cem(1, 12)	calem(15, x)	ELE_NLV_SHT(1, 22) IsoEle_SHT(1, 22)
E1_SHT25	cem(1, 12)	calem(15, x)	ELE_NLV_SHT(1, 25)
E3_SH35	cem(1, 12)	calem(x, 11, 0.2)	ELE_NLV_SH(1, 35)
E3_ISH30	cem(1, 12)	calem(x, 11, 0.2)	ELE_NLV_SH(1, 30) IsoEle_SH(1, 30)
E3_SHT25	cem(1, 12)	calem(x, 11, 0.2)	ELE_NLV_SHT(1, 25)
E3_ISHT22	cem(1, 12)	calem(x, 11, 0.2)	ELE_NLV_SHT(1, 22) IsoEle_SHT(1, 22)
E4_SH35	cem(2, 6)	calem(15, x)	ELE_NLV_SH(1, 35)
E4_ISH30	cem(2, 6)	calem(15, x)	ELE_NLV_SH(1, 30) IsoEle_SH(1, 30)
E4_SHT25	cem(2, 6)	calem(15, x)	ELE_NLV_SHT(1, 25)
E4_ISHT22	cem(2, 6)	calem(15, x)	ELE_NLV_SHT(1, 22) IsoEle_SHT(1, 22)

Table 5.3: Single EM v14 triggers used in this analysis.

cem(1, 11)	one EM trigger tower with $E_T > 11$ GeV
cem(1, 12)	one EM trigger tower with $E_T > 12$ GeV
cem(2, 6)	two EM trigger towers with $E_T > 6$ GeV
cem(2, 3)cem(1, 9)	one EM trigger tower with $E_T > 9$ GeV, another EM trigger tower with $E_T > 3$ GeV

Table 5.4: L1 requirements for each trigger used in this analysis.

calem(15, x)	EM cluster with $E_T \geq 15$ GeV
calem(x, 11, 0.2)	single tower EM object with iso < 0.2 and $E_T > 11$ GeV,

Table 5.5: L2 requirements for each trigger used in this analysis.

ELE_NLV_SH(1, 30)	one electron with $E_T > 30$ GeV passing loose shower shape requirement
ELE_NLV_SH(1, 35)	one electron with $E_T > 35$ GeV passing loose shower shape requirement
ELE_NLV_SHT(1, 20)	one electron with $E_T > 20$ GeV passing tight shower shape requirement
ELE_NLV_SHT(1, 22)	one electron with $E_T > 22$ GeV passing tight shower shape requirement
ELE_NLV_SHT(1, 25)	one electron with $E_T > 25$ GeV passing tight shower shape requirement
IsoEle_SHT(1, 22)	the IsoEle terms with any arguments add requirement that the electron must also be isolated

Table 5.6: L3 requirements for each trigger used in this analysis.

5.2 Electron Types

Each electron is assigned a 'type' based on physics pseudorapidity (η) and primary vertex z position. From these inputs, four electron types are calculated based on the number of layers of the Central Fiber Tracker (CFT) it crosses. We defined four types of electrons [14]:

- Type 1: Electrons that are reconstructed in the central region of the calorimeter. The tracks of these electrons will have been required to pass through the entire coverage of the CFT.
- Type 2: Electrons which are reconstructed in the forward region of the calorimeter but pass through the full coverage of the CFT.
- Type 3: Electrons which are reconstructed in the forward region of the calorimeter which pass through at least some of the CFT.
- Type 4: Electrons which are reconstructed in the forward region of the calorimeter which pass through none of the CFT.

Splitting the data into these types allows us to optimize specific cuts for each type that improve charge identification while retaining efficiency. The charge asymmetry is measured independently for each electron type, and then combined to get the final asymmetry. Extensive studies were done to select the optimal set of cuts for each type (you can see some of the relevant plots in the Appendix D.1), which you can see in the list below:

Types 1 and 2:

- Track fit $\chi^2 < 9.95$
- $N_{smt} > 1$ (number of SMT hits)
- $N_{cft} > 8$ (number of CFT hits)

Type 3:

- Track fit $\chi^2 < 9.95$
- $N_{smt} > 0$
- $N_{cft} > 0$

Types 4:

- Track fit $\chi^2 < 9.95$
- $N_{smt} > 8$
- Significance of curvature (curvature divided by the error of the curvature) > 2.

5.3 Data Samples

This analysis uses three data sets:

- Di-electron sample (Z candidates): The E_T spectrum of electrons from Z bosons is similar to the E_T spectrum of electrons from W boson decays, thus $Z \rightarrow ee$ events, which can be fully reconstructed, provide an excellent sample for measuring the detector and reconstruction algorithm performance. Di-electron events are required to have:
  - Two loose (as described in Sec. 4.1) electron candidates with $E_T > 25$ GeV
  - Invariant mass $M_{ee} > 50$ GeV
  - For both electrons, the distance of closest approach (DCA) between the electron track and the primary vertex should be less than 0.02 cm
  - Z position of the primary vertex |VtxZ| < 40 cm
  - For both electrons, the distance between the electron track and the primary vertex along the Z axis must have $|\Delta Z| < 2$ cm (Fig. 5.1)

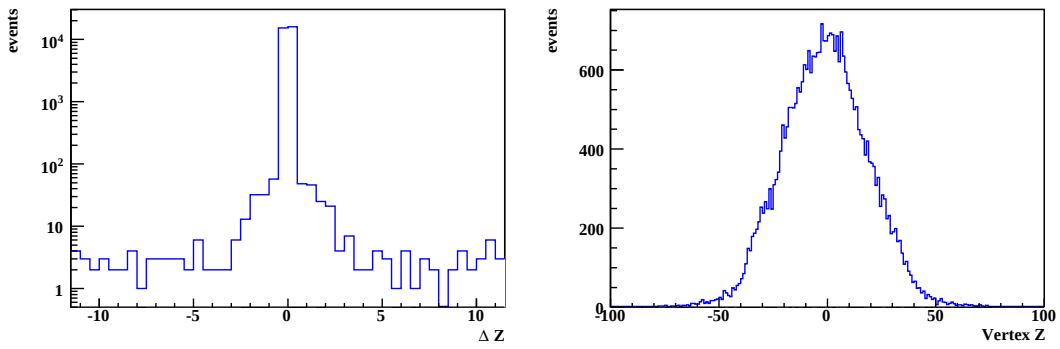

Figure 5.1: The distance between electron track and primary vertex (left, logarithmic scale) and the vertex z position distributions for the $Z \rightarrow ee$ sample.

- EM + Jet sample (QCD di-jet candidates): QCD background studies require event samples enriched in 'fake' electrons. This selection comprises mainly of QCD di-jet events where one jet has been mis-identified as an electron. Events are required to have:
  - Only one good jet (as described in section 4.3)
  - Only one loose electron
  - Electron and jet are back-to-back in ϕ with $\pi > \Delta\phi > 2.8$
  - Missing transverse energy is required to be $\not\!\!E_T < 10$ GeV to reduce the contamination from real W to electron decays (Fig. 5.2)

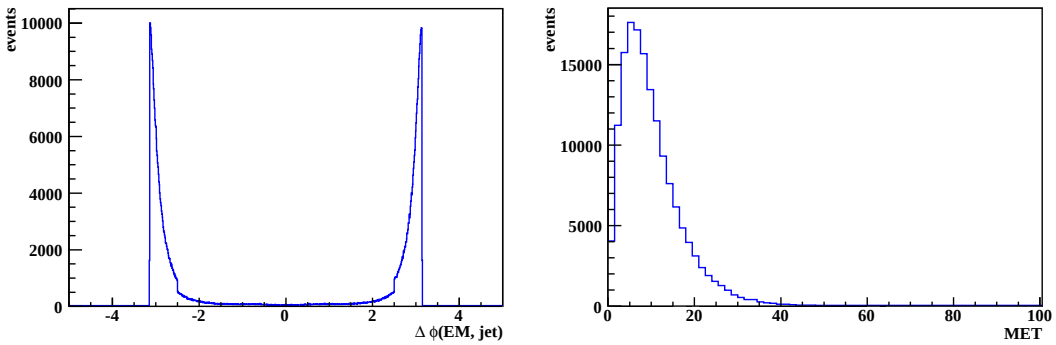

Figure 5.2: ϕ(EM,jet) and $\not\!\!E_T$ distributions for the EM + Jet sample.

- EM $+\not\!\!E_T$ (W candidates): This is the signal sample for this analysis. Events are required to have:
  - One tight electron with $E_T > 25$ GeV (as described in Sec. 4.1)
  - $\not\!\!E_T > 25$ GeV
  - Transverse mass $M_T > 50$ GeV
  - Distance of closest approach (DCA) for the electron < 0.02 cm
  - Z position of primary vertex $|\mathrm{VtxZ}| < 40$ cm
  - The distance between the electron track and the primary vertex along Z axis $|\Delta\mathrm{Z}| < 2$ cm (Fig. 5.3)

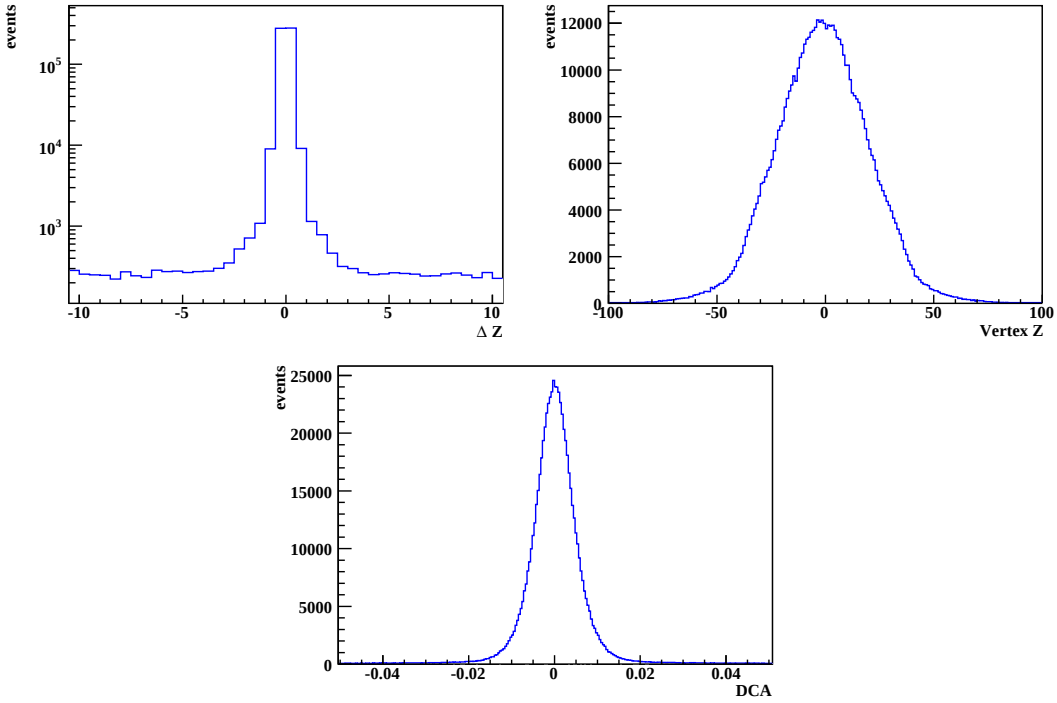

Figure 5.3: The distance between electron track and primary vertex (top left, logarithmic scale), the vertex z position (top right) and DCA (bottom) distributions for the $W \to e\nu$ sample.

5.4 MC Samples

One of the advantages of this analysis is that it does not depend much on the MC simulation. We use the MC simulation to determine the electroweak backgrounds due

to $W \rightarrow \tau\nu$ where the τ decays to an electron (≈400,000 events) and $Z \rightarrow ee$ where one electron is not reconstructed and thus causes significant missing energy (≈1,800,000 events). We also use the MC simulation to estimate the detector effects on the charge asymmetry measurement. We use the PYTHIA event generator to simulate $p\overline{p}$ interactions, particle production and decay. The generated events are then processed by a detector simulation package to add detector effects (GEANT) (see details in Chap. 7).

5.5 Data After Selection

After the cuts described in Sec. 4.1 and Sec. 4.3, Sec. 5.2 and Sec. 5.3, we have ∼ 491k W candidates, ∼ 40k Z candidates and ∼ 74k em+jet candidates. For W candidates, we are left with 358,336 events with an electron in CC region, and 132,914 events with electron in EC region.

Fig. 5.4 shows the M_T, electron E_T, $\not\!\!E_T$ and electron/positron rapidity distributions for W candidates with all selection requirements applied. Fig. 5.5 shows the invariant mass, electron E_T, Z boson E_T and electron physics η distributions for Z candidates with all selection requirements applied.

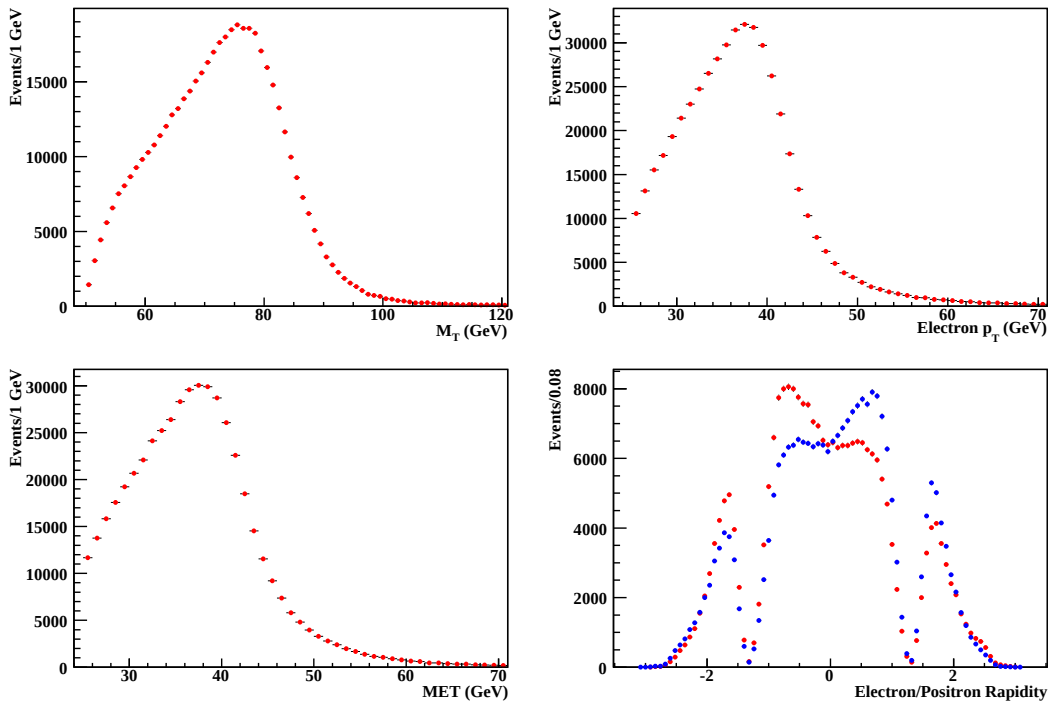

Figure 5.4: Distributions for W samples: Top left: M_T distribution; Top right: electron E_T distribution; Bottom left: $\not\!\!E_T$ distribution; Bottom right: electron and positron rapidity distribution, red for electrons and blue for positrons.

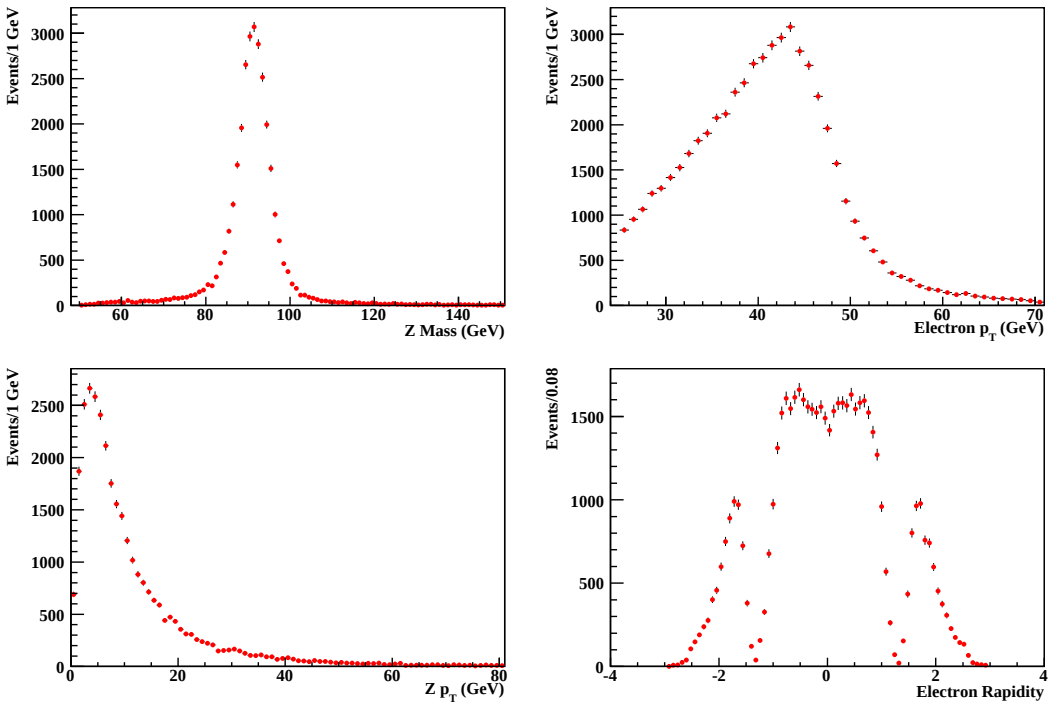

Figure 5.5: Distributions for Z sample: Top left: invariant mass distribution; Top right: electron E_T distribution; Bottom left: Z boson E_T distribution; Bottom right: electron rapidity distribution.

Chapter 6

Matrix Method

6.1 Introduction

Our signal sample is contaminated with electroweak backgrounds (mostly $Z \rightarrow ee$ and $W \rightarrow \tau\nu$) and events where one of the jets is misidentified as an electron, which we will call the QCD multijet background. We measure the electroweak backgrounds using the GEANT MC simulation and remove their contributions as described in Chap. 7. The QCD multijet background, where one of the jets is mis-measured and the other jet reconstructed as an electron, is measured using the matrix method by solving two linear equations with the loose and tight electron requirements:

$$N_L = N_W + N_{QCD} \tag{6.1}$$

$$N_T = \varepsilon \cdot N_W + f \cdot N_{QCD} \tag{6.2}$$

where N_L, N_T, N_W and N_{QCD} are the number of events that passed the loose cuts, the number of events passed tight cuts, the number of W events and the number of QCD events, respectively. ε is the efficiency for a real electron that already passed the loose cuts to also pass the tight cuts. A similar quantity for the fake electrons is f, which we call the EM-like jet ID probability, which is the probability that a QCD jet that already passed the loose electron cuts to pass the tight selection cuts.

The signal efficiency, ε, can be measured using the Z candidate sample, where the Z decays into an e^+e^- pair, and is described in Sec. 6.2. The fake rate, f, can be estimated using the electron + jet sample and that is discussed in Sec. 6.3. N_L and N_T can be counted directly from the signal sample. Substituting these values into Eqns. 6.1 and 6.2, one can solve for the values of N_W and N_{QCD}. We have very little QCD contamination in our signal sample (see Tables 10.1 to 10.4), so the N_{QCD} is very sensitive to the

signal efficiency measurement; therefore our measured N_{QCD} can, and for some bins does fluctuate below zero.

In order to measure the charge asymmetry, it is also important to determine the charge of the reconstructed track matched to the electron candidate. This is incorporated into the method described above by extending it to three equations and introducing the charge mis-identification rate, g, as follows:

$$N_L = N_{T^+} + N_{T^-} + N_{nt} = N_{e^+} + N_{e^-} + N_{QCD} \tag{6.3}$$

$$N_{T^+} = \varepsilon \cdot (1-g) \cdot N_{e^+} + f \cdot N_{QCD}/2 + \varepsilon \cdot g \cdot N_{e^-} \tag{6.4}$$

$$N_{T^-} = \varepsilon \cdot (1-g) \cdot N_{e^-} + f \cdot N_{QCD}/2 + \varepsilon \cdot g \cdot N_{e^+} \tag{6.5}$$

where N_{T^+} and N_{T^-} are the number of positrons and electrons that pass the tight "electron" selection cuts, N_{nt} is the number of events for which the EM cluster pass the loose cuts but fail the tight cuts and N_{e^+} and N_{e^-} are the number of real electrons and positrons. It is implicit in these equations that the signal efficiency, charge mis-identification rate and the fake rate are charge independent, which is discussed in Chp. 8.

If we subtract Eqn. 6.5 from Eqn. 6.4, the N_{QCD} terms will cancel and we will get:

$$N_{T^+} - N_{T^-} = \varepsilon \cdot (1-2g) \cdot (N_{e^+} - N_{e^-}) \tag{6.6}$$

And if we add those two equations and use the value of N_{QCD} from the Eqn. 6.3 we will get:

$$N_{T^+} + N_{T^-} = (\varepsilon - f) \cdot (N_{e^+} + N_{e^-}) + f \cdot (N_{T^+} + N_{T^-} + N_{nt}) \tag{6.7}$$

We can take value of $N_{e^+} - N_{e^-}$ from Eqn. 6.6, $N_{e^+} + N_{e^-}$ from Eqn. 6.7, divide one by the other and get the final asymmetry formula:

$$A = \frac{N_{e^+} - N_{e^-}}{N_{e^+} + N_{e^-}} = \frac{\varepsilon - f}{\varepsilon(1-2g)} \cdot \frac{N_{T^+} - N_{T^-}}{(1-f) \cdot (N_{T^+} + N_{T^-}) - f \cdot N_{nt}} \tag{6.8}$$

This formula only takes into account the QCD background, so we first subtract the physics backgrounds bin by bin and only after that do we use this formula to calculate the asymmetry. The estimation of electroweak backgrounds can be found in Chapter 7.

As can be seen in Eqn. 6.8, we need to measure ε, f and g, which will be described in sections 6.2, 6.3 and 6.4.

6.1.1 Error Propagation

The contribution from each variable in Eqn. 6.8 in the final uncertainty of the asymmetry is equal to the partial derivative with respect to that variable times the total uncertainty of that variable. The partial derivatives for the six independent variables ε, g, f, N_{T^+}, N_{T^-} and N_{nt} are the following:

$$\frac{\partial A}{\partial \varepsilon} = \frac{N_{T^+} - N_{T^-}}{\varepsilon(1-2g)\cdot((1-f)(N_{T^+}+N_{T^-}) - fN_{nt})} - \frac{(\varepsilon - f)(N_{T^+} - N_{T^-})}{\varepsilon^2(1-2g)\cdot((1-f)(N_{T^+}+N_{T^-}) - fN_{nt})} \tag{6.9}$$

$$\frac{\partial A}{\partial g} = \frac{2(\varepsilon - f)(N_{T^+} - N_{T^-})}{\varepsilon(1-2g)^2\cdot((1-f)(N_{T^+}+N_{T^-}) - fN_{nt})} \tag{6.10}$$

$$\frac{\partial A}{\partial f} = \frac{(\varepsilon - f)(N_{T^+} - N_{T^-})(N_{T^+}+N_{T^-}+N_{nt})}{\varepsilon(1-2g)\cdot((1-f)(N_{T^+}+N_{T^-}) - fN_{nt})^2} - \frac{(N_{T^+} - N_{T^-})}{\varepsilon(1-2g)\cdot((1-f)(N_{T^+}+N_{T^-}) - fN_{nt})} \tag{6.11}$$

$$\frac{\partial A}{\partial N_{T^+}} = -\frac{(\varepsilon - f)(N_{T^+} - N_{T^-})(1-f)}{\varepsilon(1-2g)\cdot((1-f)(N_{T^+}+N_{T^-}) - fN_{nt})^2} + \frac{(\varepsilon - f)}{\varepsilon(1-2g)\cdot((1-f)(N_{T^+}+N_{T^-}) - fN_{nt})} \tag{6.12}$$

$$\frac{\partial A}{\partial N_{T^-}} = -\frac{(\varepsilon - f)(N_{T^+} - N_{T^-})(1-f)}{\varepsilon(1-2g)\cdot((1-f)(N_{T^+}+N_{T^-}) - fN_{nt})^2} - \frac{(\varepsilon - f)}{\varepsilon(1-2g)\cdot((1-f)(N_{T^+}+N_{T^-}) - fN_{nt})} \tag{6.13}$$

$$\frac{\partial A}{\partial N_{nt}} = \frac{(\varepsilon - f)(N_{T^+} - N_{T^-})f}{\varepsilon(1-2g)\cdot((1-f)(N_{T^+}+N_{T^-}) - fN_{nt})^2} \tag{6.14}$$

6.2 Signal Efficiency (ε)

Signal efficiency (ε) is the probability that a real electron and positron that pass the loose cuts will also pass the tight cuts. The difference between the loose cuts and the tight cuts is the shower shape variable (HMx7 in CC and HMx8 in EC) as defined in Sec. 4.1.

The efficiency is measured using a 'tag and probe' method, where the tag is a tight electron and the probe is a loose electron. This method is applied to the $Z \rightarrow ee$ sample to assure the efficiency is measured on an electron rich sample. Both, the electron and the positron are considered as a tag, with the requirement that they pass all tight selection cuts and that the probe passes the track cuts (which are different for each electron

type). Probe electrons that fail the tight condition and pass the loose condition (N_{fail}) and electrons that pass the tight condition (N_{pass}) are binned in rapidity in separate histograms such that for a pure $Z \to ee$ sample, we have:

$$\varepsilon = \frac{N_{pass}}{N_{pass} + N_{fail}} \tag{6.15}$$

The QCD background is subtracted from both the pass and the fail samples. The background subtraction is performed bin-by-bin in rapidity. The dielectron invariant mass spectrum for each probe electron rapidity bin is fit with the sum of a convolution of a Gaussian function with a Breit-Wigner function for the signal and an exponential function for the QCD background (see Appendix A.1). The Breit-Wigner function is used to model resonances, it arises from the propagator of an unstable particle. We multiply it by the Gaussian to account for the smearing arising from detector resolution. The Z distribution lies on the tail of the exponential distribution of the Drell-Yan processes, therefore a linear shape is a good approximation. We did the measurement using an exponential shape instead of a linear shape, but the difference was too small to include as an additional systematic uncertainty. The number of signal events is determined by integrating the Gaussian function and Breit-Wigner function using the fit parameters. To calculate systematic uncertainty associated with fitting we use a linear background shape instead of an exponential. The difference between these two efficiencies is one of the systematic uncertainties, which turns out to be negligible. The biggest source of systematic uncertainty is the 'tag and probe' method bias. It is calculated by measuring the signal efficiency using the tag and probe method and using the "truth" method on the same MC set. (In the "truth" method we look at the generator level information of the MC particle to make sure that it is an electron or positron.) We measured the difference between the two methods in order to determine the efficiencies for each rapidity bin and fitted the difference with flat line. We fit the CC and EC sections separately and measured values of 0.25% and 1.00% respectively.

Fig. 6.1 shows the efficiency as a function of electron rapidity for the four electron types. We binned the electron physics η into 24 bins for $-3.2 < \eta < 3.2$, as listed in Table 6.1. The ε values for each type and each rapidity bin can be found in Table 6.2 to Table 6.5. The fit of the dielectron invariant mass distribution for each rapidity bin can be found in Appendix A.

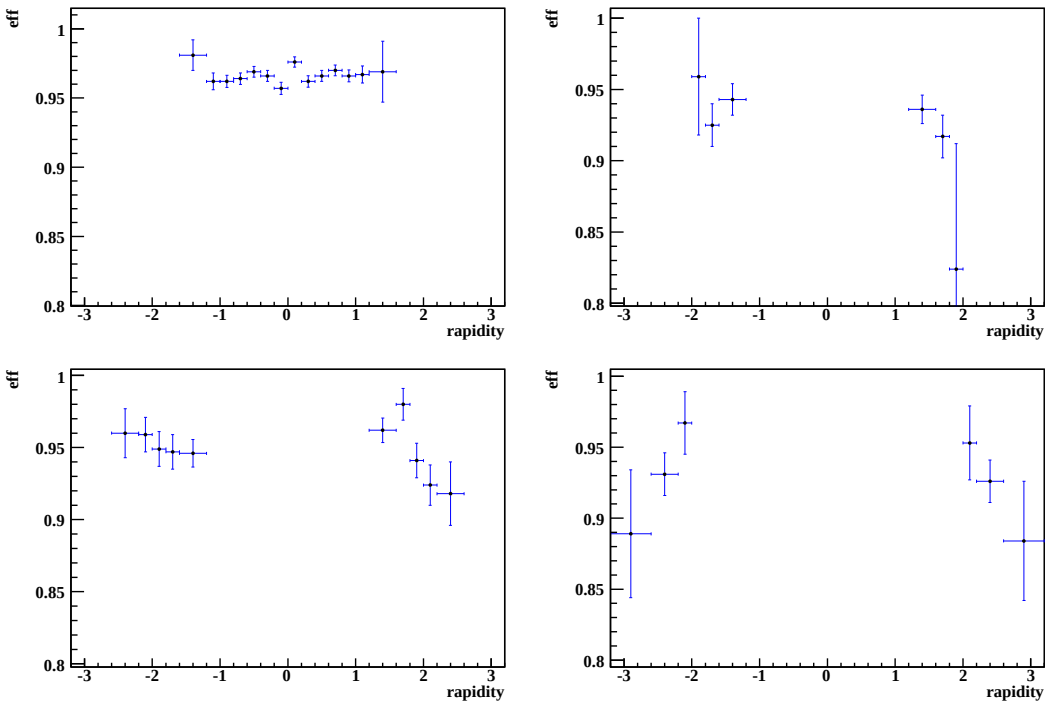

Figure 6.1: The efficiency for a real electron that passes the loose electron cuts to also pass the tight electron cuts as a function of electron rapidity for all four electron types. Top left: type 1, top right: type 2, bottom left: type 3, bottom right: type 4. A loose electron is required to have HMx7$<$ 50 in the CC and HMx8$<$ 75 in the EC, while a tight electron is required to have HMx7$<$ 10 in the CC and HMx8$<$ 10 in the EC. The error bars correspond to the total uncertainties.

Bin	Eta Region (width)	$< \eta >$
0	-3.2 - -2.6 (0.6)	-2.80
1	-2.6 - -2.2 (0.4)	-2.37
2	-2.2 - -2.0 (0.2)	-2.09
3	-2.0 - -1.8 (0.2)	-1.90
4	-1.8 - -1.6 (0.2)	-1.70
5	-1.6 - -1.2 (0.4)	-1.39
6	-1.2 - -1.0 (0.2)	-1.10
7	-1.0 - -0.8 (0.2)	-0.90
8	-0.8 - -0.6 (0.2)	-0.70
9	-0.6 - -0.4 (0.2)	-0.50
10	-0.4 - -0.2 (0.2)	-0.30
11	-0.2 - 0 (0.2)	-0.10
12	0 - 0.2 (0.2)	0.10
13	0.2 - 0.4 (0.2)	0.30
14	0.4 - 0.6 (0.2)	0.50
15	0.6 - 0.8 (0.2)	0.70
16	0.8 - 1.0 (0.2)	0.90
17	1.0 - 1.2 (0.2)	1.10
18	1.2 - 1.6 (0.4)	1.39
19	1.6 - 1.8 (0.2)	1.70
20	1.8 - 2.0 (0.2)	1.90
21	2.0 - 2.2 (0.2)	2.09
22	2.2 - 2.6 (0.4)	2.37
23	2.6 - 3.2 (0.6)	2.80

Table 6.1: Binning used for Physics rapidity. The average $< \eta >$ is the weighted average of all particles' η-s which are calculated for each region using RESBOS+PHOTOS events. All electron types are binned in this way. These $< \eta >$ values are used for data points in the asymmetry plots.

bin	Signal Efficiency	Stat. Uncertainty	Syst. Uncertainty	Total Uncert.
5	0.981	0.011	0.0025	0.011
6	0.962	0.0055	0.0025	0.0061
7	0.962	0.0036	0.0025	0.0044
8	0.964	0.0032	0.0025	0.0041
9	0.969	0.003	0.0025	0.0039
10	0.966	0.0032	0.0025	0.004
11	0.957	0.0036	0.0025	0.0044
12	0.976	0.0027	0.0025	0.0037
13	0.962	0.0033	0.0025	0.0041
14	0.966	0.0031	0.0025	0.004
15	0.97	0.003	0.0025	0.0039
16	0.966	0.0035	0.0025	0.0043
17	0.967	0.0056	0.0025	0.0061
18	0.969	0.022	0.0025	0.022

Table 6.2: Detailed values of Signal Efficiencies and Uncertainties for type 1 (CC, full CFT) electrons. The systematic uncertainty is dominated by the "tag and probe" method bias, which is 0.25% for CC electrons and 1% for EC electrons.

bin	Signal Efficiency	Stat. Uncertainty	Syst. Uncertainty	Total Uncert.
3	0.959	0.04	0.01	0.041
4	0.925	0.011	0.01	0.015
5	0.943	0.011	0.0025	0.011
18	0.936	0.0098	0.0025	0.01
19	0.917	0.011	0.01	0.015
20	0.824	0.088	0.01	0.088

Table 6.3: Detailed values of Signal Efficiencies and Uncertainties for type 2 (EC, full CFT) electrons. The systematic uncertainty is dominated by the "tag and probe" method bias, which is 0.25% for CC electrons and 1% for EC electrons.

bin	Signal Efficiency	Stat. Uncertainty	Syst. Uncertainty	Total Uncert.
1	0.96	0.013	0.01	0.017
2	0.959	0.0073	0.01	0.012
3	0.949	0.0057	0.01	0.012
4	0.947	0.006	0.01	0.012
5	0.946	0.0093	0.0025	0.0096
18	0.962	0.0082	0.0025	0.0085
19	0.98	0.0039	0.01	0.011
20	0.941	0.0062	0.01	0.012
21	0.924	0.0098	0.01	0.014
22	0.918	0.019	0.01	0.022

Table 6.4: Detailed values of Signal Efficiencies and Uncertainties for type 3 (EC, partial CFT) electrons. The systematic uncertainty is dominated by the "tag and probe" method bias, which is 0.25% for CC electrons and 1% for EC electrons.

bin	Signal Efficiency	Stat. Uncertainty	Syst. Uncertainty	Total Uncert.
0	0.889	0.044	0.01	0.045
1	0.931	0.012	0.01	0.015
2	0.967	0.019	0.01	0.022
21	0.953	0.024	0.01	0.026
22	0.926	0.012	0.01	0.015
23	0.884	0.04	0.01	0.042

Table 6.5: Detailed values of Signal Efficiencies and Uncertainties for type 4 (EC, no CFT) electrons. The systematic uncertainty is dominated by the "tag and probe" method bias, which is 0.25% for CC electrons and 1% for EC electrons.

6.3 EM-like jet ID probability (f)

The EM-like jet probability ("fake rate"), f, is defined as the probability for a real jet that has already passed the loose electron cuts to also pass the tight electron cuts. The difference between the loose electron cuts and the tight electron cuts is the shower shape variable, as defined in Sec. 4.1. The fake rate is measured using EM+jet events, and it can be simply defined as the ratio:

$$f = \frac{N_T}{N_L} \tag{6.16}$$

where N_L is the number of events where a loose electron candidate was reconstructed and N_T is the number of events where the loose electron also passed the tight cuts.

The EM+Jet sample is used to measure this fake rate and the selection requirements for that sample are described in Sec. 5.3. To calculate the EM-like jet ID probability we use the $\not\!\!E_T$ distributions of the EM+Jet sample. We have a $\not\!\!E_T$ distribution for the tight sample and for the loose sample, we divide the former by the latter and fit the ratio with a constant number for $\not\!\!E_T < 10$ GeV (see the ratio plots in the Appendix B.). We only look at the low $\not\!\!E_T$ to suppress the W contamination. We also measure the EM-like jet ID probability for events with $\not\!\!E_T < 15$ GeV, and use the difference between these two fake rates as the systematic uncertainty (Tables 6.6 to 6.9). We estimate real electron contamination in our multijet sample by running our code on the GEANT $Z \to ee$ and $W \to \tau\nu$ samples; the contamination is less than 1%.

Fig. 6.2 shows the probability as a function of electron rapidity for the four types. The f values for each type and each rapidity bin, as well as statistical and systematic uncertainties, can be found in Table 6.6 to Table 6.9. The probability as a function of $\not\!\!E_T$ for each rapidity bin can be found in Appendix B.

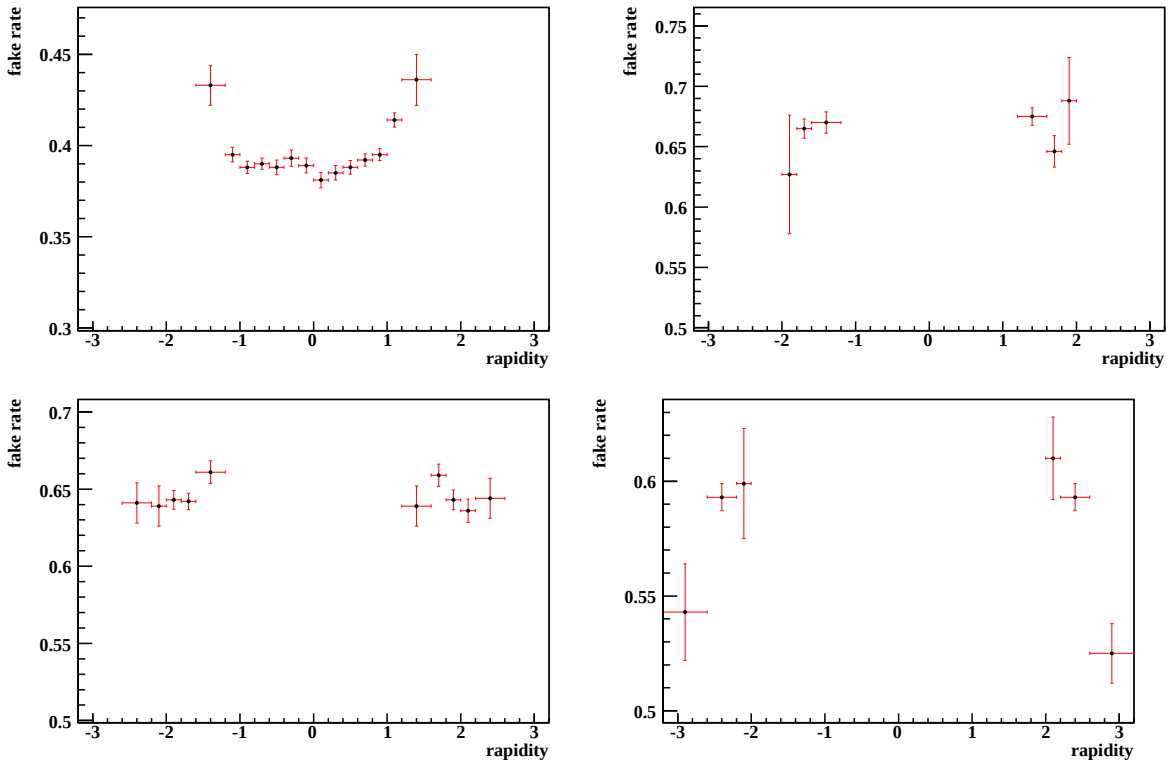

Figure 6.2: The EM-like jet ID probability for a real jet that has already passed the loose electron cuts to also pass the tight electron cuts as a function of electron rapidity for all four types. Top left: type 1 (CC, full CFT), top right: type 2 (EC, full CFT), bottom left: type 3 (EC, partial CFT), bottom right: type 4 (EC, no CFT). The loose electron is required to have HMx7< 50 in CC and HMx8< 75 in EC, while the tight electron is required to have HMx7< 10 in CC and HMx8< 10 in EC. The error bars correspond to the total uncertainties.

bin	EM-like jet ID prob.	Stat. Uncert.	Syst. Uncert.	Total Uncert.
5	0.433	0.0097	0.0049	0.011
6	0.395	0.0034	0.0021	0.004
7	0.388	0.0027	0.0019	0.0033
8	0.39	0.003	0.00044	0.0031
9	0.388	0.0034	0.0021	0.004
10	0.393	0.0038	0.0022	0.0044
11	0.389	0.004	0.00048	0.0041
12	0.381	0.0041	0.0012	0.0042
13	0.385	0.0038	0.00099	0.004
14	0.388	0.0034	0.0015	0.0038
15	0.392	0.0031	0.0013	0.0033
16	0.395	0.0029	0.0015	0.0033
17	0.414	0.0038	0.0009	0.0039
18	0.436	0.014	0.0013	0.014

Table 6.6: Detailed values of EM-like jet ID probabilities and uncertainties for type 1 electron-like jets. The systematic uncertainty is the difference between the fake rates measured using $\not\!\!E_T < 10$ GeV and $\not\!\!E_T < 15$ GeV.

bin	EM-like jet ID prob.	Stat. Uncert.	Syst. Uncert.	Total Uncert.
3	0.627	0.029	0.039	0.049
4	0.665	0.0067	0.0042	0.0079
5	0.67	0.0075	0.0045	0.0088
18	0.675	0.0065	0.003	0.0072
19	0.646	0.0068	0.011	0.013
20	0.688	0.029	0.021	0.036

Table 6.7: Detailed values of EM-like jet ID probabilities and uncertainties for type 2 electron-like jets. The systematic uncertainty is the difference between the fake rates measured using $\not\!\!E_T < 10$ GeV and $\not\!\!E_T < 15$ GeV.

bin	EM-like jet ID prob.	Stat. Uncert.	Syst. Uncert.	Total Uncert.
1	0.641	0.013	0.0041	0.013
2	0.639	0.0067	0.011	0.013
3	0.643	0.005	0.0035	0.0061
4	0.642	0.0048	0.0023	0.0053
5	0.661	0.007	0.002	0.0073
18	0.639	0.0081	0.0096	0.013
19	0.659	0.0051	0.0052	0.0072
20	0.643	0.0052	0.0038	0.0064
21	0.636	0.0069	0.0028	0.0075
22	0.644	0.012	0.0034	0.013

Table 6.8: Detailed values of EM-like jet ID probabilities and uncertainties for type 3 electron-like jets. The systematic uncertainty is the difference between the fake rates measured using $\not\!\!E_T < 10$ GeV and $\not\!\!E_T < 15$ GeV.

bin	EM-like jet ID prob.	Stat. Uncert.	Syst. Uncert.	Total Uncert.
0	0.543	0.013	0.017	0.021
1	0.593	0.0059	5.6e-05	0.0059
2	0.599	0.016	0.019	0.024
21	0.61	0.018	0.0025	0.018
22	0.593	0.0059	0.00026	0.0059
23	0.525	0.012	0.004	0.013

Table 6.9: Detailed values of EM-like jet ID probabilities and uncertainties for type 4 electron-like jets. The systematic uncertainty is the difference between the fake rates measured using $\not\!\!E_T < 10$ GeV and $\not\!\!E_T < 15$ GeV.

6.4 Charge Mis-identification rate (g)

The charge mis-identification rate (g) is the probability that a real electron will be assigned an incorrect charge. To ensure that real electrons are tested, the dielectron ($Z \rightarrow ee$) sample set is used. The mis-identification rate is measured using the 'tag and probe' method, where the tag is an electron with high curvature significance (curvature divided by the error of the curvature) where we assume its charge is measured correctly and the probe is the other electron. If the charge of the probe is the same as the charge of the tag, we say the charge of the probe was mis-identified. If they are opposite, then we say it was identified correctly. Each electron is tested separately.

We studied the charge mis-identification dependence on the electron E_T (Fig. 6.3). The low statistics does not allow us to draw clear conclusions, for this analysis we do not include it as additional source of systematics.

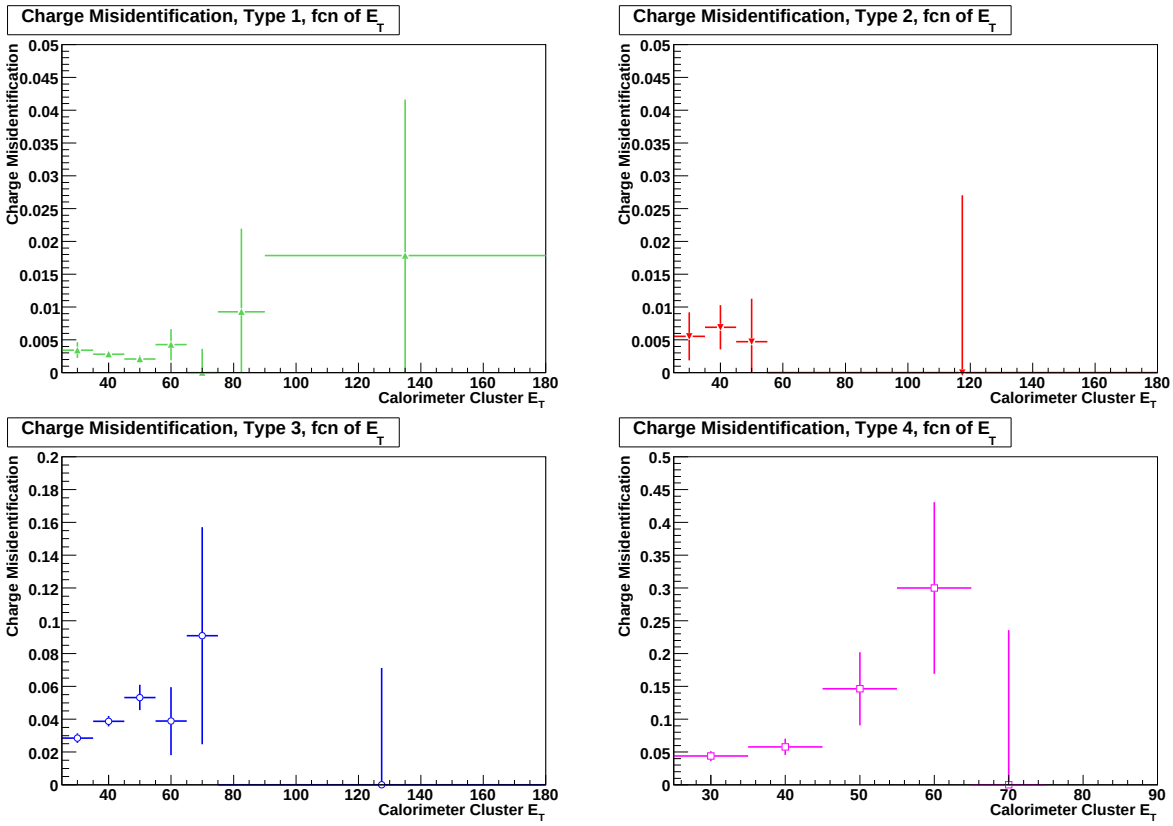

Figure 6.3: Charge misidentification rate as a function of E_T. Top left: type 1, top right: type 2, bottom left: type 3, bottom right: type 4.

The 'tag and probe' method is also applied on GEANT MC sample, and the measured charge mis-identification rates are compared with the rates obtained using the MC "truth" information. Both measurements agree with each other within statistical

uncertainties.

Charge mis-identification for this analysis is studied in great detail in D0note 5564 [14]. The charge misidentification rate as a function of electron rapidity for the four different electron types can be found in Fig. 6.4. The g values for each type and each rapidity bin can be found in Table 6.10 to Table 6.13.

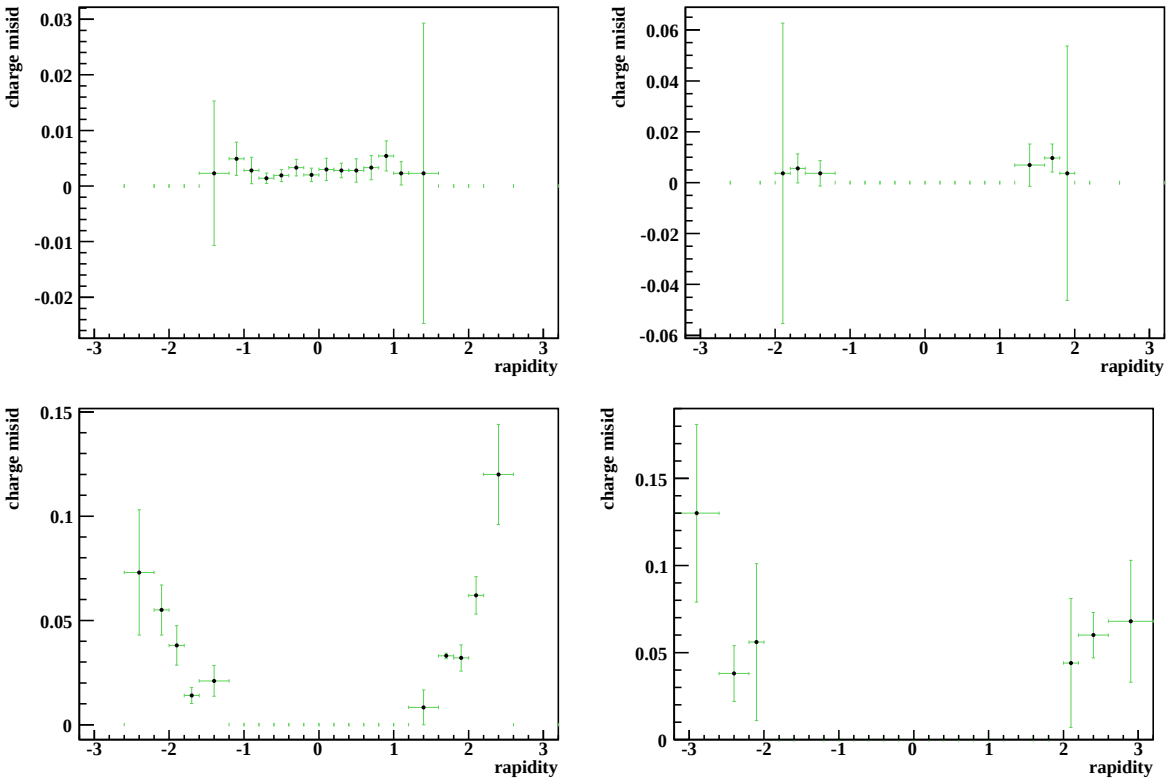

Figure 6.4: Charge mis-identification rate as a function of electron rapidity for all four electron types. Top left: type 1, top right: type 2, bottom left: type 3, bottom right: type 4.

Bin	Charge Misid. Rate	Stat. uncert.	Sys. Uncert.	Total Uncert.
5	0.0023	0.013	0.0023	0.013
6	0.0049	0.0027	0.0013	0.0030
7	0.0028	0.0014	0.0019	0.0024
8	0.0014	0.00093	0.00015	0.00094
9	0.0019	0.0010	0.00037	0.0011
10	0.0033	0.0013	0.00060	0.0015
11	0.0020	0.0011	0.00046	0.0012
12	0.0030	0.0013	0.0015	0.0020
13	0.0028	0.0012	0.00056	0.0013
14	0.0028	0.0012	0.0017	0.0021
15	0.0033	0.0013	0.0018	0.0022
16	0.0054	0.0019	0.0020	0.0027
17	0.0023	0.0015	0.0014	0.0021
18	0.0023	0.027	0.0023	0.027

Table 6.10: Detailed Values of charge misidentification and uncertainties for Type 1 (CC, full CFT) Electrons. These are the charge misidentification rates with the previously mentioned (Chps. 4 and 5) quality cuts applied.

Bin	Charge Misid. Rate	Stat. uncert.	Sys. Uncert.	Total Uncert.
3	0.0037	0.059	0.0037	0.059
4	0.0056	0.0048	0.0030	0.0057
5	0.0037	0.0035	0.0037	0.0035
18	0.0069	0.0046	0.0070	0.0083
19	0.0097	0.0053	0.0013	0.0055
20	0.0037	0.050	0.0037	0.050

Table 6.11: Detailed Values of charge misidentification and uncertainties for Type 2 (EC, full CFT) Electrons. These are the charge misidentification rates with the previously mentioned (Chps. 4 and 5) quality cuts applied.

Bin	Charge Misid. Rate	Stat. uncert.	Sys. Uncert.	Total Uncert.
1	0.059	0.0078	0.012	0.015
2	0.038	0.0054	0.0077	0.0094
3	0.014	0.0033	0.0022	0.0039
4	0.021	0.0063	0.0039	0.0074
19	0.0083	0.0046	0.0069	0.0083
20	0.033	0.0052	0.0115	0.0012
21	0.032	0.0049	0.0039	0.0063
22	0.075	0.0084	0.0043	0.0094

Table 6.12: Detailed Values of charge misidentification and uncertainties for Type 3 (EC, partial CFT) Electrons. These are the charge misidentification rates with the previously mentioned (Chps. 4 and 5) quality cuts applied.

Bin	Charge Misid. Rate	Stat. uncert.	Sys. Uncert.	Total Uncert.
0	0.13	0.047	0.019	0.051
1	0.041	0.0089	0.016	0.018
22	0.058	0.010	0.0091	0.014
23	0.068	0.031	0.017	0.035

Table 6.13: Detailed Values of charge misidentification and uncertainties for Type 4 (EC, no CFT) Electrons. These are the charge misidentification rates with the previously mentioned (Chps. 4 and 5) quality cuts applied.

Chapter 7

Non-QCD backgrounds

The Matrix method described in Chapt. 6 addresses only the QCD multijet backgrounds; other sources of background contamination are: $W \to \tau\nu$ events where the τ decays to an electron and neutrinos; $Z \to ee$ events where one of the electrons is outside the calorimeter fiducial region and gets reconstructed as missing energy. Other possible backgrounds such as WW and WZ are negligible as their cross sections are ≈200 times smaller than that of a W.

We measured N_{T^+}, N_{T^-} and N_{nt} for the GEANT MC samples listed in the Sec. 5.4. We normalized those numbers so that they would correspond to our ~ 750 pb^{-1} of data. The NLO inclusive W and Z cross sections used are taken from Ref. [15].

The GEANT MC simulation is tuned to agree with the data by applying electron and $\not\!\!E_T$ smearing. To account for the difference between data and MC acceptances, we calculated each of them separately using $Z \to ee$ events and the tag and probe method. We found them to be slightly different, so by dividing one by the other we calculated the scale factors between data and GEANT MC and we did this for each rapidity bin separately. The systematic uncertainties on the electroweak backgrounds are estimated by varying the electron energy smearing parameters, the $\not\!\!E_T$ smearing parameters and the acceptance scale factors by their respective uncertainties and observing the effect on the GEANT MC sample. The estimated electroweak backgrounds for each rapidity bin can be found in Table 7.1 to Table 7.4. They are subtracted from the real data distribution bin by bin before we use the matrix method to estimate the QCD background.

The overall background contribution is 1.3% for the $Z \to ee$ background, 2.1% due to the $W \to \tau\nu$ background.

In these tables, $N^{tight}_{Z\to ee^+}$ is the number of the $Z \to ee$ events in our signal sample that fake W^+ events with the tight electron requirements, $N^{tight}_{Z\to ee^-}$ is the same thing for W^- events and $N^{nottight}_{Z\to ee}$ for the $Z \to ee$ events that fake W events where the electron passes

loose but not tight selection requirements. $N^{tight}_{W\to\tau\nu^+}$, $N^{tight}_{W\to\tau\nu^-}$ and $N^{nottight}_{W\to\tau\nu}$ are similar quantities for the $W \to \tau\nu$ process.

bin	$N^{tight}_{Z\to ee^+}$	$N^{tight}_{Z\to ee^-}$	$N^{nottight}_{Z\to ee}$	$N^{tight}_{W\to\tau\nu^+}$	$N^{tight}_{W\to\tau\nu^-}$	$N^{nottight}_{W\to\tau\nu}$
5	7.97	8.48	0.302	4.78	27.3	4.64
6	96.5	86.9	4.09	86.0	167	21.4
7	175	183	10.7	229	360	50.2
8	222	209	12.4	394	459	41.3
9	232	239	13.9	401	298	46.8
10	237	251	15.2	405	381	58.5
11	231	224	14.2	342	371	25.8
12	208	217	13.8	325	353	45.6
13	231	234	13.4	415	373	74
14	228	231	12.0	406	322	59.5
15	229	230	13.8	403	342	48.8
16	157	157	8.13	327	245	40
17	63.3	66.4	4.14	102	123	16.4
18	3.18	3.58	0.191	0	18.4	0

Table 7.1: Type 1 (CC, full CFT) bin number, the number of $Z \to ee$ background events with positive charge that pass the tight cut, the number of $Z \to ee$ background events with negative charge that pass the tight cut, the number of $Z \to ee$ background events that pass the loose cut, but fail the tight cut, the number of $W \to \tau\nu$ background events with positive charge that pass the tight cut, the number of $W \to \tau\nu$ background events with negative charge that pass the tight cut, the number of $W \to \tau\nu$ background events that pass the loose cut, but fail the tight cut.

bin	$N^{tight}_{Z\to ee^+}$	$N^{tight}_{Z\to ee^-}$	$N^{nottight}_{Z\to ee}$	$N^{tight}_{W\to\tau\nu^+}$	$N^{tight}_{W\to\tau\nu^-}$	$N^{nottight}_{W\to\tau\nu}$
3	1.99	1.96	0.287	0	0	0
4	35.7	36.4	2.34	40.7	64.4	4.95
5	27.1	26.6	3.38	42.5	28.9	9.34
18	34.8	34.6	2.63	58.8	62.5	3.03
19	32.2	36.5	2.26	71.6	43.4	8.53
20	1.76	1.91	0.121	0	0	0

Table 7.2: Type 2 (EC, full CFT) bin number, the number of $Z \to ee$ background events with positive charge that pass the tight cut, the number of $Z \to ee$ background events with negative charge that pass the tight cut, the number of $Z \to ee$ background events that pass the loose cut, but fail the tight cut, the number of $W \to \tau\nu$ background events with positive charge that pass the tight cut, the number of $W \to \tau\nu$ background events with negative charge that pass the tight cut, the number of $W \to \tau\nu$ background events that pass the loose cut, but fail the tight cut.

bin	$N^{tight}_{Z\to ee^+}$	$N^{tight}_{Z\to ee^-}$	$N^{nottight}_{Z\to ee}$	$N^{tight}_{W\to\tau\nu^+}$	$N^{tight}_{W\to\tau\nu^-}$	$N^{nottight}_{W\to\tau\nu}$
1	16.3	16.6	2.01	27.8	25.9	0
2	51.1	55.0	3.09	91.5	45.5	5.11
3	96.7	90.1	6.56	108	132	8.43
4	88.5	84.0	7.37	122	121	11.8
5	47.9	44.3	3.20	64.6	81.4	0
18	43.7	43.9	2.81	61.9	64.2	16.8
19	97.8	93.2	5.65	133	152	0
20	109	110	9.85	178	128	11.7
21	47.9	48.5	3.77	79.5	60.5	0
22	15.2	14.7	1.63	28.1	10.8	0

Table 7.3: Type 3 (EC, partial CFT)bin number, the number of $Z \to ee$ background events with positive charge that pass the tight cut, the number of $Z \to ee$ background events with negative charge that pass the tight cut, the number of $Z \to ee$ background events that pass the loose cut, but fail the tight cut, the number of $W \to \tau\nu$ background events with positive charge that pass the tight cut, the number of $W \to \tau\nu$ background events with negative charge that pass the tight cut, the number of $W \to \tau\nu$ background events that pass the loose cut, but fail the tight cut.

bin	$N^{tight}_{Z\to ee^+}$	$N^{tight}_{Z\to ee^-}$	$N^{nottight}_{Z\to ee}$	$N^{tight}_{W\to\tau\nu^+}$	$N^{tight}_{W\to\tau\nu^-}$	$N^{nottight}_{W\to\tau\nu}$
0	3.00	2.63	0.770	2.33	4.26	0.777
1	54.6	57.9	8.86	55.6	95.3	26.1
2	9.04	12.3	0.744	15.4	4.06	4.92
21	12.1	13.4	1.46	10.5	23.9	0
22	61.8	68.5	7.45	111	62.9	14.5
23	5.77	5.35	1.43	5.86	0	1.06

Table 7.4: Type 4 (EC, no CFT) bin number, the number of $Z \to ee$ background events with positive charge that pass the tight cut, the number of $Z \to ee$ background events with negative charge that pass the tight cut, the number of $Z \to ee$ background events that pass the loose cut, but fail the tight cut, the number of $W \to \tau\nu$ background events with positive charge that pass the tight cut, the number of $W \to \tau\nu$ background events with negative charge that pass the tight cut, the number of $W \to \tau\nu$ background events that pass the loose cut, but fail the tight cut.

Chapter 8

Detector and Selection Charge Bias

The master Eqn. 1.22 assumes that luminosity, acceptance $\times$ efficiency have no charge dependence. Though the luminosity by definition introduces no charge bias, the same does not necessarily hold for the acceptance and efficiency. To reduce effects due to detector asymmetries, the direction of the magnetic field in the solenoidal magnets was regularly reversed. Approximately 46% of the selected W bosons were collected with the solenoid at forward polarity, with 54% at reverse polarity. We did not assign any systematic uncertainties due to possible detector asymmetries since the fractions of data taken with different polarities are close to 50%, and it cancels all possible first order effects and any residual effect is suppressed by the 8% asymmetry in the running conditions.

Fig. 8.1 shows raw asymmetry distributions for forward and reverse solenoid polarizations. The errors on the plot are statistical.

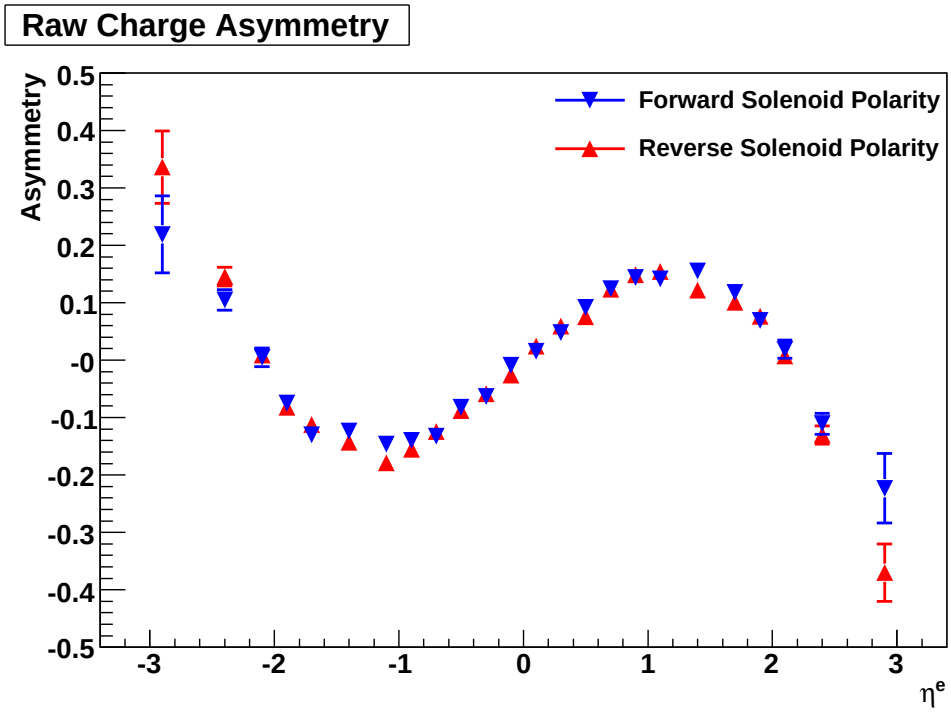

Figure 8.1: Asymmetry distribution for different polarities.

The possible charge dependence of the efficiency is investigated by comparing efficiencies measured for positrons and electrons separately and comparing them to look for significant differences. Figures 8.2 to 8.5 show the ratios for electron and positron efficiencies as well as positive and negative EM-like jet efficiencies for each electron type for forward and backward solenoid polarization. Each of those ratios is fitted with a flat line and the fit value is consistent with 1. No indications of charge-dependent efficiencies are observed.

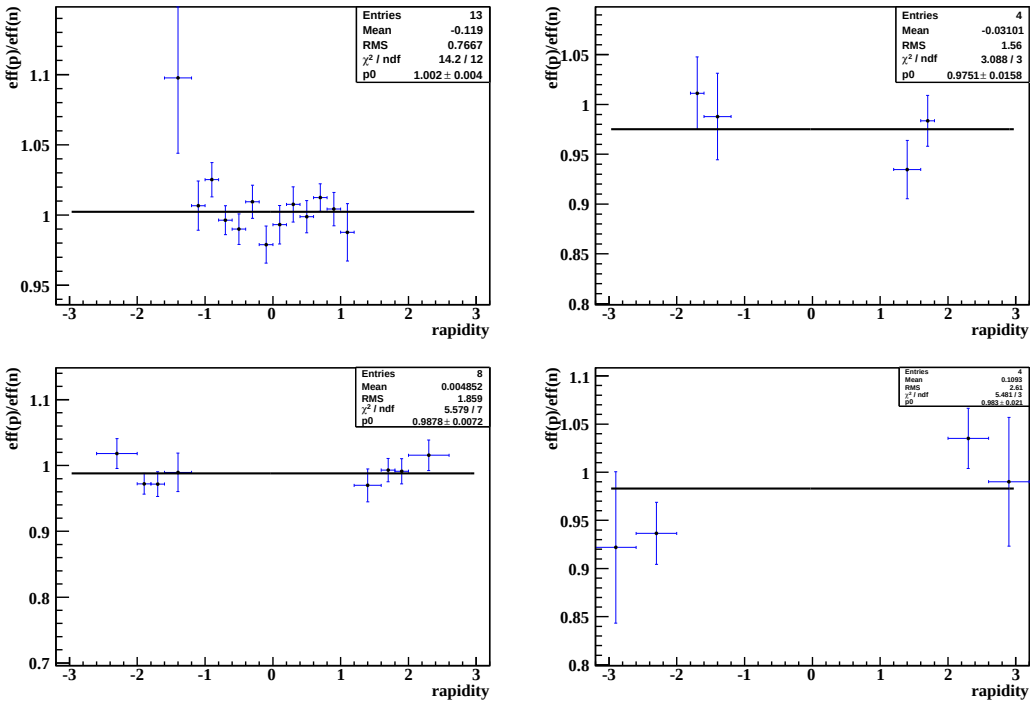

Figure 8.2: Ratio of electron and positron efficiencies for the forward solenoid polarization.

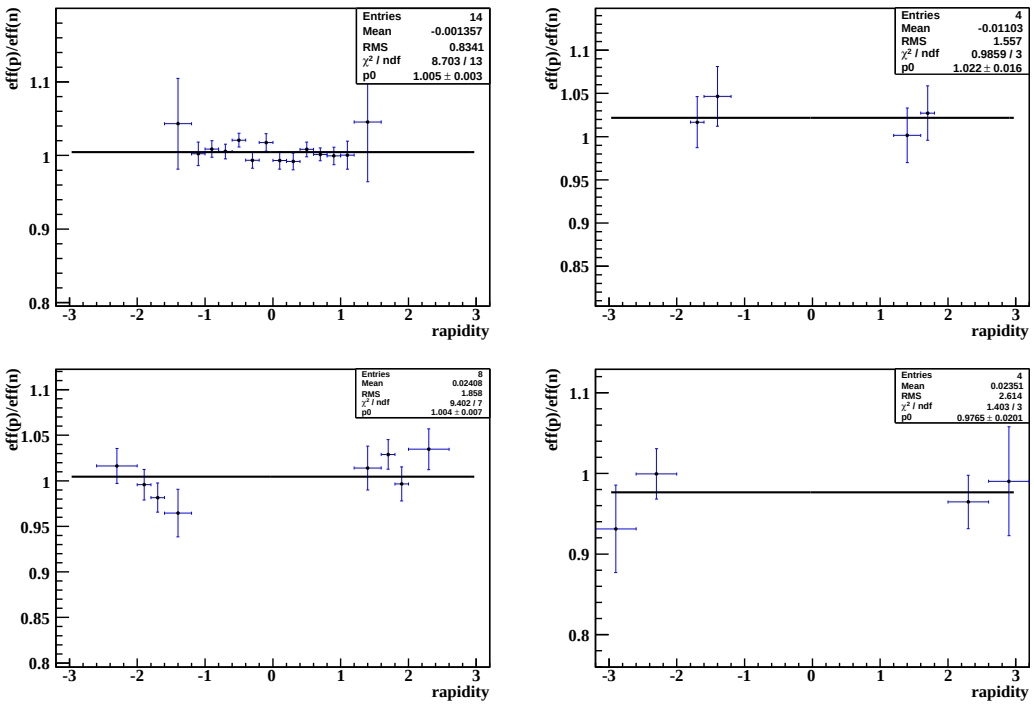

Figure 8.3: Ratio of electron and positron efficiencies for the backward solenoid polarization.

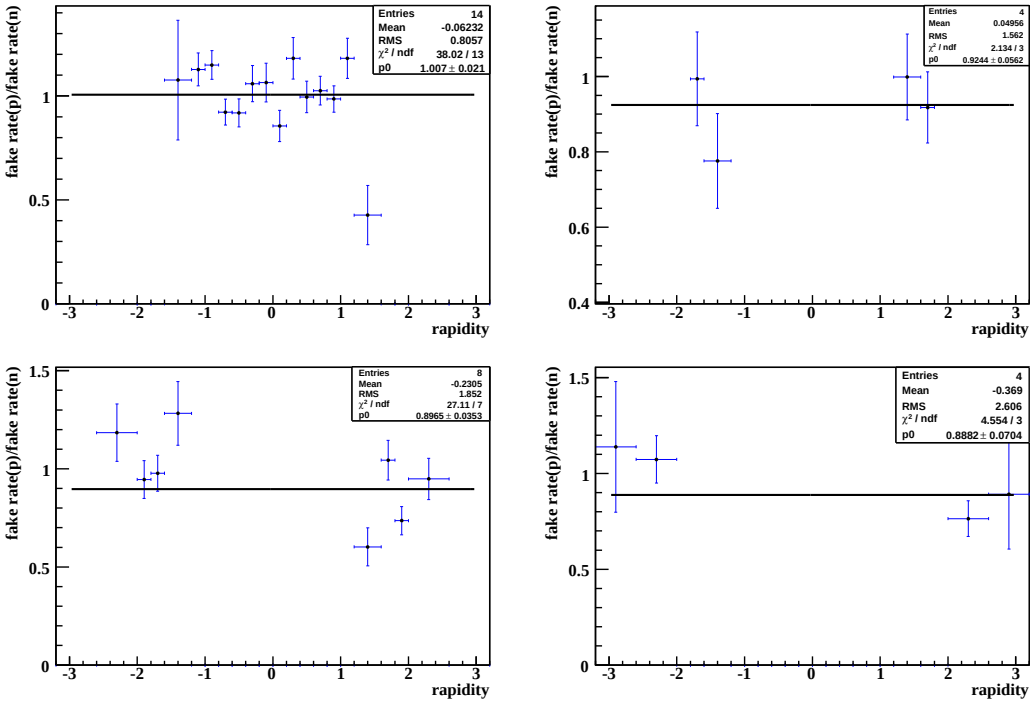

Figure 8.4: Ratio of positive and negative EM-like jet efficiencies for the forward solenoid polarization.

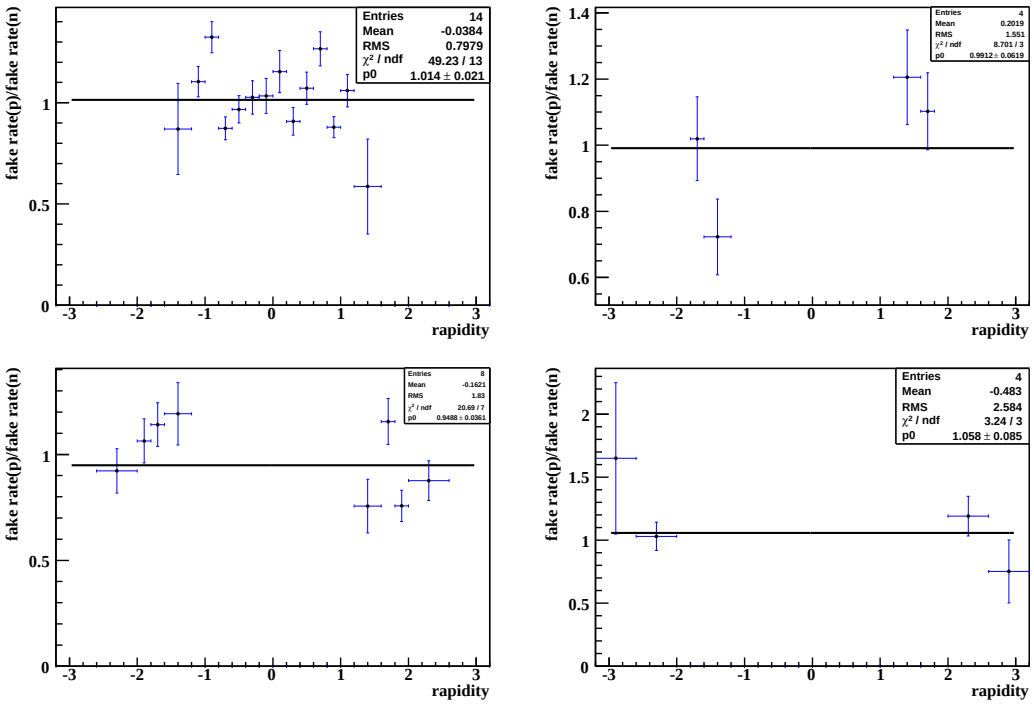

Figure 8.5: Ratio of positive and negative EM-like jet efficiencies for the backward solenoid polarization.

Chapter 9

Corrections Due to Detector Effects

The charge asymmetry we measured is for events with reconstructed electron $p_T > 25$ GeV and reconstructed $\not\!\!E_T > 25$ GeV. Both electron energy resolution and $\not\!\!E_T$ resolution can affect the final asymmetry distribution. Therefore we remove the detector effects so that our results can be directly compared with the theoretical predictions.

The corrections are estimated from the $W \rightarrow e\nu$ GEANT MC simulation sample generated with PYTHIA. The calorimeter responses to electrons and $\not\!\!E_T$ in the simulation are tuned to agree with those in data, the scale factors for electron selection efficiencies between data and GEANT MC are applied in the simulation. The additional EM scaling is done using the following formula:

$$E^{'} = \alpha \times E^{\mathrm{GEANT}} \tag{9.1}$$

and the additional EM smearing is done using the following formula:

$$E^{\mathrm{smear}} = E^{'}(1 + c \times x) \tag{9.2}$$

where E^{GEANT}, $E^{'}$ and E^{smear} are the raw energy from GEANT MC simulation, the energy after scaling, and the energy after scaling and smearing respectively. α and c are the energy scaling and smearing parameters (CC and EC electrons have different α and c), and x is a random number generated with a Gaussian distribution with zero mean and unit sigma. The scaling parameter is found to be 1.0045 ± 0.00027 for CC and 0.99085 ± 0.00048 for EC. The smearing parameter is found to be 0.028 ± 0.002 for CC and 0.025 ± 0.002 for EC [17]. The data $\not\!\!E_T$ resolution is close to 3 GeV, and we added an additional 10% (0.3 GeV) smearing. The systematic uncertainties due to detector smearing parameters and efficiencies are found to be negligible. Figs. 9.2 to 9.4 show the M_T, electron p_T and $\not\!\!E_T$ distributions for all four types between data and GEANT MC simulation, reasonable agreement is observed.

After we have a GEANT MC simulation that describes the real data reasonably well, we treat GEANT MC $W \rightarrow e\nu$ events like data (except for the charge where we use the generator level information instead of the measured charge of the EM cluster to remove the charge mis-identification effect in GEANT MC) and measure the charge asymmetry distributions for four types by cutting on the reconstructed electron p_T and reconstructed $\not\!\!E_T$. By using the truth information, we can also measure the truth asymmetry by cutting on the generator level electron p_T and neutrino p_T (which are the cuts we used to make the final theoretical predictions). The differences between the truth and the measured asymmetry distributions in the GEANT MC are the corrections that we later apply to the measured asymmetry distribution to extract the true asymmetry that can be compared to theoretical predictions. Table 9.1 shows the corrections due to the detector effects in each rapidity bin for four electron types.

To make sure that our choice of PDFs in the MC that we use to measure the corrections does not introduce a bias, we compare the corrections obtained using PYTHIA with CTEQ6L PDFs and RESBOS with CTEQ6.6 PDFs. Fig. 9.1 shows the difference between these two corrections as a function of rapidity. As the number of events used in each of the MC samples is approximately 5 times larger than what we have in our data and still the difference between the corrections is consistent with zero, therefore we conclude there is no bias.

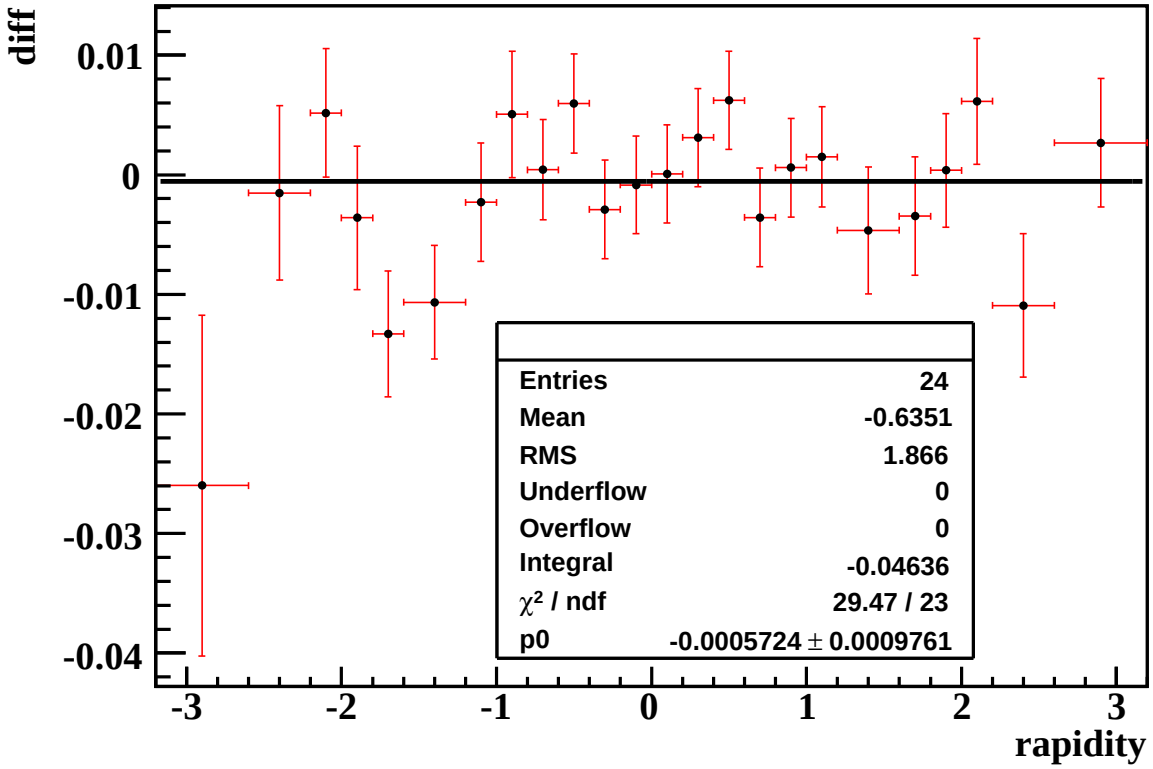

Figure 9.1: Differences between the corrections due to detector effects calculated with PYTHIA (CTEQ6L) and RESBOS (CTEQ6.6) as a function of rapidity.

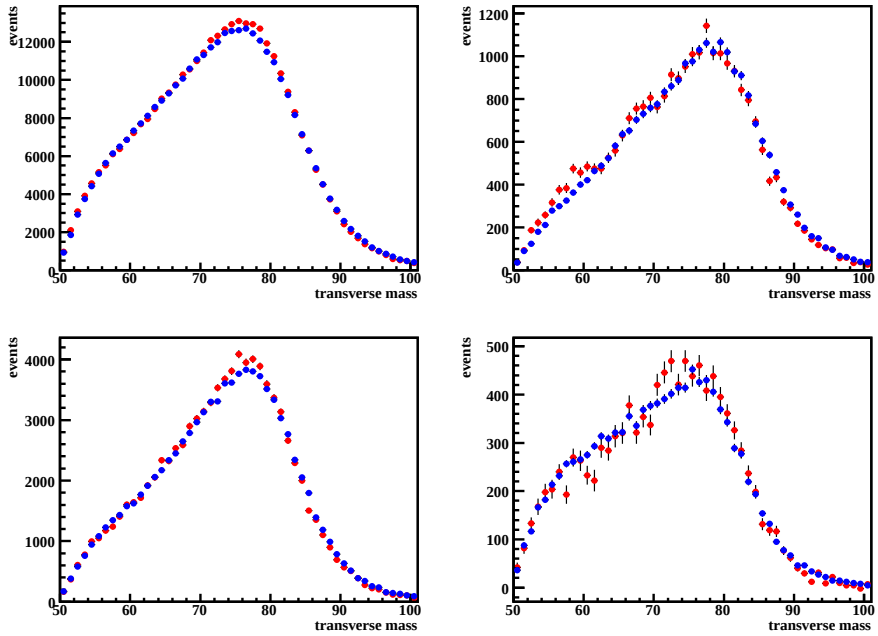

Figure 9.2: Data/MC transverse mass comparison plots for each electron type. Top left: type 1; top right: type 2; bottom left: type 3; bottom right: type 4. Red for data, blue for MC.

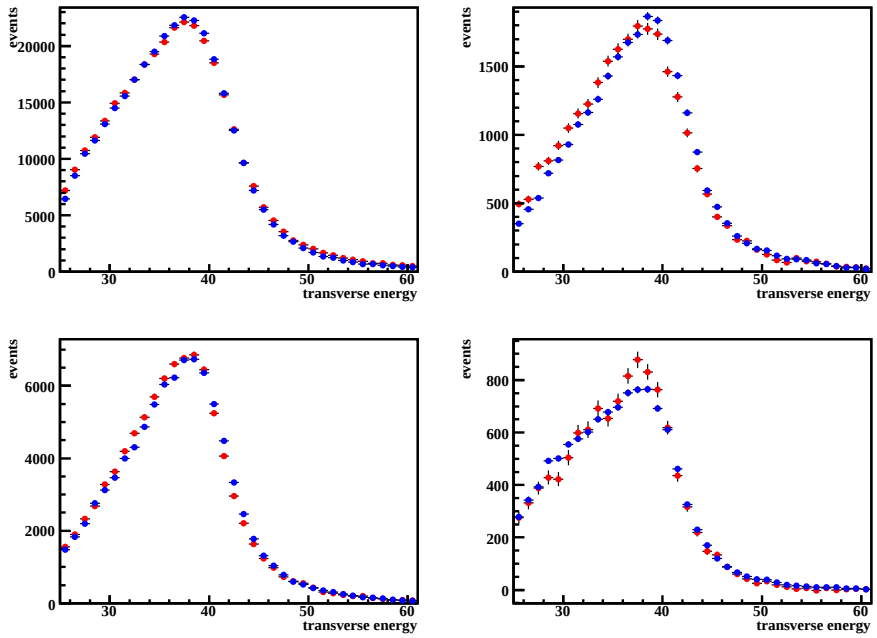

Figure 9.3: Data/MC electron p_T comparison plots for each type. Top left: type 1; top right: type 2; bottom left: type 3; bottom right: type 4. Red for data, blue for MC.

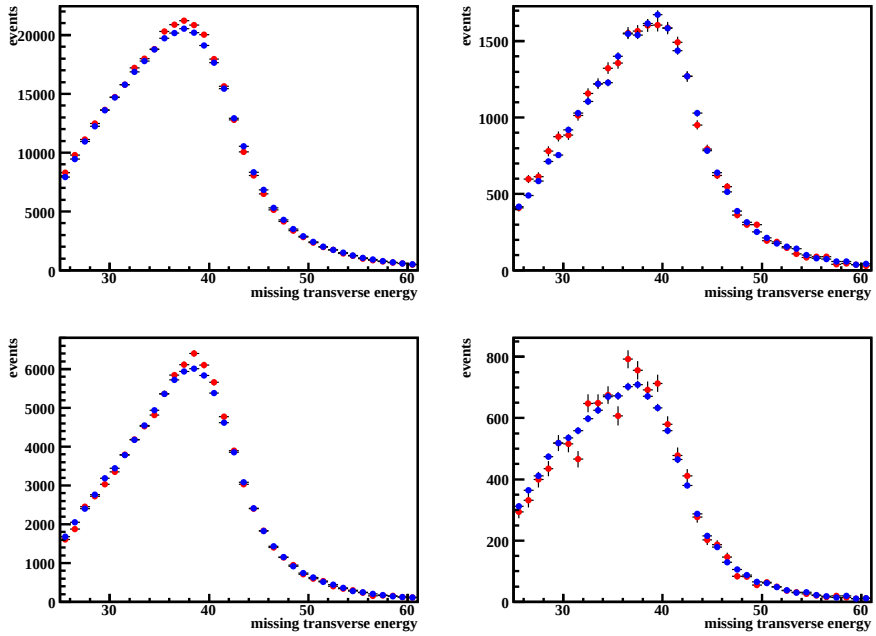

Figure 9.4: Data/MC $\not\!\!E_T$ comparison plots for each type. Top left: type 1; top right: type 2; bottom left: type 3; bottom right: type 4. Red for data, blue for MC.

bin	Type 1	Type 2	Type 3	Type 4
0	-	-	-	0.116 ± 0.0178
1	-	-	0.089 ± 0.0138	0.0519 ± 0.00795
2	-	-	0.016 ± 0.00782	0.0355 ± 0.0168
3	-	0.0849 ± 0.0396	0.0156 ± 0.00555	-0.302 ± 0.187
4	-	0.0176 ± 0.00883	0.0179 ± 0.0056	-
5	0.0352 ± 0.0189	-0.00772 ± 0.0103	0.0137 ± 0.00786	-
6	0.0063 ± 0.00594	-	-	-
7	0.00787 ± 0.00415	-	-	-
8	0.00863 ± 0.00386	-	-	-
9	0.00556 ± 0.0038	-	-	-
10	0.00455 ± 0.00382	-	-	-
11	0.00119 ± 0.00386	-	-	-
12	-0.00617 ± 0.0039	-	-	-
13	-0.00348 ± 0.00379	-	-	-
14	-0.00378 ± 0.00379	-	-	-
15	0.00252 ± 0.00376	-	-	-
16	-0.00594 ± 0.00438	-	-	-
17	-0.013 ± 0.00683	-	-	-
18	-0.00728 ± 0.0293	0.0111 ± 0.0086	0.0037 ± 0.00771	-
19	-	-0.0231 ± 0.00883	-0.0178 ± 0.00568	-
20	-	-0.0251 ± 0.0439	-0.0158 ± 0.00542	-0.0429 ± 0.129
21	-	-	-0.04 ± 0.00795	-0.0088 ± 0.0156
22	-	-	-0.0598 ± 0.0146	-0.0331 ± 0.0077
23	-	-	-	-0.122 ± 0.0141

Table 9.1: Additive corrections due to detector effects with uncertainties for each type and each bin.

Chapter 10

Results

10.1 Theoretical predictions

For the theoretical predictions of the electron charge asymmetry, we use RESBOS to generate $W \to e\nu$ events and use PHOTOS for final state radiation. We only place cuts on the "true" value of the electron E_T ($E_T(e) > 25$ GeV, $25 < E_T(e) < 35$ GeV, $E_T(e) \geq 35$ GeV) obtained from the generator information (as opposed to the smeared E_T after the detector effects) and neutrino E_T ($E_T(\nu) > 25$ GeV), no detector simulation applied. The uncertainty band is calculated using RESBOS+PHOTOS with a set of 44 error PDFs (CTEQ6.6) provided by the CTEQ collaboration [7]. The PDF uncertainty is calculated using the quadrature sum of all eigenvector contributions suggested by the CTEQ collaboration [16]:

$$\Delta A^{\pm} = \sqrt{\sum_{i=1}^{n} [A(a_i^{\pm}) - A_0]^2} \tag{10.1}$$

the range of uncertainty of A is $[A_0 - \Delta A^-, A_0 + \Delta A^+]$, A_0 is the charge asymmetry for the central PDF set, a_i^+ and a_i^- are the displaced points where $A > A_0$ and $A < A_0$, respectively.

10.2 Charge asymmetry for each electron type

After removing backgrounds, we measure the electron charge asymmetry for each type separately and get four independent measurements. We then combine these four measurements into one asymmetry measurement.

Fig. 10.1 shows the corrected electron asymmetry as a function of electron rapidity for all four types. Table 10.1 to Table 10.2 show the detailed values of the final charge

asymmetry for each electron type together with the number of signal events, background events and the asymmetry before the corrections for the detector effects.

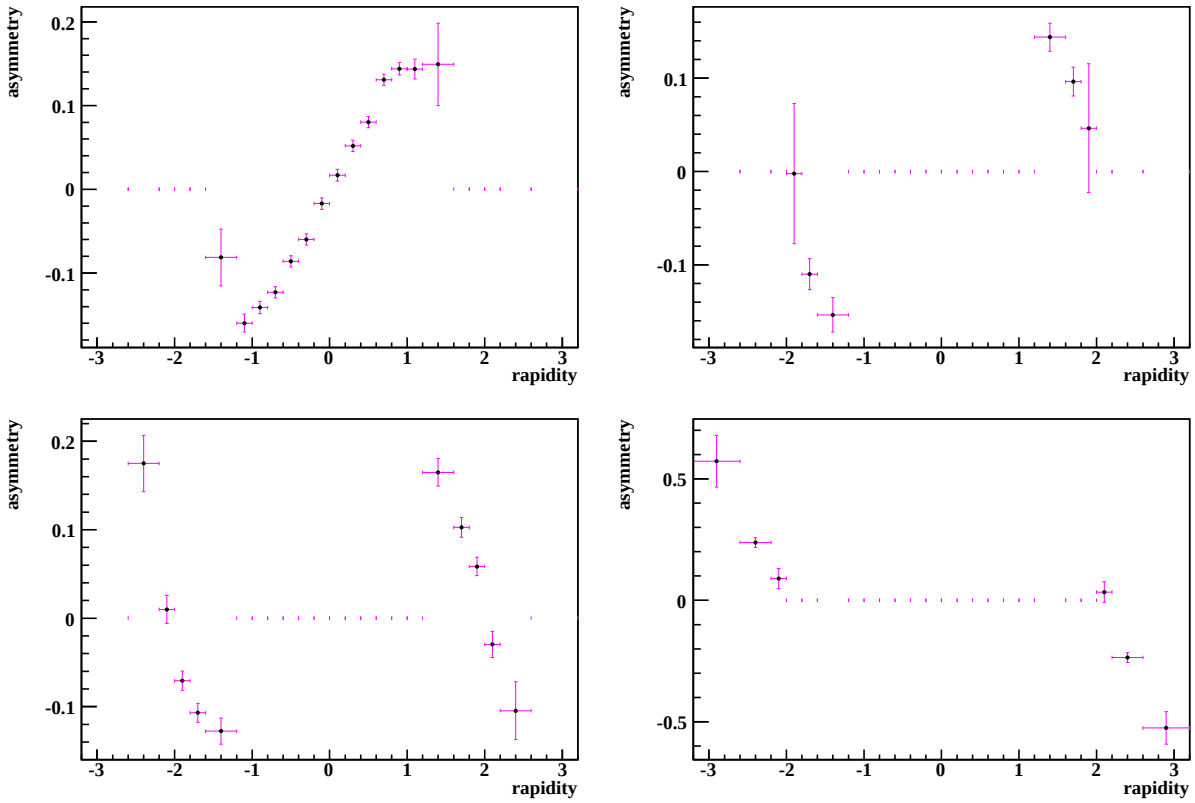

Figure 10.1: Asymmetry for all four electron types. Upper left is type 1 (CC, full CFT), upper right is type 2 (EC, full CFT), lower left is type 3 (EC, partial CFT) and lower right is type 4 (EC, no CFT) Errors include both statistical and systematic uncertainties.

bin	$N_{e^+}^{tight}$	$N_{e^-}^{tight}$	N_e^{nt}	$N_{Z\to ee}$	$N_{W\to\tau\nu}$	N_{qcd}	A'	Asymmetry
5	603	777	70	16.464	32.176	69.37 ± 32.35	-0.116	-0.0813 ± 0.034
6	5547	7721	610	183.55	253.66	127.2 ± 152.9	-0.166	-0.16 ± 0.011
7	12716	17137	1215	359.38	589.89	33.07 ± 245.4	-0.149	-0.141 ± 0.0074
8	15546	20103	1367	432.17	854.55	68.28 ± 270.6	-0.132	-0.123 ± 0.0068
9	16252	19275	1402	471.78	699.6	433.6 ± 250.5	-0.0916	-0.086 ± 0.0068
10	16017	18097	1466	488.61	787.09	410.4 ± 255	-0.0644	-0.0599 ± 0.007
11	15753	16335	1540	455.52	713.84	182.8 ± 268.5	-0.0182	-0.017 ± 0.0071
12	16535	15866	1583	426.51	679	1231 ± 214.6	0.023	0.0168 ± 0.0071
13	17911	16071	1491	465.54	789.31	189.6 ± 261.6	0.0555	0.052 ± 0.0069
14	18914	16022	1445	459.45	728.54	321.3 ± 256.9	0.0841	0.0803 ± 0.0068
15	19559	15245	1405	459.77	745.09	510.6 ± 248.3	0.128	0.131 ± 0.0069
16	16143	12015	1024	314.63	572.49	6.03 ± 227.6	0.15	0.144 ± 0.0077
17	6587	4883	433	129.78	225.44	58.46 ± 135.5	0.157	0.144 ± 0.012
18	396	310	31	6.7751	18.493	16.73 ± 31.37	0.156	0.149 ± 0.05

Table 10.1: Type 1 (CC, full CFT). Bin number, number of positrons in the signal sample that pass tight cuts, number of electrons in the signal sample that pass tight cuts, number of electrons and positrons that pass loose cuts but don't pass tight cuts (all these are before physics background subtraction), number of the $Z \to ee$ background events, number of $W \to \tau\nu$ background events, number of QCD multijet background events, asymmetry value before applying correction for the detector smearing effects and asymmetry after the corrections are applied with total uncertainties.

bin	$N_{e^+}^{tight}$	$N_{e^-}^{tight}$	N_e^{nt}	$N_{Z\to ee}$	$N_{W\to\tau\nu}$	N_{qcd}	A'	Asymmetry
3	129	152	18	3.959	0	16.61 ± 37.52	-0.087	-0.00215 ± 0.076
4	2530	3285	397	72.278	105.18	-235 ± 379.4	-0.128	-0.11 ± 0.017
5	2142	2818	333	53.779	71.589	101.8 ± 222.5	-0.146	-0.154 ± 0.019
18	4374	3375	488	69.531	121.41	-132.8 ± 335.4	0.133	0.144 ± 0.015
19	3856	3007	446	68.85	115.07	-567.9 ± 444.8	0.119	0.0964 ± 0.016
20	172	136	16	3.6736	0	-297.1 ± 414.8	0.0716	0.0465 ± 0.069

Table 10.2: Type 2 (EC, full CFT). Bin number, number of positrons in the signal sample that pass tight cuts, number of electrons in the signal sample that pass tight cuts, number of electrons and positrons that pass loose cuts but don't pass tight cuts (all these are before physics background subtraction), number of the $Z \to ee$ background events, number of $W \to \tau\nu$ background events, number of QCD multijet background events, asymmetry value before applying correction for the detector smearing effects and asymmetry after the corrections are applied with total uncertainties.

bin	$N_{e^+}^{tight}$	$N_{e^-}^{tight}$	N_e^{nt}	$N_{Z\to ee}$	$N_{W\to\tau\nu}$	N_{qcd}	$A^{'}$	Asymmetry
1	1037	903	104	33.029	53.754	75.52 ± 107	0.0859	0.175 ± 0.032
2	3668	3663	411	106.2	137.1	295.7 ± 296.5	-0.00605	0.00996 ± 0.016
3	6956	8140	811	186.85	240.73	42.72 ± 606.8	-0.0863	-0.0706 ± 0.011
4	6828	8626	953	172.65	244.41	281.7 ± 625.9	-0.125	-0.107 ± 0.011
5	3287	4306	393	92.281	146.02	-109.6 ± 282.1	-0.141	-0.128 ± 0.015
18	3803	2816	359	87.767	126.18	261 ± 186.3	0.161	0.165 ± 0.016
19	8530	6956	763	191.11	285.77	1361 ± 506.5	0.121	0.103 ± 0.011
20	8026	6941	721	220.08	306.88	-674.2 ± 657.3	0.0743	0.0585 ± 0.011
21	3897	3807	433	96.465	140.11	-602.9 ± 433.7	0.0104	-0.0296 ± 0.015
22	940	989	120	30.047	39.011	-158.2 ± 180.4	-0.0448	-0.105 ± 0.033

Table 10.3: Type 3 (EC, partial CFT). Bin number, number of positrons in the signal sample that pass tight cuts, number of electrons in the signal sample that pass tight cuts, number of electrons and positrons that pass loose cuts but don't pass tight cuts (all these are before physics background subtraction), number of the $Z \to ee$ background events, number of $W \to \tau\nu$ background events, number of QCD multijet background events, asymmetry value before applying correction for the detector smearing effects and asymmetry after the corrections are applied with total uncertainties.

bin	$N_{e^+}^{tight}$	$N_{e^-}^{tight}$	N_e^{nt}	$N_{Z\to ee}$	$N_{W\to\tau\nu}$	N_{qcd}	$A^{'}$	Asymmetry
0	277	156	96	5.6376	6.6004	107.7 ± 61.65	0.457	0.573 ± 0.11
1	2755	2034	422	112.62	151.04	136.2 ± 238.2	0.186	0.238 ± 0.02
2	551	497	73	21.355	19.535	85.83 ± 65.02	0.054	0.0895 ± 0.042
21	464	447	62	25.634	34.518	51.55 ± 72.71	0.0425	0.0337 ± 0.044
22	2111	2907	406	130.4	174.31	19.1 ± 257	-0.202	-0.236 ± 0.021
23	210	396	109	11.131	5.8603	72.11 ± 79.53	-0.404	-0.526 ± 0.068

Table 10.4: Type 4 (EC, no CFT). Bin number, number of positrons in the signal sample that pass tight cuts, number of electrons in the signal sample that pass tight cuts, number of electrons and positrons that pass loose cuts but don't pass tight cuts (all these are before physics background subtraction), number of the $Z \to ee$ background events, number of $W \to \tau\nu$ background events, number of QCD multijet background events, asymmetry value before applying correction for the detector smearing effects and asymmetry after the corrections are applied with total uncertainties.

10.3 Systematic Uncertainties

This analysis involved several steps, first we removed the physics background from the signal sample, where we calculated the backgrounds using simulated MC data. Then we used Eq. 6.8 for the asymmetry measurement. In this stage we introduced three quantities, the signal efficiency ε, the EM-like jet ID probability f and the charge misidentification rate g. And in the final step we calculated and applied the corrections to the asymmetry to account for the detector smearing effects. Each of these measurements (physics backgrounds, ε, f, g, corrections) have uncertainties associated with them and these uncertainties generate the total systematic uncertainty of the measurement. Contributions from each of the above sources of the systematic uncertainties, as well as statistical and total uncertainties are listed in Tables 10.5 to 10.8.

Each of these values and its uncertainties were calculated separately for each bin, there are only two minor exceptions: the systematic part of the signal efficiency uncertainty and the systematic part of the uncertainty of the correction for detector effects. To check the significance of the correlated uncertainties we calculated the total uncertainty with and without the correlated uncertainties for each bin. The biggest relative difference was 3% and for most bins it was less than 1%, so the correlation is insignificant.

bin	e	f	g	Phys. Bkg.	stat	corr	total
5	0.001	0.0001	0.003	0.005	0.028	0.019	0.034
6	0.001	1.12e-05	0.001	0.002	0.009	0.006	0.011
7	0.0005	9.51e-07	0.0007	0.001	0.006	0.004	0.007
8	0.0004	1.34e-06	0.0002	0.002	0.005	0.004	0.007
9	0.0002	7.67e-06	0.0002	0.001	0.005	0.004	0.007
10	0.0002	5.98e-06	0.0002	0.002	0.006	0.004	0.007
11	5.75e-05	7.42e-07	4.39e-05	0.002	0.006	0.004	0.007
12	5.61e-05	6.4e-06	9.25e-05	0.002	0.006	0.004	0.007
13	0.0002	2.13e-06	0.0001	0.002	0.006	0.004	0.007
14	0.0002	5.06e-06	0.0004	0.001	0.005	0.004	0.007
15	0.0003	1.09e-05	0.0006	0.002	0.005	0.004	0.007
16	0.0005	1.84e-07	0.0008	0.001	0.006	0.004	0.008
17	0.0007	5.6e-06	0.0007	0.002	0.009	0.007	0.012
18	0.003	9.93e-05	0.008	0.009	0.038	0.029	0.050

Table 10.5: Type 1 bin number, uncertainty from signal efficiency, uncertainty from em-like jet id probability, uncertainty from charge misidentification, uncertainty from physics background calculation, statistical uncertainty, uncertainty from detector corrections, total uncertainty.

bin	e	f	g	Phys. Bkg.	stat	corr	total
3	0.007	0.001	0.010	0.008	0.063	0.040	0.076
4	0.005	0.0001	0.001	0.002	0.013	0.009	0.017
5	0.004	9.46e-05	0.001	0.003	0.015	0.010	0.017
18	0.004	5.96e-05	0.002	0.002	0.011	0.009	0.015
19	0.005	0.0004	0.001	0.002	0.012	0.009	0.016
20	0.039	0.009	0.007	0.004	0.034	0.044	0.069

Table 10.6: Type 2 bin number, uncertainty from signal efficiency, uncertainty from em-like jet id probability, uncertainty from charge misidentification, uncertainty from physics background calculation, statistical uncertainty, uncertainty from detector corrections, total uncertainty.

bin	e	f	g	Phys. Bkg.	stat	corr	total
1	0.003	0.0001	0.006	0.006	0.028	0.014	0.032
2	0.0002	9.82e-06	0.0002	0.003	0.014	0.008	0.016
3	0.002	4.75e-06	0.002	0.002	0.009	0.006	0.011
4	0.003	3.89e-05	0.001	0.002	0.008	0.007	0.011
5	0.003	5.03e-05	0.002	0.002	0.012	0.008	0.015
18	0.003	0.0003	0.003	0.003	0.013	0.008	0.016
19	0.003	0.0003	0.0003	0.002	0.009	0.006	0.011
20	0.002	6.86e-05	0.001	0.002	0.009	0.005	0.011
21	0.0003	1.92e-05	0.0002	0.002	0.013	0.008	0.015
22	0.002	0.0002	0.003	0.006	0.029	0.015	0.033

Table 10.7: Type 3 bin number, uncertainty from signal efficiency, uncertainty from em-like jet id probability, uncertainty from charge misidentification, uncertainty from physics background calculation, statistical uncertainty, uncertainty from detector corrections, total uncertainty.

bin	e	f	g	Phys. Bkg.	stat	corr	total
0	0.037	0.007	0.063	0.015	0.076	0.018	0.108
1	0.005	9.23e-05	0.006	0.005	0.016	0.008	0.020
2	0.002	0.0003	0.005	0.008	0.037	0.017	0.042
21	0.002	0.0001	0.003	0.011	0.039	0.016	0.044
22	0.006	1.36e-05	0.006	0.005	0.016	0.008	0.021
23	0.028	0.002	0.032	0.011	0.049	0.014	0.0678

Table 10.8: Type 4 bin number, uncertainty from signal efficiency, uncertainty from em-like jet id probability, uncertainty from charge misidentification, uncertainty from physics background calculation, statistical uncertainty, uncertainty from detector corrections, total uncertainty.

10.4 Combined charge asymmetry for all electron types

We have four independent measurements of the charge asymmetry for four different electron types; we then combine them together to get one final asymmetry distribution. Only a few bins for the four types overlap with each other and we use the weighted average result for such bins. Fig. 10.2 shows the combined charge asymmetry distribution together with theoretical predictions. Table 10.9 shows the measured asymmetry and theoretical predictions for events with electron $E_T > 25$ GeV.

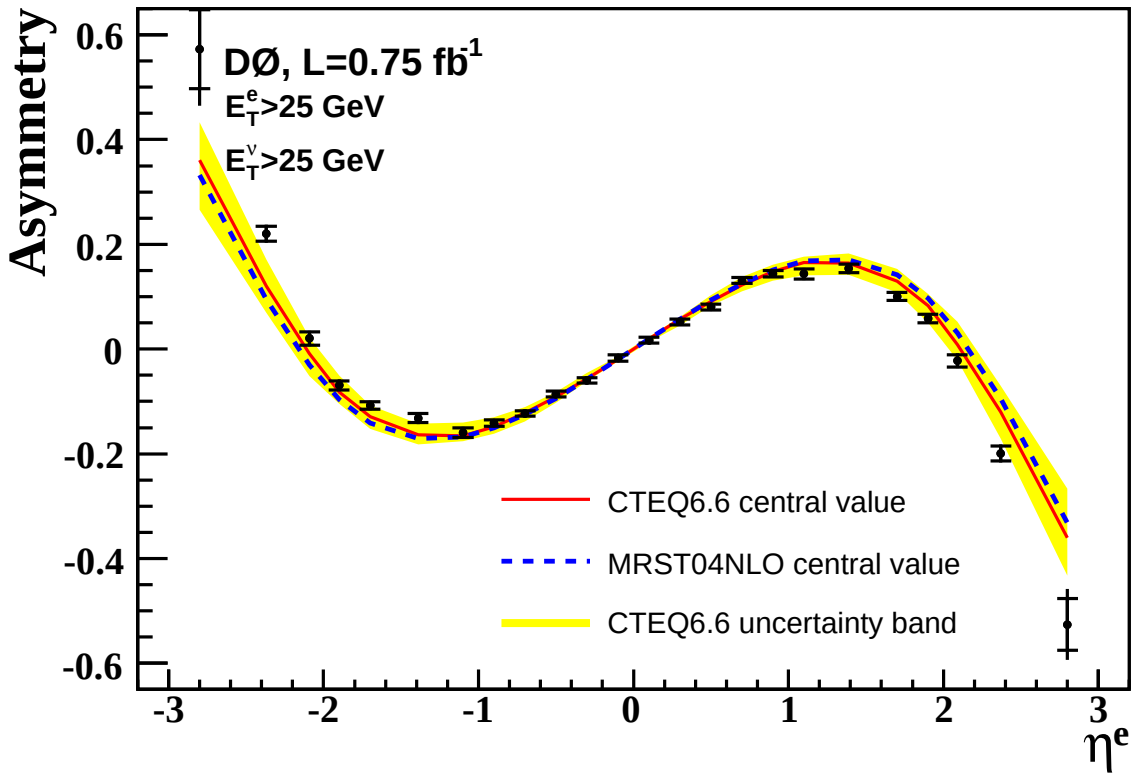

Figure 10.2: Combined electron charge asymmetry distribution. The small error bars correspond to statistical errors only, the large error bars are statistical and systematic. The yellow band is the error band determined using forty four CTEQ6.6 PDF uncertainty sets.

bin	$< \eta >$	A (Data)	A (CTEQ6.6)	A (MRST04NLO)
0	-2.80	0.573 ± 0.076 ± 0.077	0.361 + 0.072 (-0.094)	0.332
1	-2.37	0.220 ± 0.014 ± 0.010	0.120 + 0.051 (-0.051)	0.095
2	-2.09	0.020 ± 0.013 ± 0.008	-0.009 + 0.030 (-0.043)	-0.031
3	-1.90	-0.069 ± 0.009 ± 0.006	-0.083 + 0.033 (-0.022)	-0.097
4	-1.70	-0.108 ± 0.007 ± 0.006	-0.130 + 0.022 (-0.023)	-0.142
5	-1.39	-0.132 ± 0.009 ± 0.007	-0.164 + 0.022 (-0.018)	-0.171
6	-1.10	-0.160 ± 0.009 ± 0.006	-0.166 + 0.025 (-0.010)	-0.168
7	-0.90	-0.141 ± 0.006 ± 0.004	-0.148 + 0.018 (-0.013)	-0.151
8	-0.70	-0.123 ± 0.005 ± 0.004	-0.122 + 0.012 (-0.015)	-0.125
9	-0.50	-0.086 ± 0.005 ± 0.004	-0.091 + 0.009 (-0.012)	-0.094
10	-0.30	-0.060 ± 0.006 ± 0.004	-0.057 + 0.012 (-0.004)	-0.057
11	-0.10	-0.017 ± 0.006 ± 0.004	-0.019 + 0.005 (-0.004)	-0.019
12	0.10	0.017 ± 0.006 ± 0.004	0.019 + 0.004 (-0.005)	0.019
13	0.30	0.052 ± 0.006 ± 0.004	0.057 + 0.004 (-0.012)	0.057
14	0.50	0.080 ± 0.005 ± 0.004	0.091 + 0.012 (-0.009)	0.094
15	0.70	0.131 ± 0.005 ± 0.004	0.122 + 0.015 (-0.012)	0.125
16	0.90	0.144 ± 0.006 ± 0.005	0.148 + 0.013 (-0.018)	0.151
17	1.10	0.144 ± 0.009 ± 0.007	0.166 + 0.010 (-0.025)	0.168
18	1.39	0.154 ± 0.008 ± 0.007	0.164 + 0.018 (-0.022)	0.171
19	1.70	0.100 ± 0.007 ± 0.006	0.130 + 0.023 (-0.022)	0.142
20	1.90	0.058 ± 0.008 ± 0.006	0.083 + 0.022 (-0.033)	0.097
21	2.09	-0.023 ± 0.012 ± 0.008	0.009 + 0.043 (-0.030)	0.031
22	2.37	-0.199 ± 0.014 ± 0.010	-0.120 + 0.051 (-0.051)	-0.095
23	2.80	-0.526 ± 0.049 ± 0.046	-0.361 + 0.094 (-0.072)	-0.332

Table 10.9: Charge asymmetry for the data and theoretical predictions for electron $E_T > 25$ GeV using CTEQ6.6 and MRST04NLO. For the data, the first uncertainty is statistical and the second is systematic. For the CTEQ prediction, the first one is for ΔA^+ and the second one is for ΔA^-.

10.5 CP Folding

CP symmetry states that the laws of physics should be the same if a particle is interchanged with its antiparticle (C symmetry, or charge conjugation symmetry), and left and right were swapped (P symmetry, or parity symmetry). In our case, the asymmetry is expected to be CP invariant such that $A(y) = -A(-y)$ (in Fig. 10.4 you can see that this is true within the uncertainties for almost all bins), so to increase statistical significance we "fold" the data.

To get the folded result, the following steps were followed:

$$N'_{T^+}(y) = N_{T^+}(y) + N_{T^-}(-y) \tag{10.2}$$

$$N'_{T^-}(y) = N_{T^-}(y) + N_{T^+}(-y) \tag{10.3}$$

$$N'_{nt}(y) = N_{nt}(y) + N_{nt}(-y) \tag{10.4}$$

- The number of signal and physics background events were added as shown in Eqns. 10.2 to 10.4;
- Statistical uncertainties were added in quadrature;
- Signal efficiency (ε), EM-like jet id probability (f) and charge misidentification rate (g) were recalculated after folding the $\pm|\eta|$ bins;
- After the above transformations the folded asymmetry was calculated using the method described in Chap. 6.

This is the method used in the previously published $W \to \mu\nu$ asymmetry analysis [12], except that they just average the systematic uncertainties from ε, f and g while we benefit from a doubling of the statistics after folding. The asymmetry distribution after CP folding is shown in Fig. 10.3. Table 10.10 shows the folded charge asymmetry compared with CTEQ6.6 and MRST04NLO predictions.

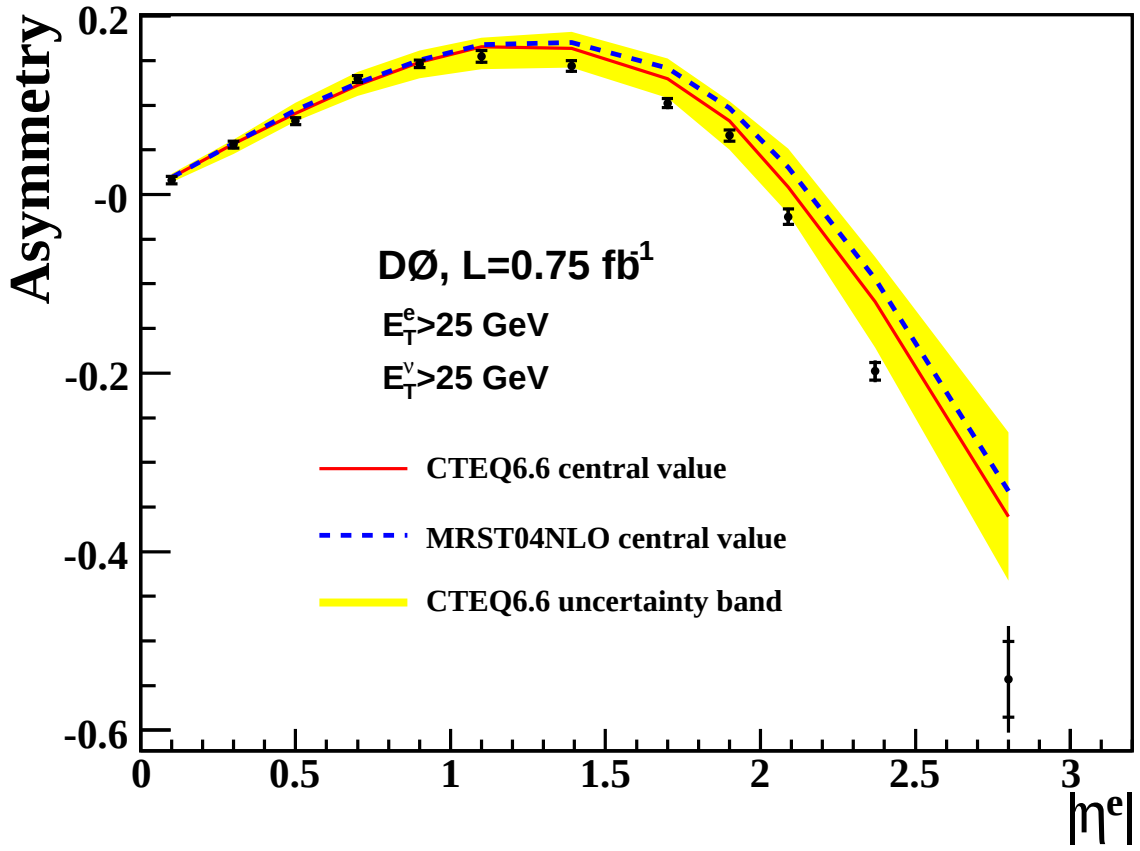

Figure 10.3: Asymmetry distribution after CP folding plotted with CTEQ error band for electron $E_T > 25$ GeV. The small error bars correspond to the statistical uncertainty and the large error bars are the total uncertainty. The red curve is the prediction using the CTEQ6.6 central PDF, the blue curve is the prediction using MRST04NLO, the yellow band is the CTEQ6.6 uncertainty band.

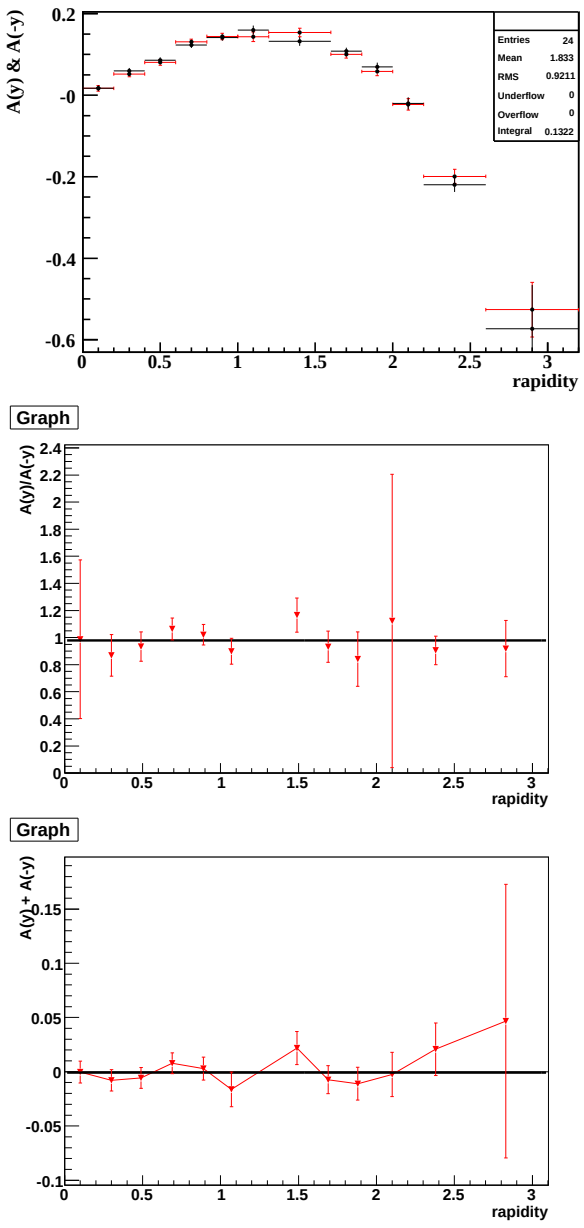

Figure 10.4: Top plot is A(y)(red) and -A(-y)(black) plotted on the same axis. Middle plot: the ratio A(y)/-A(-y). Bottom: A(y)-(-A(-y)).

bin	$< \eta >$	A (Data)	A (CTEQ6.6)	A (MRST04NLO)
0	0.10	0.016 ± 0.004 ± 0.003	0.019 + 0.004 (-0.005)	0.019
1	0.30	0.056 ± 0.004 ± 0.003	0.057 + 0.004 (-0.012)	0.057
2	0.50	0.082 ± 0.004 ± 0.003	0.091 + 0.012 (-0.009)	0.094
3	0.70	0.130 ± 0.004 ± 0.003	0.122 + 0.015 (-0.012)	0.125
4	0.90	0.146 ± 0.004 ± 0.003	0.148 + 0.013 (-0.018)	0.151
5	1.10	0.155 ± 0.006 ± 0.005	0.166 + 0.010 (-0.025)	0.168
6	1.39	0.144 ± 0.006 ± 0.005	0.164 + 0.018 (-0.022)	0.171
7	1.70	0.102 ± 0.005 ± 0.004	0.130 + 0.023 (-0.022)	0.142
8	1.90	0.066 ± 0.006 ± 0.005	0.083 + 0.022 (-0.033)	0.097
9	2.09	-0.025 ± 0.009 ± 0.006	0.009 + 0.043 (-0.030)	0.031
10	2.37	-0.198 ± 0.010 ± 0.007	-0.120 + 0.051 (-0.051)	-0.095
11	2.80	-0.543 ± 0.042 ± 0.042	-0.361 + 0.094 (-0.072)	-0.332

Table 10.10: Folded charge asymmetry for data and theoretical predictions for electron $25 < E_T < 35$ GeV using CTEQ6.6 and MRST04NLO. For the data, the first uncertainty is statistical and the second is systematic. For the CTEQ prediction, the first one is for ΔA^+ and the second one is for ΔA^-.

10.6 Charge asymmetry for different electron E_T regions

As seen on the Fig. 10.5, for a given electron rapidity different E_T regions probe different x range, therefore we measured the charge asymmetry in bins of electron E_T. We divided the data into two energy bins, 25 GeV $< E_T <$ 35 GeV and $E_T \geq$ 35 GeV. At high electron E_T, we expect $q\bar{q}$ production to dominate; whereas at low E_T, we expect relatively more qg production. As a result, measuring the asymmetry separately in different electron E_T bins should help separate the contributions. Fig. 10.6 shows how the theoretical predictions of the asymmetry change for different E_T regions.

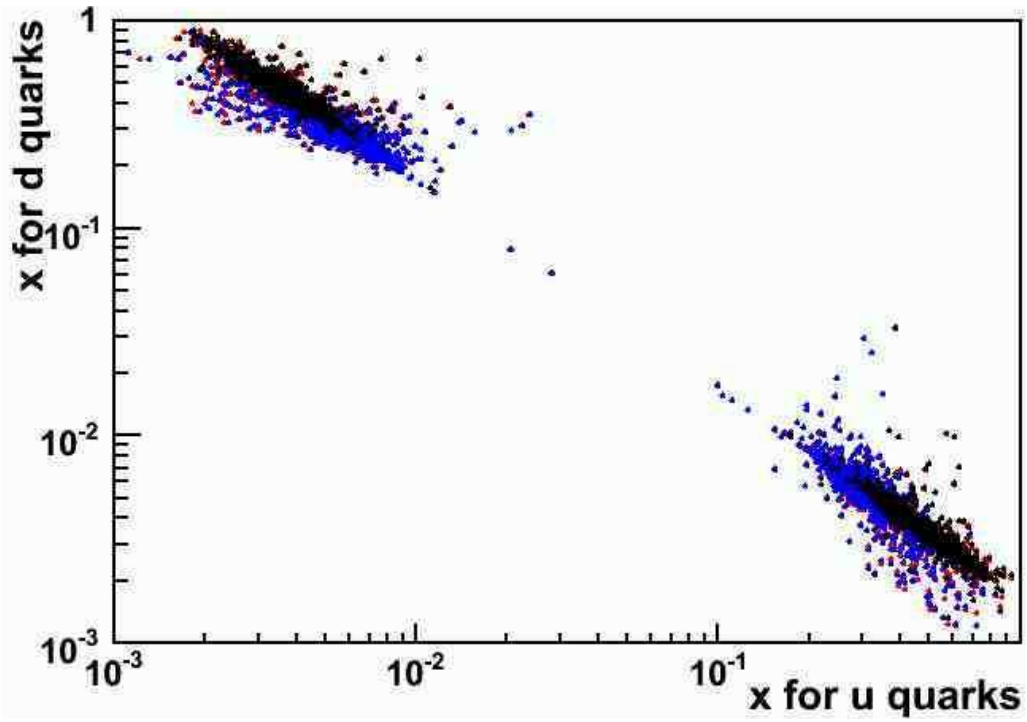

Figure 10.5: Pythia prediction for x_u vs X_d for the $\eta < 2.6$ bin. Kinematic cuts have been applied. The blue points are for electron $E_T <$ 35 GeV and the black ones are for $E_T >$ 35 GeV. The E_T cut allows us to probe very high x data.

We repeated all analysis steps described in all previous chapters and derived ε, f, g, electroweak and QCD backgrounds, and the corrections due to detector effects for the two electron E_T regions.

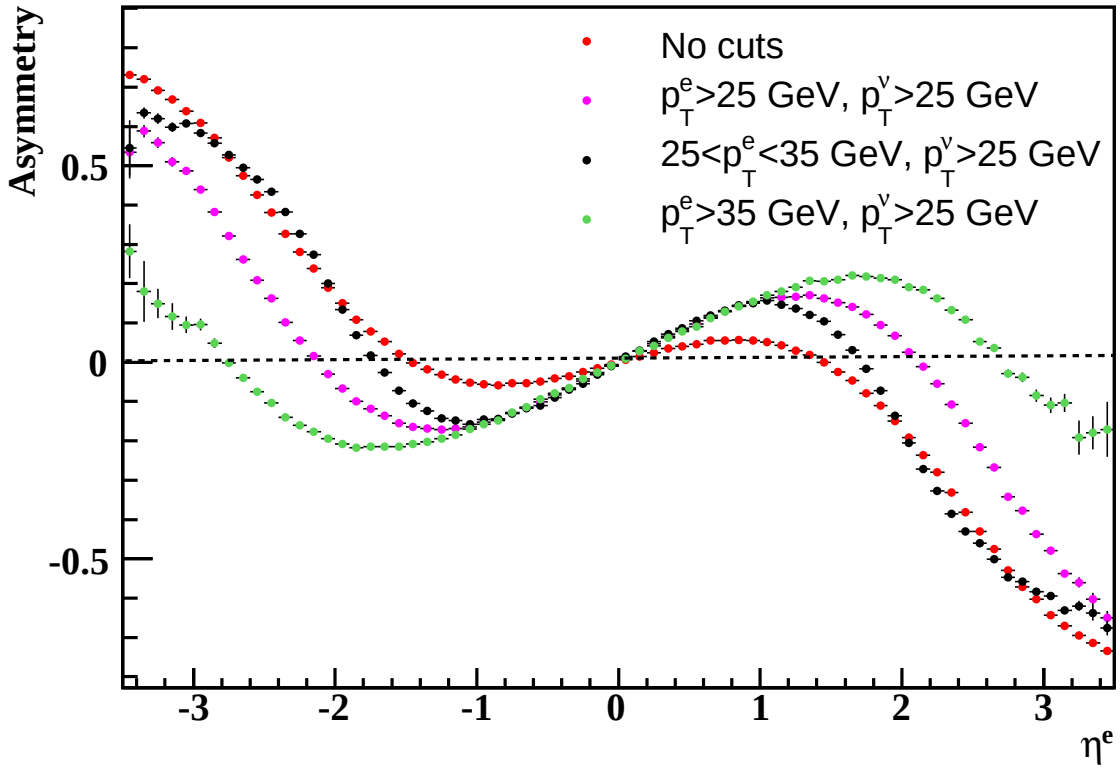

Figure 10.6: Theoretical predictions of the asymmetry with different cuts on electron E_T and neutrino E_T.

10.6.1 Results for $25 < E_T < 35$ GeV

Table 10.11 to Table 10.14 list the charge asymmetry distributions for four electron types with electron $25 < E_T < 35$ GeV. Fig. 10.7 shows the combined charge asymmetry distribution together with theoretical predictions. Table 10.15 shows the measured asymmetry and theoretical predictions for events with $25 < E_T < 35$ GeV.

bin	$N_{e^+}^{tight}$	$N_{e^-}^{tight}$	N_e^{nt}	$N_{Z\to ee}$	$N_{W\to\tau\nu}$	N_{qcd}	A'	Asymmetry
6	2268	3225	282	43.782	176.45	-224.5 ± 212	-0.169	-0.153 ± 0.017
7	4946	6742	535	83.26	429.16	29.95 ± 225	-0.153	-0.151 ± 0.012
8	6069	8103	594	100.56	668.06	-455.3 ± 308.9	-0.145	-0.138 ± 0.011
9	6520	7983	628	123.74	579.67	46.08 ± 226.9	-0.112	-0.109 ± 0.011
10	6551	7688	625	123.66	676.99	193.5 ± 197.7	-0.0859	-0.079 ± 0.011
11	6525	6845	673	115.34	585.63	85.9 ± 205.6	-0.0256	-0.0253 ± 0.011
12	6868	6637	689	105.45	553.83	53.4 ± 212.3	0.0198	0.0165 ± 0.011
13	7482	6648	658	118.01	690.73	-529.7 ± 274.9	0.0627	0.0578 ± 0.011
14	7854	6606	600	111.7	595.26	-308 ± 257.9	0.0842	0.0761 ± 0.011
15	7992	6249	632	116.69	608.34	294.5 ± 206.9	0.13	0.133 ± 0.011
16	6389	4689	444	76.584	446.03	-382.4 ± 255.3	0.154	0.15 ± 0.012
17	2617	1921	203	31.24	186.53	-153.9 ± 182.8	0.157	0.147 ± 0.019

Table 10.11: Type 1 (CC, full CFT). Bin number, number of positrons in the signal sample that pass tight cuts, number of electrons in the signal sample that pass tight cuts, number of electrons and positrons that pass loose cuts but don't pass tight cuts (all these are before physics background subtraction), number of the $Z \to ee$ background events, number of $W \to \tau\nu$ background events, number of QCD multijet background events, asymmetry value before applying correction for the detector smearing effects and asymmetry after the corrections are applied with total uncertainties. $25 < E_T < 35$ GeV.

The asymmetry distribution after CP folding is shown in Fig. 10.8. Table 10.16 shows the folded charge asymmetry compared with the CTEQ6.6 and MRST04NLO predictions.

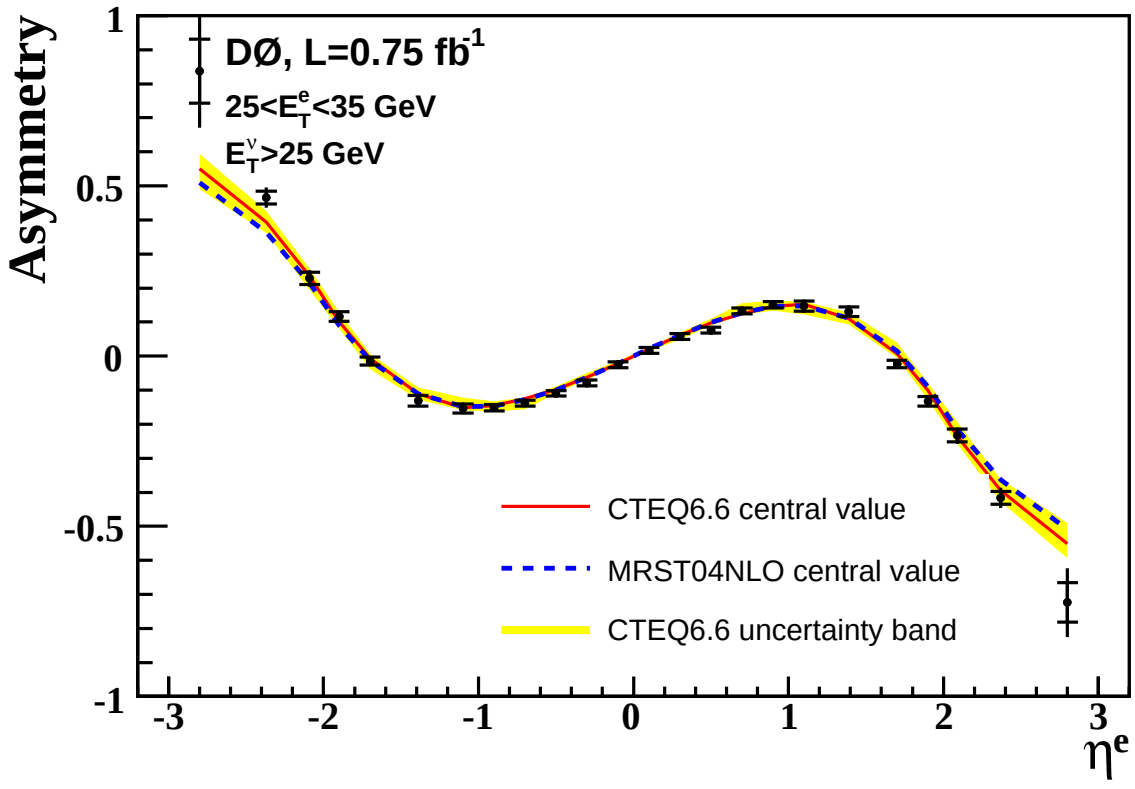

Figure 10.7: Combined electron charge asymmetry distribution for events with electron energies of $25 < E_T < 35$ GeV. The small error bars correspond to statistical errors only, the large error bars represent combined statistical and systematic uncertainties. The yellow band is the error band determined using forty four CTEQ6.6 PDF uncertainty sets.

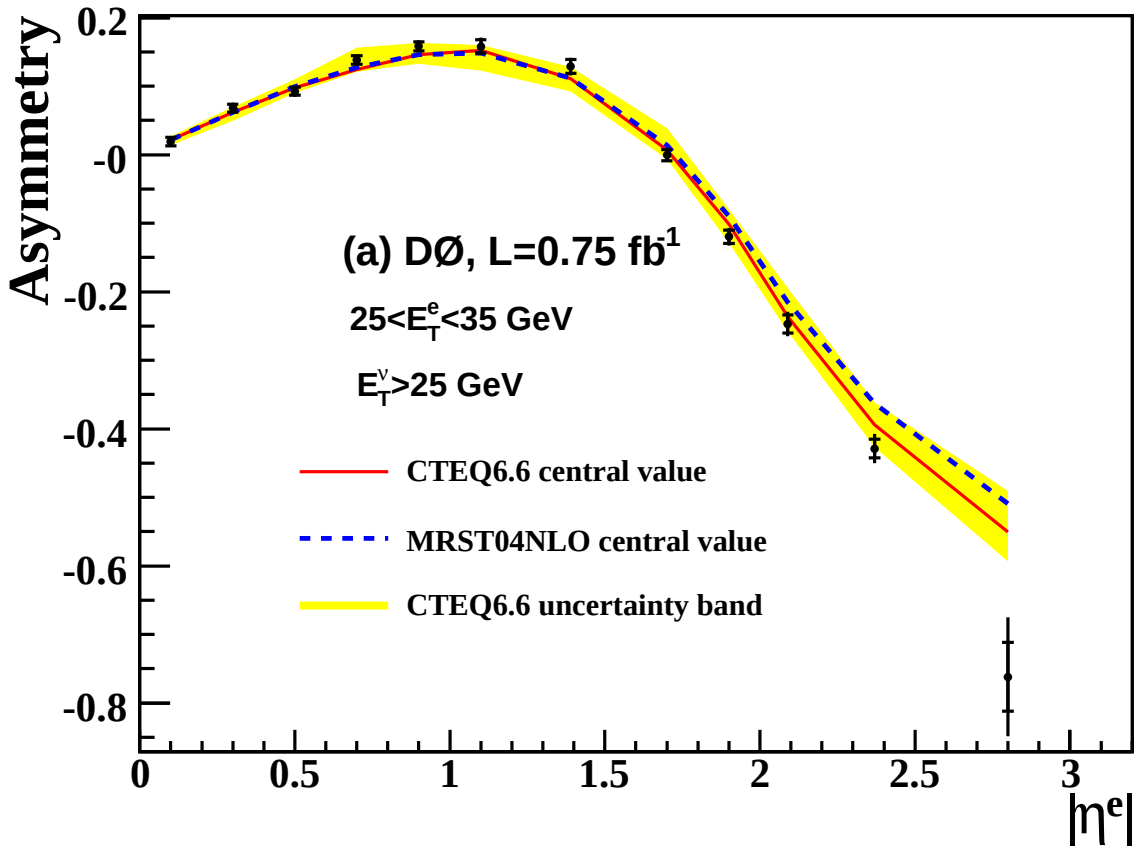

Figure 10.8: The asymmetry distribution after CP folding plotted with the CTEQ error band for electrons $25 < E_T < 35$ GeV. The small error bars correspond to the statistical uncertainty and the large error bars are the total uncertainty. The red line is the prediction using the CTEQ6.6 central PDF, the blue line is the prediction using MRST04NLO, and the yellow band is the CTEQ6.6 uncertainty band.

bin	$N_{e^+}^{tight}$	$N_{e^-}^{tight}$	N_e^{nt}	$N_{Z\to ee}$	$N_{W\to\tau\nu}$	N_{qcd}	$A^{'}$	Asymmetry
4	1172	1255	161	17.052	80.215	-214.2 ± 344.9	-0.0185	-0.0212 ± 0.026
5	910	1079	124	10.412	41.454	61.18 ± 163.6	-0.0921	-0.166 ± 0.03
18	1466	1379	164	14.773	97.692	-54.95 ± 266.9	0.0283	0.107 ± 0.025
19	1280	1252	187	17.922	99.655	-506.8 ± 445.4	0.00661	-0.0252 ± 0.024

Table 10.12: Type 2 (EC, full CFT). Bin number, number of positrons in the signal sample that pass tight cuts, number of electrons in the signal sample that pass tight cuts, number of electrons and positrons that pass loose cuts but don't pass tight cuts (all these are before physics background subtraction), number of the $Z \to ee$ background events, number of $W \to \tau\nu$ background events, number of QCD multijet background events, asymmetry value before applying correction for the detector smearing effects and asymmetry after the corrections are applied with total uncertainties. $25 < E_T < 35$ GeV.

bin	$N_{e^+}^{tight}$	$N_{e^-}^{tight}$	N_e^{nt}	$N_{Z\to ee}$	$N_{W\to\tau\nu}$	N_{qcd}	$A^{'}$	Asymmetry
1	553	307	58	10.846	42.258	137.4 ± 44.08	0.384	0.47 ± 0.058
2	1742	1195	184	31.321	110.43	-57.76 ± 220	0.187	0.213 ± 0.027
3	3238	2724	337	46.721	204.88	-68.15 ± 336.4	0.0986	0.116 ± 0.018
4	2946	3056	401	38.489	209.57	255.3 ± 318.5	-0.0192	-0.0119 ± 0.017
5	1398	1647	173	21.242	95.918	378.5 ± 116.7	-0.0941	-0.106 ± 0.025
18	1403	1118	141	21.381	107.39	45.25 ± 169.6	0.121	0.156 ± 0.026
19	3057	3096	300	52.076	244.69	21.36 ± 377.2	-0.00574	-0.0215 ± 0.017
20	2633	3150	320	55.485	247.8	-283.5 ± 380.6	-0.106	-0.133 ± 0.018
21	1306	1842	192	26.609	129.71	98.61 ± 198.4	-0.205	-0.243 ± 0.026
22	331	498	54	10.962	33.224	-91.29 ± 135.6	-0.251	-0.293 ± 0.053

Table 10.13: Type 3 (EC, partial CFT). Bin number, number of positrons in the signal sample that pass tight cuts, number of electrons in the signal sample that pass tight cuts, number of electrons and positrons that pass loose cuts but don't pass tight cuts (all these are before physics background subtraction), number of the $Z \to ee$ background events, number of $W \to \tau\nu$ background events, number of QCD multijet background events, asymmetry value before applying correction for the detector smearing effects and asymmetry after the corrections are applied with total uncertainties. $25 < E_T < 35$ GeV.

bin	$N_{e^+}^{tight}$	$N_{e^-}^{tight}$	N_e^{nt}	$N_{Z\to ee}$	$N_{W\to\tau\nu}$	N_{qcd}	A'	Asymmetry
0	185	69	48	3.4925	5.7316	67.96 ± 29.18	0.769	0.837 ± 0.17
1	1499	679	202	51.079	133.81	-108.1 ± 182.6	0.433	0.465 ± 0.034
2	294	160	34	7.6217	14.176	5.437 ± 65.86	0.302	0.315 ± 0.064
21	144	208	26	8.5756	34.518	40.26 ± 31.98	-0.191	-0.165 ± 0.075
22	783	1597	216	55.593	174.31	-91.69 ± 199.2	-0.439	-0.474 ± 0.036
23	82	258	56	5.9296	4.2559	9.762 ± 64.76	-0.638	-0.724 ± 0.1

Table 10.14: Type 4 (EC, no CFT). Bin number, number of positrons in the signal sample that pass tight cuts, number of electrons in the signal sample that pass tight cuts, number of electrons and positrons that pass loose cuts but don't pass tight cuts (all these are before physics background subtraction), number of the $Z \to ee$ background events, number of $W \to \tau\nu$ background events, number of QCD multijet background events, asymmetry value before applying correction for the detector smearing effects and asymmetry after the corrections are applied with total uncertainties. $25 < E_T < 35$ GeV.

bin	$< \eta >$	A (Data)	A (CTEQ6.6)	A (MRST04NLO)
0	-2.80	0.837 ± 0.094 ± 0.137	0.551 + 0.043 (-0.060)	0.509
1	-2.37	0.466 ± 0.019 ± 0.022	0.394 + 0.033 (-0.032)	0.363
2	-2.09	0.228 ± 0.018 ± 0.016	0.236 + 0.022 (-0.041)	0.215
3	-1.90	0.116 ± 0.014 ± 0.011	0.101 + 0.027 (-0.022)	0.090
4	-1.70	-0.015 ± 0.011 ± 0.009	-0.007 + 0.013 (-0.032)	-0.014
5	-1.39	-0.131 ± 0.016 ± 0.012	-0.111 + 0.018 (-0.018)	-0.111
6	-1.10	-0.153 ± 0.013 ± 0.011	-0.152 + 0.030 (-0.007)	-0.148
7	-0.90	-0.151 ± 0.009 ± 0.008	-0.146 + 0.013 (-0.017)	-0.146
8	-0.70	-0.138 ± 0.008 ± 0.007	-0.124 + 0.003 (-0.031)	-0.128
9	-0.50	-0.109 ± 0.009 ± 0.007	-0.098 + 0.008 (-0.012)	-0.099
10	-0.30	-0.079 ± 0.009 ± 0.007	-0.062 + 0.013 (-0.008)	-0.062
11	-0.10	-0.025 ± 0.009 ± 0.007	-0.021 + 0.008 (-0.005)	-0.022
12	0.10	0.017 ± 0.009 ± 0.007	0.021 + 0.005 (-0.008)	0.022
13	0.30	0.058 ± 0.009 ± 0.007	0.062 + 0.008 (-0.013)	0.062
14	0.50	0.076 ± 0.008 ± 0.007	0.098 + 0.012 (-0.008)	0.099
15	0.70	0.133 ± 0.009 ± 0.007	0.124 + 0.031 (-0.003)	0.128
16	0.90	0.150 ± 0.009 ± 0.008	0.146 + 0.017 (-0.013)	0.146
17	1.10	0.147 ± 0.015 ± 0.012	0.152 + 0.007 (-0.030)	0.148
18	1.39	0.131 ± 0.014 ± 0.011	0.111 + 0.018 (-0.018)	0.111
19	1.70	-0.023 ± 0.011 ± 0.009	0.007 + 0.032 (-0.013)	0.014
20	1.90	-0.133 ± 0.014 ± 0.011	-0.101 + 0.022 (-0.027)	-0.090
21	2.09	-0.234 ± 0.019 ± 0.016	-0.236 + 0.041 (-0.022)	-0.215
22	2.37	-0.417 ± 0.019 ± 0.023	-0.394 + 0.032 (-0.033)	-0.363
23	2.80	-0.724 ± 0.058 ± 0.083	-0.551 + 0.060 (-0.043)	-0.509

Table 10.15: The charge asymmetry for data and theoretical predictions for electron energies of $25 < E_T < 35$ GeV using CTEQ6.6 and MRST04NLO. For the data, the first uncertainty is statistical and the second is systematic. For the CTEQ prediction, the first one is for ΔA^+ and the second one is for ΔA^-.

bin	$< \eta >$	A (Data)	A (CTEQ6.6)	A (MRST04NLO)
0	0.10	0.019 ± 0.006 ± 0.005	0.021 + 0.005 (-0.008)	0.022
1	0.30	0.068 ± 0.006 ± 0.005	0.062 + 0.008 (-0.013)	0.062
2	0.50	0.093 ± 0.006 ± 0.005	0.098 + 0.012 (-0.008)	0.099
3	0.70	0.138 ± 0.006 ± 0.005	0.124 + 0.031 (-0.003)	0.128
4	0.90	0.158 ± 0.007 ± 0.006	0.146 + 0.017 (-0.013)	0.146
5	1.10	0.158 ± 0.010 ± 0.008	0.152 + 0.007 (-0.030)	0.148
6	1.39	0.129 ± 0.010 ± 0.008	0.111 + 0.018 (-0.018)	0.111
7	1.70	-0.001 ± 0.008 ± 0.006	0.007 + 0.032 (-0.013)	0.014
8	1.90	-0.120 ± 0.010 ± 0.008	-0.101 + 0.022 (-0.027)	-0.090
9	2.09	-0.247 ± 0.013 ± 0.012	-0.236 + 0.041 (-0.022)	-0.215
10	2.37	-0.429 ± 0.014 ± 0.016	-0.394 + 0.032 (-0.033)	-0.363
11	2.80	-0.762 ± 0.050 ± 0.071	-0.551 + 0.060 (-0.043)	-0.509

Table 10.16: The folded charge asymmetry for data and theoretical predictions for electron $25 < E_T < 35$ GeV using CTEQ6.6 and MRST04NLO. For the data, the first uncertainty is statistical and the second is systematic. For the CTEQ prediction, the first one is for ΔA^+ and the second one is for ΔA^-.

10.6.2 Results for $E_T > 35$ GeV

Table 10.17 to Table 10.20 list the charge asymmetry distributions for four electron types with electron energies of $E_T > 35$ GeV. Fig. 10.9 shows the combined charge asymmetry distribution together with theoretical predictions. Table 10.21 shows the measured asymmetry and theoretical predictions for events with $E_T > 35$ GeV.

bin	$N_{e^+}^{tight}$	$N_{e^-}^{tight}$	N_e^{nt}	$N_{Z\to ee}$	$N_{W\to\tau\nu}$	N_{qcd}	$A^{'}$	Asymmetry
5	330	466	43	11.991	0	46.22 ± 19.31	-0.177	-0.154 ± 0.044
6	3279	4496	328	139.77	77.208	37.59 ± 82.75	-0.161	-0.163 ± 0.014
7	7770	10395	680	276.12	160.73	-42.17 ± 132.7	-0.147	-0.137 ± 0.0093
8	9477	12000	773	331.61	186.5	-38.6 ± 141.3	-0.121	-0.112 ± 0.0086
9	9732	11292	774	348.04	119.93	166.3 ± 127.9	-0.0779	-0.0704 ± 0.0086
10	9466	10409	841	364.95	110.1	190.4 ± 126.6	-0.0497	-0.0468 ± 0.0089
11	9228	9490	867	340.18	128.2	48.99 ± 134.5	-0.0132	-0.0115 ± 0.0091
12	9667	9229	894	321.07	125.17	571.9 ± 110.5	0.0249	0.0168 ± 0.0091
13	10429	9423	833	347.53	98.583	67.7 ± 132.5	0.0499	0.0473 ± 0.0088
14	11060	9416	845	347.74	133.28	170.7 ± 130.3	0.083	0.0824 ± 0.0088
15	11567	8996	773	343.08	136.75	182.6 ± 129.8	0.127	0.13 ± 0.0087
16	9754	7326	580	238.05	126.46	-39.87 ± 123.1	0.145	0.14 ± 0.0097
17	3970	2962	230	98.537	38.911	-14.92 ± 73.48	0.153	0.14 ± 0.015
18	223	192	13	5.0573	4.7244	0.0657 ± 17.04	0.0896	0.0745 ± 0.064

Table 10.17: Type 1 (CC, full CFT). Bin number, number of positrons in the signal sample that pass tight cuts, number of electrons in the signal sample that pass tight cuts, number of electrons and positrons that pass loose cuts but don't pass tight cuts (all these are before physics background subtraction), number of the $Z \to ee$ background events, number of $W \to \tau\nu$ background events, number of QCD multijet background events, asymmetry value before applying correction for the detector smearing effects and asymmetry after the corrections are applied with total uncertainties. 35 GeV$< E_T$.

The asymmetry distribution after CP folding is shown in Fig. 10.10. Table 10.22 shows the folded charge asymmetry compared with the CTEQ6.6 and MRST04NLO predictions.

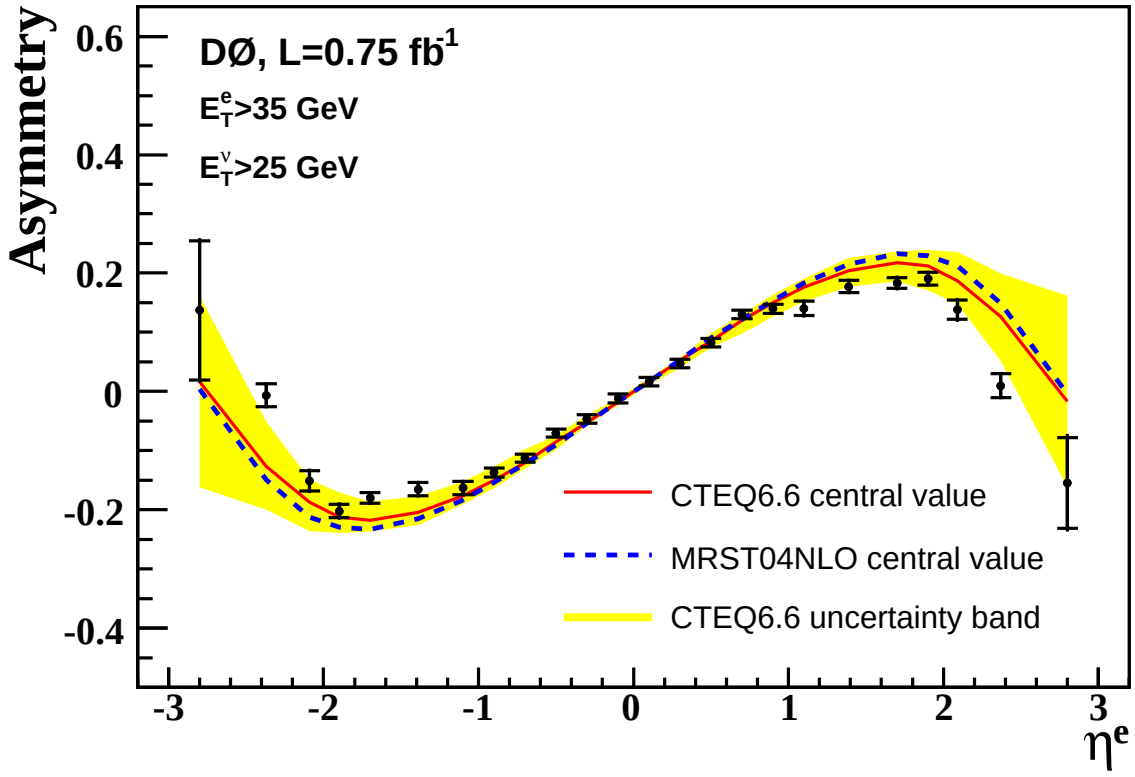

Figure 10.9: The combined electron charge asymmetry distribution for electrons of energy $E_T > 35$ GeV. The small error bars correspond to statistical errors only, the large error bars represent the quadrature sum of statistical and systematic uncertainties. The yellow band is the error band determined using forty CTEQ6.6 PDF uncertainty sets.

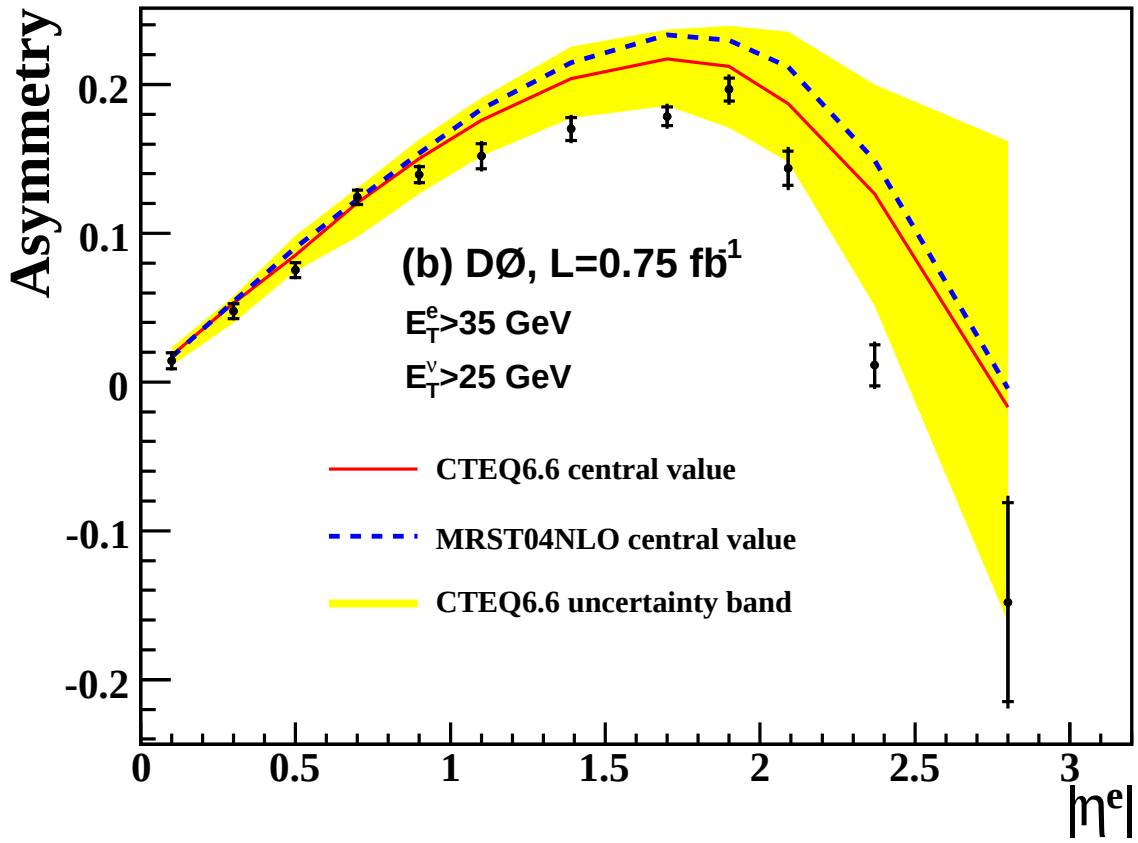

Figure 10.10: The asymmetry distribution after CP folding plotted with the CTEQ error band for electrons with $E_T > 35$ GeV. The small error bars correspond to the statistical uncertainty and the large error bars represent the total uncertainty. The red line is the prediction using the CTEQ6.6 central PDF, the blue line is the prediction using MRST04NLO, and the yellow band is the CTEQ6.6 uncertainty band.

bin	$N_{e^+}^{tight}$	$N_{e^-}^{tight}$	N_e^{nt}	$N_{Z\to ee}$	$N_{W\to\tau\nu}$	N_{qcd}	A'	Asymmetry
3	79	106	15	3.2762	0	16.01 ± 21.01	-0.159	-0.105 ± 0.096
4	1358	2030	236	55.226	24.968	-98.47 ± 161.4	-0.206	-0.194 ± 0.021
5	1232	1739	209	43.367	30.135	84.9 ± 105.5	-0.183	-0.174 ± 0.023
18	2908	1996	324	54.758	23.72	-25.42 ± 160.8	0.194	0.19 ± 0.018
19	2576	1755	259	50.928	15.414	-345.9 ± 225	0.185	0.182 ± 0.019
20	112	78	11	2.8981	0	-59.04 ± 58.67	0.163	0.212 ± 0.089

Table 10.18: Type 2 (EC, full CFT). Bin number, number of positrons in the signal sample that pass tight cuts, number of electrons in the signal sample that pass tight cuts, number of electrons and positrons that pass loose cuts but don't pass tight cuts (all these are before physics background subtraction), number of the $Z \to ee$ background events, number of $W \to \tau\nu$ background events, number of QCD multijet background events, asymmetry value before applying correction for the detector smearing effects and asymmetry after the corrections are applied with total uncertainties. 35 GeV$< E_T$.

bin	$N_{e^+}^{tight}$	$N_{e^-}^{tight}$	N_e^{nt}	$N_{Z\to ee}$	$N_{W\to\tau\nu}$	N_{qcd}	A'	Asymmetry
1	484	596	46	22.183	11.496	2.991 ± 44.28	-0.13	-0.0868 ± 0.044
2	1926	2468	227	74.881	26.671	90.67 ± 134.7	-0.142	-0.151 ± 0.021
3	3718	5416	474	140.13	35.853	-20.48 ± 284.8	-0.207	-0.205 ± 0.015
4	3882	5570	552	134.16	34.833	62.94 ± 299.7	-0.191	-0.174 ± 0.013
5	1889	2659	220	71.039	50.102	-92.43 ± 131.5	-0.179	-0.161 ± 0.019
18	2400	1698	218	66.386	18.787	125.9 ± 88.07	0.182	0.173 ± 0.019
19	5473	3860	463	139.03	41.08	620 ± 244.5	0.198	0.185 ± 0.016
20	5393	3791	401	164.6	59.083	-394.7 ± 294.8	0.188	0.19 ± 0.014
21	2591	1965	241	69.857	10.395	-300.7 ± 183.5	0.162	0.137 ± 0.021
22	609	491	66	19.085	5.7876	-75.87 ± 76.22	0.145	0.121 ± 0.05

Table 10.19: Type 3 (EC, partial CFT). Bin number, number of positrons in the signal sample that pass tight cuts, number of electrons in the signal sample that pass tight cuts, number of electrons and positrons that pass loose cuts but don't pass tight cuts (all these are before physics background subtraction), number of the $Z \to ee$ background events, number of $W \to \tau\nu$ background events, number of QCD multijet background events, asymmetry value before applying correction for the detector smearing effects and asymmetry after the corrections are applied with total uncertainties. 35 GeV$< E_T$.

bin	$N_{e^+}^{tight}$	$N_{e^-}^{tight}$	N_e^{nt}	$N_{Z\to ee}$	$N_{W\to\tau\nu}$	N_{qcd}	$A^{'}$	Asymmetry
0	92	87	48	2.1451	0.86885	50.42 ± 22.8	0.0345	0.137 ± 0.12
1	1256	1355	220	61.544	17.229	51.58 ± 94.04	-0.0352	0.0213 ± 0.026
2	257	337	39	13.734	5.3589	36.38 ± 29.08	-0.193	-0.151 ± 0.072
21	320	239	36	17.059	0	17.42 ± 34.28	0.18	0.145 ± 0.065
22	1328	1310	190	74.81	0	-34.94 ± 95.3	0.0109	-0.0192 ± 0.025
23	128	138	53	5.2018	1.6044	30.63 ± 25.88	-0.0585	-0.154 ± 0.082

Table 10.20: Type 4 (EC, no CFT). Bin number, number of positrons in the signal sample that pass tight cuts, number of electrons in the signal sample that pass tight cuts, number of electrons and positrons that pass loose cuts but don't pass tight cuts (all these are before physics background subtraction), number of the $Z \to ee$ background events, number of $W \to \tau\nu$ background events, number of QCD multijet background events, asymmetry value before applying correction for the detector smearing effects and asymmetry after the corrections are applied with total uncertainties. 35 GeV$< E_T$.

bin	$< \eta >$	A (Data)	A (CTEQ6.6)	A (MRST04NLO)
0	-2.80	0.137 ± 0.117 ± 0.034	0.017 + 0.144 (-0.179)	0.004
1	-2.37	-0.006 ± 0.019 ± 0.010	-0.126 + 0.075 (-0.074)	-0.149
2	-2.09	-0.151 ± 0.017 ± 0.012	-0.187 + 0.039 (-0.048)	-0.212
3	-1.90	-0.202 ± 0.011 ± 0.010	-0.212 + 0.041 (-0.027)	-0.230
4	-1.70	-0.180 ± 0.009 ± 0.007	-0.217 + 0.031 (-0.020)	-0.233
5	-1.39	-0.165 ± 0.011 ± 0.008	-0.204 + 0.026 (-0.022)	-0.215
6	-1.10	-0.163 ± 0.011 ± 0.008	-0.176 + 0.024 (-0.015)	-0.183
7	-0.90	-0.137 ± 0.007 ± 0.006	-0.150 + 0.024 (-0.013)	-0.154
8	-0.70	-0.112 ± 0.007 ± 0.005	-0.121 + 0.023 (-0.010)	-0.122
9	-0.50	-0.070 ± 0.007 ± 0.005	-0.085 + 0.011 (-0.013)	-0.090
10	-0.30	-0.047 ± 0.007 ± 0.005	-0.053 + 0.013 (-0.005)	-0.054
11	-0.10	-0.012 ± 0.007 ± 0.005	-0.018 + 0.007 (-0.005)	-0.017
12	0.10	0.017 ± 0.007 ± 0.005	0.018 + 0.005 (-0.007)	0.017
13	0.30	0.047 ± 0.007 ± 0.005	0.053 + 0.005 (-0.013)	0.054
14	0.50	0.082 ± 0.007 ± 0.005	0.085 + 0.013 (-0.011)	0.090
15	0.70	0.130 ± 0.007 ± 0.005	0.121 + 0.010 (-0.023)	0.122
16	0.90	0.140 ± 0.008 ± 0.006	0.150 + 0.013 (-0.024)	0.154
17	1.10	0.140 ± 0.012 ± 0.009	0.176 + 0.015 (-0.024)	0.183
18	1.39	0.177 ± 0.010 ± 0.008	0.204 + 0.022 (-0.026)	0.215
19	1.70	0.184 ± 0.009 ± 0.009	0.217 + 0.020 (-0.031)	0.233
20	1.90	0.191 ± 0.011 ± 0.008	0.212 + 0.027 (-0.041)	0.230
21	2.09	0.138 ± 0.016 ± 0.012	0.187 + 0.048 (-0.039)	0.212
22	2.37	0.010 ± 0.020 ± 0.010	0.126 + 0.074 (-0.075)	0.149
23	2.80	-0.154 ± 0.076 ± 0.031	-0.017 + 0.179 (-0.144)	-0.004

Table 10.21: Charge asymmetry for data and theoretical predictions for electron $E_T > 35$ GeV using CTEQ6.6 and MRST04NLO. For the data, the first uncertainty is statistical and the second is systematic. For the CTEQ prediction, the first one is for ΔA^+ and the second one is for ΔA^-.

bin	$< \eta >$	A (Data)	A (CTEQ6.6)	A (MRST04NLO)
0	0.10	0.014 ± 0.005 ± 0.004	0.018 + 0.005 (-0.007)	0.017
1	0.30	0.048 ± 0.005 ± 0.004	0.053 + 0.005 (-0.013)	0.054
2	0.50	0.075 ± 0.005 ± 0.004	0.085 + 0.013 (-0.011)	0.090
3	0.70	0.124 ± 0.005 ± 0.004	0.121 + 0.010 (-0.023)	0.122
4	0.90	0.139 ± 0.005 ± 0.004	0.150 + 0.013 (-0.024)	0.154
5	1.10	0.152 ± 0.008 ± 0.006	0.176 + 0.015 (-0.024)	0.183
6	1.39	0.170 ± 0.008 ± 0.006	0.204 + 0.022 (-0.026)	0.215
7	1.70	0.179 ± 0.006 ± 0.006	0.217 + 0.020 (-0.031)	0.233
8	1.90	0.197 ± 0.008 ± 0.007	0.212 + 0.027 (-0.041)	0.230
9	2.09	0.144 ± 0.012 ± 0.009	0.187 + 0.048 (-0.039)	0.212
10	2.37	0.011 ± 0.014 ± 0.007	0.126 + 0.074 (-0.075)	0.149
11	2.80	-0.148 ± 0.067 ± 0.026	-0.017 + 0.179 (-0.144)	-0.004

Table 10.22: Folded charge asymmetry for data and theoretical predictions for electron $E_T > 35$ GeV using CTEQ6.6 and MRST04NLO. For the data, the first uncertainty is statistical and the second is systematic. For the CTEQ prediction, the first one is for ΔA^+ and the second one is for ΔA^-.

$\langle\lvert\eta^e\rvert\rangle$	$A\ (\lvert\eta^e\rvert)$					
	$E_T > 25$ GeV		$25 < E_T < 35$ GeV		$E_T > 35$ GeV	
	Data	CTEQ6.6	Data	CTEQ6.6	Data	CTE
0.10	$1.6 \pm 0.4 \pm 0.3$	$1.9^{+0.4}_{-0.5}$	$1.9 \pm 0.6 \pm 0.5$	$2.1^{+0.5}_{-0.8}$	$1.4 \pm 0.5 \pm 0.4$	1.8
0.30	$5.6 \pm 0.4 \pm 0.3$	$5.7^{+0.4}_{-1.2}$	$6.8 \pm 0.6 \pm 0.5$	$6.2^{+0.8}_{-1.3}$	$4.8 \pm 0.5 \pm 0.4$	5.3
0.50	$8.2 \pm 0.4 \pm 0.3$	$9.1^{+1.2}_{-0.9}$	$9.3 \pm 0.6 \pm 0.5$	$9.8^{+1.2}_{-0.8}$	$7.5 \pm 0.5 \pm 0.4$	8.5
0.70	$13.0 \pm 0.4 \pm 0.3$	$12.2^{+1.5}_{-1.2}$	$13.8 \pm 0.6 \pm 0.5$	$12.4^{+3.1}_{-0.3}$	$12.4 \pm 0.5 \pm 0.4$	12.1
0.90	$14.6 \pm 0.4 \pm 0.3$	$14.8^{+1.3}_{-1.8}$	$15.8 \pm 0.7 \pm 0.6$	$14.6^{+1.7}_{-1.3}$	$13.9 \pm 0.5 \pm 0.4$	15.0
1.10	$15.5 \pm 0.6 \pm 0.5$	$16.6^{+1.0}_{-2.5}$	$15.8 \pm 1.0 \pm 0.8$	$15.2^{+0.7}_{-3.0}$	$15.2 \pm 0.8 \pm 0.6$	17.6
1.39	$14.4 \pm 0.6 \pm 0.5$	$16.4^{+1.8}_{-2.2}$	$12.9 \pm 1.0 \pm 0.8$	$11.1^{+1.8}_{-1.8}$	$17.0 \pm 0.8 \pm 0.6$	20.4
1.70	$10.2 \pm 0.5 \pm 0.4$	$13.0^{+2.3}_{-2.2}$	$-0.1 \pm 0.8 \pm 0.6$	$0.7^{+3.2}_{-1.3}$	$17.9 \pm 0.6 \pm 0.6$	21.7
1.90	$6.6 \pm 0.6 \pm 0.5$	$8.3^{+2.2}_{-3.3}$	$-12.0 \pm 1.0 \pm 0.8$	$-10.1^{+2.2}_{-2.7}$	$19.7 \pm 0.8 \pm 0.7$	21.2
2.09	$-2.5 \pm 0.9 \pm 0.6$	$0.9^{+4.3}_{-3.0}$	$-24.7 \pm 1.3 \pm 1.2$	$-23.6^{+4.1}_{-2.2}$	$14.4 \pm 1.2 \pm 0.9$	18.7
2.37	$-19.8 \pm 1.0 \pm 0.7$	$-12.0^{+5.1}_{-5.1}$	$-42.9 \pm 1.4 \pm 1.6$	$-39.4^{+3.2}_{-3.3}$	$1.1 \pm 1.4 \pm 0.7$	12.6
2.80	$-54.3 \pm 4.2 \pm 4.2$	$-36.1^{+9.4}_{-7.2}$	$-76.2 \pm 5.0 \pm 7.1$	$-55.1^{+6.0}_{-4.3}$	$-14.8 \pm 6.7 \pm 2.6$	−1.7

Table 10.23: The folded charge asymmetry for data and CTEQ6.6 predictions tabulated in percent. For the data, the first uncertainty is statistical and the second is systematic. For the CTEQ6.6 predictions, the first one is for ΔA^+ and the second one is for ΔA^-.

10.6.3 Summary of charge asymmetry results

Table 12.1 shows the summary of charge asymmetry measurements, in percent, for different E_T bins together with the theoretical predictions.

10.6.4 DØ and CDF comparisons

Both DØ and CDF have measured the W charge asymmetry, and the folded charge asymmetry measured by CDF (170 pb^{-1}) and DØ (750 pb^{-1}) can be found in Fig. 10.11 to 10.13. There are several conclusions that we can make from this plot:

- CDF and DØ data agree with each other within the uncertainty for all η bins;
- Both CDF and DØ data indicate smaller charge asymmetry than predicted for high η region ($|\eta| > 2$);
- DØ has larger electron η coverage, so its data is more sensitive to PDF effects;
- Total uncertainties from DØ are much smaller than the total uncertainties from CDF;
- The technique we used by dividing electrons into different types helps to reduce the uncertainties for high rapidity electrons.

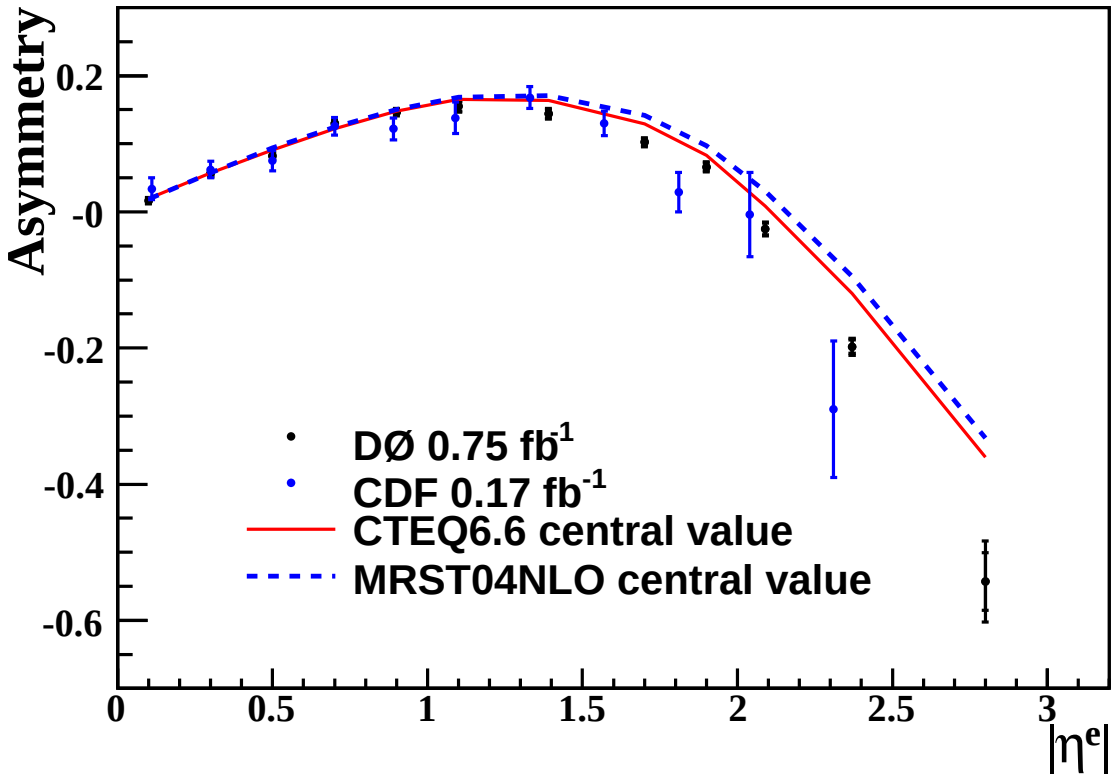

Figure 10.11: Asymmetry results between DØ and CDF for electron $E_T > 25$ GeV. Black points are D0 results, blue points are CDF results, red line is the CTEQ6.6 predictions and the blue line is the MRST04NLO predictions.

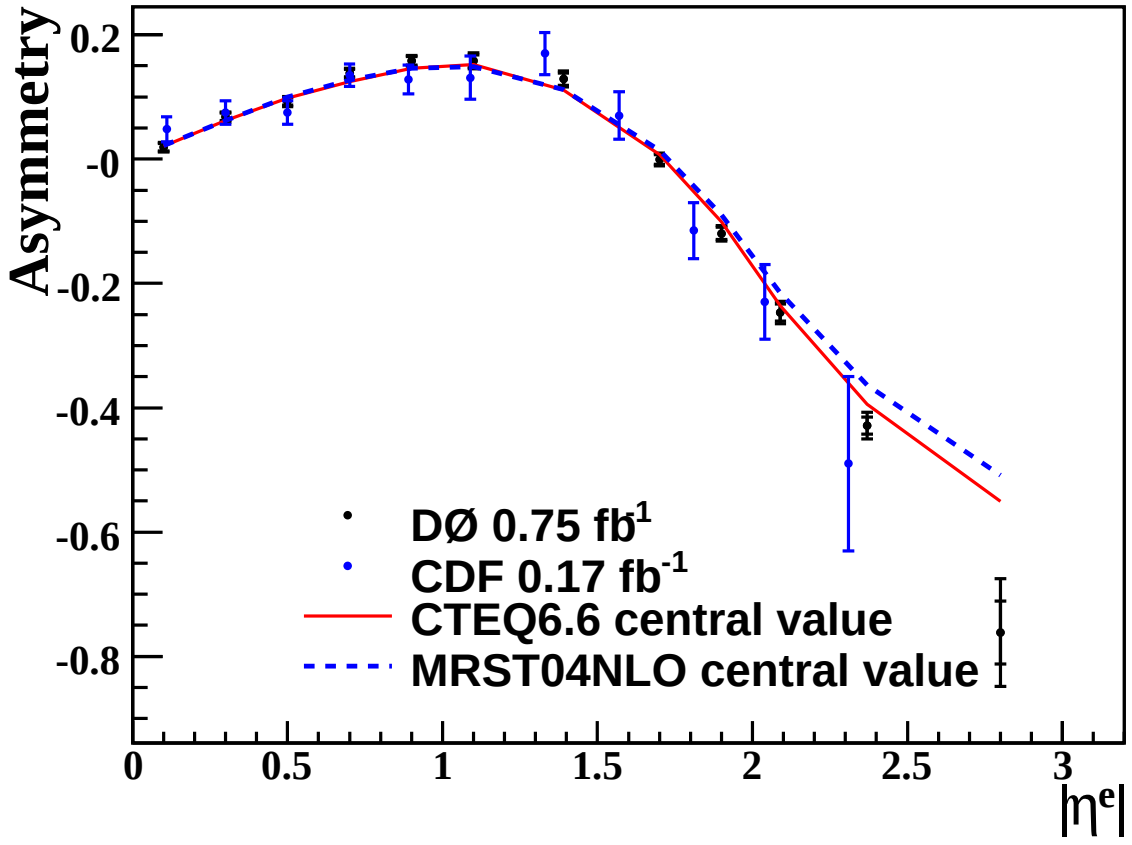

Figure 10.12: Asymmetry results between DØ and CDF for electron $25 < E_T < 35$ GeV. Black points are D0 results, blue points are CDF results, red line is the CTEQ6.6 predictions and the blue line is the MRST04NLO predictions.

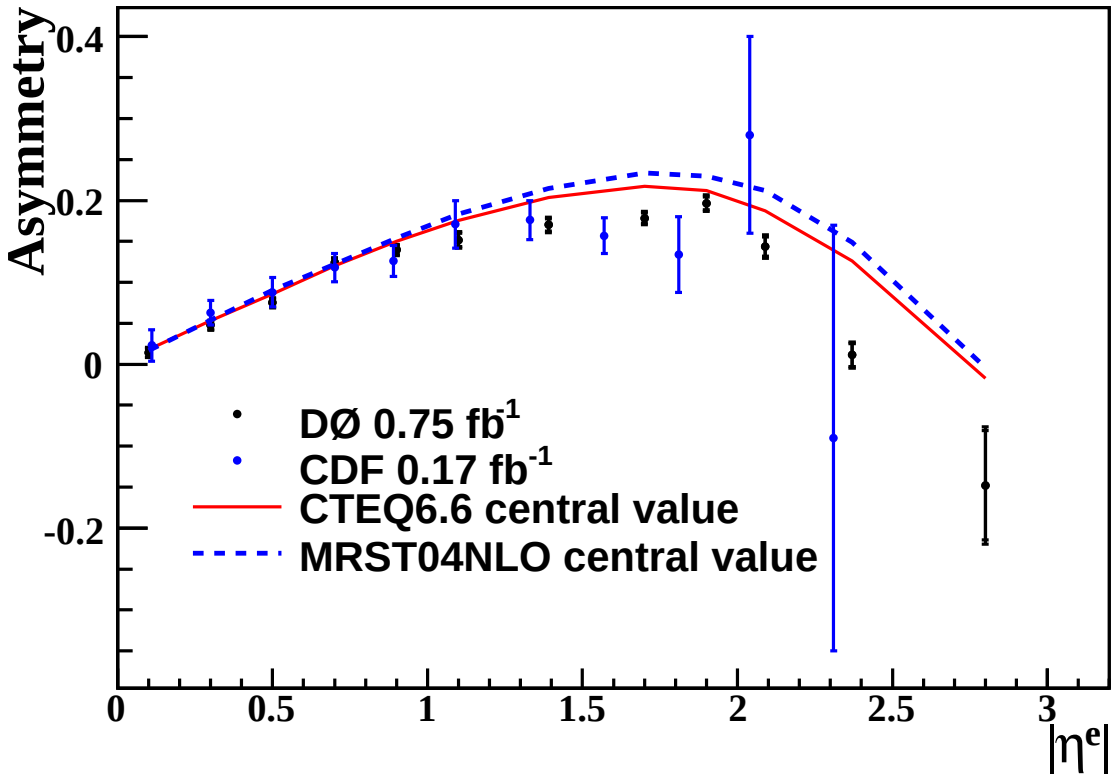

Figure 10.13: Asymmetry results between DØ and CDF for electron $E_T > 35$ GeV. Black points are D0 results, blue points are CDF results, red line is the CTEQ6.6 predictions and the blue line is the MRST04NLO predictions.

Chapter 11

Conclusions

We measured the electron charge asymmetry using $W \rightarrow e\nu$ events collected by DØdetector with an integrated luminosity of 750 pb^{-1}. The asymmetry is measured by dividing electrons into four different types and then combining them together. We also presented the asymmetry in two electron E_T regions. Predictions, from the latest CTEQ6.6 and MRST2004 PDFs, are shown for comparison. In this analysis, the electron η coverage is extended to $|\eta| < 3.2$ and is thus more sensitive to W's generated with small or large x partons. Our measurement is the most precise W charge asymmetry measurement to date, and this single measurement is superior in precision to the combined world average of all previous W charge asymmetry measurements done at the Tevatron. The measured asymmetry errors are less than the CTEQ6.6 PDF uncertainty for most rapidity bins. Inclusion of our results will further constrain future fits and improve the predictions.

Use of our results to improve PDFs is the job of the theory groups and is beyond the scope of this analysis, but we still compared our results to each of the CTEQ's 44 PDF sets, in 11.1 you can see the χ^2 values for each fit. We also made plots of the PDFs that agree best with our data and those that agree worst. You can see those PDFs, together with the central value PDF in the Fig. 11.2.

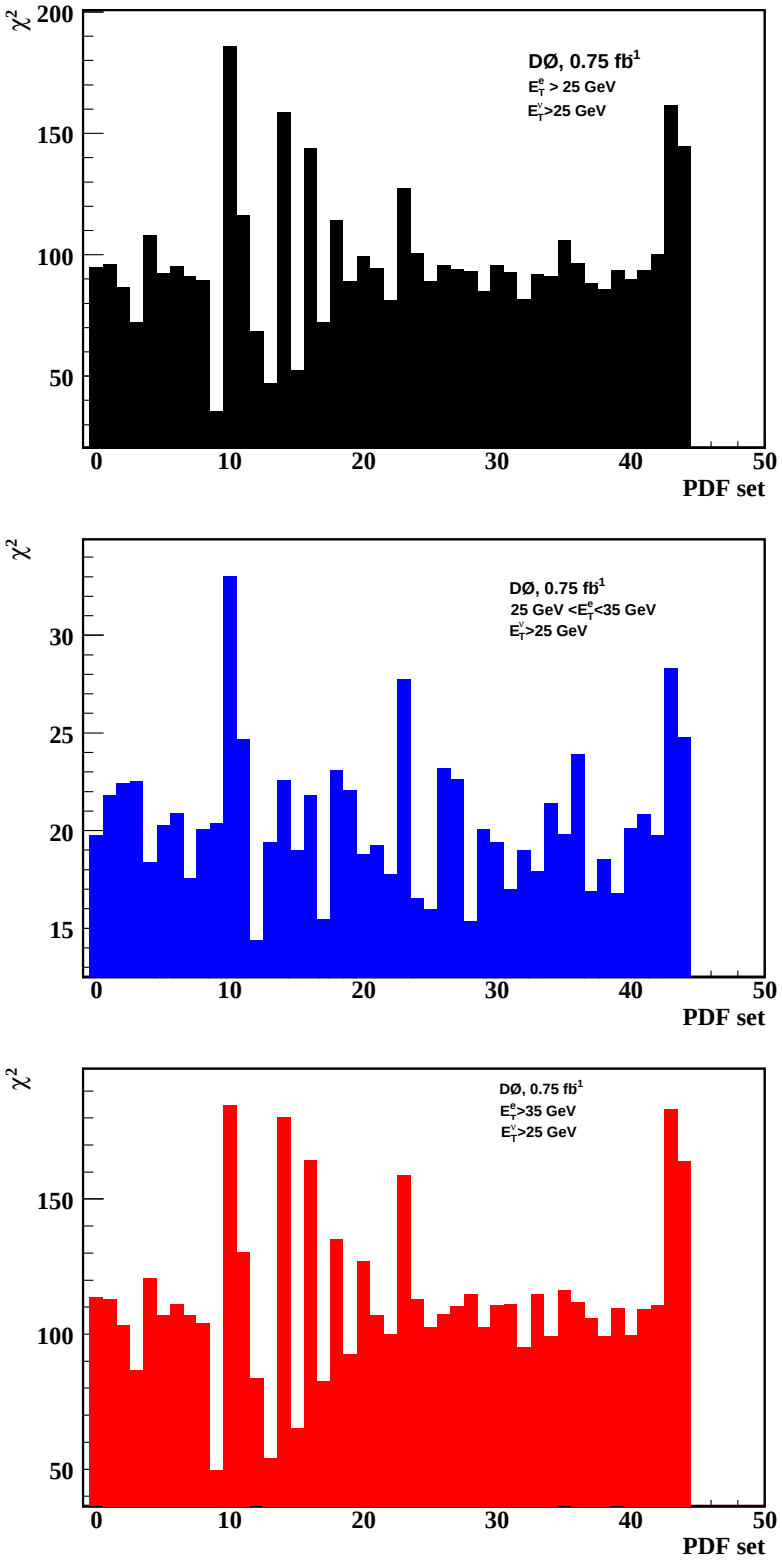

Figure 11.1: $\chi 2$ between data and CTEQ6.6 predictions for each PDF set vs PDF set number for electron $E_T > 25$ GeV, $25 < E_T < 35$ GeV and $E_T > 35$ GeV.

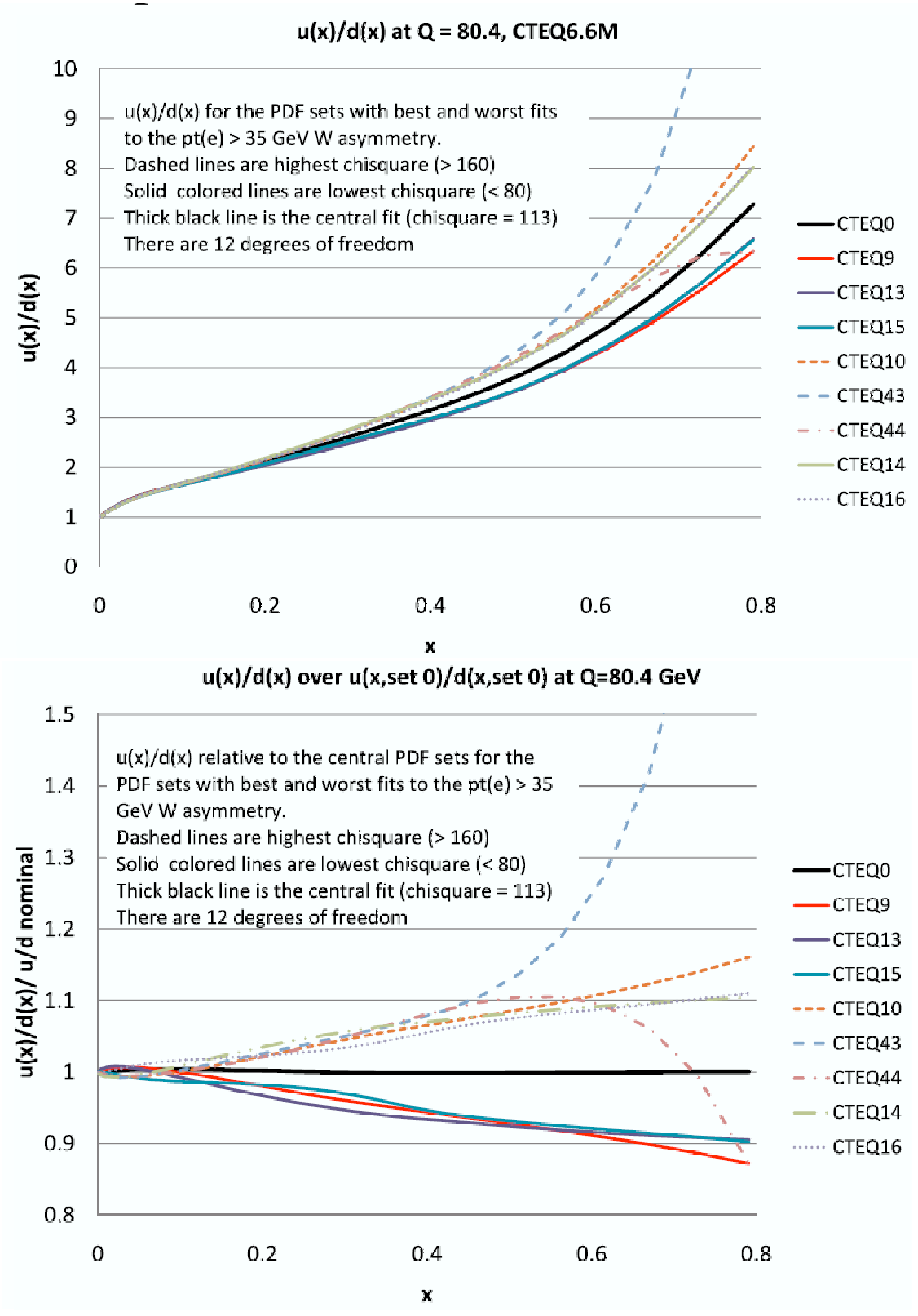

Figure 11.2: Top plot: $u(x)/d(x)$ values for the three PDFs that agree best with our data (solid lines) and for the three that agree worst (dashed lines), with the $u(x)/d(x)$ ratio for the central value (black line). Bottom plot: same distributions divided by the $u(x)/d(x)$ of the central PDF.

Chapter 12

Paper Published in PRL [1]

We present a measurement of the electron charge asymmetry in $p\bar{p} \to W + X \to e\nu + X$ events at a center of mass energy of 1.96 TeV using 0.75 fb^{-1} of data collected with the D0 detector at the Fermilab Tevatron Collider. The asymmetry is measured as a function of the electron transverse momentum and pseudorapidity in the interval $(-3.2, 3.2)$ and is compared with expectations from next-to-leading order calculations in perturbative quantum chromodynamics. These measurements will allow more accurate determinations of the proton parton distribution functions.

In $p\bar{p}$ collisions, $W^+(W^-)$ bosons are produced primarily by the annihilation of $u(d)$ quarks in the proton with $\bar{d}(\bar{u})$ quarks in the antiproton. The probability of finding a parton carrying momentum fraction x of the proton can be expressed by parton distribution functions (PDFs). Any difference between the u- and d-quark PDFs will result in an asymmetry in the W boson rapidity distribution between W^+ and W^- boson production [1]. In this Letter, we present a measurement of the charged lepton asymmetry with much larger statistical precision and over a wider kinematic range than previous measurements [2; 3]. This information provides constraints on the ratio of u- and d- quark PDFs, $u(x)/d(x)$. PDFs are necessary inputs for cross section calculations at hadron colliders. Many measurements have significant uncertainties associated with the accuracy of the PDFs, therefore understanding the PDFs is extremely important. Throughout this Letter, we use the notation "electron" to mean "electron and positron", unless specified otherwise.

We detect W bosons via the direct decay $W \to e\nu$. The boson rapidity (y_W) can not be measured due to the unknown longitudinal momentum of the neutrino. We instead measure the electron charge asymmetry, which is a convolution of the W boson production asymmetry and the parity violating asymmetry from the W boson decay. Since the V-A interaction is well understood, the lepton charge asymmetry retains sensitivity to

the underlying W boson asymmetry. The electron charge asymmetry ($A(\eta^e)$) is defined as:

$$A(\eta^e) = \frac{d\sigma^+/d\eta^e - d\sigma^-/d\eta^e}{d\sigma^+/d\eta^e + d\sigma^-/d\eta^e}, \tag{12.1}$$

where η^e is the pseudorapidity of the electron [4] and $d\sigma^+/d\eta^e$ ($d\sigma^-/d\eta^e$) is the differential cross section for the electrons from W^+ (W^-) bosons as a function of the electron pseudorapidity. When the detection efficiencies and acceptances for positrons and electrons are identical, the asymmetry becomes the difference in the number of positron and electron events over the sum.

In this Letter, we present results obtained from more than twice the integrated luminosity of previous measurements by the CDF [2] and D0 [3] collaborations and extend the measurement for leptons with $|\eta^\ell| < 3.2$, compared to $|\eta^\ell| < 2.5$ for CDF and $|\eta^\ell| < 2.0$ for the previous D0 measurement. By extending to higher rapidity leptons, we can provide information about the PDFs for a broader x range ($0.002 < x < 1.0$ for $|y_W| < 3.2$) at high $Q^2 \sim M_W^2$, where Q^2 is the momentum transfer squaredand M_W is the W boson mass.

The data sample used in this measurement was collected with the D0 detector [5] at the Fermilab Tevatron Collider using a set of inclusive single-electron triggers based only on calorimeter information [13]. The integrated luminosity is 750 ± 46 pb^{-1} [7].

The D0 detector includes a central tracking system, composed of a silicon microstrip tracker (SMT) and a central fiber tracker (CFT), both located within a 2 T superconducting solenoidal magnet and covering pseudorapidities of $|\eta_D| < 3.0$ and $|\eta_D| < 2.5$ respectively [4]. Three liquid argon and uranium calorimeters provide coverage out to $|\eta_D| \approx 4.2$: a central section (CC) with coverage of $|\eta_D| < 1.1$ and two end calorimeters (EC) with a coverage of $1.5 < |\eta_D| < 4.2$.

W boson candidates are identified by one isolated electromagnetic cluster accompanied by large missing transverse energy ($\not\!\!E_T$). $\not\!\!E_T$ is determined by the vector sum of the transverse components of the energy deposited in the calorimeter and the transverse momentum (E_T) of the electron. Electron candidates are further required to have shower shapes consistent with that of an electron. The E_T of the electron and the $\not\!\!E_T$ are required to be greater than 25 GeV. Additionally, the transverse mass M_T of the electron and $\not\!\!E_T$ is required to be greater than 50 GeV, where $M_T = \sqrt{2E_T \not\!\!E_T(1 - \cos\Delta\phi)}$, and $\Delta\phi$ is the azimuthal angle between the electron and $\not\!\!E_T$.

Electrons are required to fall within the fiducial region of the calorimeters, and must be spatially matched to a reconstructed track in the central tracking system. Because

of the different geometrical coverage of the calorimeters and the tracker, the electrons are divided into four different types depending on the locations of the electrons in the calorimeter and the associated track polar angle and the collision vertex: CC electrons within the full coverage of the CFT, EC electrons within the full coverage of the CFT, EC electrons within the partial coverage of the CFT, and EC electrons outside the coverage of the CFT. Optimized choices for selection criteria are established for each type. SMT hits are required in all four types, with tracks outside the CFT fiducial region requiring at least nine SMT hits. A total of 491,250 events satisfy the selection, with 358,336 events with electrons in the CC and 132,914 events with electrons in the EC. The charge asymmetry is measured in 24 electron pseudorapidity bins for $|\eta^e| < 3.2$.

The asymmetry measurement is sensitive to misidentification of the electron charge. We measure the charge misidentification rate with $Z \rightarrow ee$ events using a "tag-and-probe" method [13] where a track matched to one electron tags the charge of the other. Tight conditions are applied on the tag electron to make sure its charge is correctly determined. The rate ranges from 0.2% at $|\eta^e| \approx 0$ to 9% at $|\eta^e| \approx 3$. The absolute uncertainty in the charge misidentification changes from 0.1% to 2.6% depending on the electron pseudorapidity, and is dominated by the statistics of the Z boson sample.

Sources of charge bias in the event selection are investigated by studying $Z \rightarrow ee$ events. All selection efficiencies are measured for electrons and positrons separately, and no charge dependent biases in acceptance or efficiencies are found. To reduce any possible residual charge determination biases due to instrumental effects, the direction of the magnetic field in the solenoidal magnet was regularly reversed. Approximately 46% of the selected W bosons were collected with the solenoid at forward polarity, and 54% at reverse polarity. The charge asymmetry is measured separately for each solenoid polarity and no significant differences are observed.

Three sources of background can dilute the charge asymmetry: $Z \rightarrow ee$ events where one electron is not detected by the calorimeter, $W \rightarrow \tau\nu \rightarrow e\nu\nu\nu$ events, and multijet events in which one jet is misidentified as an electron and a large $\not\!\!E_T$ is produced by fragmentation fluctuations or misreconstruction. The $A(\eta^e)$ values are corrected for the backgrounds in each bin.

Events with electrons from $Z \rightarrow ee$ and $W \rightarrow \tau\nu \rightarrow e\nu\nu\nu$ decays exhibit charge asymmetries, and these two background contributions are evaluated using Monte Carlo (MC) events generated with PYTHIA [8] and processed with a detailed detector simulation based on GEANT [9]. The fractions of $Z \rightarrow ee$ and $W \rightarrow \tau\nu \rightarrow e\nu\nu\nu$ events estimated

to contribute to the candidate sample are $(1.3 \pm 0.1)\%$ and $(2.1 \pm 0.1)\%$, respectively.

The background fraction from multijet events is estimated by starting from a sample of candidate events with loose shower shape requirements and then selecting a subset of events which satisfy the final tighter requirement. From $Z \to ee$ events, and a sample of multijet events passing the preselection but with low $\not\!\!E_T$, we determine the probabilities with which real and fake electrons will pass the final shower shape requirement. These two probabilities (verified to be charge symmetric), along with the number of events selected in the loose and tight samples allow us to calculate the fraction of multijet events within our final selection. The final background contamination from multijet events is estimated to be $(0.8 \pm 0.4)\%$.

The final charge asymmetry is corrected for electron energy scale and resolution, $\not\!\!E_T$ resolution and trigger efficiency. The correction is estimated by comparing the asymmetry from the generator level PYTHIA $W \to e\nu$ MC to the GEANT-simulated results for each electron type.

The electron charge asymmetry is determined separately for each electron pseudorapidity bin and for each of the four electron types and then combined. The charge misidentification and background estimations are performed independently for each of these measurements. Assuming $A(-\eta^e) = -A(\eta^e)$ due to CP invariance, we fold the data to increase the available statistics and obtain a more precise measurement of $A(\eta^e)$.

Figure 12.1 shows the folded electron charge asymmetry. The dominant sources of systematic uncertainties originate from the estimation of charge misidentification and multijet backgrounds. The bin-by-bin correlations of these systematic uncertainties are negligible. Also shown in Fig. 12.1 are the theoretical predictions obtained using the RESBOS event generator [5] (with gluon resummation at low boson p_T and NLO perturbative QCD calculations at high boson p_T) with PHOTOS [6] (for QED final state radiation). The PDFs used to generate these predictions are the CTEQ6.6 NLO PDFs [7] and MRST04NLO PDFs [13]. Theoretical uncertainties derived from the 44 CTEQ6.6 PDF uncertainty sets are also shown. These curves are generated by applying a 25 GeV cut on the electron and neutrino generator-level transverse momenta. The asymmetric PDF uncertainty band is calculated using the formula described in Ref. [14].

We also measure the asymmetry in two bins of electron E_T: $25 < E_T < 35$ GeV and $E_T > 35$ GeV. For a given η^e, the two E_T regions probe different ranges of y_W and thus allow a finer probe of the x dependence. The folded electron charge asymmetries, along with the theoretical predictions, for the two E_T bins are shown in Fig. 12.2.

The measured values of the asymmetry and uncertainties, together with the CTEQ6.6

predictions, for $E_T > 25$ GeV and the two separate E_T bins are listed in Table 12.1. The measured charge asymmetries tend to be lower than the theoretical predictions using both CTEQ6.6 central PDF set and MRST04NLO PDFs for high pseudorapidity electrons. For most η^e bins, the experimental uncertainties are smaller than the uncertainties given by the most recent CTEQ6.6 uncertainty sets, demonstrating the sensitivity of our measurement.

A complete interpretation of the impact of these data on the PDFs will require revised NLO QCD fits to all available data. However, we can estimate the impact of this measurement by investigating the behavior of the $u(x)/d(x)$ ratio at $Q^2 = M_W^2$ for the 44 CTEQ6.6 PDF uncertainty sets. We observe that they differ by 10-20% for $x > 0.2$, which illustrates the current limited knowledge on this ratio at high x. We find that the sets which best match our data consistently correspond to $u(x)/d(x)$ ratios which lie below the central prediction by 5-10% for $x > 0.2$, while those with the worst agreement lie above the central prediction by a similar amount. We conclude that our data favor smaller $u(x)/d(x)$ ratios at high x.

In summary, we have measured the charge asymmetry of electrons in $p\bar{p} \to W + X \to e\nu + X$ using 0.75 fb^{-1} of data. The electron coverage is extended to $|\eta^e| < 3.2$ and the asymmetry is measured for electron $E_T > 25$ GeV, as well as two separate E_T bins to improve sensitivity to the PDFs. This measurement is the most precise electron charge asymmetry measurement to date, and the experimental uncertainties are smaller than the theoretical uncertainties across almost all electron pseudorapidities. Our result can be used to improve the precision and accuracy of next generation PDF sets, and will help to reduce the PDF uncertainty for high precision M_W measurements and also improve the predictions for the Higgs boson production at the hadron colliders.

We thank P. Nadolsky for many useful discussions about the theoretical predictions. We thank the staffs at Fermilab and collaborating institutions, and acknowledge support from the DOE and NSF (USA); CEA and CNRS/IN2P3 (France); FASI, Rosatom and RFBR (Russia); CNPq, FAPERJ, FAPESP and FUNDUNESP (Brazil); DAE and DST (India); Colciencias (Colombia); CONACyT (Mexico); KRF and KOSEF (Korea); CONICET and UBACyT (Argentina); FOM (The Netherlands); STFC (United Kingdom); MSMT and GACR (Czech Republic); CRC Program, CFI, NSERC and WestGrid Project (Canada); BMBF and DFG (Germany); SFI (Ireland); The Swedish Research Council (Sweden); CAS and CNSF (China); and the Alexander von Humboldt Foundation (Germany).

η^e region	$\langle\lvert\eta^e\rvert\rangle$	$A\ (\lvert\eta^e\rvert)$				
		$E_T > 25$ GeV		$25 < E_T < 35$ GeV		E
		Data	Prediction	Data	Prediction	Dat
$0.0 - 0.2$	0.10	$1.6 \pm 0.4 \pm 0.3$	$1.9^{+0.4}_{-0.5}$	$1.9 \pm 0.6 \pm 0.5$	$2.1^{+0.5}_{-0.8}$	1.4 ± 0
$0.2 - 0.4$	0.30	$5.6 \pm 0.4 \pm 0.3$	$5.7^{+0.4}_{-1.2}$	$6.8 \pm 0.6 \pm 0.5$	$6.2^{+0.8}_{-1.3}$	4.8 ± 0
$0.4 - 0.6$	0.50	$8.2 \pm 0.4 \pm 0.3$	$9.1^{+1.2}_{-0.9}$	$9.3 \pm 0.6 \pm 0.5$	$9.8^{+1.2}_{-0.8}$	7.5 ± 0
$0.6 - 0.8$	0.70	$13.0 \pm 0.4 \pm 0.3$	$12.2^{+1.5}_{-1.2}$	$13.8 \pm 0.6 \pm 0.5$	$12.4^{+3.1}_{-0.3}$	12.4 ± 0
$0.8 - 1.0$	0.90	$14.6 \pm 0.4 \pm 0.3$	$14.8^{+1.3}_{-1.8}$	$15.8 \pm 0.7 \pm 0.6$	$14.6^{+1.7}_{-1.3}$	13.9 ± 0
$1.0 - 1.2$	1.10	$15.5 \pm 0.6 \pm 0.5$	$16.6^{+1.0}_{-2.5}$	$15.8 \pm 1.0 \pm 0.8$	$15.2^{+0.7}_{-3.0}$	15.2 ± 0
$1.2 - 1.6$	1.39	$14.4 \pm 0.6 \pm 0.5$	$16.4^{+1.8}_{-2.2}$	$12.9 \pm 1.0 \pm 0.8$	$11.1^{+1.8}_{-1.8}$	17.0 ± 0
$1.6 - 1.8$	1.70	$10.2 \pm 0.5 \pm 0.4$	$13.0^{+2.3}_{-2.2}$	$-0.1 \pm 0.8 \pm 0.6$	$0.7^{+3.2}_{-1.3}$	17.9 ± 0
$1.8 - 2.0$	1.90	$6.6 \pm 0.6 \pm 0.5$	$8.3^{+2.2}_{-3.3}$	$-12.0 \pm 1.0 \pm 0.8$	$-10.1^{+2.2}_{-2.7}$	19.7 ± 0
$2.0 - 2.2$	2.09	$-2.5 \pm 0.9 \pm 0.6$	$0.9^{+4.3}_{-3.0}$	$-24.7 \pm 1.3 \pm 1.2$	$-23.6^{+4.1}_{-2.2}$	14.4 ± 1
$2.2 - 2.6$	2.37	$-19.8 \pm 1.0 \pm 0.7$	$-12.0^{+5.1}_{-5.1}$	$-42.9 \pm 1.4 \pm 1.6$	$-39.4^{+3.2}_{-3.3}$	1.1 ± 1
$2.6 - 3.2$	2.80	$-54.3 \pm 4.2 \pm 4.2$	$-36.1^{+9.4}_{-7.2}$	$-76.2 \pm 5.0 \pm 7.1$	$-55.1^{+6.0}_{-4.3}$	-14.8 ± 6

Table 12.1: Folded electron charge asymmetry for data and predictions from RESBOS with PHOTOS using CTEQ6.6 PDFs tabulated in percent. $\langle\lvert\eta^e\rvert\rangle$ is the cross section weighted average of electron pseudorapidity in each bin from RESBOS with PHOTOS. For data, the first uncertainty is statistical and the second is systematic. For the predictions, the uncertainties are from the PDFs only.

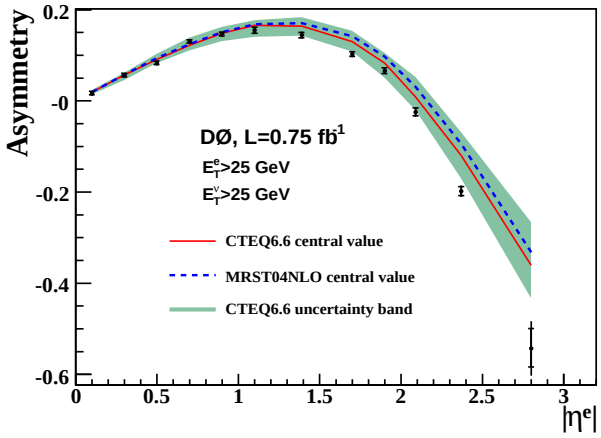

Figure 12.1: The folded electron charge asymmetry distribution. The horizontal bars show the statistical uncertainty and the full vertical lines show the total uncertainty on each point. The total uncertainty is the sum in quadrature of the statistical and systematic uncertainties. The solid (dashed) line is the theoretical prediction for the asymmetry using the CTEQ6.6 (MRST04NLO) central PDF set. The shaded band is the uncertainty band determined using the 44 CTEQ6.6 PDF uncertainty sets. All three were determined using RESBOS with PHOTOS.

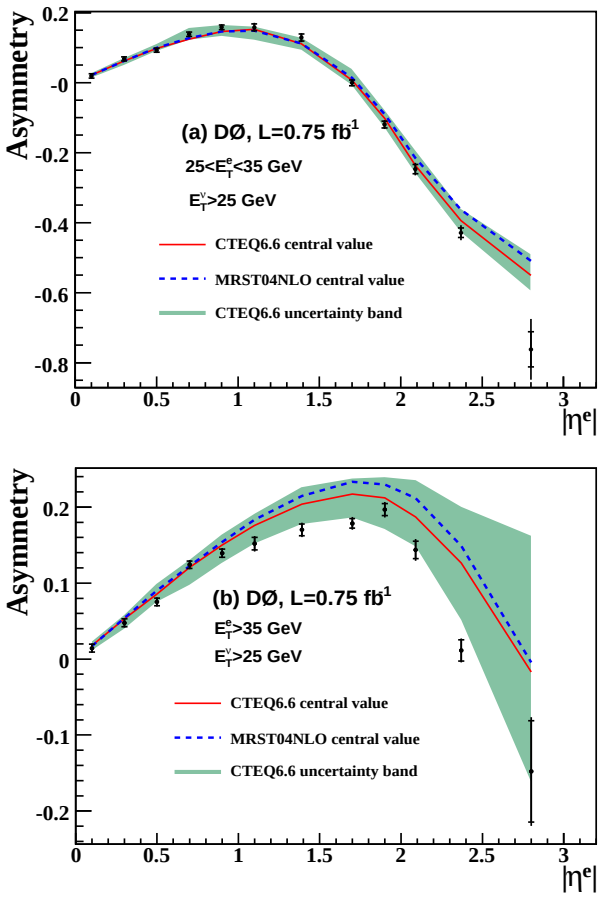

Figure 12.2: The folded electron charge asymmetry distribution in two electron E_T bins: $25 < E_T < 35$ GeV for (a) and $E_T > 35$ GeV for (b). In each plot, the horizontal bars show the statistical uncertainty and the full vertical lines show the total uncertainty on each point. The total uncertainty is the sum in quadrature of the statistical and systematic uncertainties. The solid (dashed) line is the theoretical prediction for the asymmetry using the CTEQ6.6 (MRST04NLO) central PDF set. The shaded band is the uncertainty band determined using the 44 CTEQ6.6 PDF uncertainty sets. All three were determined using RESBOS with PHOTOS.

References

[a] Visitor from Augustana College, Sioux Falls, SD, USA.

[b] Visitor from The University of Liverpool, Liverpool, UK.

[c] Visitor from ECFM, Universidad Autonoma de Sinaloa, Culiacán, Mexico.

[d] Visitor from II. Physikalisches Institut, Georg-August-University, Göttingen, Germany.

[e] Visitor from Helsinki Institute of Physics, Helsinki, Finland.

[f] Visitor from Universität Bern, Bern, Switzerland.

[g] Visitor from Universität Zürich, Zürich, Switzerland.

[‡] Deceased.

[1] E.L. Berger, F. Halzen, C.S. Kim, and S. Willenbrock, Phys. Rev. D **40**, 83 (1989); **40**, 3789(E) (1989).

[2] F. Abe *et al.* (CDF Collaboration), Phys. Rev. Lett. **74**, 850 (1995); F. Abe *et al.* (CDF Collaboration), Phys. Rev. Lett. **81**, 5754 (19 98); D. Acosta *et al.* (CDF Collaboration), Phys. Rev. D **71**, 051104(R) (2005).

[3] V. Abazov *et al.* (D0 Collaboration), Phys. Rev. D **77**, 011106(R) (2008).

[4] D0 uses a cylindrical coordinate system with the z axis running along the beam axis in the proton direction. Angles θ and ϕ are the polar and azimuthal angles, respectively. Pseudorapidity is defined as $\eta = -\ln[\tan(\theta/2)]$ where θ is measured with respect to the interaction vertex. In the massless limit, η is equivalent to the rapidity $y = (1/2)\ln[(E + p_z)/(E - p_z)]$. η_D is the pseudorapidity measured with respect to the center of the detector. Due to the distribution of the interactions within the detector, electrons may have larger η than η_D.

[5] V. Abazov *et al.* (D0 Collaboration), Nucl. Instrum. Methods Phys. Res., Sect. A **565**, 463 (2006).

[13] V. Abazov *et al.* (D0 Collaboration), Phys. Rev. D **76**, 012003 (2007).

[7] T. Andeen *et al.*, FERMILAB-TM-2365 (2007).

[8] T. Sjőstrand *et. al.*, Comput. Phys. Commun. **135**, 238 (2001).

[9] R. Brun and F. Carminati, CERN Program Library Long Writeup W5013, 1993 (unpublished).

[5] C. Balazs and C.P. Yuan, Phys. Rev. D **56**, 5558 (1997).

[6] E. Barberio and Z. Was, Comput. Phys. Commun **79**, 291 (1994); we use PHOTOS version 2.0.

[7] P.M. Nadolsky *et al.*, Phys. Rev. D **78**, 013004 (2008).

[13] A.D. Martin, R.G. Roberts, W.J. Stirling, and R.S. Thorne, Phys. Lett. B **604**, 61 (2004).

[14] D. Stump *et al.*, JHEP **0310**, 046 (2003).

References

[1] V.M. Abazov et al. (D0 Collaboration), Phys.Rev.Lett.101:211801,(2008).

[2] Stefano Forte. Structure functions and parton distributions. Nucl. Phys., A755:100-110, 2005.

[3] E.L. Berger, F. Halzen, C.S. Kim and S. Willenbrock, Phys. Rev. D **40**, 83 (1989).

[4] A.D. Martin, R.G. Roberts, and W.J. Stirling, Mod. Phys. Lett. A **4**, 1135 (1989).

[5] C. Balazs and C.-P. Yuan, Phys. Rev. D **56**, 5558 (1997).

[6] E. Barberio and Z. Was, Comput. Phys. Commun. **79**, 291 (1994).

[7] P.M. Nadolsky et al, arXiv:0802.0007.

[8] A.D. Martin, R.G. Roberts, W.J. Stirling, and R.S. Thorne, Phys. Lett. B **604**, 61 (2004).

[9] F. Abe et al. (CDF Collaboration), Phys. Rev. Lett. **74**, 850 (1995).

[10] F. Abe et al. (CDF Collaboration), Phys. Rev. Lett. **81**, 5754 (1998).

[11] D. Acosta et al. (CDF Collaboration), Phys. Rev. D **71**, 051104 (R) (2005).

[12] V.M. Abazov et al. (D0 Collaboration), Phys. Rev. D **77** 011106(R) (2008).

[13] H. Schellman, D0 Note 5374.

[14] A. Askew, D. Khatidze, H. Yin and J. Zhu, D0 Note 5564.

[15] R. Hamberg, W. van Neerven, and T. Matsuura, Nucl. Phys. B **359**, 343 (1991); **644**, 403 (E) (2002).

[16] D. Stump et al., JHEP **0310**, 046 (2003).

[17] L. Han et al., D0 Note 5603.

[18] http://www-d0.fnal.gov/computing/algorithms/#intro.

Chapter 13

Appendices

Appendix A

Signal Efficiency

A.1 Appendix A

Below are the Z mass distributions fitted with Gaus $\otimes$ Breit-Wigner + exp that we use in the signal efficiency calculations in Sec. 6.2. We have separate numerator and denominator plots for each bin and each type. The plots in the left column consist of events in the pass sample (numerator) and in the right column we have the pass plus fail sample (denominator) for the same bin.

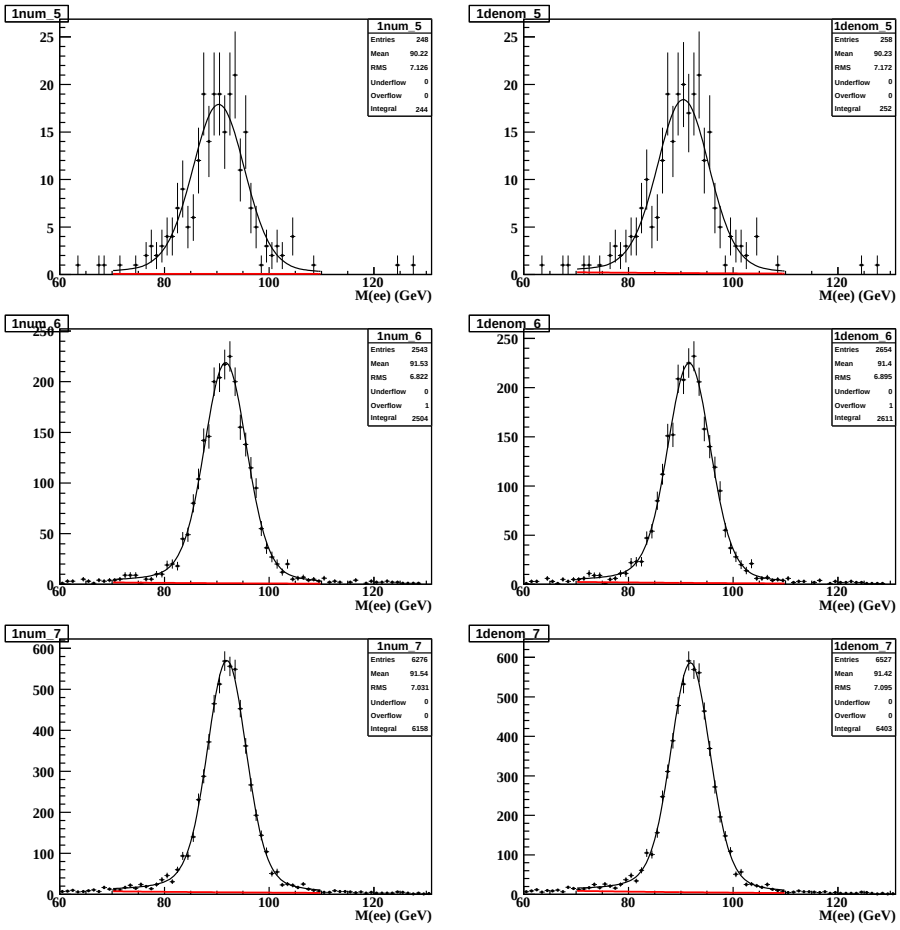

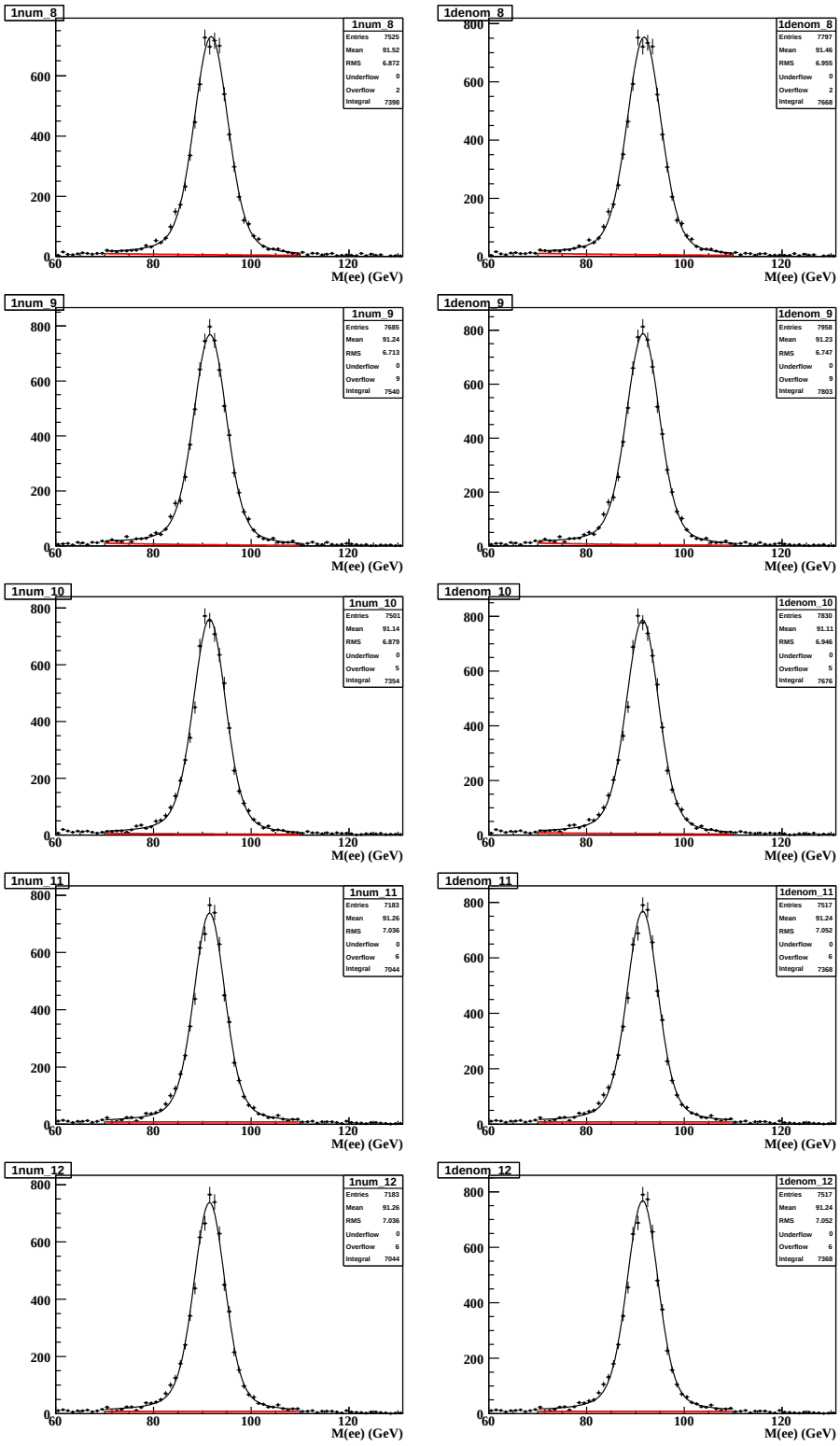
1num_8
1num_8
Entries 7525
Mean 91.52
RMS 6.872
Underflow 0
Overflow 2
Integral 7398
1denom_8
1denom_8
Entries 7797
Mean 91.46
RMS 6.955
Underflow 0
Overflow 2
Integral 7668
1num_9
1num_9
Entries 7685
Mean 91.24
RMS 6.713
Underflow 0
Overflow 9
Integral 7540
1denom_9
1denom_9
Entries 7958
Mean 91.23
RMS 6.747
Underflow 0
Overflow 9
Integral 7803
1num_10
1num_10
Entries 7501
Mean 91.14
RMS 6.879
Underflow 0
Overflow 5
Integral 7354
1denom_10
1denom_10
Entries 7830
Mean 91.11
RMS 6.946
Underflow 0
Overflow 5
Integral 7676
1num_11
1num_11
Entries 7183
Mean 91.26
RMS 7.036
Underflow 0
Overflow 6
Integral 7044
1denom_11
1denom_11
Entries 7517
Mean 91.24
RMS 7.052
Underflow 0
Overflow 6
Integral 7368
1num_12
1num_12
Entries 7183
Mean 91.26
RMS 7.036
Underflow 0
Overflow 6
Integral 7044
1denom_12
1denom_12
Entries 7517
Mean 91.24
RMS 7.052
Underflow 0
Overflow 6
Integral 7368
M(ee) (GeV)

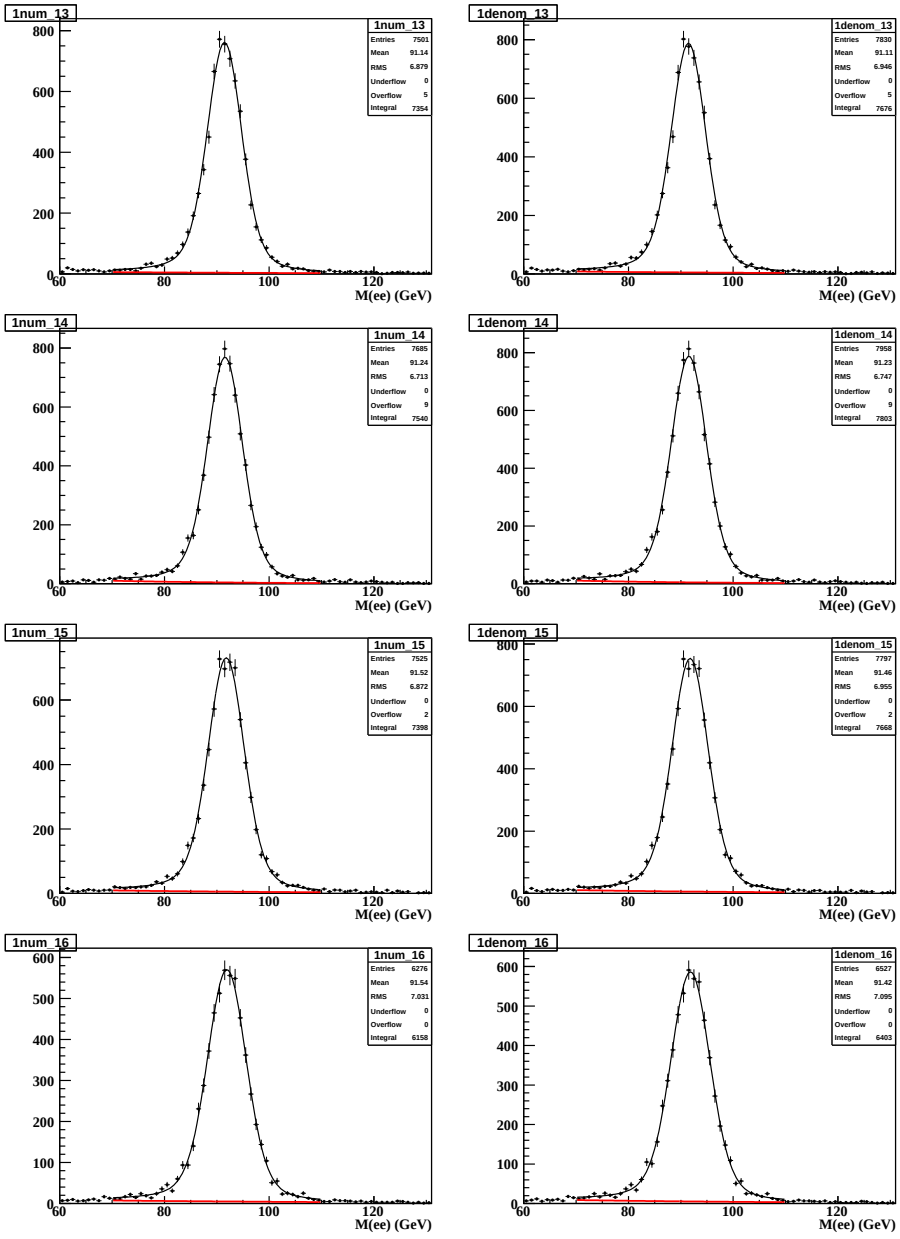
1num_13
Entries 7501
Mean 91.14
RMS 6.879
Underflow 0
Overflow 5
Integral 7354
1denom_13
Entries 7830
Mean 91.11
RMS 6.946
Underflow 0
Overflow 5
Integral 7676
1num_14
Entries 7685
Mean 91.24
RMS 6.713
Underflow 0
Overflow 9
Integral 7540
1denom_14
Entries 7958
Mean 91.23
RMS 6.747
Underflow 0
Overflow 9
Integral 7803
1num_15
Entries 7525
Mean 91.52
RMS 6.872
Underflow 0
Overflow 2
Integral 7398
1denom_15
Entries 7797
Mean 91.46
RMS 6.955
Underflow 0
Overflow 2
Integral 7668
1num_16
Entries 6276
Mean 91.54
RMS 7.031
Underflow 0
Overflow 0
Integral 6158
1denom_16
Entries 6527
Mean 91.42
RMS 7.095
Underflow 0
Overflow 0
Integral 6403
M(ee) (GeV)

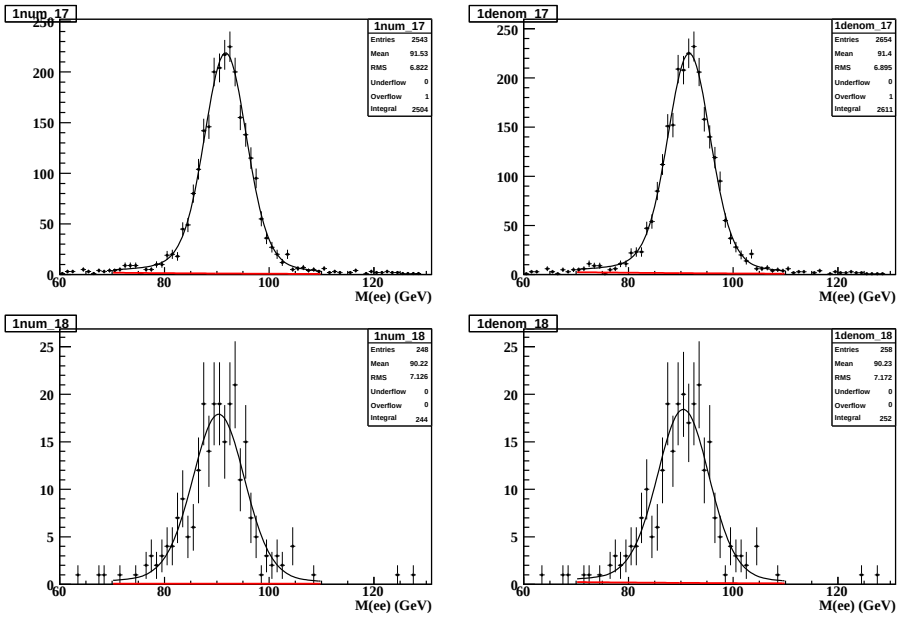

Figure 13.1: Numerator and denominator fits for signal efficiency for type 1 electrons.

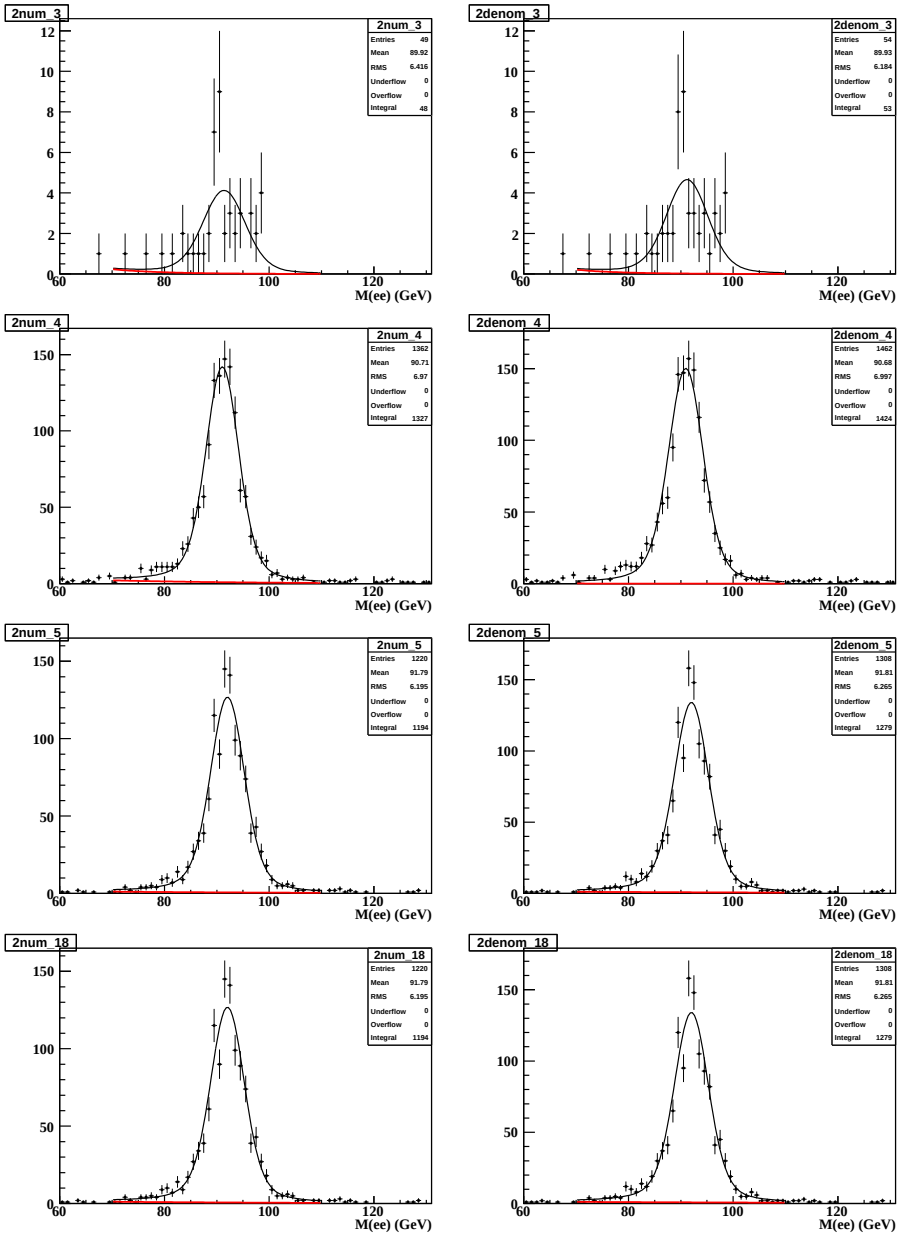
2num_3
Entries 49
Mean 89.92
RMS 6.416
Underflow 0
Overflow 0
Integral 48
2denom_3
Entries 54
Mean 89.93
RMS 6.184
Underflow 0
Overflow 0
Integral 53
2num_4
Entries 1362
Mean 90.71
RMS 6.97
Underflow 0
Overflow 0
Integral 1327
2denom_4
Entries 1462
Mean 90.68
RMS 6.997
Underflow 0
Overflow 0
Integral 1424
2num_5
Entries 1220
Mean 91.79
RMS 6.195
Underflow 0
Overflow 0
Integral 1194
2denom_5
Entries 1308
Mean 91.81
RMS 6.265
Underflow 0
Overflow 0
Integral 1279
2num_18
Entries 1220
Mean 91.79
RMS 6.195
Underflow 0
Overflow 0
Integral 1194
2denom_18
Entries 1308
Mean 91.81
RMS 6.265
Underflow 0
Overflow 0
Integral 1279
M(ee) (GeV)

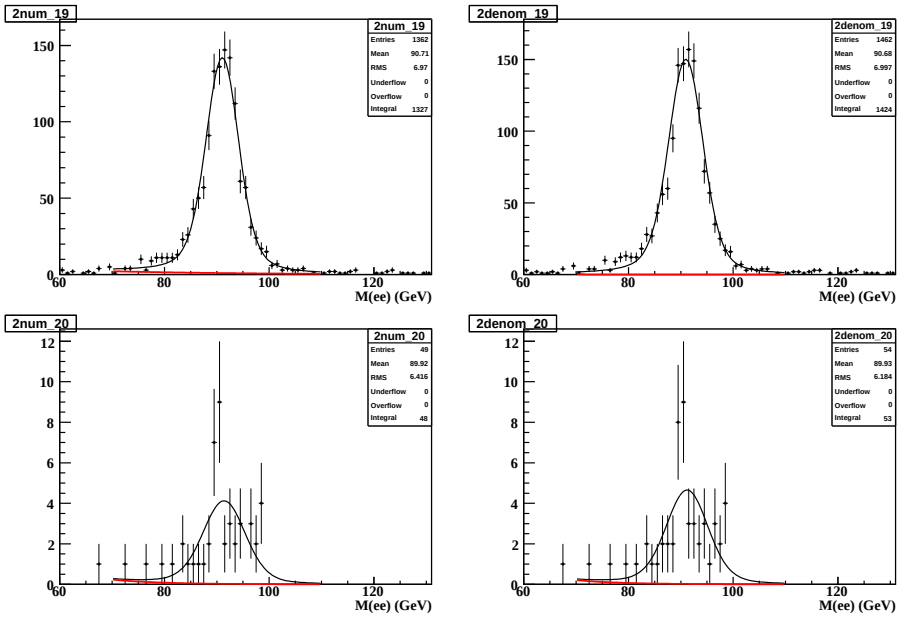

Figure 13.2: Numerator and denominator fits for signal efficiency for type 2 electrons.

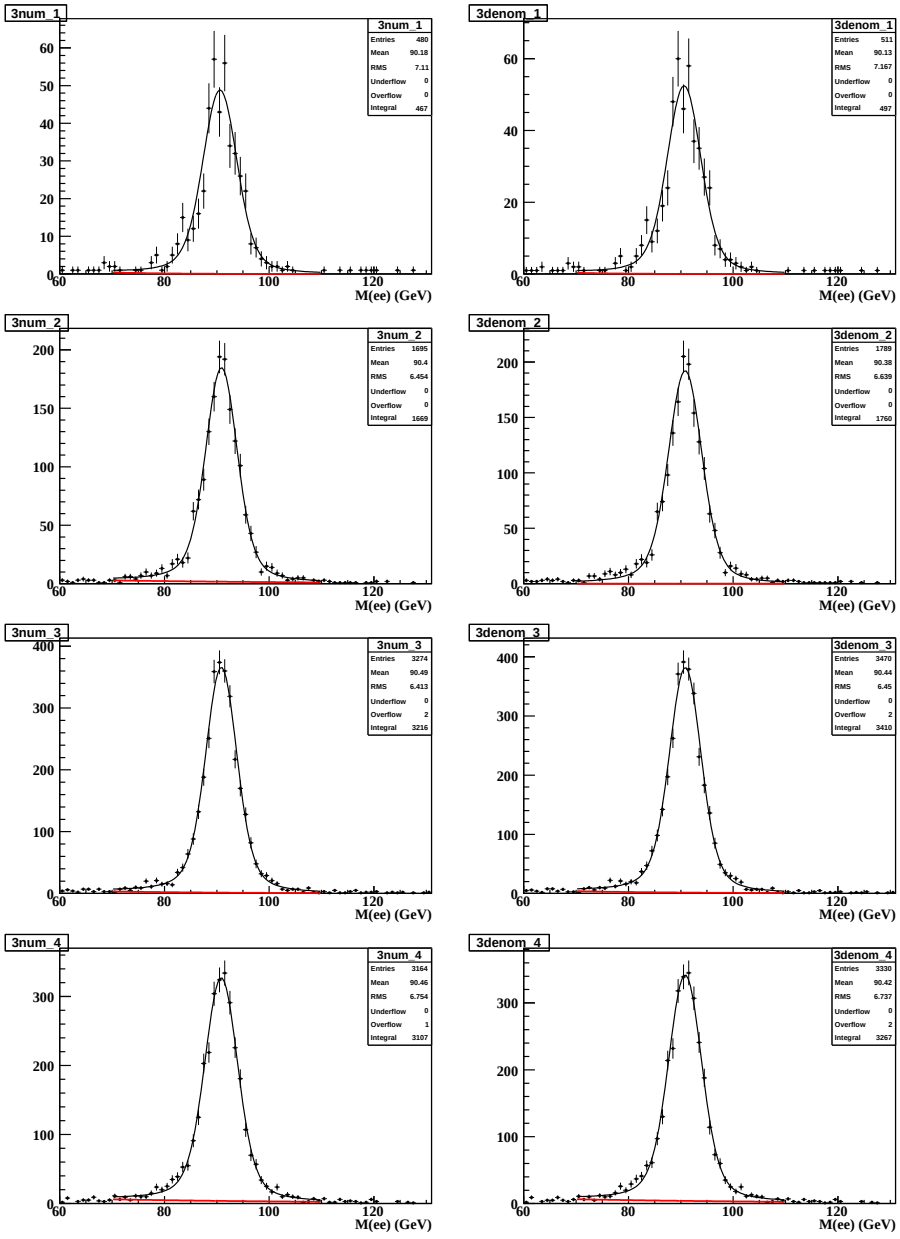
3num_1
Entries 480
Mean 90.18
RMS 7.11
Underflow 0
Overflow 0
Integral 467
M(ee) (GeV)
3denom_1
Entries 511
Mean 90.13
RMS 7.167
Underflow 0
Overflow 0
Integral 497
M(ee) (GeV)
3num_2
Entries 1695
Mean 90.4
RMS 6.454
Underflow 0
Overflow 0
Integral 1669
M(ee) (GeV)
3denom_2
Entries 1789
Mean 90.38
RMS 6.639
Underflow 0
Overflow 0
Integral 1760
M(ee) (GeV)
3num_3
Entries 3274
Mean 90.49
RMS 6.413
Underflow 0
Overflow 2
Integral 3216
M(ee) (GeV)
3denom_3
Entries 3470
Mean 90.44
RMS 6.45
Underflow 0
Overflow 2
Integral 3410
M(ee) (GeV)
3num_4
Entries 3164
Mean 90.46
RMS 6.754
Underflow 0
Overflow 1
Integral 3107
M(ee) (GeV)
3denom_4
Entries 3330
Mean 90.42
RMS 6.737
Underflow 0
Overflow 2
Integral 3267
M(ee) (GeV)

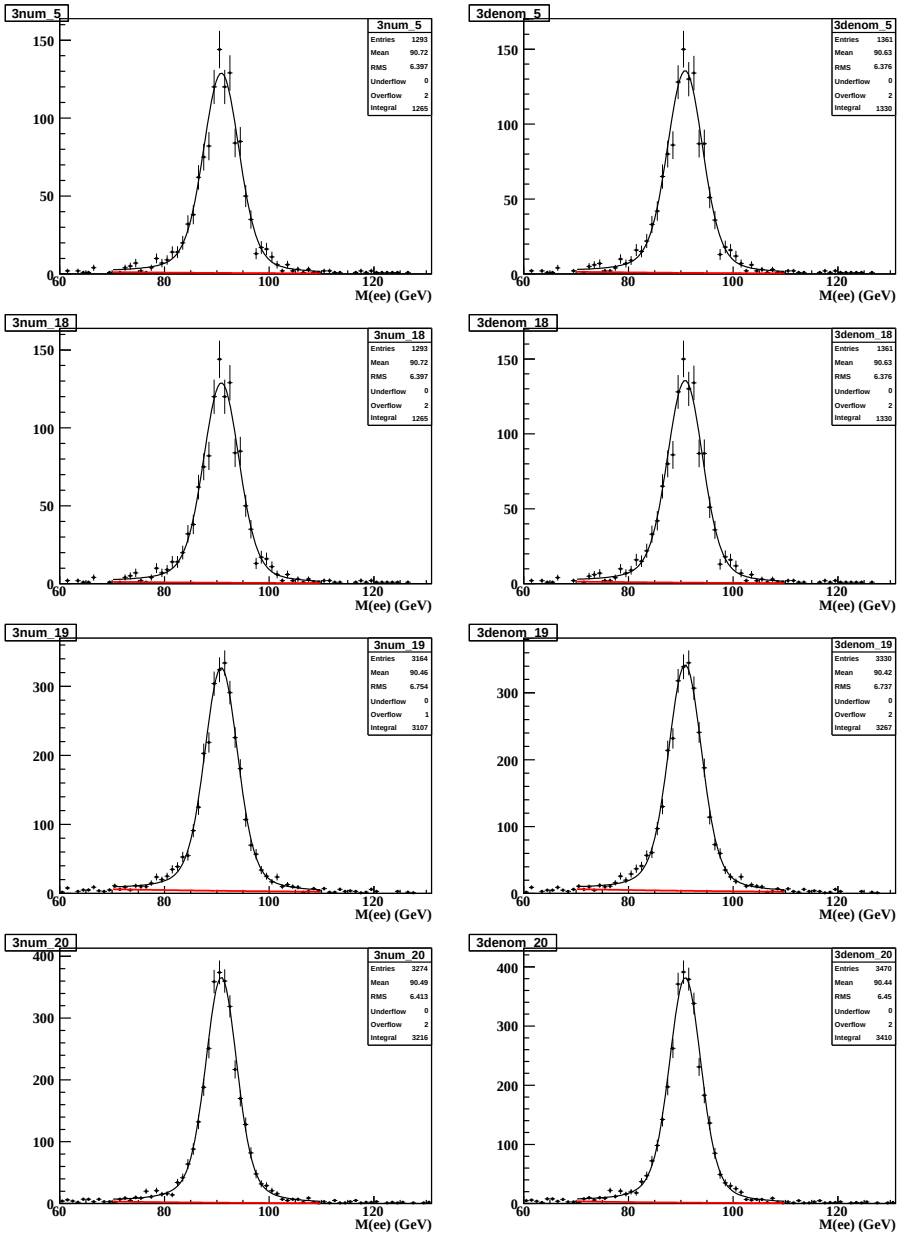
3num_5
Entries 1293
Mean 90.72
RMS 6.397
Underflow 0
Overflow 2
Integral 1265
3denom_5
Entries 1361
Mean 90.63
RMS 6.376
Underflow 0
Overflow 2
Integral 1330
3num_18
Entries 1293
Mean 90.72
RMS 6.397
Underflow 0
Overflow 2
Integral 1265
3denom_18
Entries 1361
Mean 90.63
RMS 6.376
Underflow 0
Overflow 2
Integral 1330
3num_19
Entries 3164
Mean 90.46
RMS 6.754
Underflow 0
Overflow 1
Integral 3107
3denom_19
Entries 3330
Mean 90.42
RMS 6.737
Underflow 0
Overflow 2
Integral 3267
3num_20
Entries 3274
Mean 90.49
RMS 6.413
Underflow 0
Overflow 2
Integral 3216
3denom_20
Entries 3470
Mean 90.44
RMS 6.45
Underflow 0
Overflow 2
Integral 3410
M(ee) (GeV)

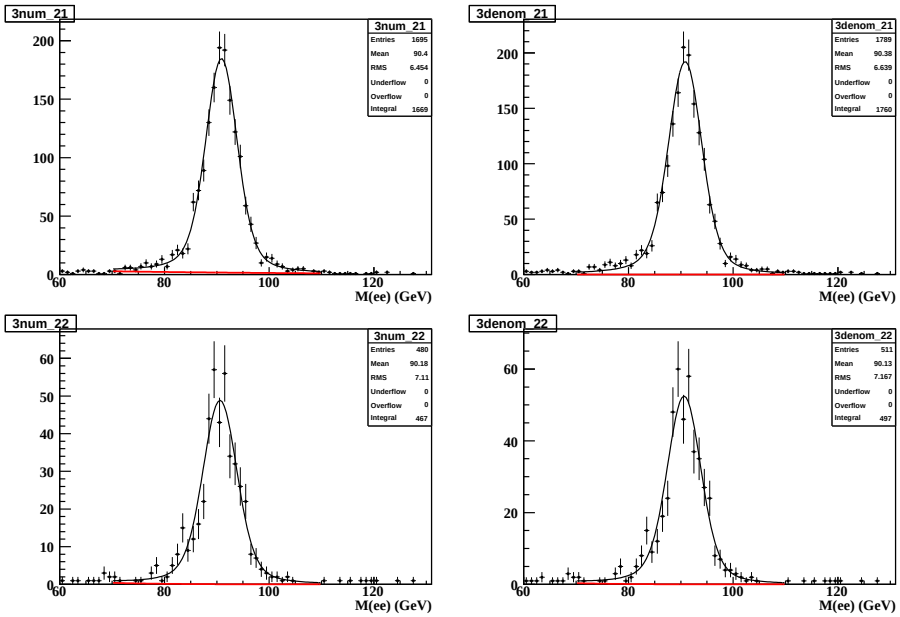

Figure 13.3: Numerator and denominator fits for signal efficiency for type 3 electrons.

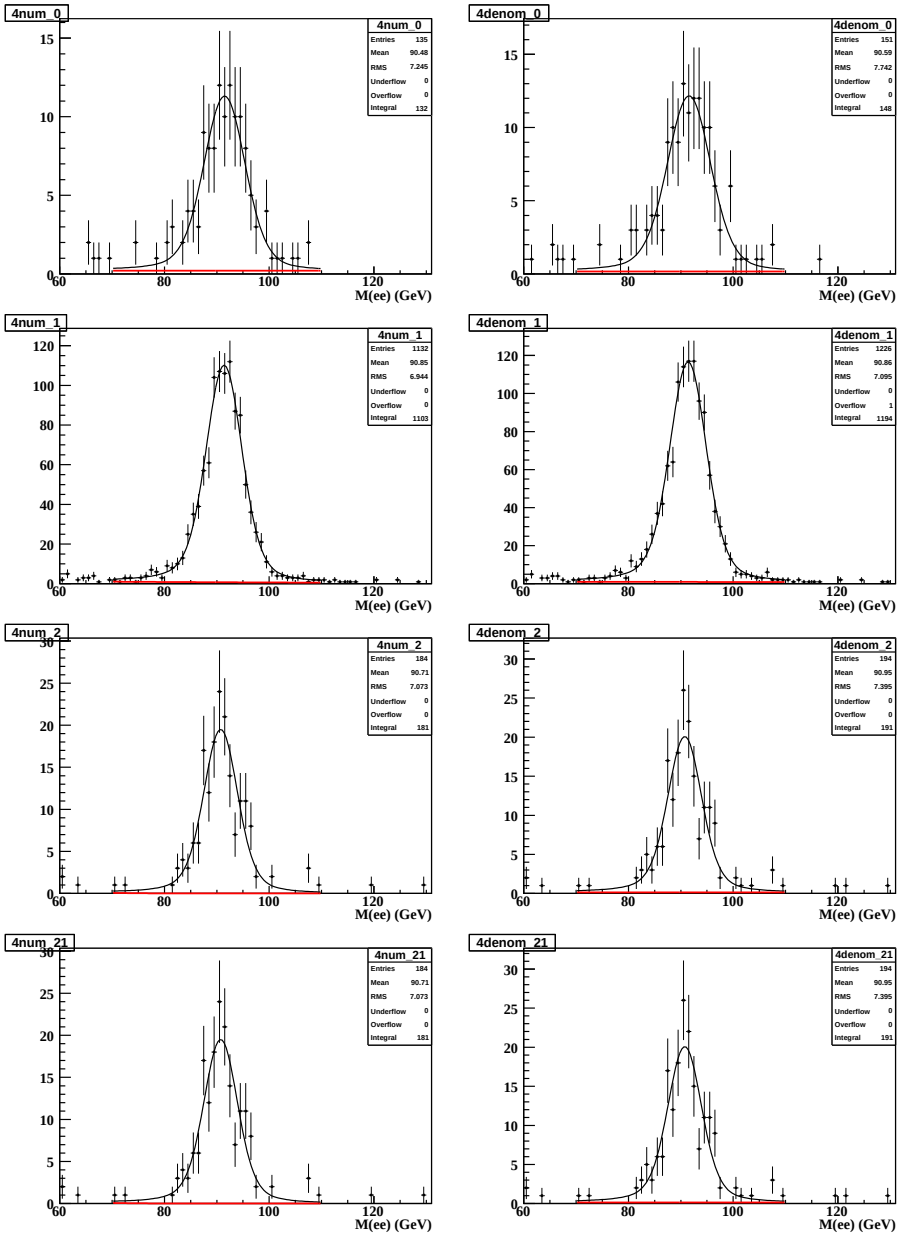
4num_0
4num_0
Entries 135
Mean 90.48
RMS 7.245
Underflow 0
Overflow 0
Integral 132
M(ee) (GeV)
4denom_0
4denom_0
Entries 151
Mean 90.59
RMS 7.742
Underflow 0
Overflow 0
Integral 148
M(ee) (GeV)
4num_1
4num_1
Entries 1132
Mean 90.85
RMS 6.944
Underflow 0
Overflow 0
Integral 1103
M(ee) (GeV)
4denom_1
4denom_1
Entries 1226
Mean 90.86
RMS 7.095
Underflow 0
Overflow 1
Integral 1194
M(ee) (GeV)
4num_2
4num_2
Entries 184
Mean 90.71
RMS 7.073
Underflow 0
Overflow 0
Integral 181
M(ee) (GeV)
4denom_2
4denom_2
Entries 194
Mean 90.95
RMS 7.395
Underflow 0
Overflow 0
Integral 191
M(ee) (GeV)
4num_21
4num_21
Entries 184
Mean 90.71
RMS 7.073
Underflow 0
Overflow 0
Integral 181
M(ee) (GeV)
4denom_21
4denom_21
Entries 194
Mean 90.95
RMS 7.395
Underflow 0
Overflow 0
Integral 191
M(ee) (GeV)

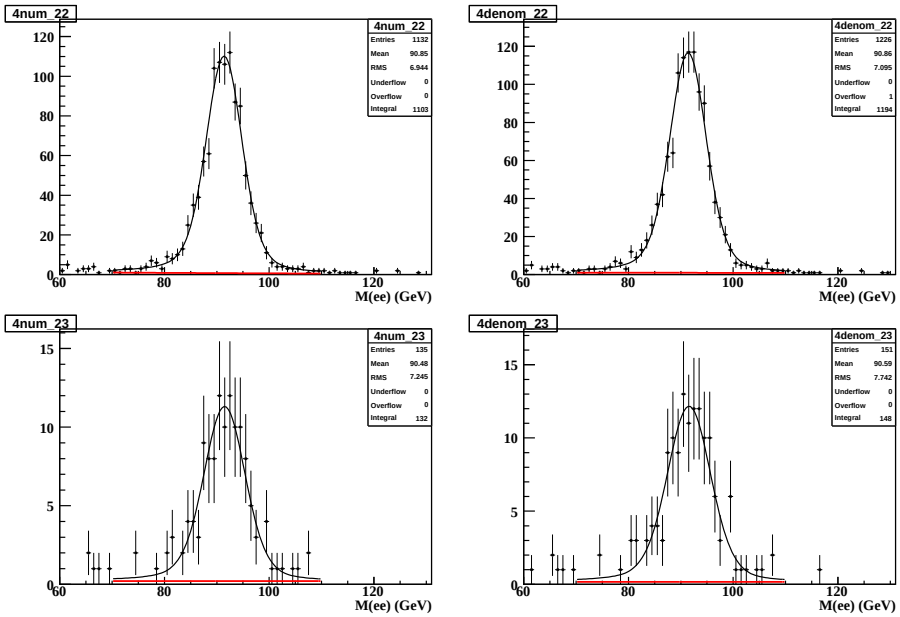

Figure 13.4: Numerator and denominator fits for signal efficiency for type 4 electrons

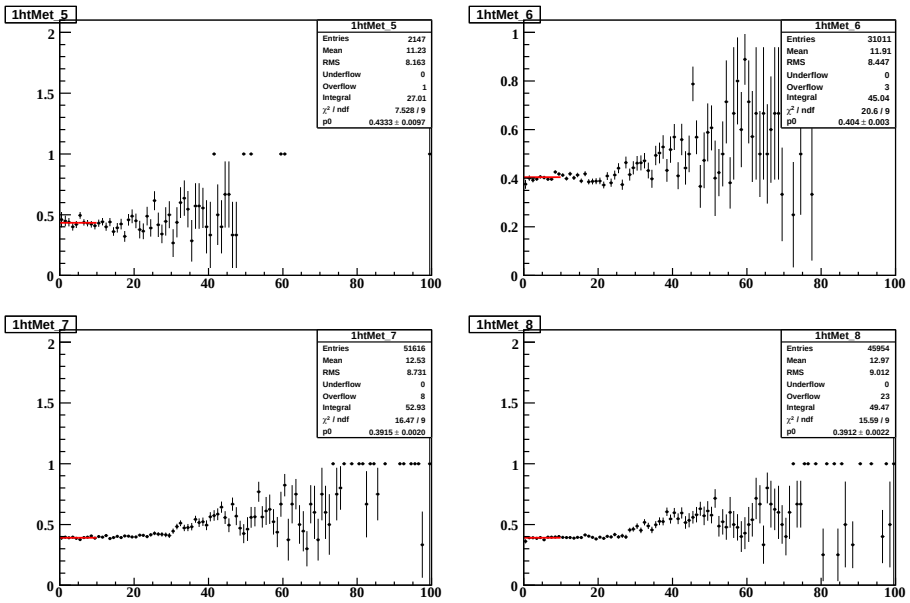

Appendix B

EM-like jet ID probability

B.1 Appendix B

As we described in Sec. 6.3 we use ratios of MET distributions for the em+jet sample. Below are the plots of those ratios fitted with a const line in the 0-10 GeV range. We have plots for each type and each rapidity bin separately.

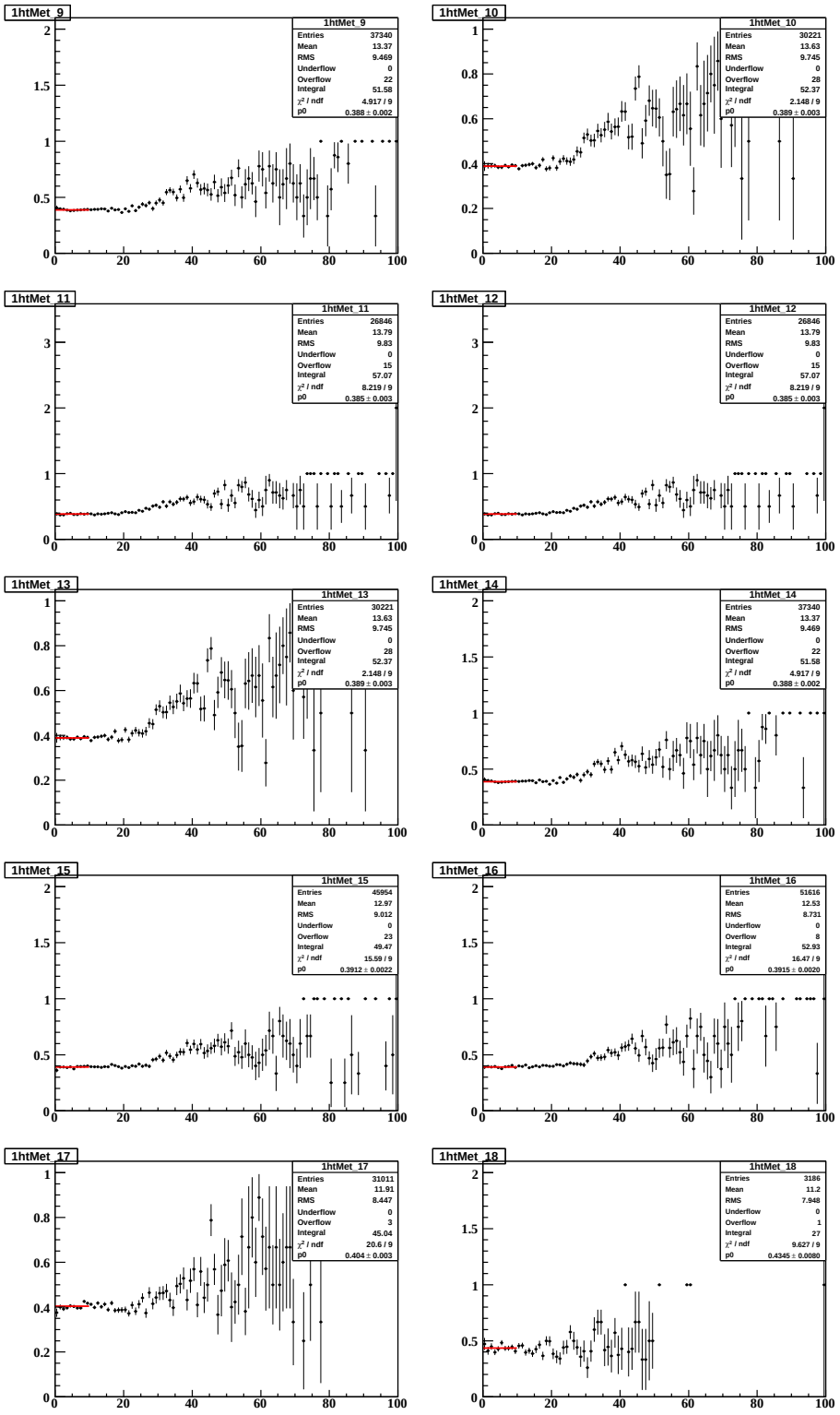

Figure 13.5: Ratios of loose and tight MET plots fitted with a const. line. Type 1.

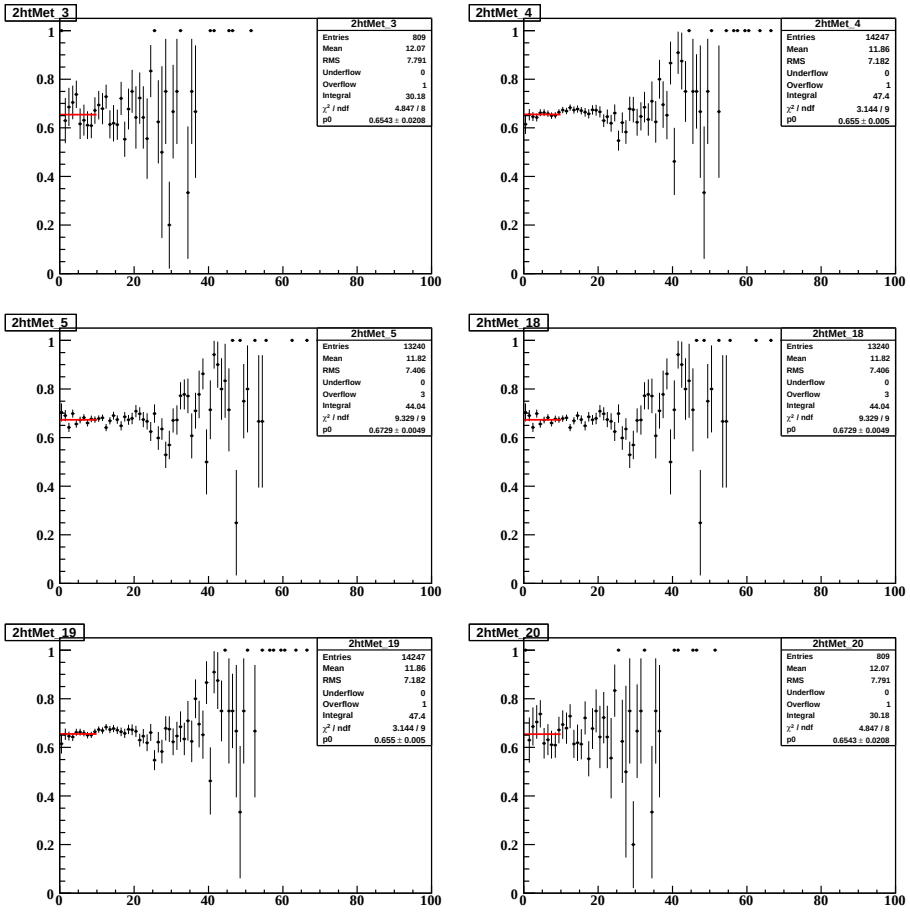

Figure 13.6: Ratios of loose and tight MET plots fitted with a const. line. Type 2.

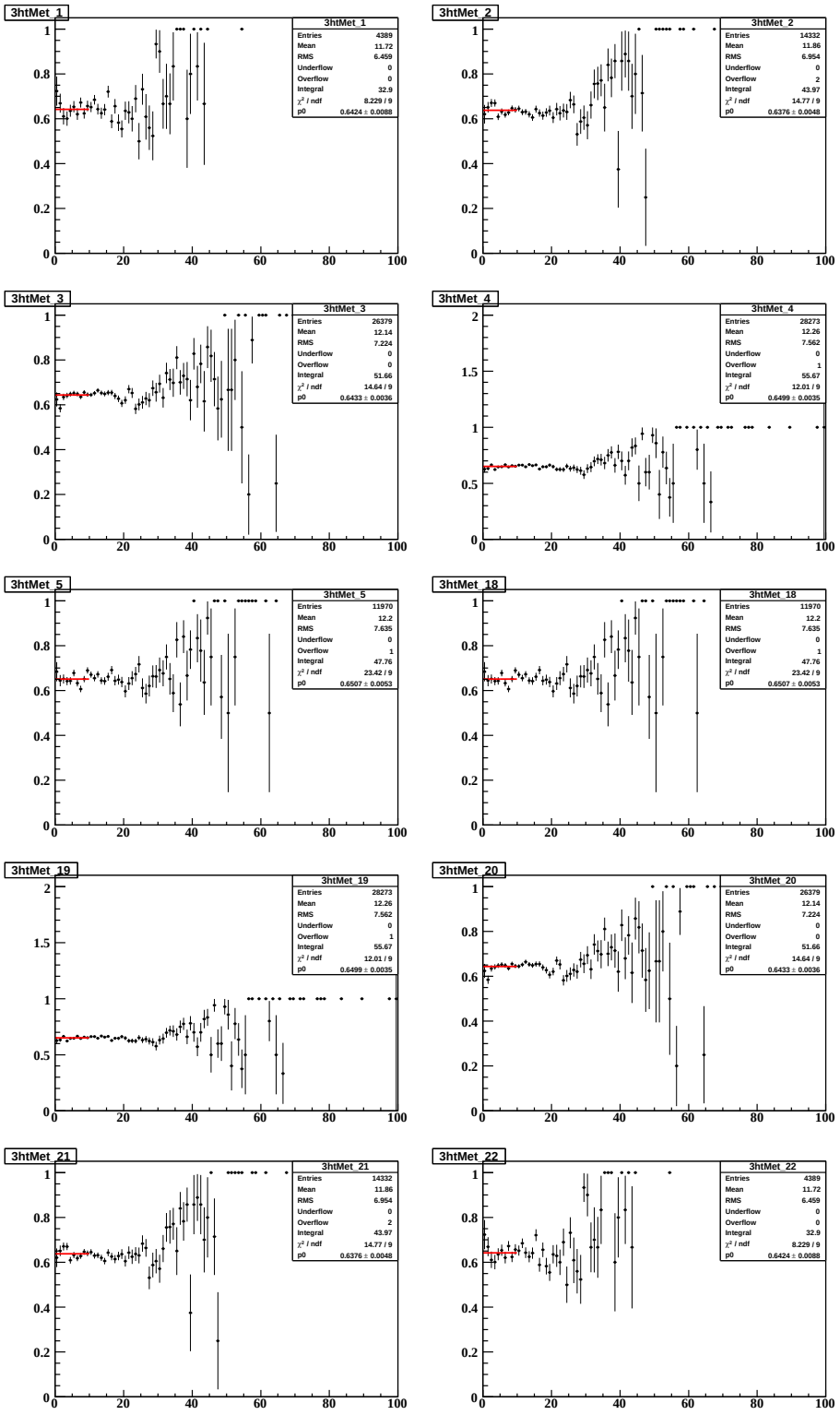

Figure 13.7: Ratios of loose and tight MET plots fitted with a const. line. Type 3.

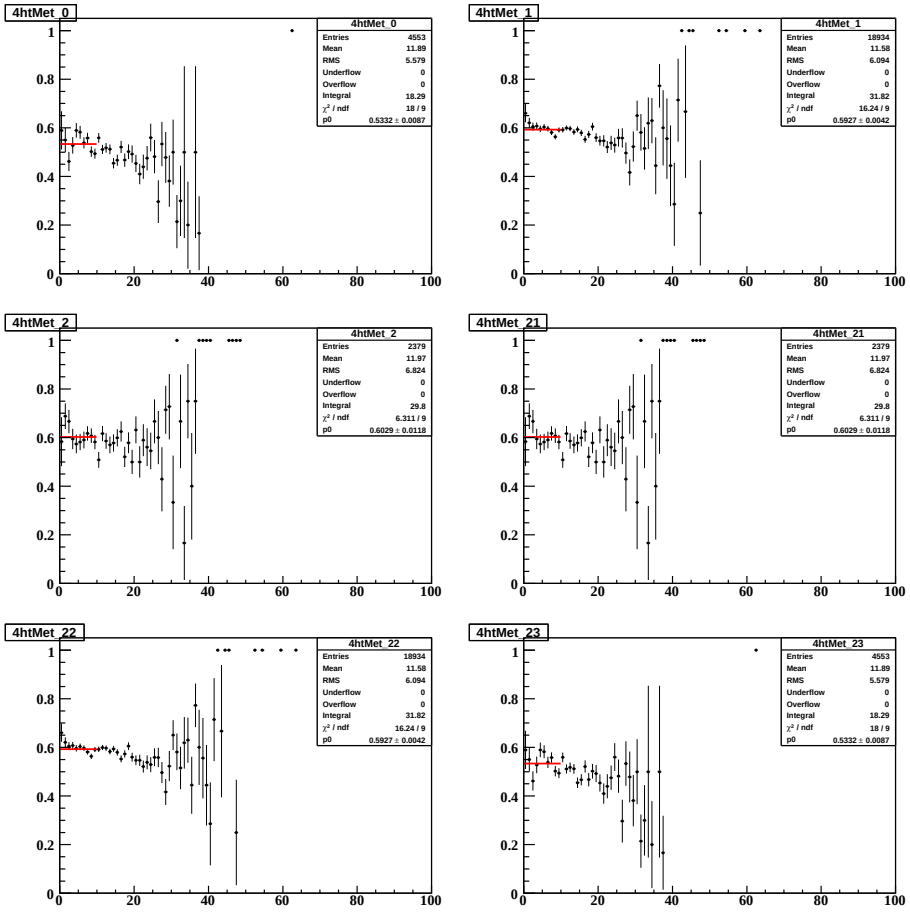

Figure 13.8: Ratios of loose and tight MET plots fitted with a const. line. Type 4.

Appendix C

Plots and tables for two E_T bins

C.1 $E_T < 35$ GeV

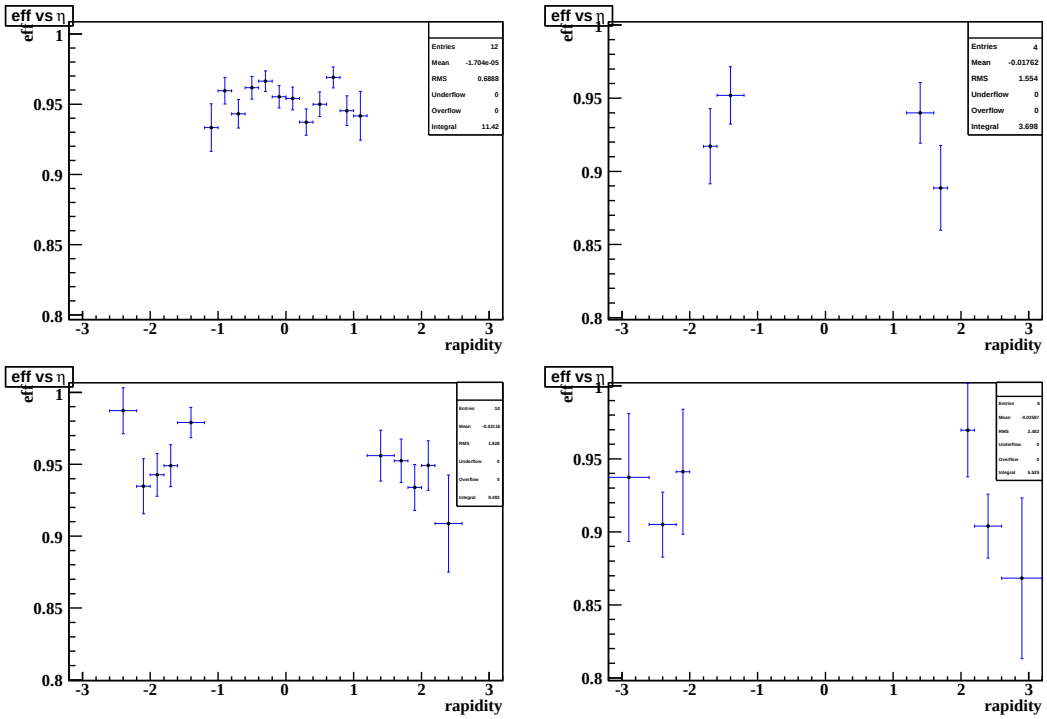

Figure 13.9: Efficiency for a real electron that passes the loose electron cuts to also pass the tight electron cuts as a function of electron rapidity for all four electron types. Top left: type 1, top right: type 2, bottom left: type 3, bottom right: type 4. Loose electron is required to have HMx7< 50 in CC and HMx8< 75 in EC, while tight electron is required to have HMx7< 10 in CC and HMx8< 10 in EC. $E_T < 35$ GeV

bin	Signal Efficiency	Stat. uncertainty	Syst. Uncertainty	Total Uncert.
6	0.933	0.017	0.0025	0.017
7	0.96	0.0091	0.0025	0.0094
8	0.943	0.0098	0.0025	0.01
9	0.962	0.0077	0.0025	0.0081
10	0.966	0.0068	0.0025	0.0072
11	0.955	0.0076	0.0025	0.008
12	0.954	0.0077	0.0025	0.0081
13	0.937	0.0091	0.0025	0.0094
14	0.95	0.0084	0.0025	0.0088
15	0.969	0.0071	0.0025	0.0075
16	0.945	0.01	0.0025	0.011
17	0.942	0.017	0.0025	0.017

Table 13.1: Detailed values of Signal Efficiencies and Uncertainties for type 1 Electrons with $25 < E_T < 35$ GeV

bin	Signal Efficiency	Stat. uncertainty	Syst. Uncertainty	Total Uncert.
4	0.917	0.024	0.01	0.026
5	0.952	0.019	0.0025	0.02
18	0.94	0.021	0.0025	0.021
19	0.889	0.027	0.01	0.029

Table 13.2: Detailed values of Signal Efficiencies and Uncertainties for type 2 Electrons with $25 < E_T < 35$ GeV.

bin	Signal Efficiency	Stat. uncertainty	Syst. Uncertainty	Total Uncert.
1	0.987	0.012	0.01	0.016
2	0.935	0.016	0.01	0.019
3	0.943	0.011	0.01	0.015
4	0.949	0.011	0.01	0.015
5	0.979	0.01	0.0025	0.011
18	0.956	0.018	0.0025	0.018
19	0.952	0.011	0.01	0.015
20	0.934	0.012	0.01	0.016
21	0.949	0.014	0.01	0.017
22	0.909	0.032	0.01	0.034

Table 13.3: Detailed values of Signal Efficiencies and Uncertainties for type 3 Electrons with $25 < E_T < 35$ GeV.

bin	Signal Efficiency	Stat. uncertainty	Syst. Uncertainty	Total Uncert.
0	0.937	0.043	0.01	0.044
1	0.905	0.02	0.01	0.022
2	0.941	0.042	0.01	0.043
21	0.97	0.03	0.01	0.032
22	0.904	0.019	0.01	0.022
23	0.868	0.054	0.01	0.055

Table 13.4: Detailed values of Signal Efficiencies and Uncertainties for type 4 Electrons with $25 < E_T < 35$ GeV.

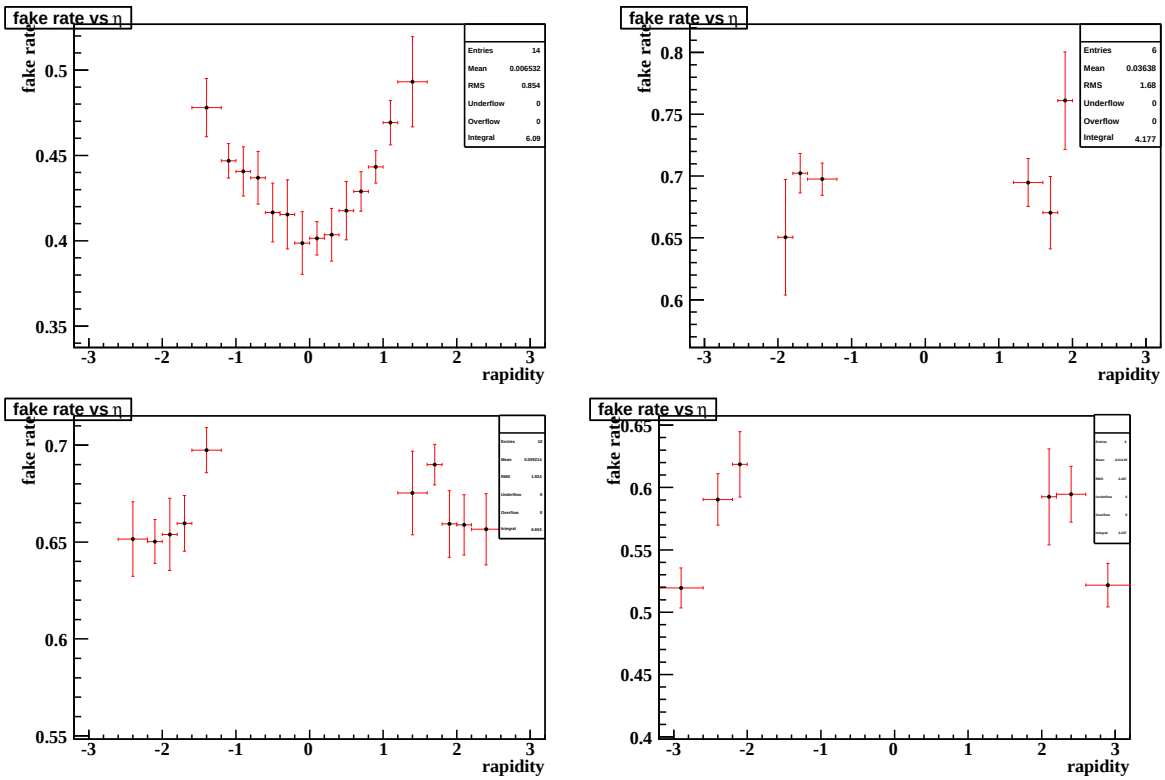

Figure 13.10: EM-like jet ID probability (fake rate) for a real jet that already passes the loose electron cuts to also pass the tight electron cuts as a function of electron rapidity for all four types. Top left: type 1, top right: type 2, bottom left: type 3, bottom right: type 4. Loose electron is required to have HMx7< 50 in CC and HMx8< 75 in EC, while tight electron is required to have HMx7< 10 in CC and HMx8< 10 in EC.E_T < 35 GeV

bin	EM-like jet ID prob.	Stat. Uncert.	Syst. Uncert.	Total Uncert.
5	0.478	0.017	0.0078	0.018
6	0.447	0.0058	0.0083	0.01
7	0.441	0.0048	0.014	0.014
8	0.437	0.0052	0.015	0.015
9	0.417	0.0057	0.016	0.017
10	0.415	0.0064	0.019	0.02
11	0.399	0.0067	0.017	0.018
12	0.401	0.0067	0.0071	0.0098
13	0.404	0.0064	0.014	0.015
14	0.418	0.0058	0.016	0.017
15	0.429	0.0052	0.01	0.012
16	0.443	0.0049	0.0081	0.0095
17	0.469	0.0065	0.011	0.013

Table 13.5: Detailed values of EM-like jet ID probabilities and uncertainties for type 1 electron-like jets with $25 < E_T < 35$ GeV.

bin	EM-like jet ID prob.	Stat. Uncert.	Syst. Uncert.	Total Uncert.
4	0.702	0.0097	0.013	0.016
5	0.698	0.011	0.0074	0.013
18	0.695	0.0096	0.017	0.019
19	0.67	0.011	0.027	0.029

Table 13.6: Detailed values of EM-like jet ID probabilities and uncertainties for type 2 electron-like jets with $25 < E_T < 35$ GeV.

bin	EM-like jet ID prob.	Stat. Uncert.	Syst. Uncert.	Total Uncert.
1	0.652	0.019	0.0049	0.019
2	0.65	0.01	0.0052	0.011
3	0.654	0.0075	0.017	0.019
4	0.66	0.0072	0.012	0.014
5	0.697	0.01	0.0055	0.012
18	0.675	0.012	0.018	0.022
19	0.69	0.0077	0.0071	0.01
20	0.659	0.008	0.015	0.017
21	0.659	0.011	0.011	0.016
22	0.657	0.018	0.0045	0.018

Table 13.7: Detailed values of EM-like jet ID probabilities and uncertainties for type 3 electron-like jets with $25 < E_T < 35$ GeV.

bin	EM-like jet ID prob.	Stat. Uncert.	Syst. Uncert.	Total Uncert.
0	0.52	0.016	0.0016	0.016
1	0.59	0.0086	0.019	0.021
2	0.619	0.025	0.0083	0.026
21	0.593	0.029	0.025	0.038
22	0.595	0.0088	0.021	0.022
23	0.522	0.015	0.0088	0.017

Table 13.8: Detailed values of EM-like jet ID probabilities and uncertainties for type 4 electron-like jets with $25 < E_T < 35$ GeV.

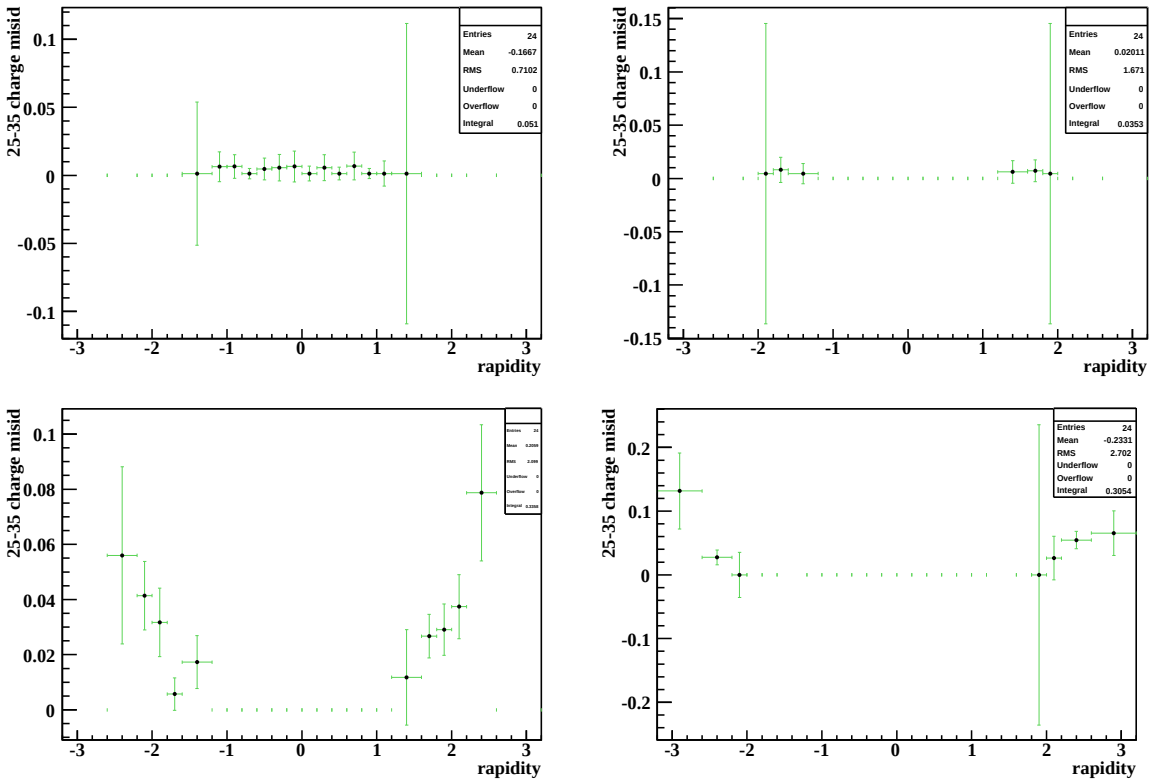

Figure 13.11: Charge mis-identification rate as a function of electron rapidity for all four electron types. Top left: type 1, top right: type 2, bottom left: type 3, bottom right: type 4.$E_T < 35$ GeV

Bin	Charge Misid. Rate	Stat. uncert.	Sys. Uncert.	Total Uncert.
5	0.00133664	0.0525503	0.00133664	0.0525673
6	0.00632911	0.0087561	0.00645697	0.0108794
7	0.00649351	0.00555121	0.00658308	0.00861121
8	0.00133664	0.00353355	0.00133664	0.00377791
9	0.00456621	0.00635577	0.00489831	0.00802429
10	0.00561798	0.00779136	0.00573683	0.00967556
11	0.00645161	0.0089218	0.0069689	0.011321
12	0.00133664	0.00520826	0.00133664	0.00537704
13	0.00555556	0.00770645	0.00553204	0.00948646
14	0.00133664	0.00380225	0.00271739	0.00467347
15	0.00680272	0.00581199	0.00843652	0.0102447
16	0.00133664	0.00344826	0.00133664	0.00369826
17	0.00133664	0.00704208	0.00584795	0.00915366
18	0.00133664	0.11024	0.00133664	0.110248

Table 13.9: Detailed Values of charge misidentification and uncertainties for Type 1 Electrons with $25 < E_T < 35$ GeV. These are the charge misidentification rates with the previously mentioned quality cuts applied.

Bin	Charge Misid. Rate	Stat. uncert.	Sys. Uncert.	Total Uncert.
3	0.00455259	0.140859	0.00455259	0.140933
4	0.00813008	0.0111782	0.00391481	0.0118439
5	0.00455259	0.00840306	0.00455259	0.00955707
18	0.00617284	0.0085445	0.00621335	0.0105648
19	0.00719424	0.00992337	0.00274934	0.0102972
20	0.00455259	0.140859	0.00455259	0.140933

Table 13.10: Detailed Values of charge misidentification and uncertainties for Type 2 Electrons with $25 < E_T < 35$ GeV. These are the charge misidentification rates with the previously mentioned quality cuts applied.

Bin	Charge Misid. Rate	Stat. uncert.	Sys. Uncert.	Total Uncert.
1	0.0560748	0.0233736	0.0220637	0.0321424
2	0.0414013	0.0115572	0.00451623	0.0124083
3	0.0317164	0.00774571	0.00963709	0.012364
4	0.00570342	0.00376993	0.00448249	0.00585706
5	0.017316	0.00947302	0.00163887	0.00961374
18	0.0117647	0.00995297	0.0141932	0.0173352
19	0.0266667	0.00785265	0.000810048	0.00789432
20	0.0290698	0.00759449	0.00540635	0.00932228
21	0.0373563	0.0104595	0.00511976	0.0116453
22	0.0787402	0.0244949	0.00347551	0.0247402

Table 13.11: Detailed Values of charge misidentification and uncertainties for Type 3 Electrons with $25 < E_T < 35$ GeV. These are the charge misidentification rates with the previously mentioned quality cuts applied.

Bin	Charge Misid. Rate	Stat. uncert.	Sys. Uncert.	Total Uncert.
0	0.131579	0.0557652	0.021431	0.0597415
1	0.0274914	0.0100633	0.00570151	0.0115662
21	0.0263158	0.0340373	0.00442783	0.0343241
22	0.0546075	0.013545	0.00277234	0.0138258
23	0.0655738	0.0337885	0.00875407	0.0349041

Table 13.12: Detailed Values of charge misidentification and uncertainties for Type 4 Electrons with $25 < E_T < 35$ GeV. These are the charge misidentification rates with the previously mentioned quality cuts applied.

bin	$N^{tight}_{Z\to ee^+}$	$N^{tight}_{Z\to ee^-}$	$N^{nottight}_{Z\to ee}$	$N^{tight}_{W\to \tau\nu^+}$	$N^{tight}_{W\to \tau\nu^-}$	$N^{nottight}_{W\to \tau\nu}$
6	24.204	19.579	0.82663	56.289	120.16	21.4
7	41.213	42.047	3.0771	159.47	269.69	44.8
8	52.429	48.133	5.1905	301.49	366.57	24.8
9	63.591	60.145	4.9391	319.45	260.22	46.8
10	59.399	64.265	5.1459	339.73	337.26	42.2
11	57.816	57.522	3.1152	292.45	293.19	25.8
12	55.505	49.941	4.7717	263.28	290.55	35.2
13	57.205	60.803	4.0617	344.61	346.11	63
14	55.179	56.522	4.2844	339.5	255.76	42.9
15	58.56	58.134	4.0646	317.58	290.76	31.6
16	38.753	37.831	2.4905	248.03	198	34.8
17	15.289	15.951	1.7248	96.688	89.843	10.9

Table 13.13: Type 1 (CC, full CFT) bin number, the number of $Z \to ee$ background events with positive charge that pass the tight cut, the number of $Z \to ee$ background event with negative charge that passes the tight cut, the number of $Z \to ee$ background events that pass the loose cut, but fail the tight cut, the number of $W \to \tau\nu$ background events with positive charge that pass the tight cut, the number of $W \to \tau\nu$ background event with negative charge that passes the tight cut, the number of $W \to \tau\nu$ background events that pass the loose cut, but fail the tight cut. $25 < E_T < 35$ GeV.

bin	$N^{tight}_{Z\to ee^+}$	$N^{tight}_{Z\to ee^-}$	$N^{nottight}_{Z\to ee}$	$N^{tight}_{W\to \tau\nu^+}$	$N^{tight}_{W\to \tau\nu^-}$	$N^{nottight}_{W\to \tau\nu}$
4	8.8982	8.1535	0.64804	20.826	59.388	0
5	5.3525	5.0591	0.58829	22.478	18.976	9.34
18	6.9931	7.7797	0.77316	54.085	43.607	3.03
19	7.5929	10.33	0.56073	56.218	43.437	8.53

Table 13.14: Type 2 (EC, full CFT) bin number, the number of $Z \to ee$ background events with positive charge that pass the tight cut, the number of $Z \to ee$ background event with negative charge that passes the tight cut, the number of $Z \to ee$ background events that pass the loose cut, but fail the tight cut, the number of $W \to \tau\nu$ background events with positive charge that pass the tight cut, the number of $W \to \tau\nu$ background event with negative charge that passes the tight cut, the number of $W \to \tau\nu$ background events that pass the loose cut, but fail the tight cut. $25 < E_T < 35$ GeV.

bin	$N^{tight}_{Z\to ee^+}$	$N^{tight}_{Z\to ee^-}$	$N^{nottight}_{Z\to ee}$	$N^{tight}_{W\to\tau\nu^+}$	$N^{tight}_{W\to\tau\nu^-}$	$N^{nottight}_{W\to\tau\nu}$
1	5.2496	5.596	0.81787	22.096	20.162	0
2	14.955	16.366	1.1771	86.286	24.144	5.11
3	23.745	22.975	1.6974	93.367	111.51	8.43
4	19.487	19.002	2.0947	102.62	106.96	11.8
5	10.557	10.685	1.2325	44.55	51.369	0
18	9.988	11.393	0.85637	57.196	50.197	16.8
19	26.459	25.617	1.2668	118.29	126.41	0
20	27.659	27.826	3.454	149.03	98.77	11.7
21	12.765	13.844	1.5985	74.301	55.41	0
22	5.5957	5.3661	0.57184	22.353	10.871	0

Table 13.15: Type 3 (EC, partial CFT) bin number, the number of $Z \to ee$ background events with positive charge that pass the tight cut, the number of $Z \to ee$ background event with negative charge that passes the tight cut, the number of $Z \to ee$ background events that pass the loose cut, but fail the tight cut, the number of $W \to \tau\nu$ background events with positive charge that pass the tight cut, the number of $W \to \tau\nu$ background event with negative charge that passes the tight cut, the number of $W \to \tau\nu$ background events that pass the loose cut, but fail the tight cut. $25 < E_T < 35$ GeV.

bin	$N^{tight}_{Z\to ee^+}$	$N^{tight}_{Z\to ee^-}$	$N^{nottight}_{Z\to ee}$	$N^{tight}_{W\to\tau\nu^+}$	$N^{tight}_{W\to\tau\nu^-}$	$N^{nottight}_{W\to\tau\nu}$
0	1.8158	1.6767	0.55744	1.4688	4.2628	0.777
1	25.817	25.261	4.3664	55.638	78.17	26.1
2	3.0283	4.5934	0.20469	10.11	4.0654	4.92
21	4.8147	3.7609	0.68995	10.561	23.958	0
22	27.547	28.046	4.3581	111.35	62.958	14.5
23	2.8282	3.1014	1.0091	4.2559	0	1.06

Table 13.16: Type 4 (EC, no CFT) bin number, the number of $Z \to ee$ background events with positive charge that pass the tight cut, the number of $Z \to ee$ background event with negative charge that passes the tight cut, the number of $Z \to ee$ background events that pass the loose cut, but fail the tight cut, the number of $W \to \tau\nu$ background events with positive charge that pass the tight cut, the number of $W \to \tau\nu$ background event with negative charge that passes the tight cut, the number of $W \to \tau\nu$ background events that pass the loose cut, but fail the tight cut. $25 < E_T < 35$ GeV.

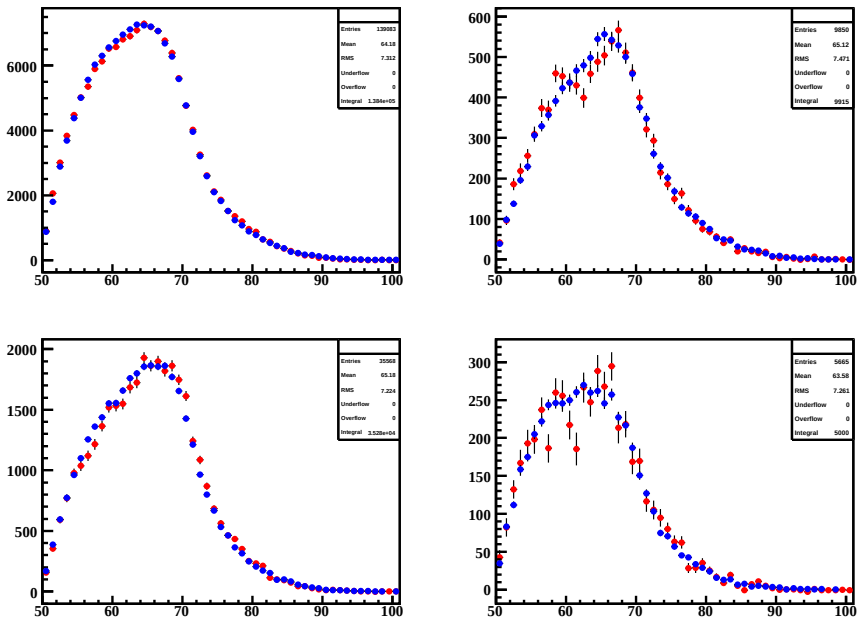

Figure 13.12: Data/MC transverse mass comparison plots for each type. Top left: type 1; top right: type 2; bottom left: type 3; bottom right: type 4. Red for data, blue for MC. $E_T <$ 35 GeV

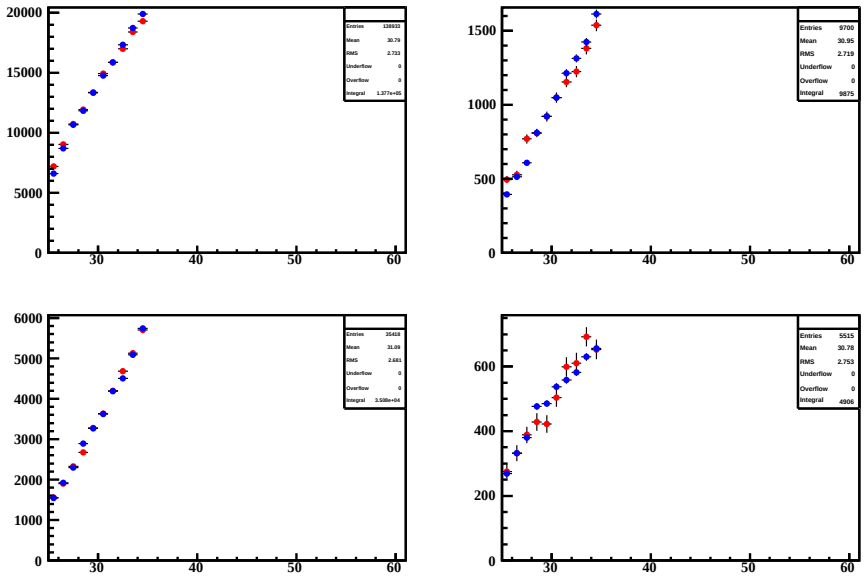

Figure 13.13: Data/MC electron E_T comparison plots for each type. Top left: type 1; top right: type 2; bottom left: type 3; bottom right: type 4. Red for data, blue for MC. $E_T < 35$ GeV

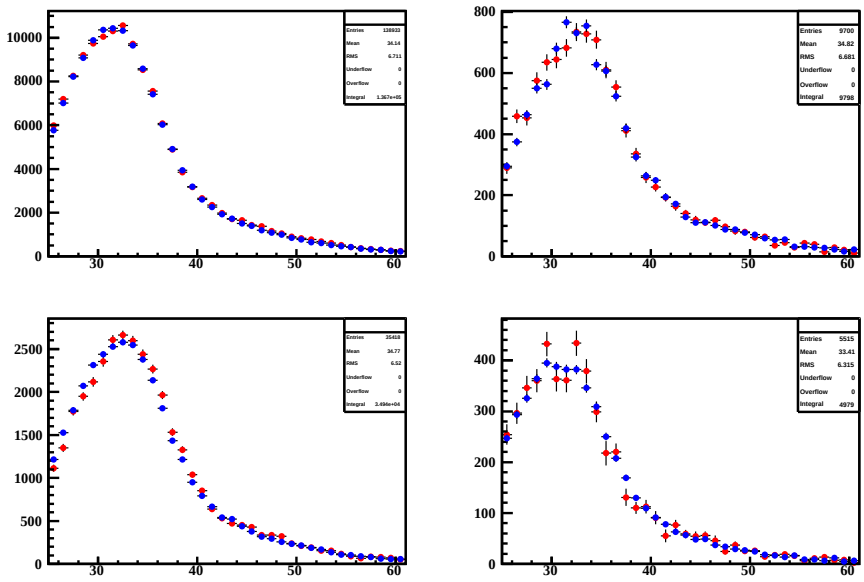

Figure 13.14: Data/MC $\not\!\!E_T$ comparison plots for each type. Top left: type 1; top right: type 2; bottom left: type 3; bottom right: type 4. Red for data, blue for MC. $E_T < 35$ GeV

C.2 $E_T > 35$ GeV

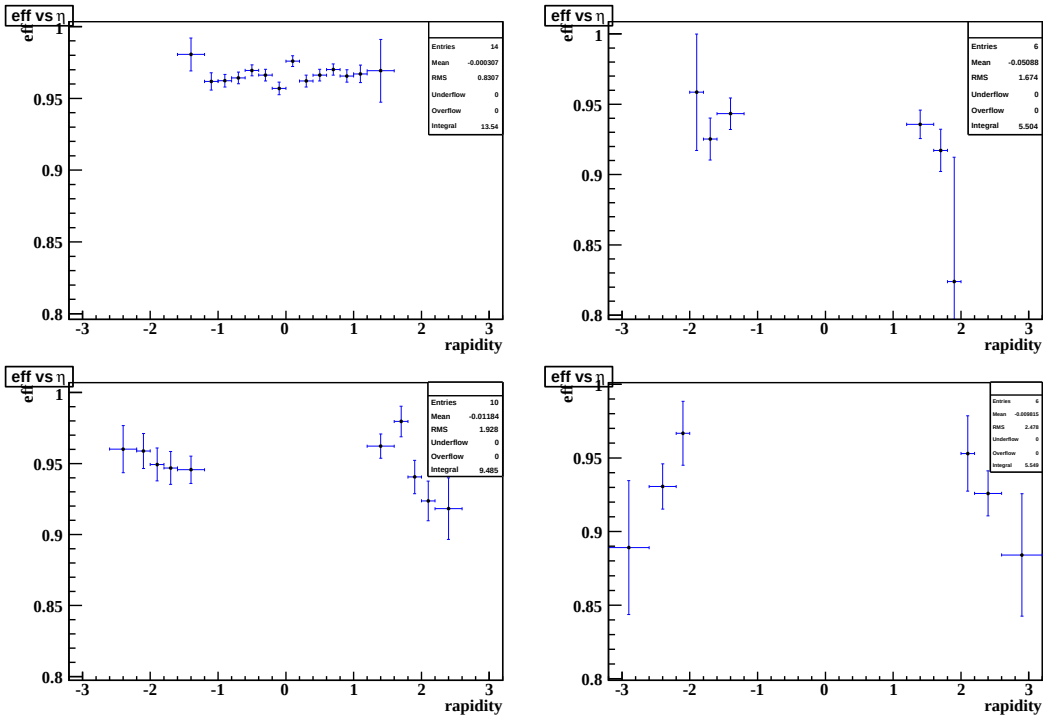

Figure 13.15: Efficiency for a real electron that passes the loose electron cuts to also pass the tight electron cuts as a function of electron rapidity for all four electron types. Top left: type 1, top right: type 2, bottom left: type 3, bottom right: type 4. Loose electron is required to have HMx7< 50 in CC and HMx8< 75 in EC, while tight electron is required to have HMx7< 10 in CC and HMx8< 10 in EC. $E_T > 35$ GeV

bin	Signal Efficiency	Stat. uncertainty	Syst. Uncertainty	Total Uncert.
5	0.981	0.011	0.0025	0.011
6	0.962	0.0055	0.0025	0.0061
7	0.962	0.0036	0.0025	0.0044
8	0.964	0.0032	0.0025	0.0041
9	0.969	0.003	0.0025	0.0039
10	0.966	0.0032	0.0025	0.004
11	0.957	0.0036	0.0025	0.0044
12	0.976	0.0027	0.0025	0.0037
13	0.962	0.0033	0.0025	0.0041
14	0.966	0.0031	0.0025	0.004
15	0.97	0.003	0.0025	0.0039
16	0.966	0.0035	0.0025	0.0043
17	0.967	0.0056	0.0025	0.0061
18	0.969	0.022	0.0025	0.022

Table 13.17: Detailed values of Signal Efficiencies and Uncertainties for type 1 electrons with $E_T > 35$ GeV.

bin	Signal Efficiency	Stat. uncertainty	Syst. Uncertainty	Total Uncert.
3	0.959	0.04	0.01	0.041
4	0.925	0.011	0.01	0.015
5	0.943	0.011	0.0025	0.011
18	0.936	0.0098	0.0025	0.01
19	0.917	0.011	0.01	0.015
20	0.824	0.088	0.01	0.088

Table 13.18: Detailed values of Signal Efficiencies and Uncertainties for type 2 electrons with $E_T > 35$ GeV.

bin	Signal Efficiency	Stat. uncertainty	Syst. Uncertainty	Total Uncert.
1	0.96	0.013	0.01	0.017
2	0.959	0.0073	0.01	0.012
3	0.949	0.0057	0.01	0.012
4	0.947	0.006	0.01	0.012
5	0.946	0.0093	0.0025	0.0096
18	0.962	0.0082	0.0025	0.0085
19	0.98	0.0039	0.01	0.011
20	0.941	0.0062	0.01	0.012
21	0.924	0.0098	0.01	0.014
22	0.918	0.019	0.01	0.022

Table 13.19: Detailed values of Signal Efficiencies and Uncertainties for type 3 electrons with $E_T > 35$ GeV.

bin	Signal Efficiency	Stat. uncertainty	Syst. Uncertainty	Total Uncert.
0	0.889	0.044	0.01	0.045
1	0.931	0.012	0.01	0.015
2	0.967	0.019	0.01	0.022
21	0.953	0.024	0.01	0.026
22	0.926	0.012	0.01	0.015
23	0.884	0.04	0.01	0.042

Table 13.20: Detailed values of Signal Efficiencies and Uncertainties for type 4 electrons with $E_T > 35$ GeV.

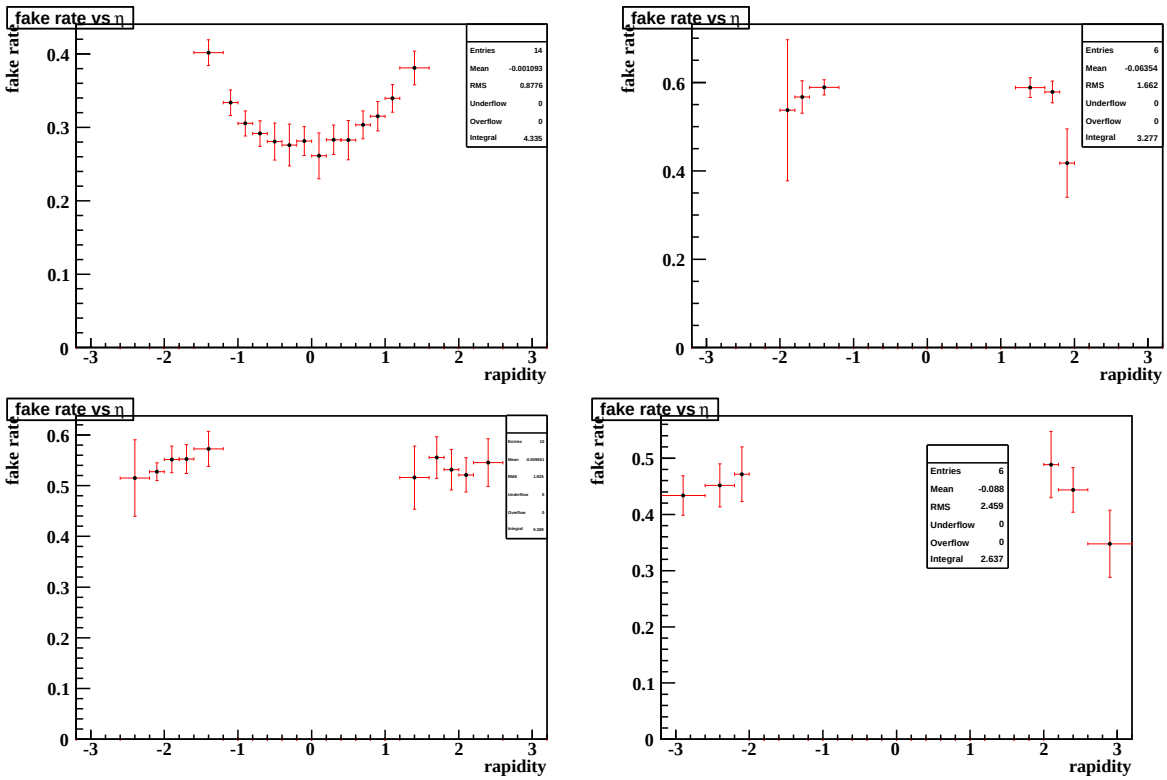

Figure 13.16: EM-like jet ID probability (fake rate) for a real jet that already passes the loose electron cuts to also pass the tight electron cuts as a function of electron rapidity for all four types. Top left: type 1, top right: type 2, bottom left: type 3, bottom right: type 4. Loose electron is required to have HMx7< 50 in CC and HMx8< 75 in EC, while tight electron is required to have HMx7< 10 in CC and HMx8< 10 in EC.$E_T > 35$ GeV

bin	EM-like jet ID prob.	Stat. Uncert.	Syst. Uncert.	Total Uncert.
5	0.402	0.016	0.0069	0.018
6	0.334	0.0056	0.017	0.017
7	0.305	0.0045	0.017	0.017
8	0.291	0.0052	0.017	0.017
9	0.281	0.0058	0.025	0.025
10	0.276	0.0066	0.028	0.028
11	0.281	0.0072	0.018	0.02
12	0.261	0.0072	0.03	0.031
13	0.283	0.0067	0.019	0.02
14	0.283	0.006	0.026	0.027
15	0.303	0.0053	0.018	0.019
16	0.315	0.0049	0.019	0.02
17	0.339	0.0063	0.018	0.019
18	0.381	0.023	0.0034	0.023

Table 13.21: Detailed values of EM-like jet ID probabilities and uncertainties for type 1 electron-like jets with $E_T > 35$ GeV.

bin	EM-like jet ID prob.	Stat. Uncert.	Syst. Uncert.	Total Uncert.
3	0.537	0.077	0.14	0.16
4	0.567	0.015	0.033	0.037
5	0.589	0.017	0.00033	0.017
18	0.588	0.016	0.015	0.022
19	0.579	0.016	0.019	0.025
20	0.418	0.077	0.01	0.077

Table 13.22: Detailed values of EM-like jet ID probabilities and uncertainties for type 2 electron-like jets with $E_T > 35$ GeV.

bin	EM-like jet ID prob.	Stat. Uncert.	Syst. Uncert.	Total Uncert.
1	0.515	0.032	0.068	0.075
2	0.527	0.017	0.0026	0.017
3	0.552	0.012	0.023	0.026
4	0.553	0.011	0.026	0.029
5	0.573	0.016	0.031	0.034
18	0.516	0.018	0.059	0.062
19	0.556	0.012	0.039	0.041
20	0.532	0.013	0.038	0.04
21	0.521	0.018	0.029	0.034
22	0.545	0.033	0.034	0.047

Table 13.23: Detailed values of EM-like jet ID probabilities and uncertainties for type 3 electron-like jets with $E_T > 35$ GeV.

bin	EM-like jet ID prob.	Stat. Uncert.	Syst. Uncert.	Total Uncert.
0	0.434	0.035	0.001	0.035
1	0.452	0.015	0.035	0.038
2	0.471	0.037	0.032	0.049
21	0.489	0.047	0.035	0.059
22	0.444	0.015	0.037	0.04
23	0.348	0.028	0.053	0.06

Table 13.24: Detailed values of EM-like jet ID probabilities and uncertainties for type 4 electron-like jets with $E_T > 35$ GeV.

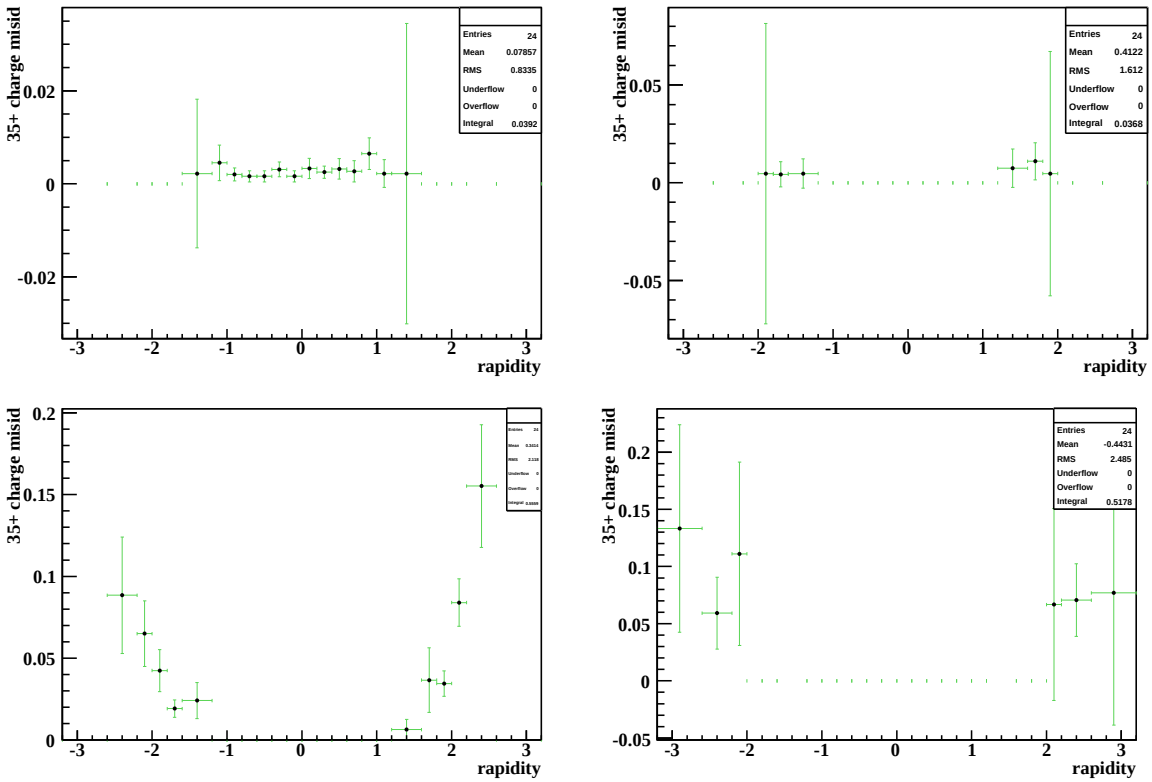

Figure 13.17: Charge mis-identification rate as a function of electron rapidity for all four electron types. Top left: type 1, top right: type 2, bottom left: type 3, bottom right: type 4.$E_T > 35$ GeV

Bin	Charge Misid. Rate	Stat. uncert.	Sys. Uncert.	Total Uncert.
5	0.00221094	0.015871	0.00221094	0.0160243
6	0.00453172	0.0030007	0.00232078	0.00379344
7	0.00203528	0.00135272	0.000175663	0.00136408
8	0.00161117	0.00107152	0.000599773	0.00122796
9	0.00155602	0.00103493	0.000654923	0.00122475
10	0.00309598	0.00136098	0.000885037	0.00162344
11	0.00161031	0.00107095	0.000600633	0.00122788
12	0.00334821	0.00147149	0.00162585	0.00219287
13	0.00252143	0.00123182	0.000310487	0.00127035
14	0.00318302	0.00139912	0.00163906	0.00215501
15	0.00273523	0.00133596	0.00183689	0.00227133
16	0.0065312	0.00228236	0.00250122	0.00338604
17	0.00221094	0.00195312	0.00221094	0.00295008
18	0.00221094	0.0322401	0.00221094	0.0323158

Table 13.25: Detailed Values of charge misidentification and uncertainties for Type 1 Electrons with $E_T > 35$ GeV. These are the charge misidentification rates with the previously mentioned quality cuts applied.

Bin	Charge Misid. Rate	Stat. uncert.	Sys. Uncert.	Total Uncert.
3	0.00468119	0.0766555	0.00468119	0.0767983
4	0.00425532	0.00592942	0.00247102	0.0064237
5	0.00468119	0.00584785	0.00468119	0.00749072
18	0.00740741	0.00632101	0.00742667	0.00975247
19	0.0109091	0.00715499	0.00622791	0.00948582
20	0.00468119	0.062361	0.00468119	0.0625365

Table 13.26: Detailed Values of charge misidentification and uncertainties for Type 2 Electrons with $E_T > 35$ GeV. These are the charge misidentification rates with the previously mentioned quality cuts applied.

Bin	Charge Misid. Rate	Stat. uncert.	Sys. Uncert.	Total Uncert.
1	0.0884956	0.0273078	0.0228938	0.0356348
2	0.0653266	0.0125286	0.0153116	0.0197841
3	0.0424403	0.00742602	0.0104001	0.0127792
4	0.0192077	0.0048844	0.00205686	0.00529982
5	0.0240964	0.00884696	0.00641633	0.0109288
18	0.00638978	0.00546366	0.00282157	0.00614921
19	0.0366492	0.00689137	0.0184716	0.0197152
20	0.0345253	0.00650062	0.00425831	0.00777118
21	0.0839506	0.0138797	0.00414888	0.0144865
22	0.155172	0.033693	0.0163989	0.0374719

Table 13.27: Detailed Values of charge misidentification and uncertainties for Type 3 Electrons with $E_T > 35$ GeV. These are the charge misidentification rates with the previously mentioned quality cuts applied.

Bin	Charge Misid. Rate	Stat. uncert.	Sys. Uncert.	Total Uncert.
0	0.133333	0.0898544	0.0126549	0.0907412
1	0.0592105	0.0197922	0.024313	0.0313505
2	0.111111	0.0541285	0.0591007	0.0801423
21	0.0666667	0.0507403	0.0667968	0.0838832
22	0.0705882	0.0200964	0.0246445	0.0317997
23	0.0769231	0.0849837	0.0782636	0.115531

Table 13.28: Detailed Values of charge misidentification and uncertainties for Type 4 Electrons with $E_T > 35$ GeV. These are the charge misidentification rates with the previously mentioned quality cuts applied.

bin	$N^{tight}_{Z\to ee^+}$	$N^{tight}_{Z\to ee^-}$	$N^{nottight}_{Z\to ee}$	$N^{tight}_{W\to\tau\nu^+}$	$N^{tight}_{W\to\tau\nu^-}$	$N^{nottight}_{W\to\tau\nu}$
5	5.4696	6.5216	0.20681	0	0	0
6	72.384	67.381	3.2702	29.756	47.452	0
7	134.59	141.52	7.6837	69.535	91.195	5.4
8	170.33	161.28	7.2253	93.258	93.237	16.5
9	168.54	179.5	8.9804	81.822	38.106	0
10	178.11	186.84	10.105	66.024	44.072	16.3
11	173.37	166.81	11.158	50.037	78.164	0
12	153.47	167.6	9.0512	62.687	62.487	10.4
13	174.09	173.44	9.3717	71.162	27.42	11
14	173.23	174.52	7.7693	66.502	66.78	16.6
15	170.55	172.53	9.7666	85.43	51.323	17.2
16	118.61	119.44	5.6447	79.122	47.338	5.27
17	48.031	50.506	2.4243	5.5551	33.356	5.55
18	2.3252	2.7321	0.096133	0	4.7244	0

Table 13.29: Type 1 (CC, full CFT) bin number, the number of $Z \to ee$ background events with positive charge that pass the tight cut, the number of $Z \to ee$ background event with negative charge that passes the tight cut, the number of $Z \to ee$ background events that pass the loose cut, but fail the tight cut, the number of $W \to \tau\nu$ background events with positive charge that pass the tight cut, the number of $W \to \tau\nu$ background event with negative charge that passes the tight cut, the number of $W \to \tau\nu$ background events that pass the loose cut, but fail the tight cut. $E_T > 35$ GeV.

bin	$N^{tight}_{Z\to ee^+}$	$N^{tight}_{Z\to ee^-}$	$N^{nottight}_{Z\to ee}$	$N^{tight}_{W\to\tau\nu^+}$	$N^{tight}_{W\to\tau\nu^-}$	$N^{nottight}_{W\to\tau\nu}$
3	1.8019	1.4743	0.10517	0	0	0
4	26.894	28.332	1.6944	19.939	5.0289	4.95
5	21.78	21.587	2.7944	20.114	10.021	0
18	27.867	26.891	1.8609	4.752	18.968	0
19	24.697	26.231	1.6992	15.414	0	0
20	1.3333	1.5648	0.12137	0	0	0

Table 13.30: Type 2 (EC, full CFT) bin number, the number of $Z \to ee$ background events with positive charge that pass the tight cut, the number of $Z \to ee$ background event with negative charge that passes the tight cut, the number of $Z \to ee$ background events that pass the loose cut, but fail the tight cut, the number of $W \to \tau\nu$ background events with positive charge that pass the tight cut, the number of $W \to \tau\nu$ background event with negative charge that passes the tight cut, the number of $W \to \tau\nu$ background events that pass the loose cut, but fail the tight cut. $E_T > 35$ GeV.

bin	$N^{tight}_{Z\to ee^+}$	$N^{tight}_{Z\to ee^-}$	$N^{nottight}_{Z\to ee}$	$N^{tight}_{W\to\tau\nu^+}$	$N^{tight}_{W\to\tau\nu^-}$	$N^{nottight}_{W\to\tau\nu}$
1	11.099	11.084	1.1905	5.7105	5.7856	0
2	36.192	38.689	1.9186	5.3005	21.37	0
3	72.958	67.172	4.8661	15.312	20.541	0
4	69.086	65.071	5.2829	19.867	14.966	0
5	37.351	33.688	1.9725	20.069	30.033	0
18	33.781	32.604	1.9546	4.752	14.035	0
19	71.379	67.656	4.3875	15.176	25.904	0
20	82.26	82.336	6.4003	29.749	29.334	0
21	35.156	34.7	2.1735	5.2703	5.1248	0
22	9.6558	9.429	1.0639	5.7876	0	0

Table 13.31: Type 3 (EC, partial CFT) bin number, the number of $Z \to ee$ background events with positive charge that pass the tight cut, the number of $Z \to ee$ background event with negative charge that passes the tight cut, the number of $Z \to ee$ background events that pass the loose cut, but fail the tight cut, the number of $W \to \tau\nu$ background events with positive charge that pass the tight cut, the number of $W \to \tau\nu$ background event with negative charge that passes the tight cut, the number of $W \to \tau\nu$ background events that pass the loose cut, but fail the tight cut. $E_T > 35$ GeV.

bin	$N^{tight}_{Z\to ee^+}$	$N^{tight}_{Z\to ee^-}$	$N^{nottight}_{Z\to ee}$	$N^{tight}_{W\to\tau\nu^+}$	$N^{tight}_{W\to\tau\nu^-}$	$N^{nottight}_{W\to\tau\nu}$
0	1.1889	0.95625	0.21306	0.86885	0	0
1	28.864	32.68	4.5019	0	17.229	0
2	6.0156	7.718	0.53967	5.3589	0	0
21	7.3207	9.7381	0.77253	0	0	0
22	34.333	40.477	3.0923	0	0	0
23	2.9481	2.2536	0.42836	1.6044	0	0

Table 13.32: Type 4 (EC, no CFT) bin number, the number of $Z \to ee$ background events with positive charge that pass the tight cut, the number of $Z \to ee$ background event with negative charge that passes the tight cut, the number of $Z \to ee$ background events that pass the loose cut, but fail the tight cut, the number of $W \to \tau\nu$ background events with positive charge that pass the tight cut, the number of $W \to \tau\nu$ background event with negative charge that passes the tight cut, the number of $W \to \tau\nu$ background events that pass the loose cut, but fail the tight cut. $E_T > 35$ GeV.

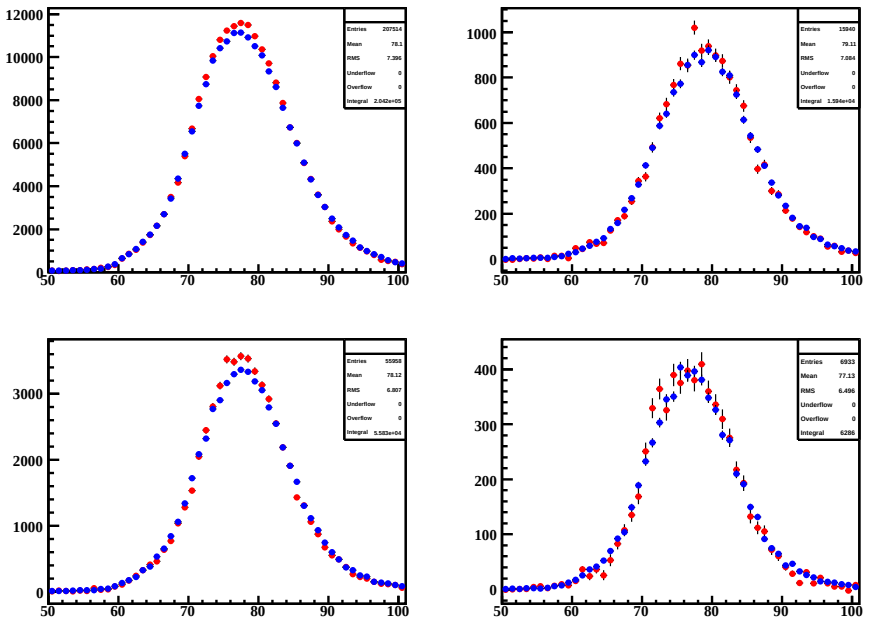

Figure 13.18: Data/MC transverse mass comparison plots for each type. Top left: type 1; top right: type 2; bottom left: type 3; bottom right: type 4. Red for data, blue for MC. $E_T >$ 35 GeV

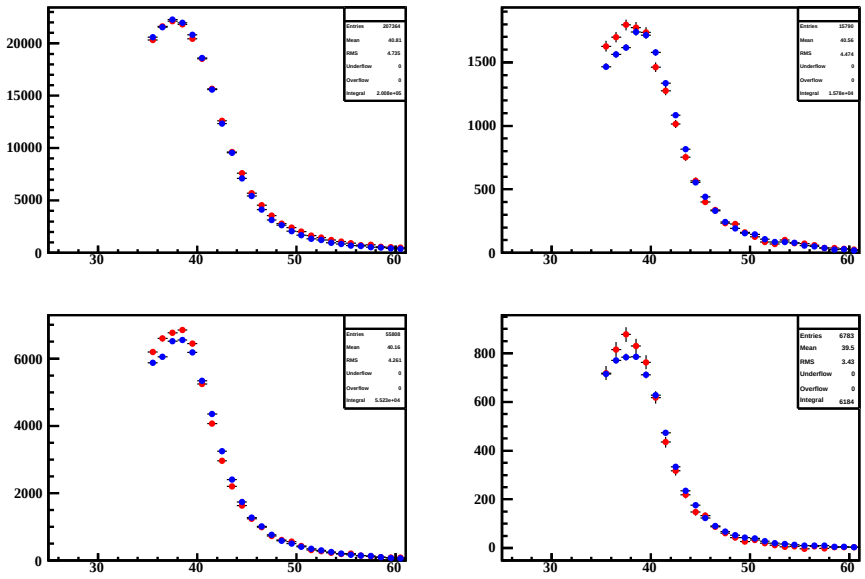

Figure 13.19: Data/MC electron E_T comparison plots for each type. Top left: type 1; top right: type 2; bottom left: type 3; bottom right: type 4. Red for data, blue for MC. $E_T > 35$ GeV

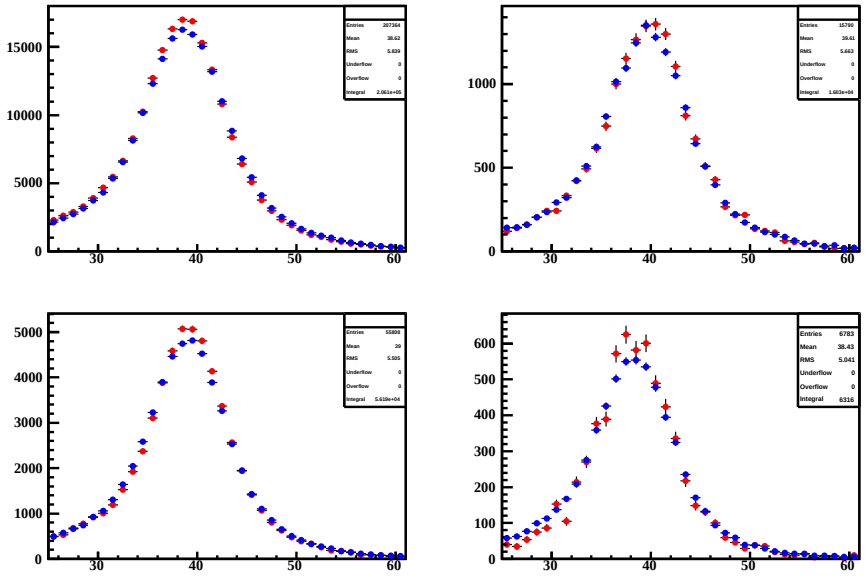

Figure 13.20: Data/MC $\not\!\!E_T$ comparison plots for each type. Top left: type 1; top right: type 2; bottom left: type 3; bottom right: type 4. Red for data, blue for MC. $E_T > 35$ GeV

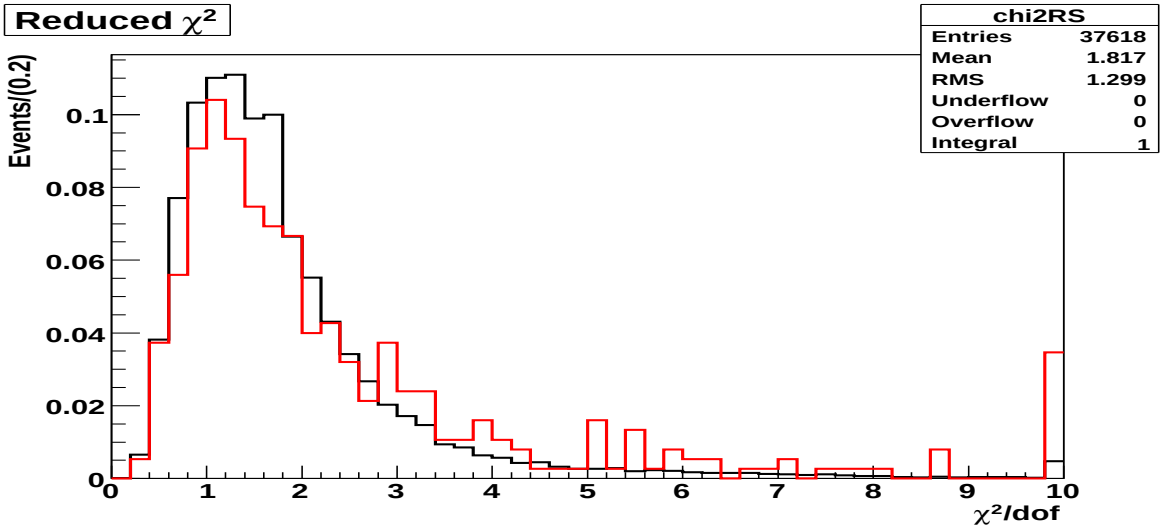

Figure 13.21: Track fit reduced χ^2 distribution for Type 1 electrons after the application of cuts on SMT, CFT and DCA cuts. The histograms are unit normalized, the black histogram has the correct charge assigned, the red has the incorrect charge assigned.

Appendix D

Comparison plots for selection cuts

D.1 Appendix D

D.2 Invariant mass for probe electrons

For reference, the invariant mass in each populated bin, for each type, for both correctly assigned charges (black) and incorrectly assigned charges (red) is shown in Figures 13.37 - 13.70.

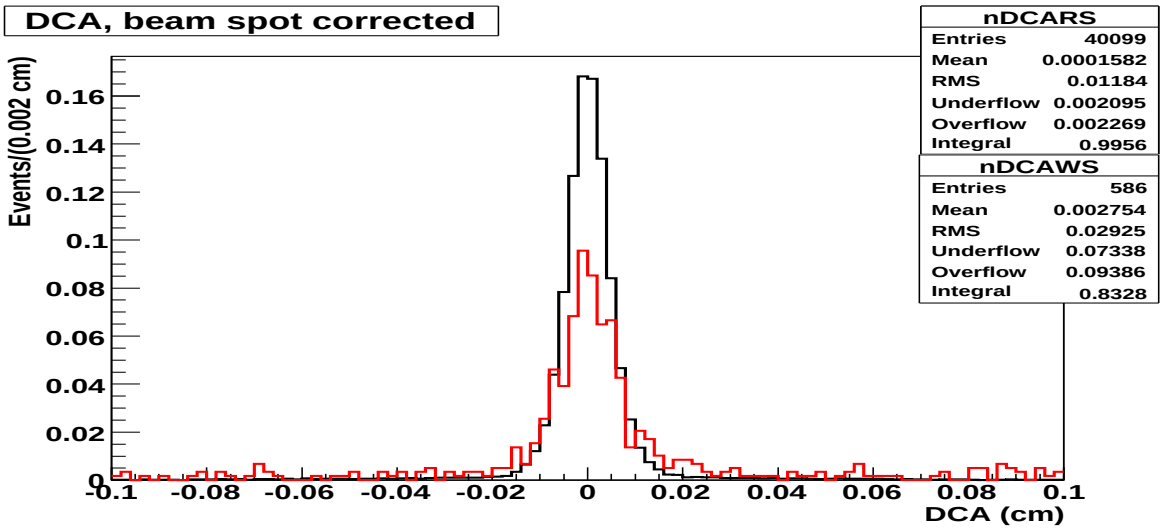

Figure 13.22: Beam spot corrected distance of closest approach distribution for Type 1 electrons after the application of CFT and DCA and χ^2 cuts. Because of resolution differences, SMT hit cut has been omitted. Note overflows. The histograms are unit normalized, the black histogram has the correct charge assigned, the red has the incorrect charge assigned.

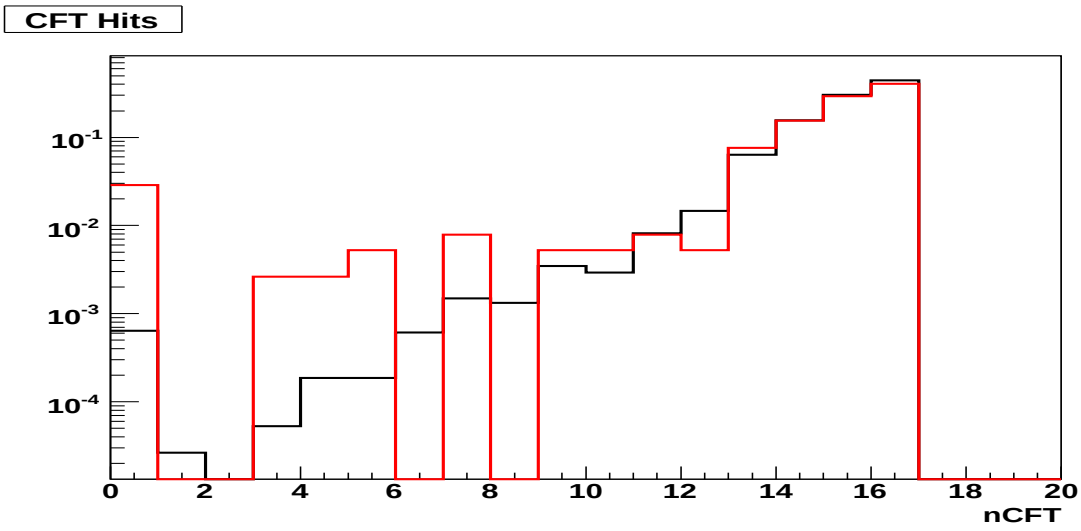

Figure 13.23: Number of CFT hits distribution for Type 1 electrons after the application of cuts on nSMT, DCA and χ^2. The histograms are unit normalized, the black histogram has the correct charge assigned, the red has the incorrect charge assigned.

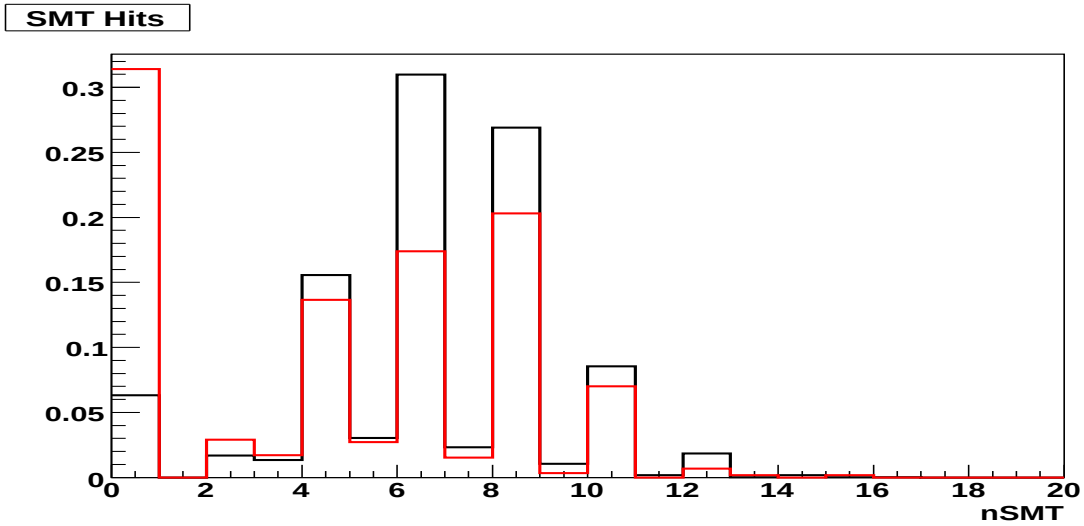

Figure 13.24: Number of SMT hits distribution for Type 1 electrons after the application of cuts on nCFT and χ^2. The histograms are unit normalized, the black histogram has the correct charge assigned, the red has the incorrect charge assigned.

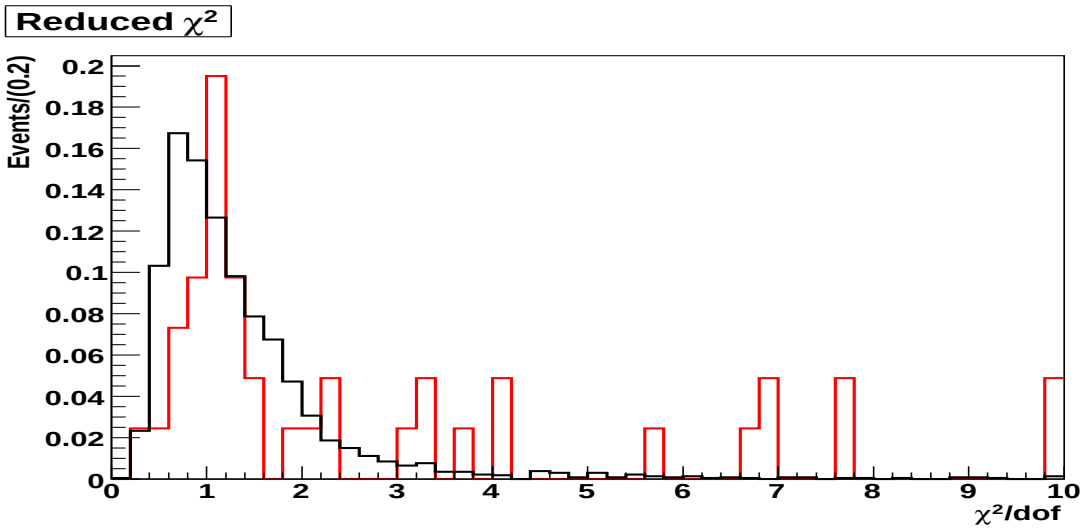

Figure 13.25: Track fit reduced χ^2 distribution for Type 2 electrons after the application of cuts on SMT, CFT and DCA cuts. The histograms are unit normalized, the black histogram has the correct charge assigned, the red has the incorrect charge assigned.

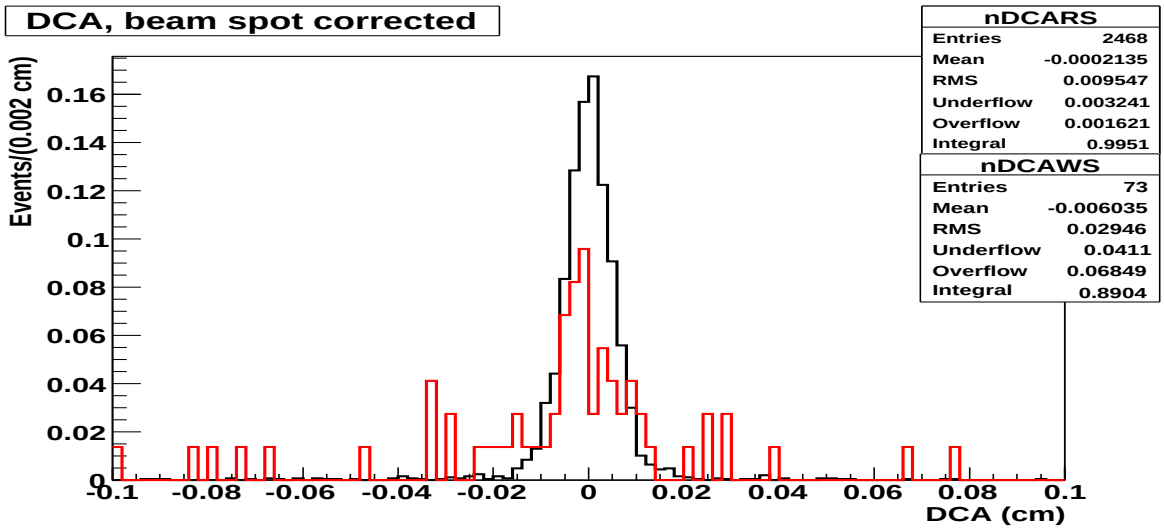

Figure 13.26: Beam spot corrected distance of closest approach distribution for Type 2 electrons after the application of CFT and DCA and χ^2 cuts. Because of resolution differences, SMT hit cut has been omitted. Note overflows. The histograms are unit normalized, the black histogram has the correct charge assigned, the red has the incorrect charge assigned.

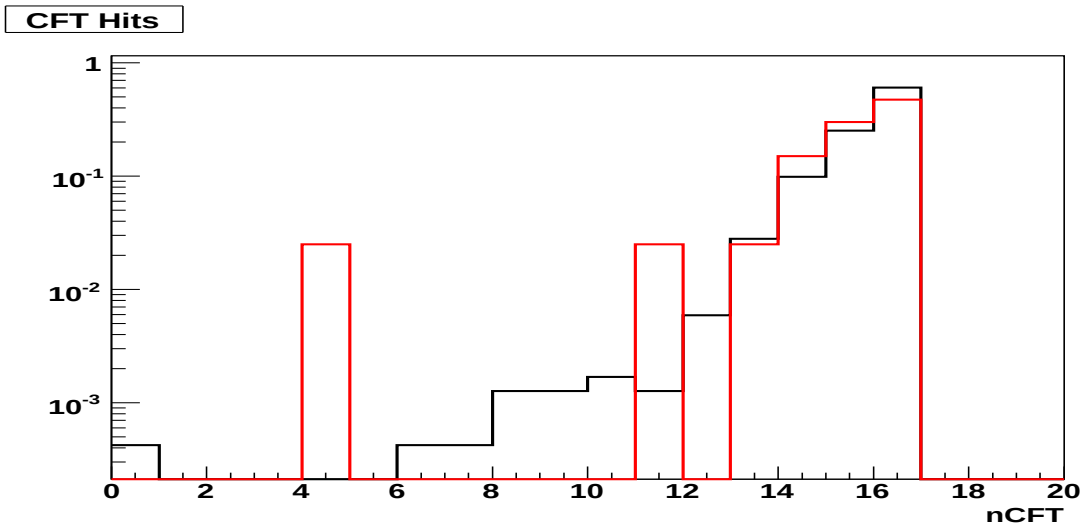

Figure 13.27: Number of CFT hits distribution for Type 2 electrons after the application of cuts on nSMT, DCA and χ^2. The histograms are unit normalized, the black histogram has the correct charge assigned, the red has the incorrect charge assigned.

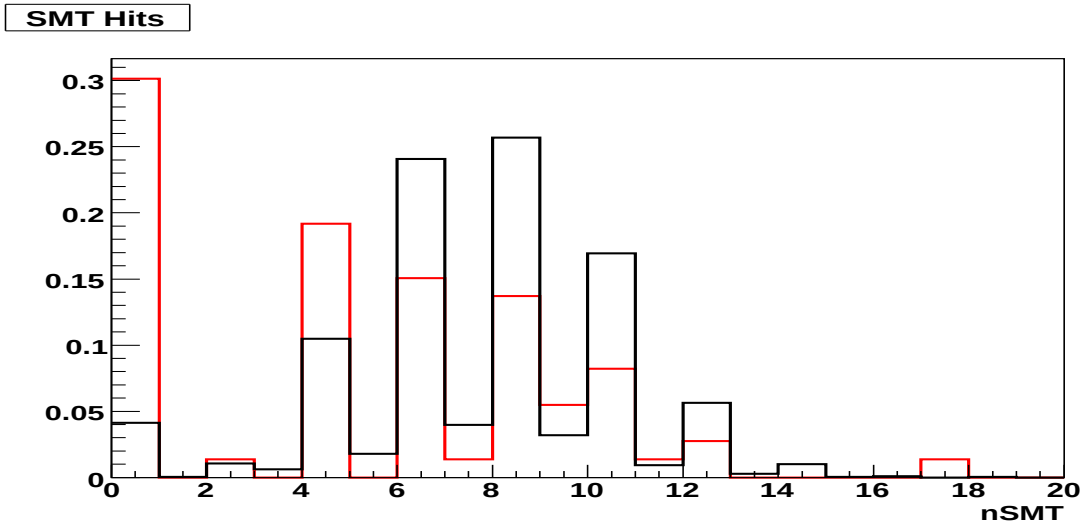

Figure 13.28: Number of SMT hits distribution for Type 2 electrons after the application of cuts on nCFT and χ^2. The histograms are unit normalized, the black histogram has the correct charge assigned, the red has the incorrect charge assigned.

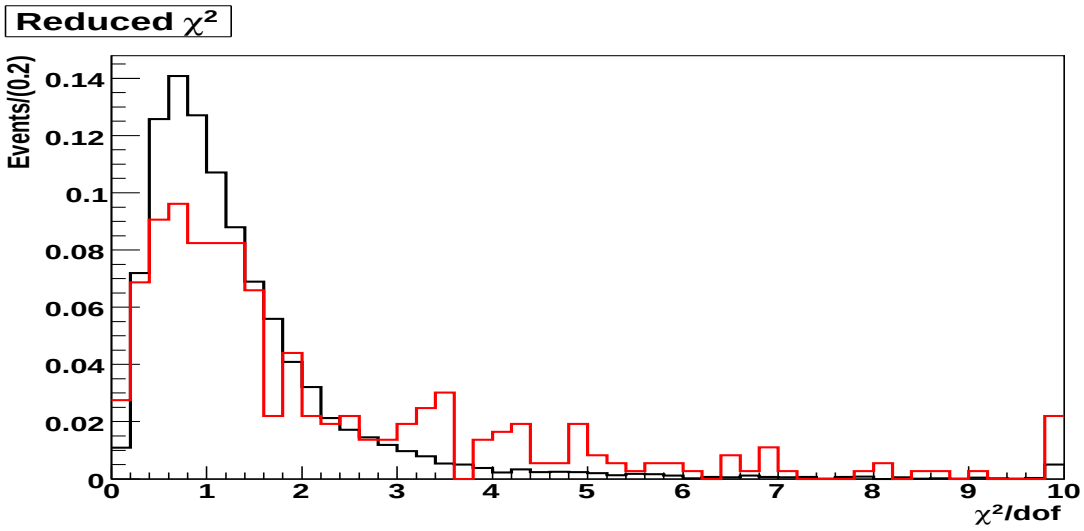

Figure 13.29: Track fit reduced χ^2 distribution for Type 3 electrons after the application of cuts on SMT, CFT and DCA cuts. The histograms are unit normalized, the black histogram has the correct charge assigned, the red has the incorrect charge assigned.

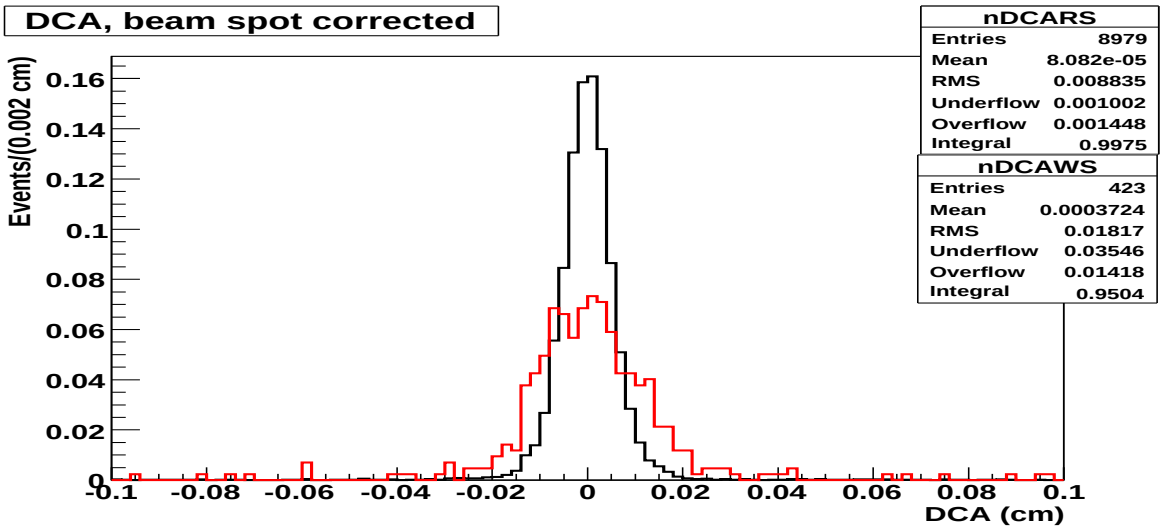

Figure 13.30: Beam spot corrected distance of closest approach distribution for Type 3 electrons after the application of CFT and DCA and χ^2 cuts. Because of resolution differences, SMT hit cut has been omitted. Note overflows. The histograms are unit normalized, the black histogram has the correct charge assigned, the red has the incorrect charge assigned.

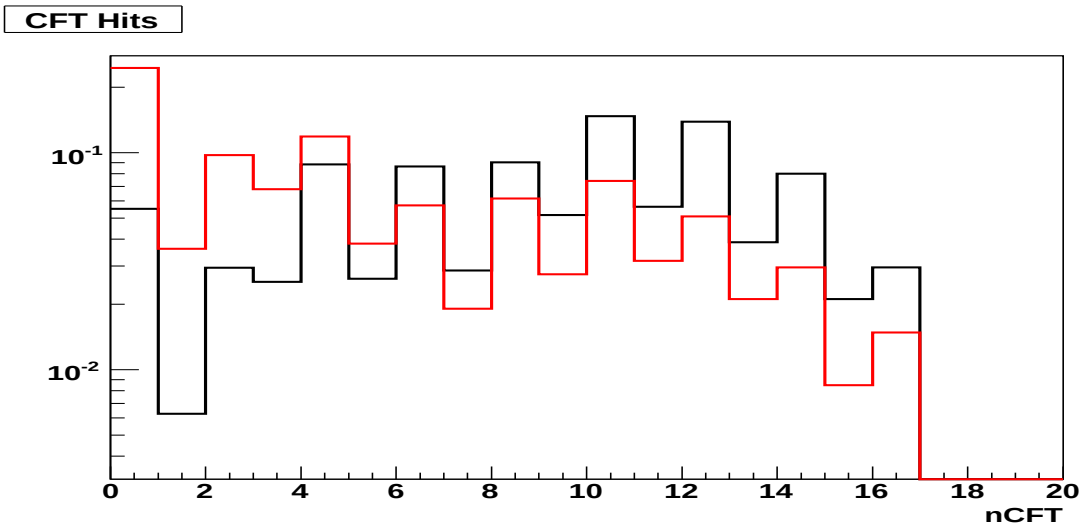

Figure 13.31: Number of CFT hits distribution for Type 3 electrons after the application of cuts on nSMT, DCA and χ^2. The histograms are unit normalized, the black histogram has the correct charge assigned, the red has the incorrect charge assigned.

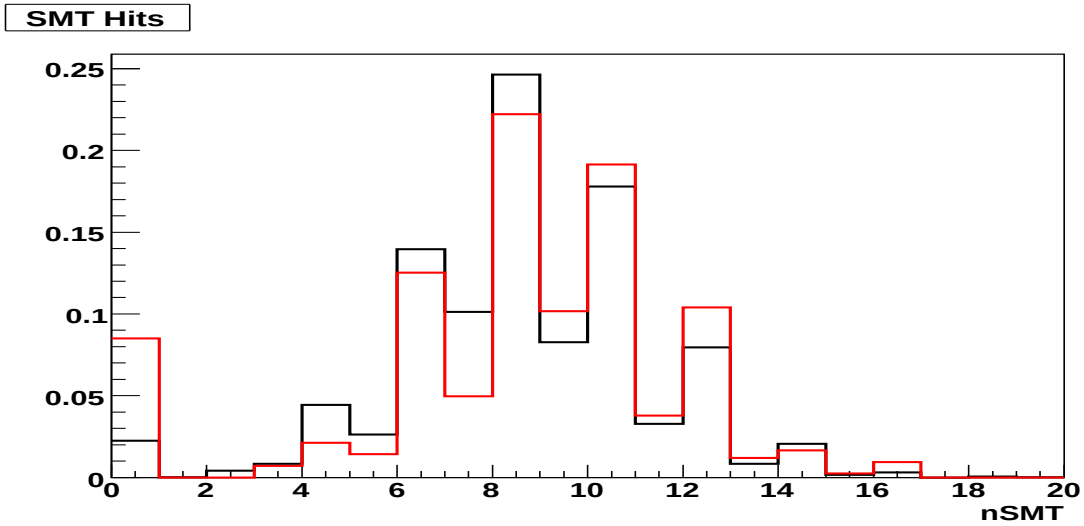

Figure 13.32: Number of SMT hits distribution for Type 3 electrons after the application of cuts on nCFT and χ^2. The histograms are unit normalized, the black histogram has the correct charge assigned, the red has the incorrect charge assigned.

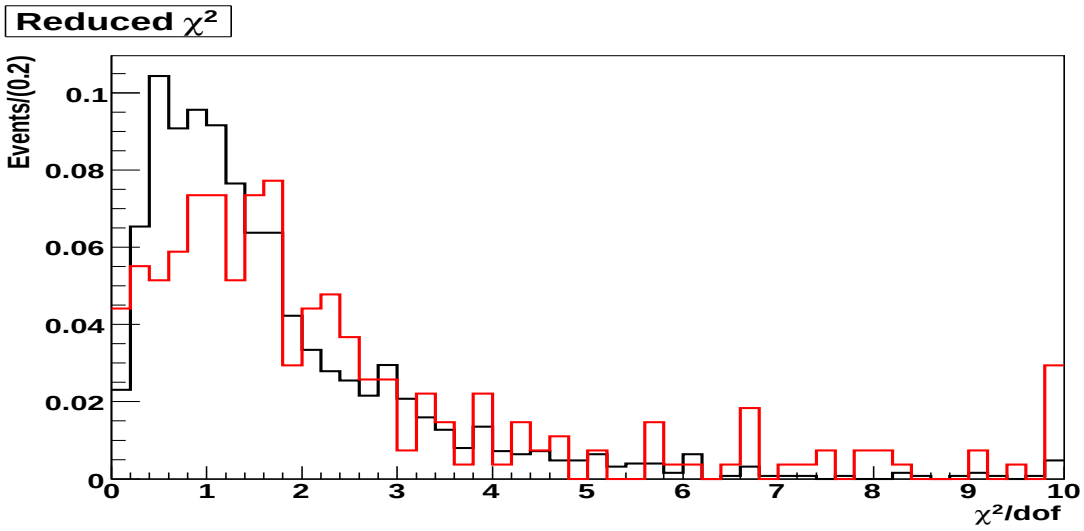

Figure 13.33: Track fit reduced χ^2 distribution for Type 4 electrons after the application of cuts on SMT, CFT and DCA cuts. The histograms are unit normalized, the black histogram has the correct charge assigned, the red has the incorrect charge assigned.

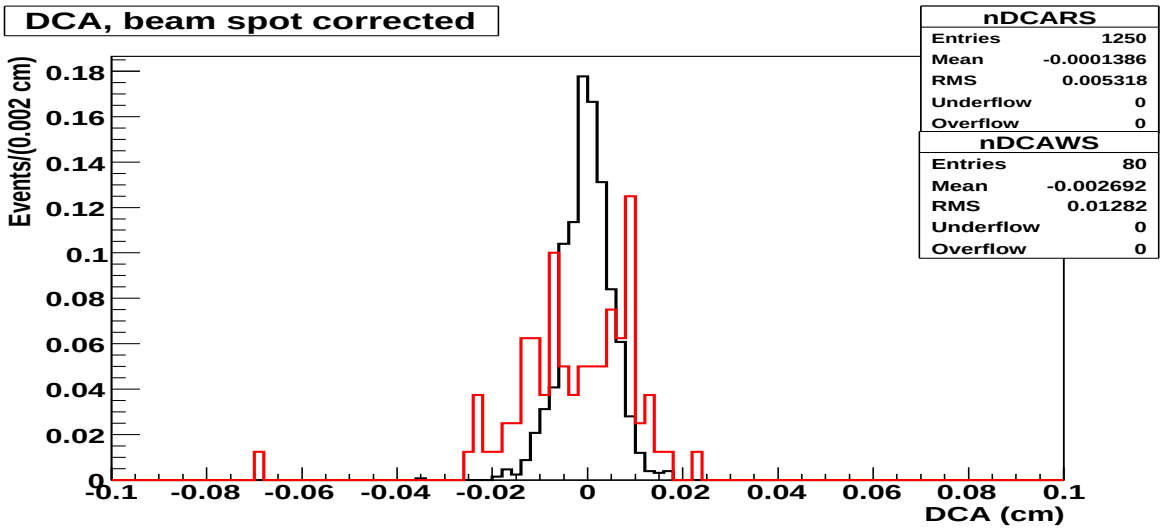

Figure 13.34: Beam spot corrected distance of closest approach distribution for Type 4 electrons after the application of CFT and DCA and χ^2 cuts. Because of resolution differences, SMT hit cut has been omitted. Note overflows. The histograms are unit normalized, the black histogram has the correct charge assigned, the red has the incorrect charge assigned.

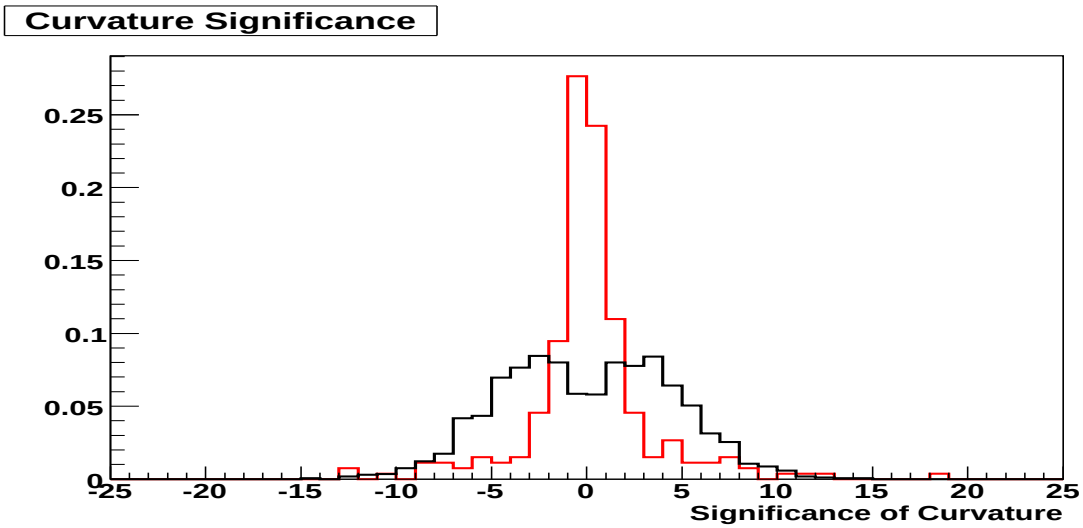

Figure 13.35: Significance of Curvature for Type 4 electrons after the application of cuts on nSMT, DCA and χ^2. The histograms are unit normalized, the black histogram has the correct charge assigned, the red has the incorrect charge assigned.

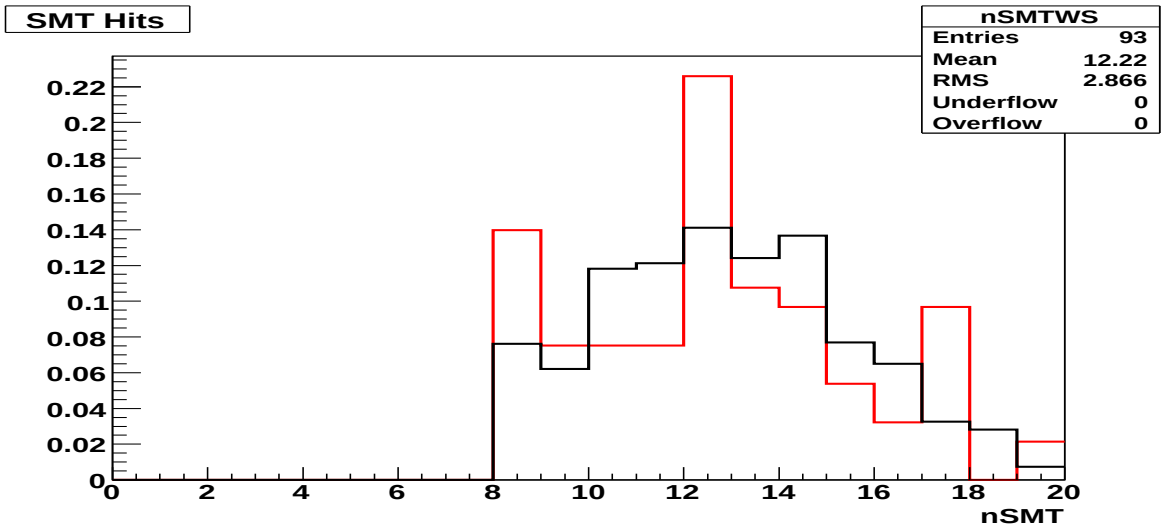

Figure 13.36: Number of SMT hits distribution for Type 4 electrons after the application of cuts on nCFT and χ^2. The histograms are unit normalized, the black histogram has the correct charge assigned, the red has the incorrect charge assigned.

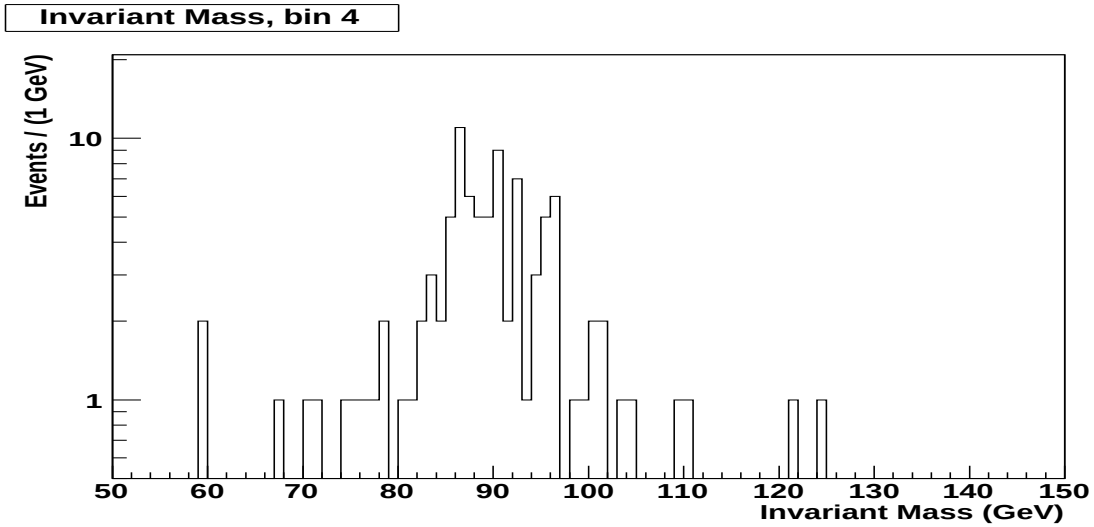

Figure 13.37: Invariant mass for Type 1 electrons in Bin 5. Correctly assigned charges are shown in black, incorrectly assigned charges are shown in red.

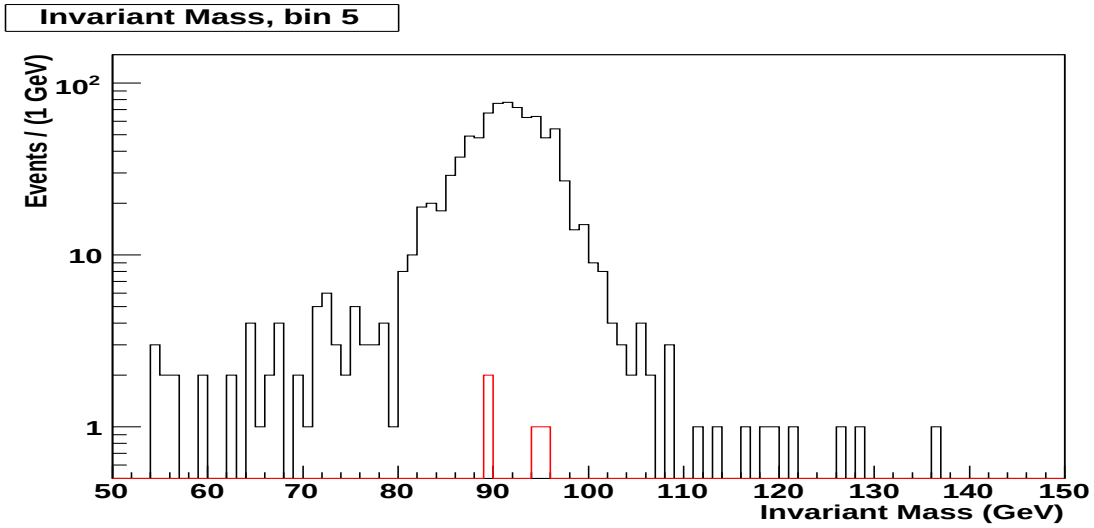

Figure 13.38: Invariant mass for Type 1 electrons in Bin 6. Correctly assigned charges are shown in black, incorrectly assigned charges are shown in red.

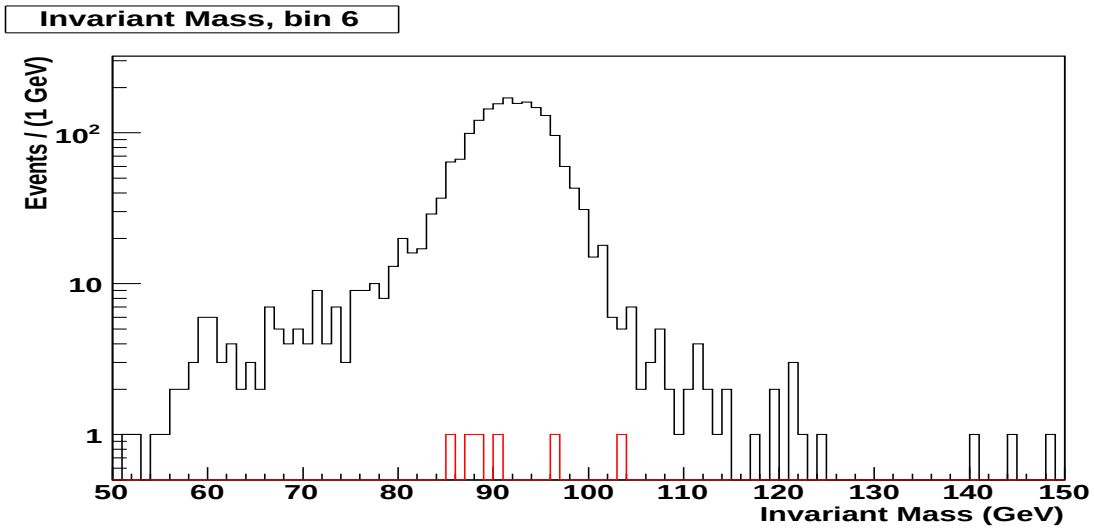

Figure 13.39: Invariant mass for Type 1 electrons in Bin 7. Correctly assigned charges are shown in black, incorrectly assigned charges are shown in red.

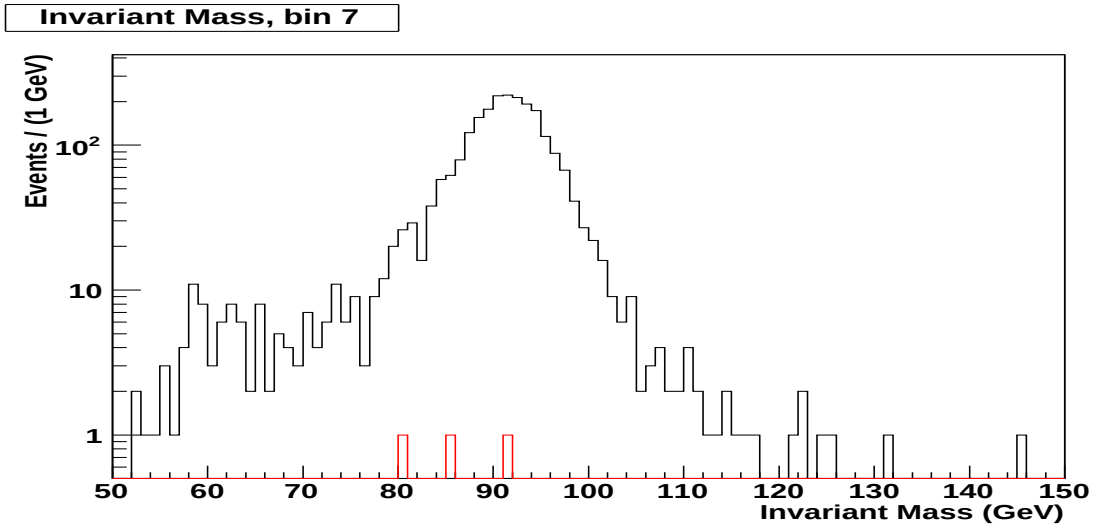

Figure 13.40: Invariant mass for Type 1 electrons in Bin 8. Correctly assigned charges are shown in black, incorrectly assigned charges are shown in red.

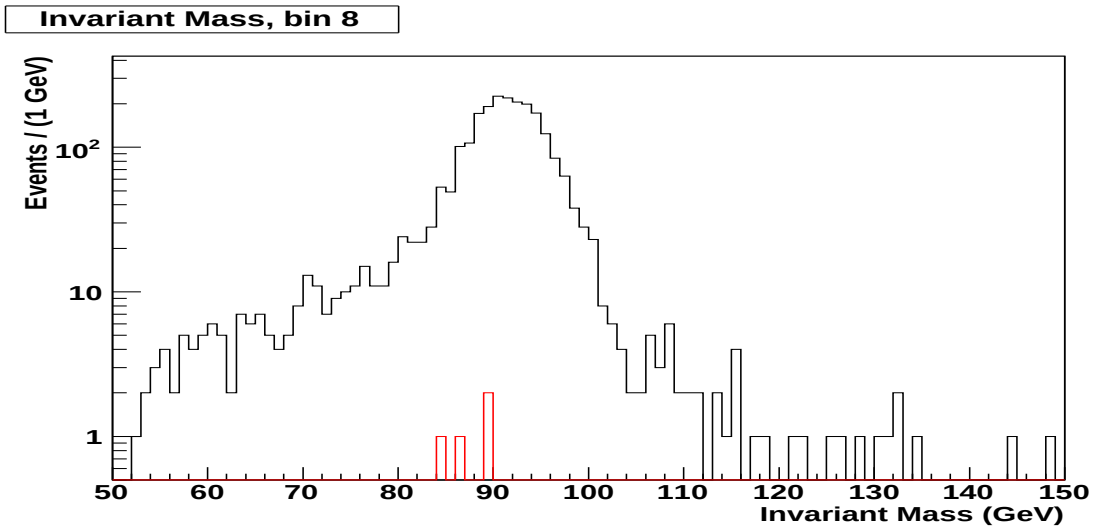

Figure 13.41: Invariant mass for Type 1 electrons in Bin 9. Correctly assigned charges are shown in black, incorrectly assigned charges are shown in red.

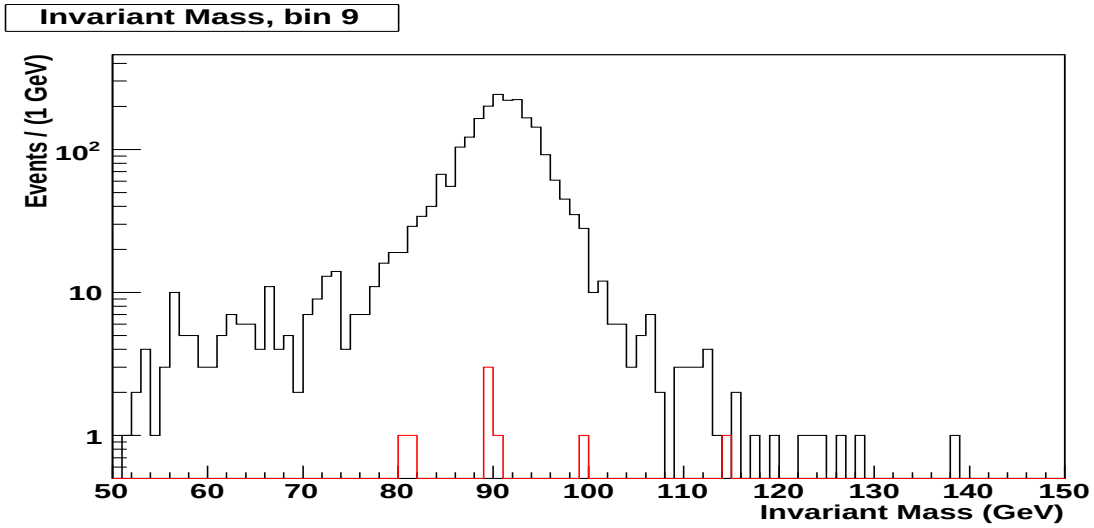

Figure 13.42: Invariant mass for Type 1 electrons in Bin 10. Correctly assigned charges are shown in black, incorrectly assigned charges are shown in red.

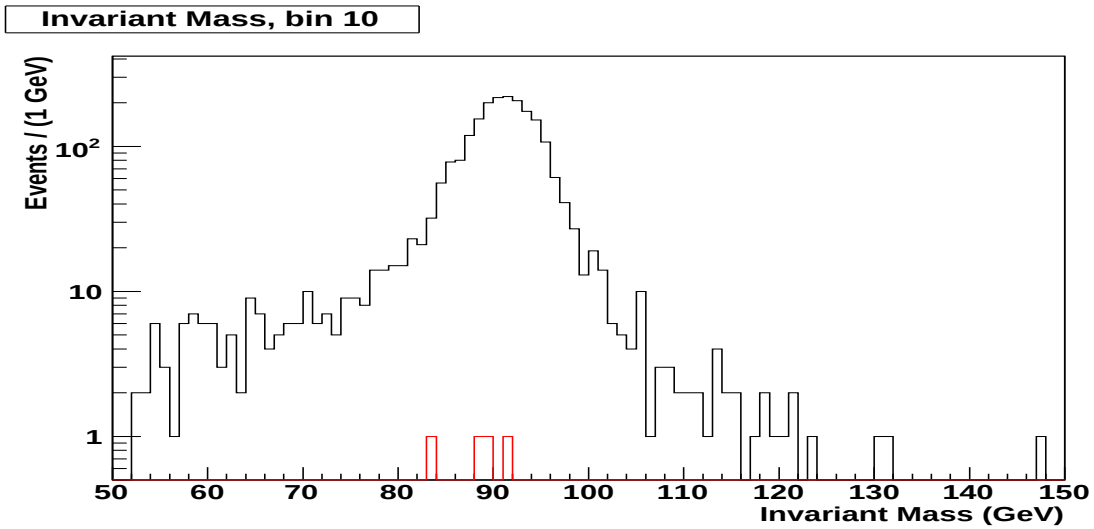

Figure 13.43: Invariant mass for Type 1 electrons in Bin 11. Correctly assigned charges are shown in black, incorrectly assigned charges are shown in red.

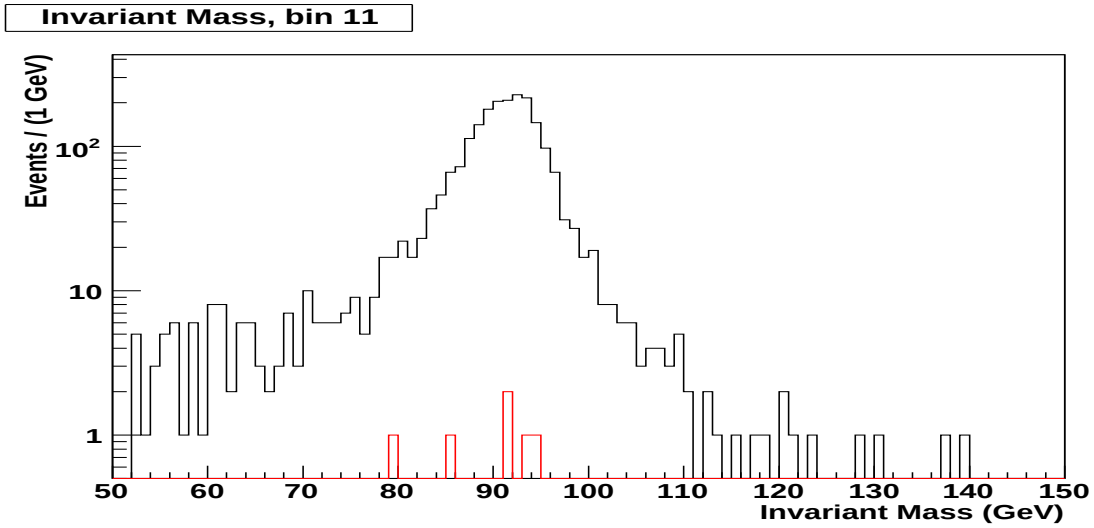

Figure 13.44: Invariant mass for Type 1 electrons in Bin 12. Correctly assigned charges are shown in black, incorrectly assigned charges are shown in red.

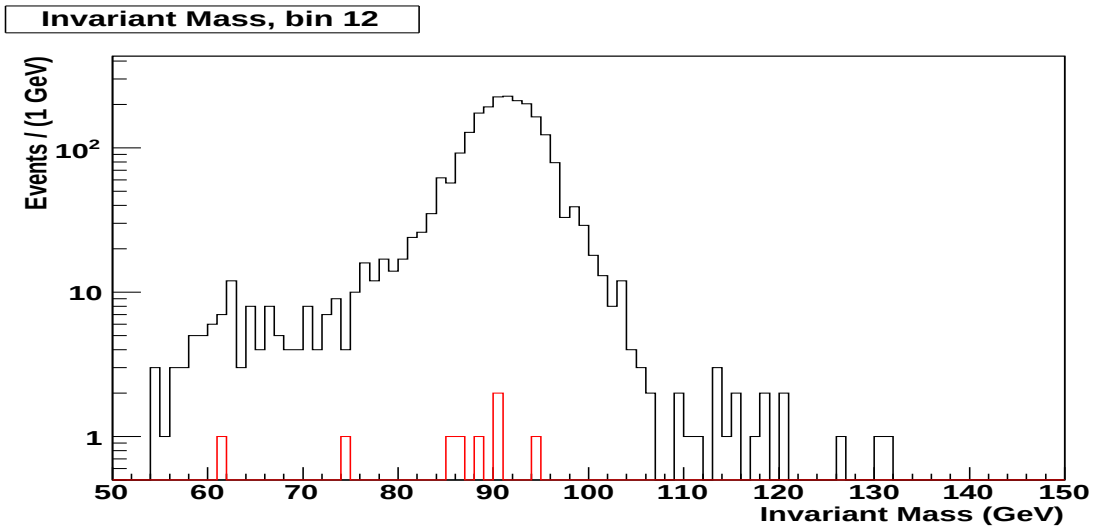

Figure 13.45: Invariant mass for Type 1 electrons in Bin 13. Correctly assigned charges are shown in black, incorrectly assigned charges are shown in red.

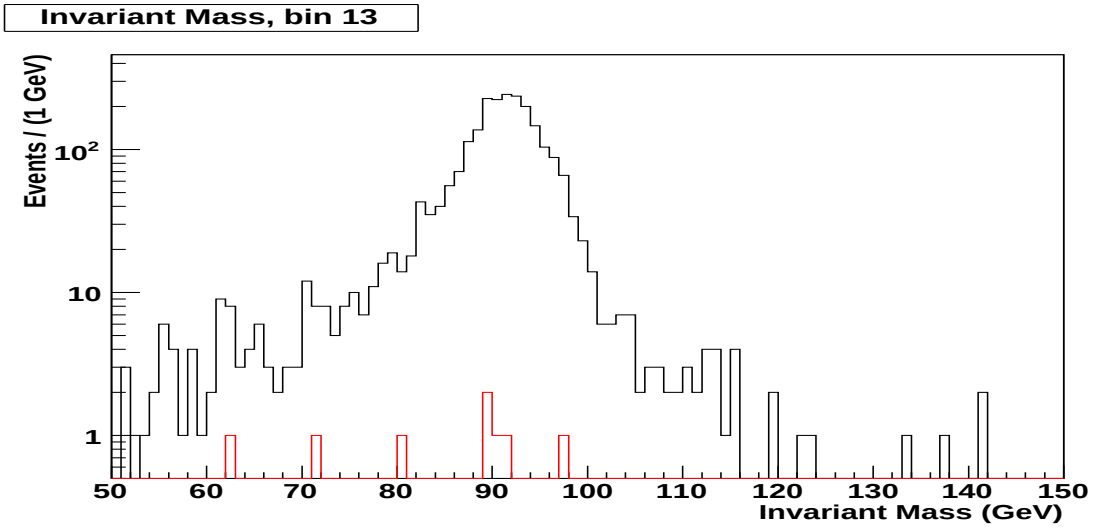

Figure 13.46: Invariant mass for Type 1 electrons in Bin 14. Correctly assigned charges are shown in black, incorrectly assigned charges are shown in red.

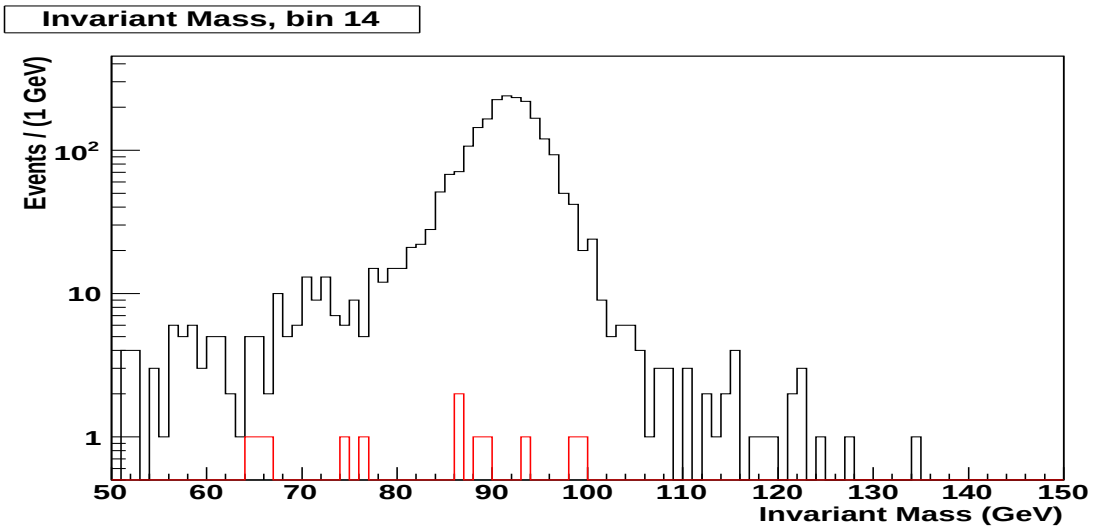

Figure 13.47: Invariant mass for Type 1 electrons in Bin 15. Correctly assigned charges are shown in black, incorrectly assigned charges are shown in red.

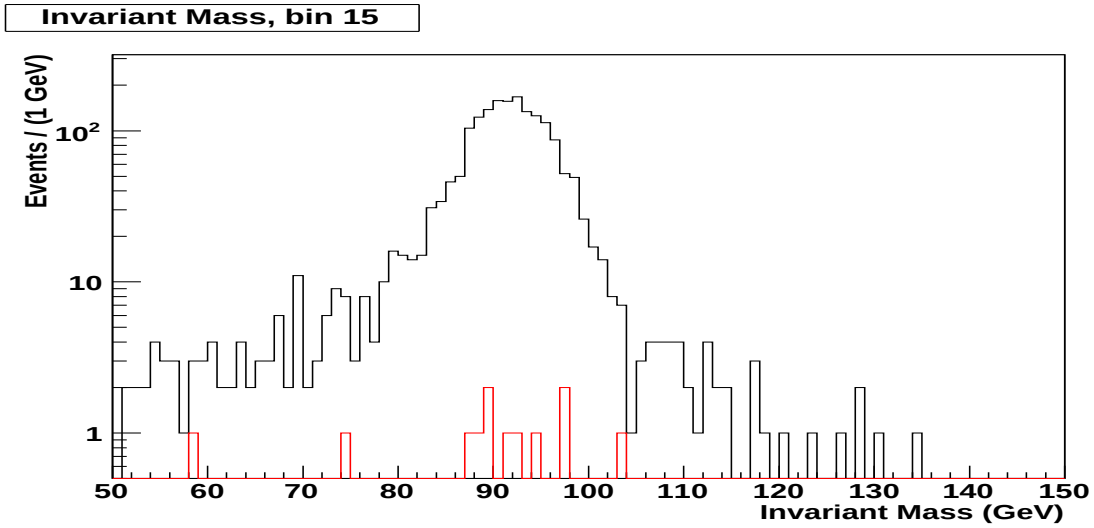

Figure 13.48: Invariant mass for Type 1 electrons in Bin 16. Correctly assigned charges are shown in black, incorrectly assigned charges are shown in red.

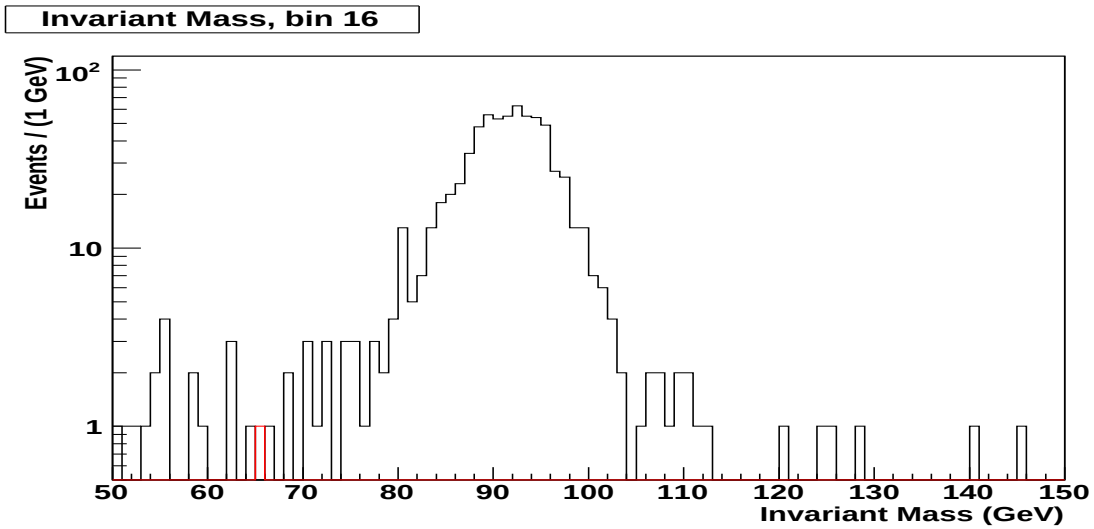

Figure 13.49: Invariant mass for Type 1 electrons in Bin 17. Correctly assigned charges are shown in black, incorrectly assigned charges are shown in red.

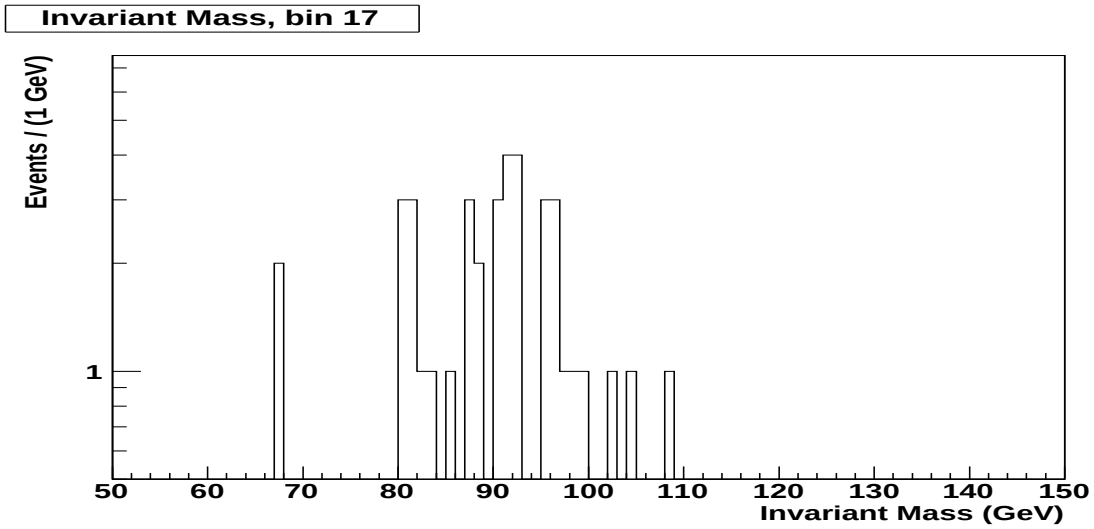

Figure 13.50: Invariant mass for Type 1 electrons in Bin 18. Correctly assigned charges are shown in black, incorrectly assigned charges are shown in red.

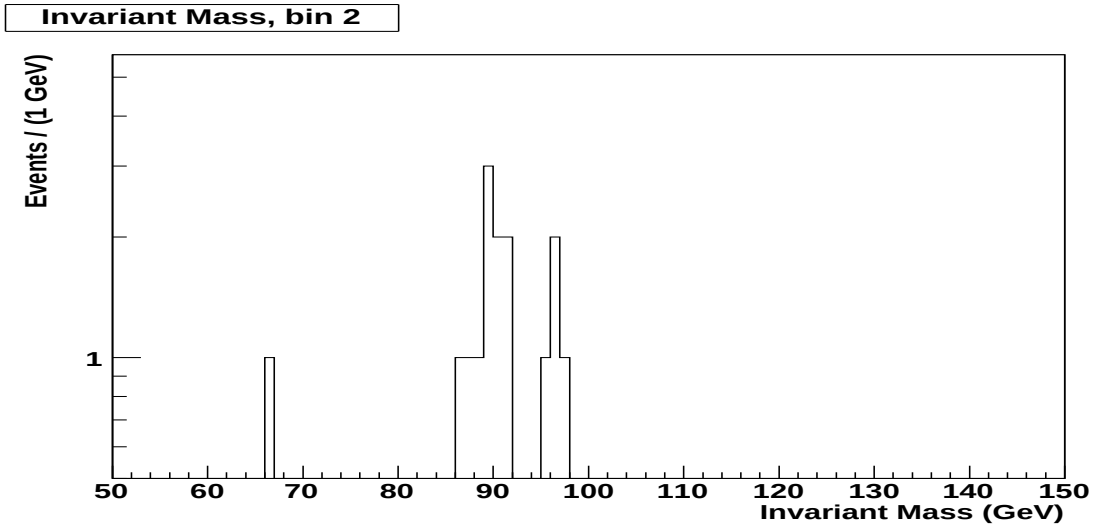

Figure 13.51: Invariant mass for Type 2 electrons in Bin 3. Correctly assigned charges are shown in black, incorrectly assigned charges are shown in red.

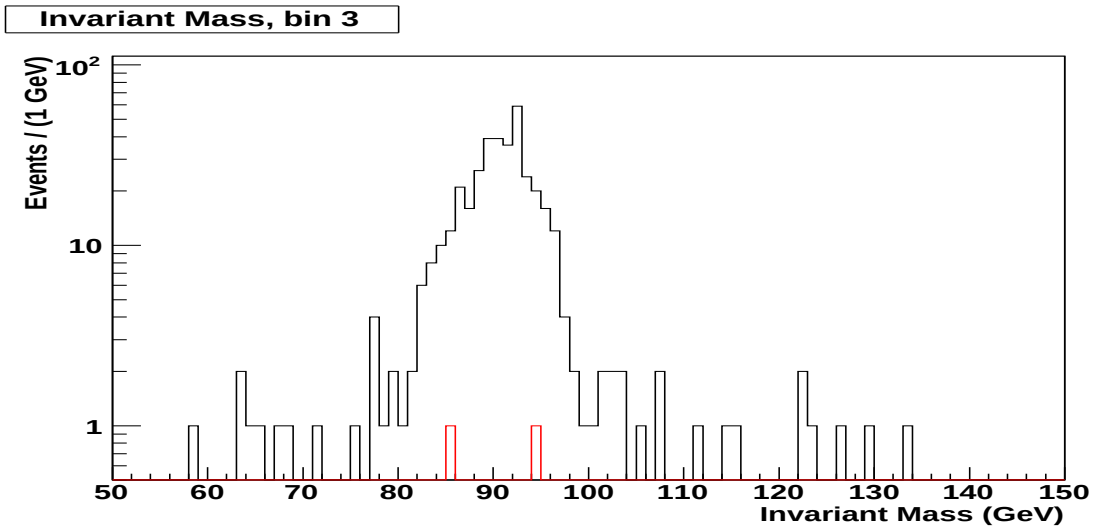

Figure 13.52: Invariant mass for Type 2 electrons in Bin 4. Correctly assigned charges are shown in black, incorrectly assigned charges are shown in red.

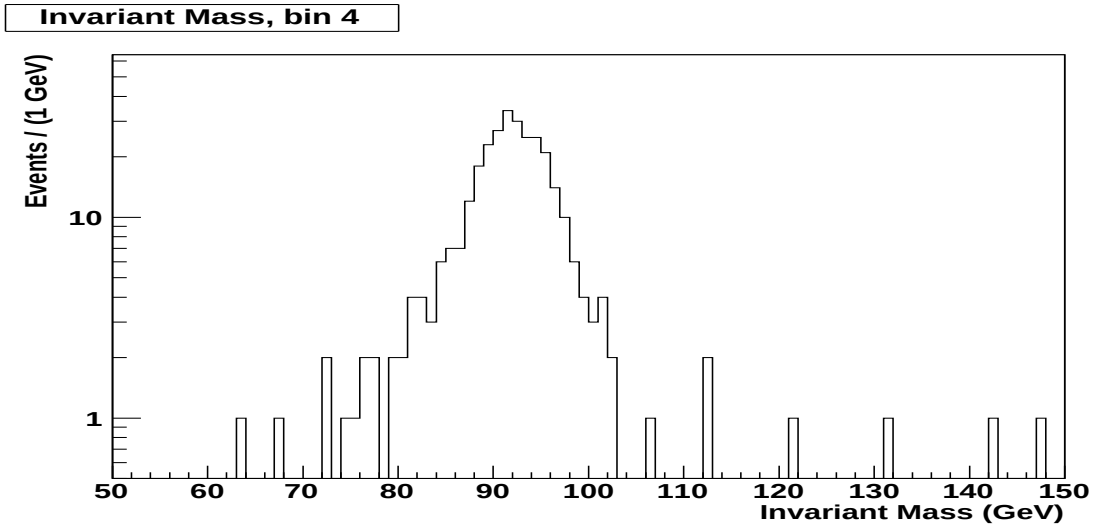

Figure 13.53: Invariant mass for Type 2 electrons in Bin 5. Correctly assigned charges are shown in black, incorrectly assigned charges are shown in red.

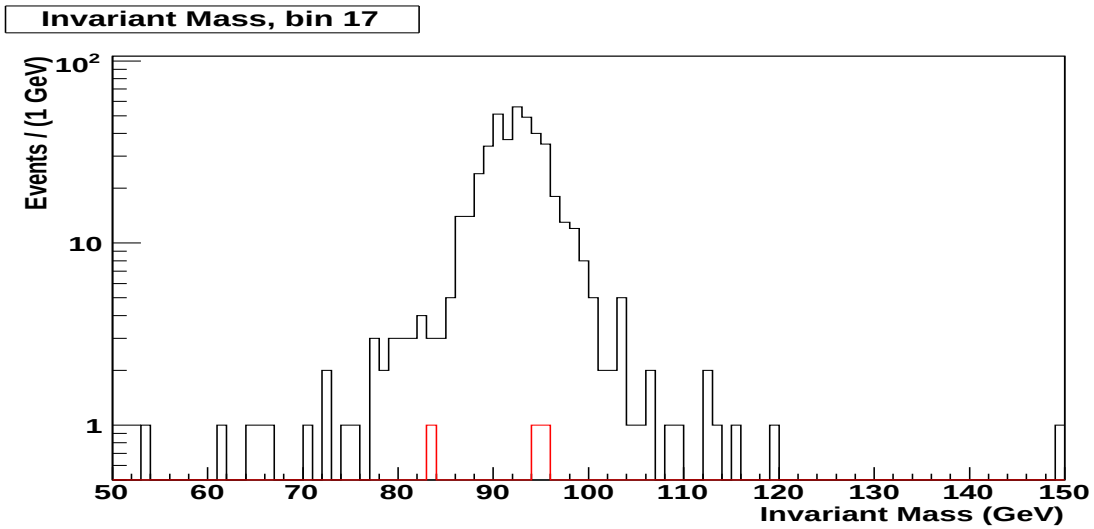

Figure 13.54: Invariant mass for Type 2 electrons in Bin 18. Correctly assigned charges are shown in black, incorrectly assigned charges are shown in red.

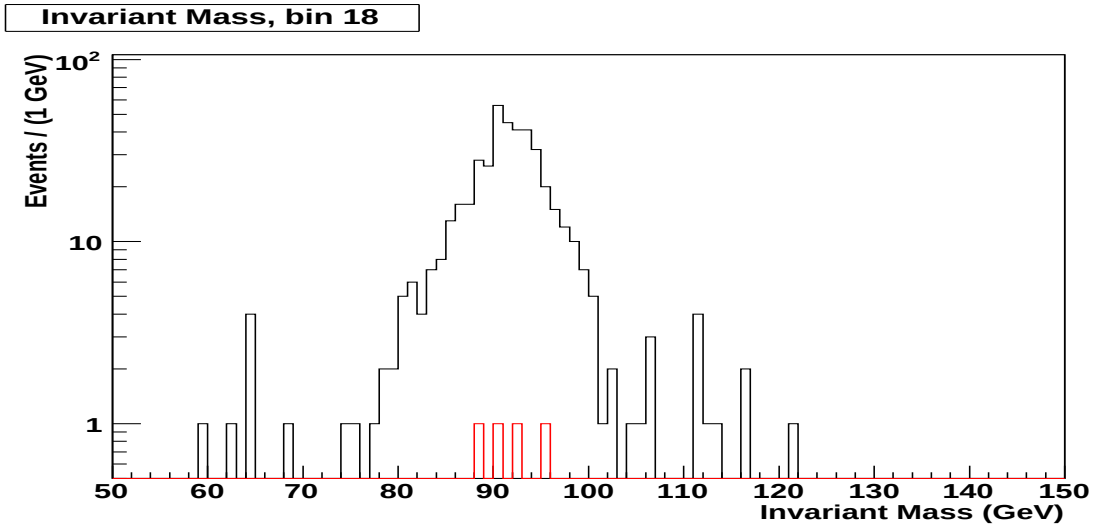

Figure 13.55: Invariant mass for Type 2 electrons in Bin 19. Correctly assigned charges are shown in black, incorrectly assigned charges are shown in red.

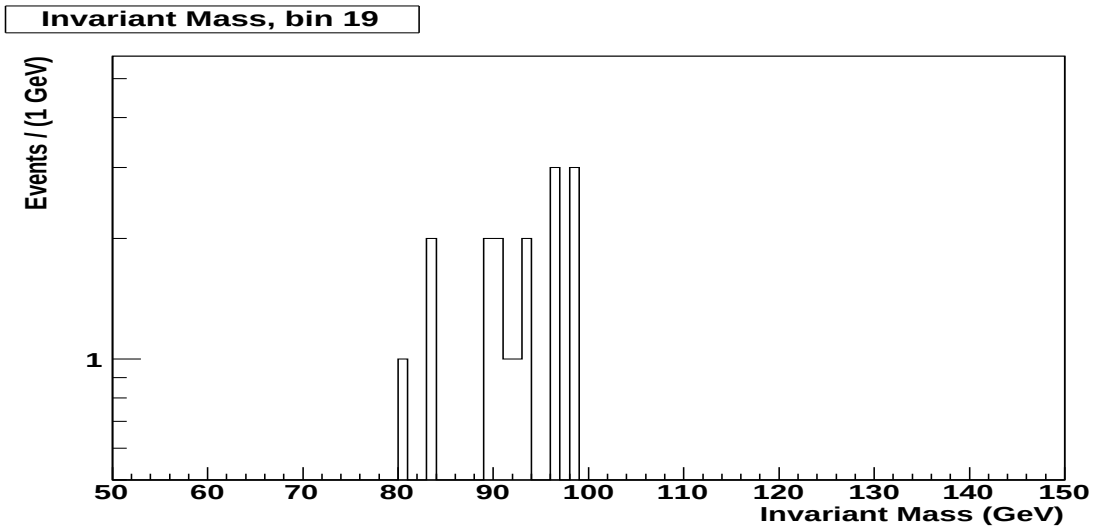

Figure 13.56: Invariant mass for Type 2 electrons in Bin 20. Correctly assigned charges are shown in black, incorrectly assigned charges are shown in red.

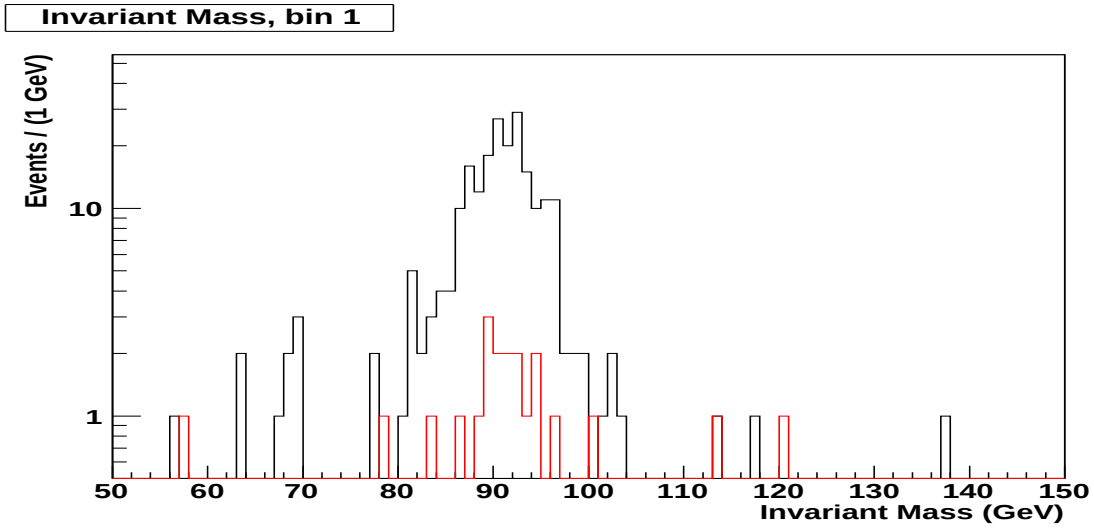

Figure 13.57: Invariant mass for Type 3 electrons in Bin 1. Correctly assigned charges are shown in black, incorrectly assigned charges are shown in red.

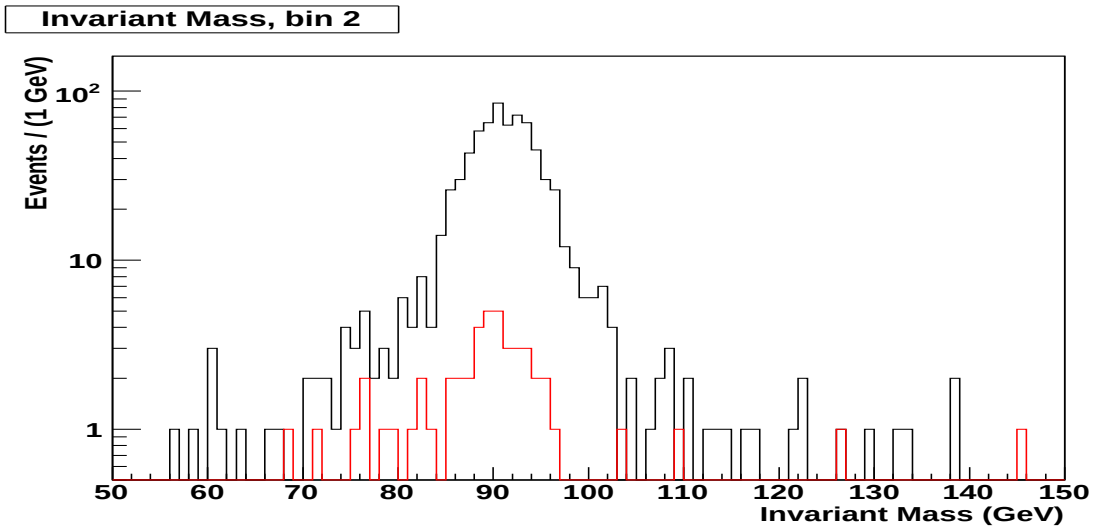

Figure 13.58: Invariant mass for Type 3 electrons in Bin 2. Correctly assigned charges are shown in black, incorrectly assigned charges are shown in red.

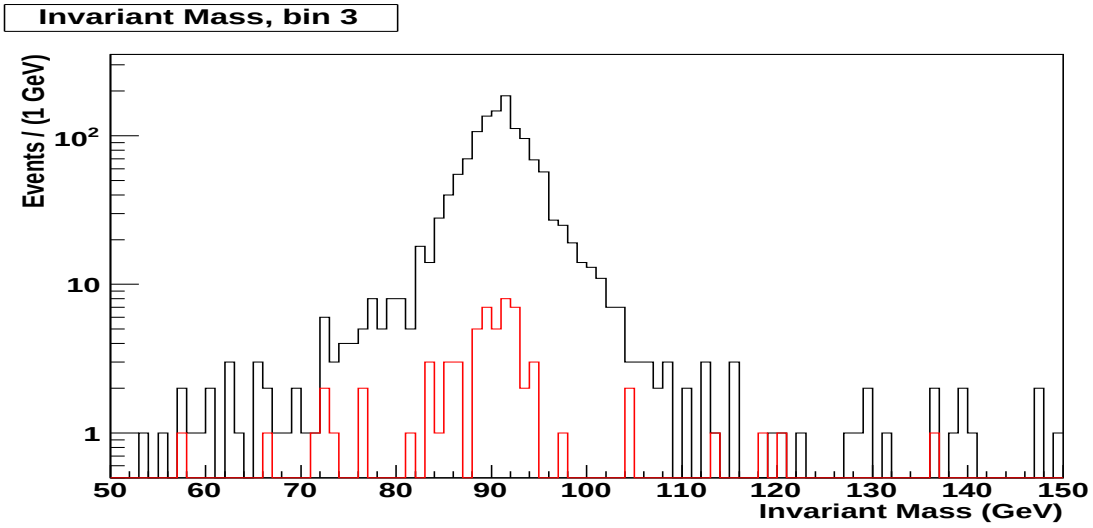

Figure 13.59: Invariant mass for Type 3 electrons in Bin 3. Correctly assigned charges are shown in black, incorrectly assigned charges are shown in red.

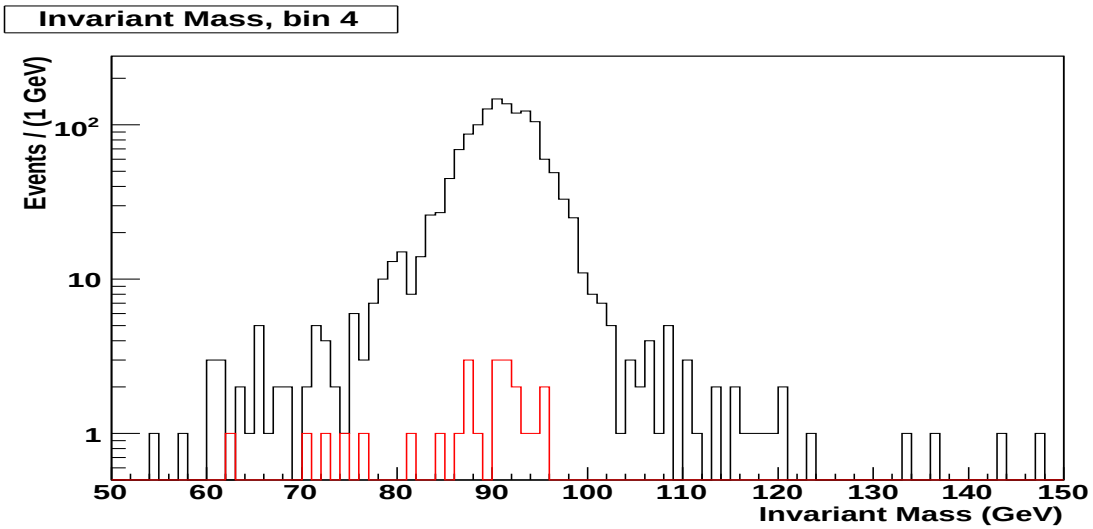

Figure 13.60: Invariant mass for Type 3 electrons in Bin 4. Correctly assigned charges are shown in black, incorrectly assigned charges are shown in red.

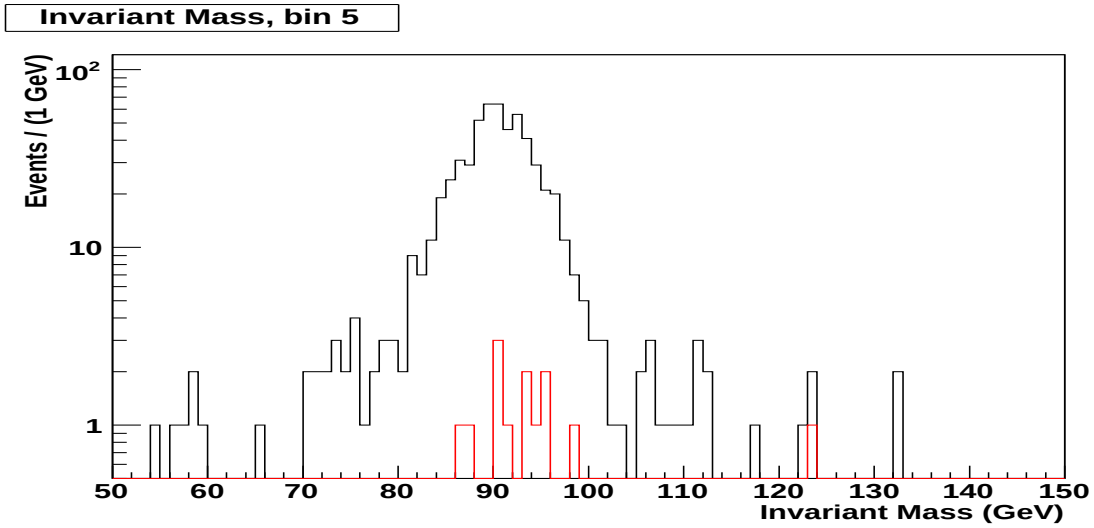

Figure 13.61: Invariant mass for Type 3 electrons in Bin 5. Correctly assigned charges are shown in black, incorrectly assigned charges are shown in red.

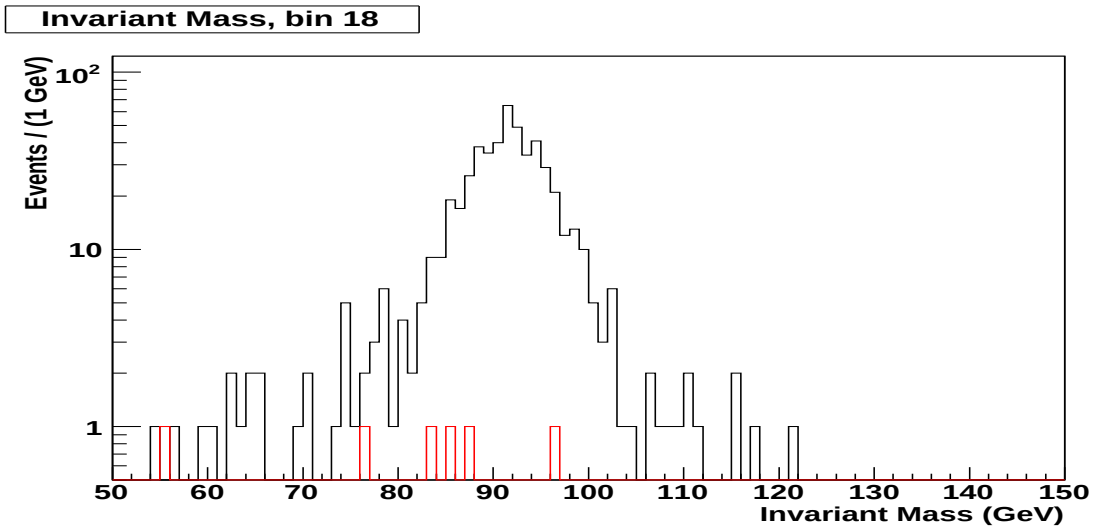

Figure 13.62: Invariant mass for Type 3 electrons in Bin 18. Correctly assigned charges are shown in black, incorrectly assigned charges are shown in red.

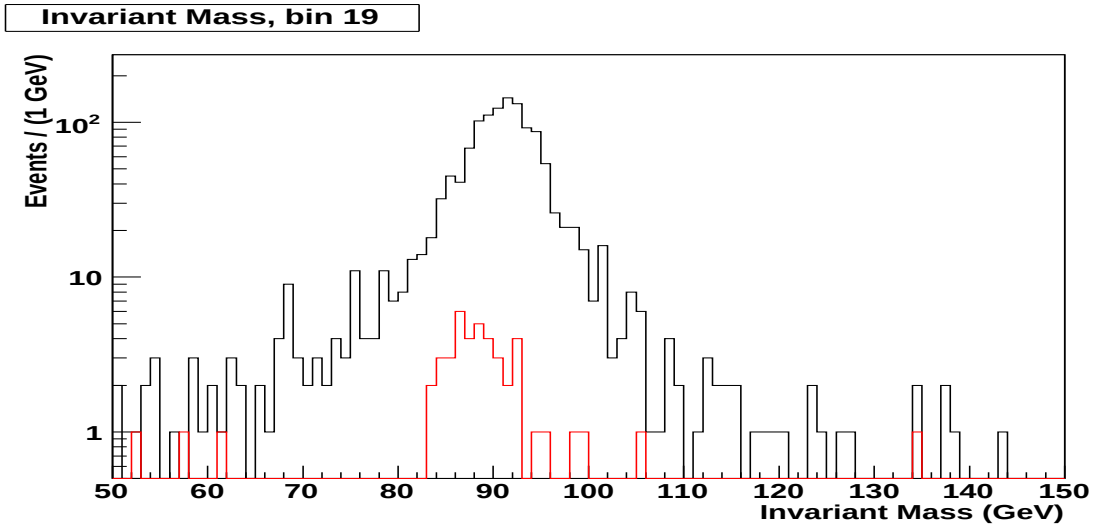

Figure 13.63: Invariant mass for Type 3 electrons in Bin 19. Correctly assigned charges are shown in black, incorrectly assigned charges are shown in red.

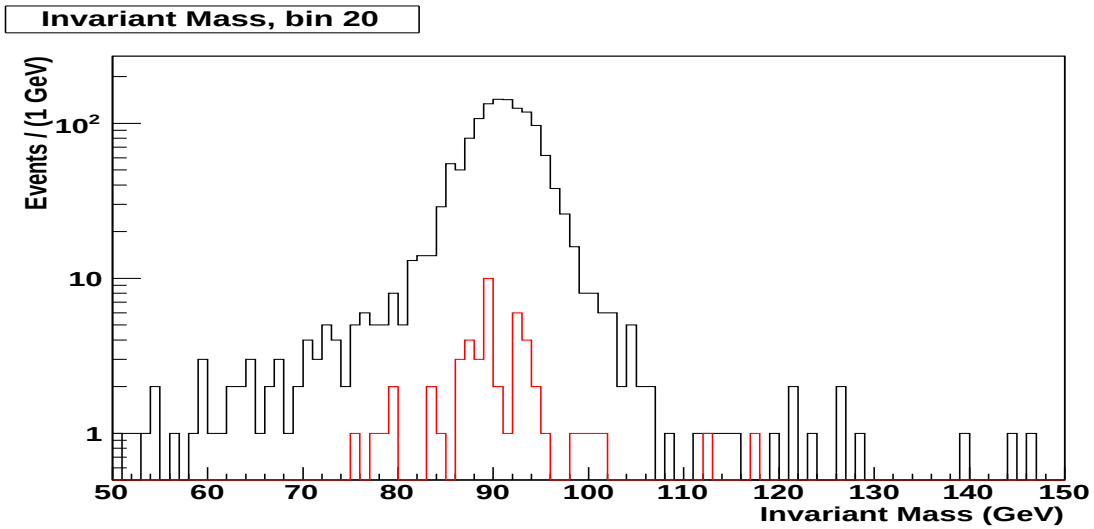

Figure 13.64: Invariant mass for Type 3 electrons in Bin 20. Correctly assigned charges are shown in black, incorrectly assigned charges are shown in red.

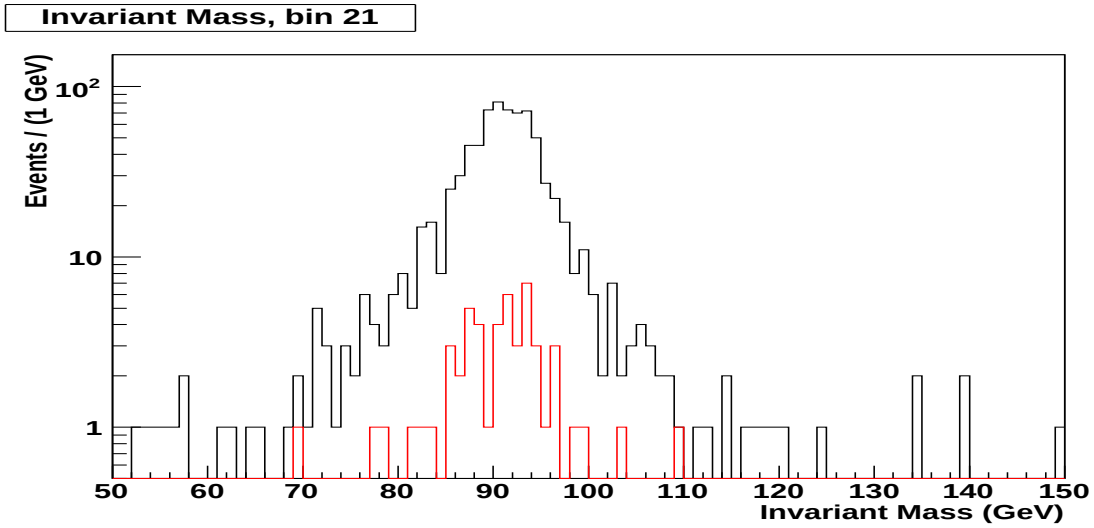

Figure 13.65: Invariant mass for Type 3 electrons in Bin 21. Correctly assigned charges are shown in black, incorrectly assigned charges are shown in red.

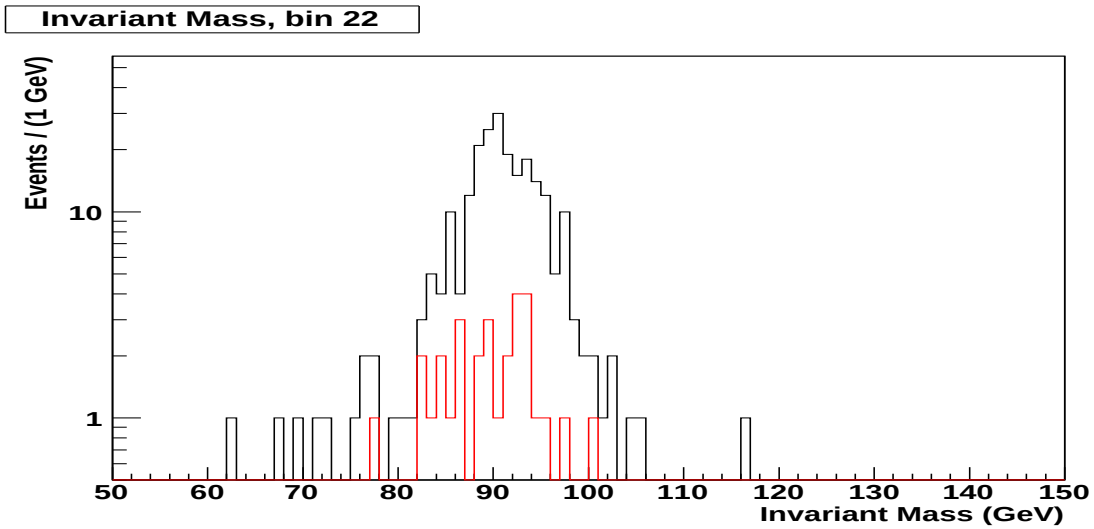

Figure 13.66: Invariant mass for Type 3 electrons in Bin 22. Correctly assigned charges are shown in black, incorrectly assigned charges are shown in red.

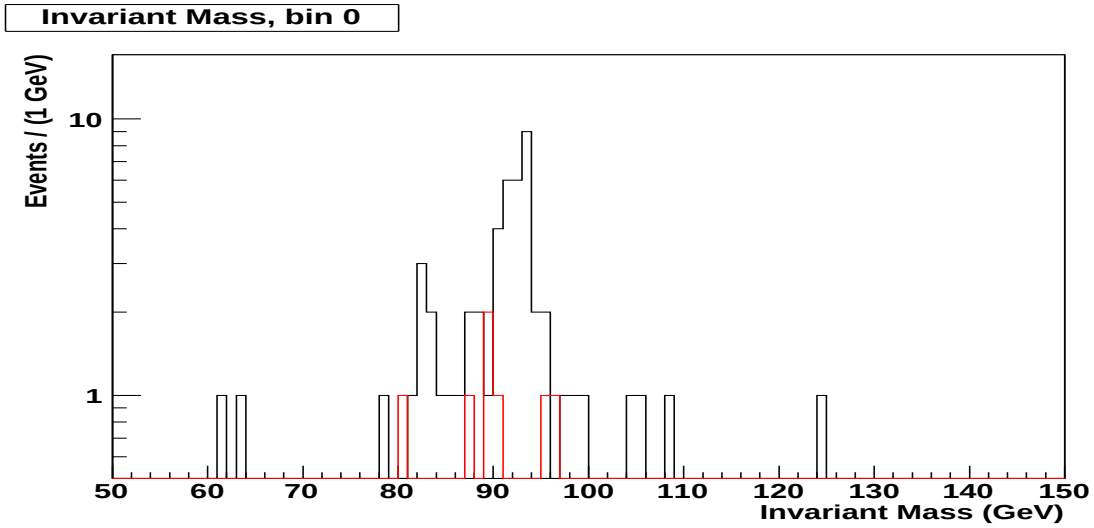

Figure 13.67: Invariant mass for Type 4 electrons in Bin 0. Correctly assigned charges are shown in black, incorrectly assigned charges are shown in red.

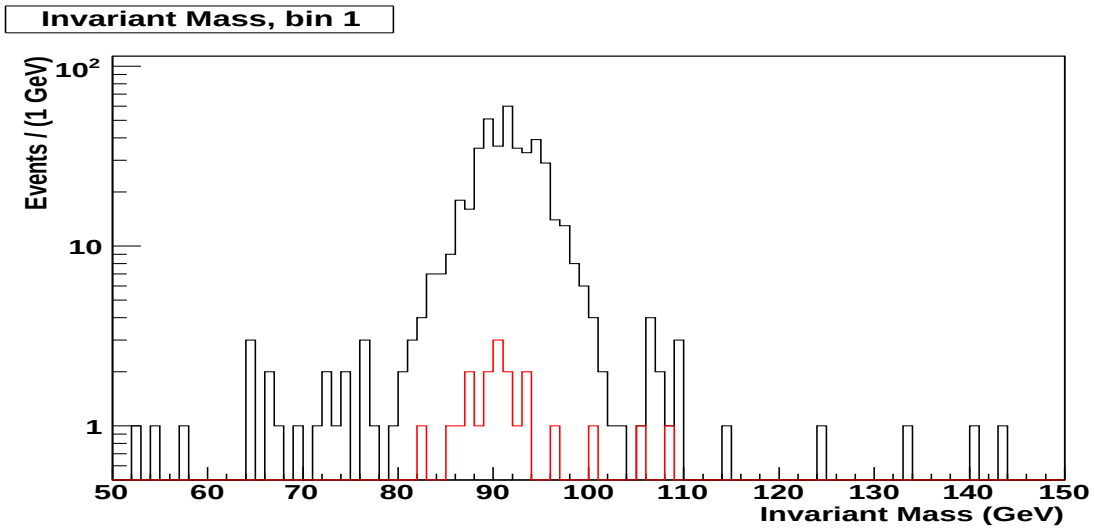

Figure 13.68: Invariant mass for Type 4 electrons in Bin 1. Correctly assigned charges are shown in black, incorrectly assigned charges are shown in red.

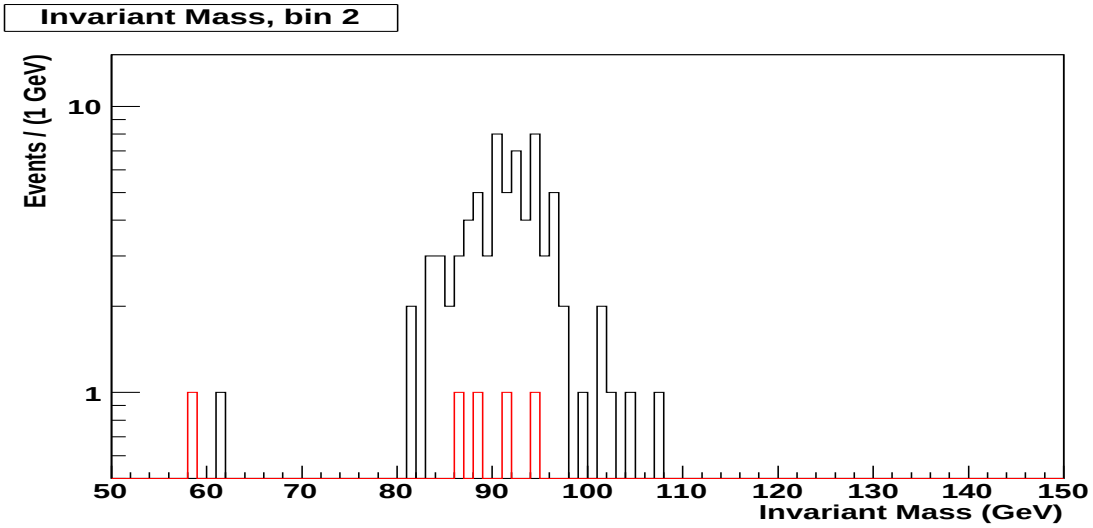

Figure 13.69: Invariant mass for Type 4 electrons in Bin 2. Correctly assigned charges are shown in black, incorrectly assigned charges are shown in red.

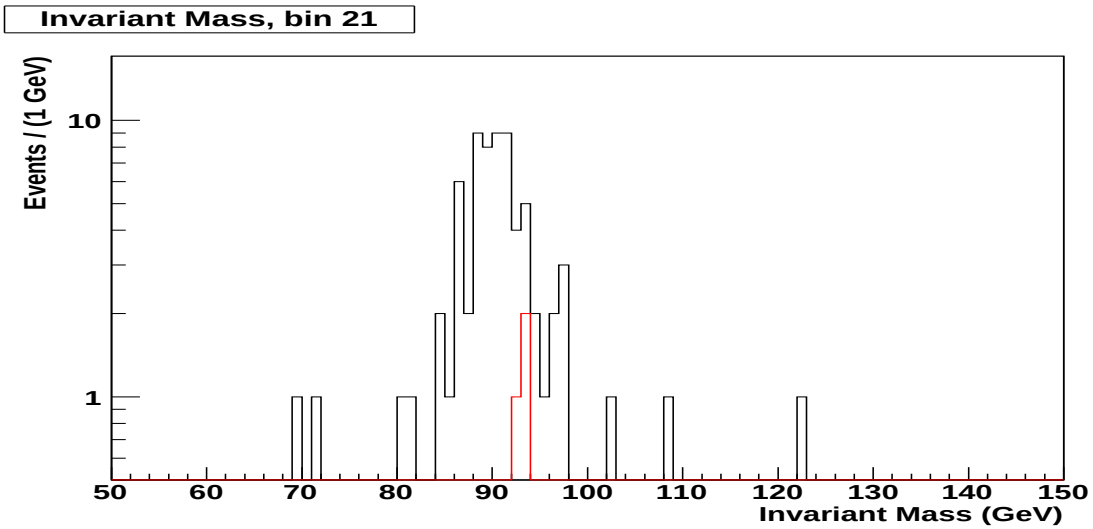

Figure 13.70: Invariant mass for Type 4 electrons in Bin 21. Correctly assigned charges are shown in black, incorrectly assigned charges are shown in red.

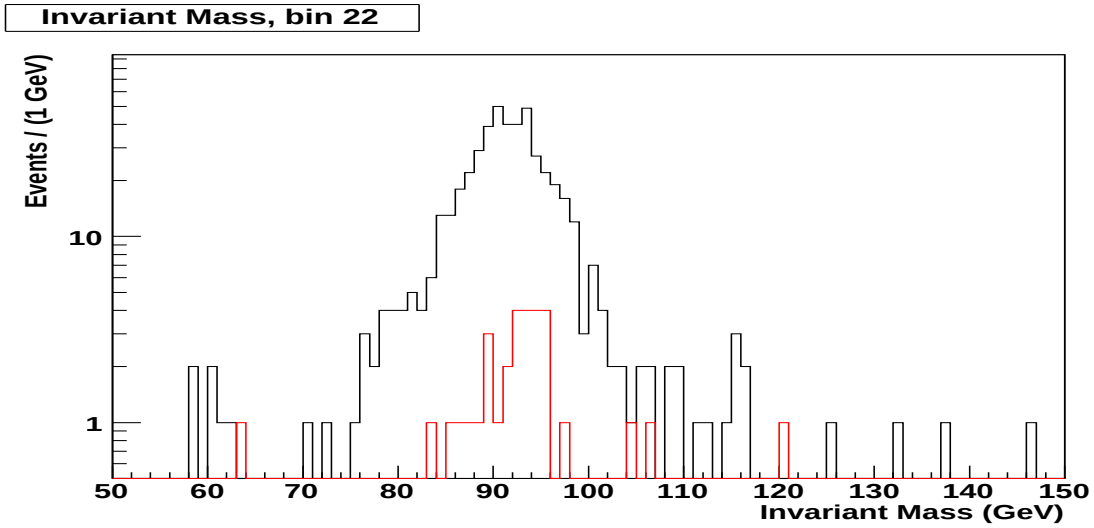

Figure 13.71: Invariant mass for Type 4 electrons in Bin 22. Correctly assigned charges are shown in black, incorrectly assigned charges are shown in red.

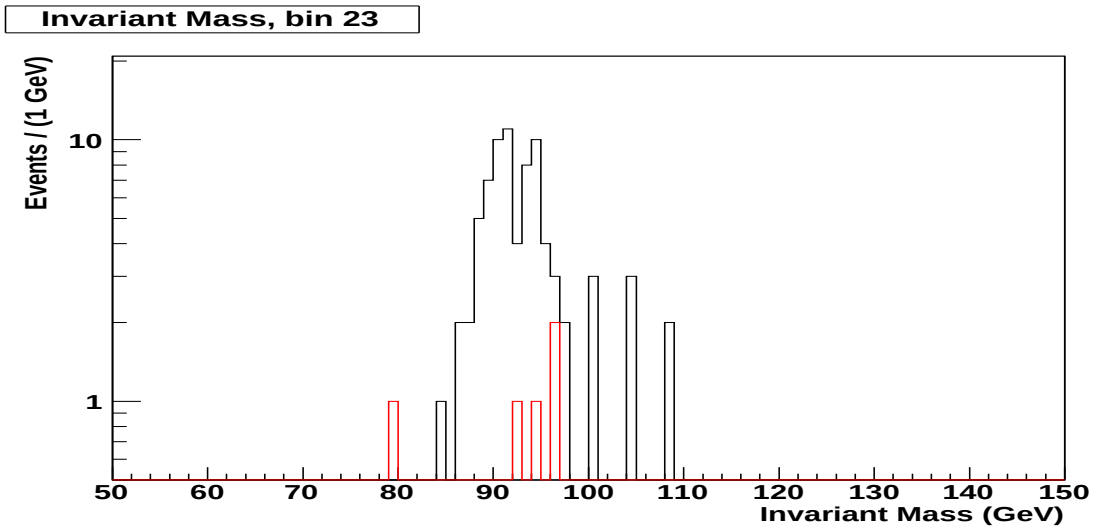

Figure 13.72: Invariant mass for Type 4 electrons in Bin 23. Correctly assigned charges are shown in black, incorrectly assigned charges are shown in red.